Interfaculty Institute for Cell Biology

Department of Immunology

# Influence of Toll-like receptor (TLR)- and other B-cell signalling pathways on MyD88-mutation-mediated lymphomagenesis

Dissertation
submitted for a doctoral degree in
medicine

at the
Faculty of Medicine
of the Eberhard Karls University
Tübingen

submitted by
Obermüller, Carina

2020

Dean: Professor Dr. B. Pichler

First reviewer: Professor Dr. A. Weber

Second reviewer: Professor Dr. K. Schilbach-Stückle

Date of the oral examination: 04.10.2021

# Table of Contents

# List of Tables

# List of Figures

## List of Abbreviations (in alphabetical order)

| | |
|---|---|
| ABC | Activated B-cell-like subtype of DLBCL |
| ALL | Acute lymphoblastic leukaemia |
| AP1 | Activator protein 1 |
| ARDS | Acute respiratory distress syndrome |
| BAFF | B-cell activating factor |
| BAFF-R | BAFF receptor |
| BCAP | B-cell adaptor for phosphoinositide-3-kinase |
| BCL | B-cell lymphoma |
| BCMA | B-cell maturation antigen |
| BLIMP-1 | B lymphocyte-induced maturation protein-1 |
| BLNK | B-cell linker protein |
| Bq | Becquerel |
| BTK | Bruton’s tyrosine kinase |
| CAGS | Cytomegalovirus early enhancer/chicken β-actin |
| CARD11 | Caspase recruitment domain-containing protein 11 |
| CAR-T-cells | Chimeric antigen receptor T-cells |
| CCL | C-C motif chemokine ligand |
| CLL | Chronic lymphocytic leukaemia |
| CpG | Cytosine guanosine deoxynucleotide |
| CR | Complete remission |
| CREB | CAMP response element-binding protein |
| CXCR4 | C-X-C chemokine receptor type 4 |
| CXCL4 | C-X-C chemokine ligand type 4 |
| DAG | Diacylglycerol |
| DD | Death domain |
| df | Degrees of freedom |
| DLBCL | Diffuse large B-cell lymphoma |
| dsRNA | Double-stranded RNA |
| EMA | European medicines agency |

| | |
|---|---|
| FCS | Fetal calf serum |
| FDA | Food and drug administration |
| FDG | [$^{18}$F]-deoxyglucose |
| FL | Follicular lymphoma |
| FLT | [$^{18}$F]-thymidine |
| GC | Germinal center |
| GCB | Germinal center B-cell subtype of DLBCL |
| GEB | Gene expression profiling |
| ID | Injected dose |
| Ig | Immunoglobulin |
| IGH | Immunoglobulin heavy chain |
| IκB | Inhibitor of κB |
| IKKγ | IκB kinase, synonymous to NEMO (NF-κB essential modulator) |
| IL | Interleukin |
| IL1R8 | Interleukin-1 receptor 8 |
| IL1RL1 | Interleukin-1 receptor-like 1 |
| iODN | Inhibitory oligodeoxynucleotide |
| IP3 | Inositol-1,4,5-trisphosphate |
| IRAK-M | IL-1-receptor (IL-1R)-associated kinase M |
| IRAK1 | Interleukin-1 receptor-associated kinase 1 |
| IRAK4 | Interleukin-1 receptor-associated kinase 4 |
| IRF | Interferon regulatory factor |
| ITAMs | Immunoreceptor tyrosine-based activation motifs |
| JAK | Janus kinase |
| JNK | C-Jun terminal kinase |
| KLHL14 | Kelch Like Family Member 14 |
| LPS | Lipopolysaccharide |
| LRR | Leucine-rich-repeat-domain |
| LUBAC | Linear ubiquitin chain assembly complex |
| LYN | Lck/Yes novel tyrosine kinase |

| | |
|---|---|
| Mal | MyD88 adaptor-like |
| MALT | Mucosa-associated lymphoid tissue |
| MALT1 | Mucosa-associated lymphoid tissue lymphoma translocation protein 1 |
| MAPK | Mitogen-activated protein kinase |
| MAPK14 | Mitogen-activated protein kinase 14, synonymous to p38 |
| MBC | Mice with the *Myd88*$^{p.L252P}$ mutation and *Bcl2* amplifications |
| MC | Mice with the *Myd88*$^{p.L252P}$ mutation |
| MCL | Mantle cell lymphoma |
| MFI | Mean fluorescence intensity |
| MHC | Major histocompatibility complex |
| MM | Multiple myeloma |
| mTOR | Mammalian target of rapamycin |
| MYC | Myelocytomatosis |
| MyD88 | Myeloid differentiation primary response protein (MyD) 88 |
| MyD88$^{L265P}$ | MyD88 in which leucine was switched to proline at position 265 |
| MyD88$^{p.L252P}$ | Murine analogue to MyD88$^{L265P}$ |
| MyD88s | MyD88 short |
| MZL | Marginal zone lymphoma |
| NEC | Necrotizing enterocolitis |
| NEMO | NF-κB essential modulator, synonymous to IKK |
| NF-κB | Nuclear factor-κB |
| NFAT | Nuclear factor of activated T-cells |
| NIRF | Near-infrared fluorescence |
| NLRP | NLR family pyrin domain containing |
| ORR | Objective response rate |
| p38 | Synonymous to MAPK14 |
| PBS | Phosphate-buffered saline |
| PCK | Protein kinase C |
| PCR | Polymerase chain reaction |
| PD | Progressive disease |

| | |
|---|---|
| PD-1 | Programmed cell death protein 1 |
| PD-L | Programmed death-ligand |
| PET | Positron emission tomography |
| PI3K | Phosphoinositide 3-kinase |
| PIP2 | Phosphatidylinositol-4,5-bisphosphate |
| PIP3 | Phosphatidylinositol-3,4,5-triphosphate |
| PLA | Proximity-ligation-assay |
| PLC-γ2 | Phospholipase C γ2 |
| Poly I:C | Polyinosinic:polycytidylic acid |
| PR | Partial remission |
| R848 | Resiquimod |
| RGD | Peptide with Arg-Gly-Asp sequence |
| ROI | Region of interest |
| S | Svedberg sedimentation coefficient |
| SARM | Sterile alpha- and armadillo-motif-containing protein |
| SD | Stable disease |
| SIGIRR | Single immunoglobulin IL-1R-related molecule |
| SLE | Systemic lupus erythematosus |
| Sm/RNP | Smith/Ribonucleoprotein |
| SMZL | Splenic marginal zone lymphoma |
| SOCS1 | Suppressor of cytokine signalling 1 |
| SPF | Specific pathogen free |
| SPOP | Speckle-type BTB–POZ protein |
| ssRNA | Single-stranded RNA |
| STAT | Signal transducer and activator of transcription |
| SYK | Spleen tyrosine kinase |
| TACI | Transmembrane activator and calcium-modulating cyclophilin ligand interactor |
| TAK1 | Transforming growth factor-β-activated kinase |
| TBL1XR1 | TBL1X Receptor 1 |

| | |
|---|---|
| Tfh | follicular helper T-cells |
| Th1 | Helper T-cells type 1 |
| Th17 | Helper T-cells type 17 |
| Th2 | Helper T-cells type 2 |
| TIRAP | TIR-domain-containing adaptor protein |
| TLR | Toll-like receptor |
| TNF | Tumour necrosis factor |
| TP53 | Tumor protein p53 |
| TRAF6 | Tumour necrosis factor receptor-associated factor 6 |
| TRAM | TRIF-related adaptor molecule |
| Treg | Regulatory T-cells |
| TRIF | TIR-domain-containing adaptor protein inducing interferon-β |
| TSE | Turbo spin echo |
| U | Mann-Whitney U |
| UBC13 | Ubiquitin-conjugating enzyme |
| WM | Waldenström macroglobulinemia |
| WT | Wildtype mice or cells without genetic modification, in particular no *Myd88*$^{p.L252P}$ mutation, *Bcl2* amplification or *Cd19* modification |

# 1. Introduction

## 1.1. The immune system

The immune system aims to defend the body against anything that is non-self. It consists of several parts, including specialized organs such as the spleen, the lymph nodes and the bone marrow, various cell types and soluble factors such as cytokines and antibodies. Its purpose is to fend of dangers from microorganisms and tumourigenic transformation. It does so by distinguishing between self and non-self or altered-self, or more specifically, between harmful and non-harmful. Given the many pathogens constantly present, including microbes, viruses and fungi, some dangerous, some beneficial, this is a difficult task within any organism. The key question becomes: How does the immune system sense and prevent a pathogenic attack on the organism? Looking at immune responses in general, three categories of defence can be distinguished: It starts with physical and chemical barriers such as the skin and low pH and moves up to complex innate and adaptive immune responses mediated by various specialized organs, cells and molecules. Interestingly, these defence mechanisms are not necessarily separated but interact with each other at different levels and time points of many immune responses.

## 1.2. The innate immune system

### 1.2.1. Overview

The innate immune system is in many cases the first mechanism of defence following barrier mechanisms such as the skin and low pH. It is conserved throughout many species, including plants. Its mechanisms in humans include cells such as neutrophils, DCs (dendritic cells), NK (natural killer) cells, monocytes and macrophages and soluble factors including many cytokines and the complement system. Janeway first postulated in 1989 that there is an innate immune system that distinguishes self from non-self via so-called PRRs (pattern-recognition receptors) (Janeway, 1989). Further research later revealed that both intracellular and extracellular microbial components can be detected via these germ-line encoded and thus invariable pattern-recognition receptors (Brubaker et al., 2015). Based on protein domain homology, most pattern-recognition receptors fit into one of five families: TLRs (Toll-like receptors), CLRs (C-type lectin receptors), NLRs (NOD-like receptors), RLRs (RIG-1-like receptors) and ALRs (AIM2-like receptors). While TLRs and CLRs are located on the cell surface;

RLRs, ALRs and NLRs are located in the cytoplasm (Brubaker et al., 2015). Activation of PRRs leads to changes on a transcriptional and non-transcriptional level that regulate the course of any further immune responses, both innate and adaptive. Transcriptional changes include NF-κB (nuclear factor-κB) activation and the production of inflammatory cytokines like IL (interleukin) 1 and 18 as well as interferons like IRF (interferon regulatory factor) 3 and 7 (Brubaker et al., 2015). Non-transcriptional changes include the induction of apoptosis and phagocytosis (Brubaker et al., 2015). Ideally, PPRs only recognize molecular patterns unique to microbes and absent in host tissue. The patterns recognized by PRRs have been coined as PAMPs (pathogen-associated molecular patterns) or, recognizing the fact that not only harmful but also beneficial microbes are recognized by PRRs, as MAMPs (microbe-associated molecular patterns). Furthermore, PRRs recognize so-called DAMPs (damage-associated molecular patterns) (Matzinger, 2002), which are released by cells present in various inflammatory diseases (Roh and Sohn, 2018) and even cancers (Patidar et al., 2018). Deregulation in pattern recognition by PRRs can thus lead to both autoinflammatory diseases and outbreak of cancer.

As already mentioned in section 1.1, the innate immune system also interacts with the adaptive immune system, for example via specialized antigen-presenting cells like dendritic cells. Antigens and APCs (antigen-presenting cells) are present in the tissue and interstitium and get transported to nearby lymph nodes via the lymph. APCs can process antigens internally to peptides that they then present on MHC (major histocompatibility complex) class I and MHC class II molecules on their cell surface. In the lymph nodes, APCs display these antigen-derived peptides to T-cells. This leads to a clonal expansion of lymphocytes and thus production of more lymphocytes (Willard-Mack, 2006). While MHC class II molecules are expressed mostly on APCs, MHC class I molecules are present on cells of many different tissues. Some APCs have the ability to present exogenous antigens on MHC I as well, which is then referred to as cross presentation.

### 1.2.2. The Toll-like receptors

TLRs are membrane-bound PPRs found on many immune cells. The main outcomes of TLR signalling are the production of inflammatory cytokines or type I interferons (IFNα and β) (De Nardo, 2015). TLRs bind a variety of different ligands (see Table 1) including lipoproteins, LPS (lipopolysaccharide), flagellin and nucleic acids. In humans, ten different TLRs are known (TLR1-10). Mice do not have TLR10, but express three further TLRs (TLR11-13). Several TLRs recognise nucleic acids (TLR3, TLR7, TLR8, TLR9 and TLR13), which are not exclusive to pathogens but present in both humans and mice and thus require several safety mechanisms to prevent accidental activation. These safety mechanisms include compartmentalisation of TLR sensing to endosomes (see Table 1), activation only upon low pH present in endosomes and focusing on pathogen-specific features. One example of pathogen-specific features are CG motives, which are almost always methylated in the human genome. This makes non-methylated CG repeats more specific for non-human genomes and therefore a good target for PRR sensing – in this case for TLR9. Failing of these safety measures can lead to chronic inflammatory diseases such as atherosclerosis or rheumatoid arthritis as well as autoimmunity as described in SLE (systemic lupus erythematosus) or multiple sclerosis (De Nardo, 2015).

Table 1 **TLR receptors**. Adapted from De Nardo et al., 2015 and Janeway et al., 2017: 89. dsRNA = double-stranded RNA, poly I:C = polyinosinic:polycytidylic acid, LPS = lipopolysaccharide, ssRNA = single-stranded RNA, R848 = Resiquimod, CpG = cytosine triphosphate deoxynucleotide linked to a guanine triphosphate deoxynucleotide via a phosphodiester, S = svedberg sedimentation coefficient (a measure of how fast a molecule moves during centrifugation, thereby a measure for its density and thus an approximate for its size).

| TLR | Species | Localisation | Ligands (microbial and synthetic) |
|---|---|---|---|
| **TLR1:TLR2 heterodimer** | Human, mouse | Plasma membrane | • Lipomannans (*mycobacteria*)<br>• Lipoproteins (*gram-negative bacteria*)<br>• Lipoteichoic acids (*gram-positive bacteria*)<br>• Cell-wall ß-glucans (*bacteria and fungi*)<br>• Zymosan (*fungi*) |
| **TLR2:TLR6 heterodimer** | Human, mouse | Plasma membrane | |
| **TLR3** | Human, mouse | Endosome | • dsRNA (*viruses*)<br>• poly I:C (*synthetic*) |
| **TLR4** | Human, mouse | Plasma membrane, Endosome | • LPS (*gram-negative bacteria*)<br>• Lipoteichoic acids (*gram-positive bacteria*) |
| **TLR5** | Human, mouse | Plasma membrane | • Flagellin (*bacteria*) |
| **TLR7** | Human, mouse | Endosome | • ssRNA (*viruses and bacteria*)<br>• R848 (*synthetic*)<br>• Imiquimod (*synthetic*) |
| **TLR8** | Human, mouse | Endosome | • ssRNA (*viruses and bacteria*)<br>• R848 (*synthetic*)<br>• Imiquimod (*synthetic*) |
| **TLR9** | Human, mouse | Endosome | • DNA with non-methylated CpG (*bacteria and herpesviruses*)<br>• CpG (*synthetic*) |
| **TLR10** | Human | Plasma membrane | • Unknown |
| **TLR11** | Mouse | Endosome | • Profilin and profilin-like proteins (*Toxoplasma gondii, uropathogenic bacteria*) |
| **TLR12** | Mouse | Endosome | • Profilin (*Toxoplasma gondii*) |
| **TLR13** | Mouse | Endosome | • 23S ribosomal RNA (*bacteria*) |

TLRs are type I transmembrane proteins, meaning they have a single transmembrane domain. Their N-terminal, ligand binding domain lies on the extracellular side of the membrane. In the case of endosomal TLRs, the ligand binding end lies in the lumen of the endosomes. The N-terminus features a repetitive LRR (leucine-rich-repeat) domain, a horseshoe-shaped protein motif with 19 to 25 repeats per TLR and 24 to 29 amino acids per repeat (Akira and Takeda, 2004). The cytosolic C-terminus has a TIR (Toll/interleukin-1 receptor) domain that can bind to TIR domains of downstream adaptor proteins via homotypic domain interaction to promote subsequent signal transduction.

### 1.2.3. The Toll-like receptor signalling pathway

TLR activation via ligand binding to the LRR domain leads to homo- or heterodimerization (see Table 1) of TLRs and further downstream signalling via adaptor proteins. MyD88 (myeloid differentiation primary-response protein 88) is the predominant adaptor molecule for all TLRs, except for TLR3, which only uses TRIF (TIR-domain-containing adaptor protein inducing interferon-β) as an adaptor (Akira and Takeda, 2004). TLR4 uses TRIF too but needs TRAM (TRIF-related adaptor molecule) as an intermediate adaptor (De Nardo, 2015). Besides MyD88, TRIF and TRAM, TIRAP (TIR-domain-containing adaptor protein), also called Mal (MyD88 adaptor-like), serves as an adaptor as well (Akira and Takeda, 2004). The adaptor SARM (sterile alpha- and armadillo-motif-containing protein) is a negative regulator of TLR3 and TLR4 signalling by directly binding to TRIF and possibly also a negative regulator of MyD88 (Carlsson et al., 2016). Other negative regulators of the TLR pathway include IRAK-M (IL-1-receptor-associated kinase M), SOCS1 (suppressor of cytokine signalling 1), MyD88s (MyD88 short), SIGIRR (single immunoglobulin IL-1R-related molecule) and IL1RL1 (interleukin-1 receptor-like 1) (Akira and Takeda, 2004). Recently, SPOP (Speckle-type BTB–POZ protein) was also identified as an important negative regulator of MyD88 in emergency haematopoiesis (Guillamot et al., 2019).

Besides the TIR domain, MyD88 has a DD (death domain) that associates with the DDs of IRAK (interleukin-1 receptor-associated kinase) 1 and 4, forming the so-called Myddosome. MyD88 can pair with Mal as additional signalling molecule. IRAK1 and IRAK4 autophosphorylate within the Myddosome and then phosphorylate TRAF6 (tumour necrosis factor receptor-associated factor 6). TRAF6 is a ubiquitin E3 ligase that transfers ubiquitin to its target proteins TAB (TAK1-

binding protein) 1 and 2 by ligation at lysine 63, leading to K63-linked polyubiquitin scaffolds. The E2 ligase UBC13 (ubiquitin-conjugating enzyme), which binds ubiquitin transiently, and the cofactor Uve1A are also involved in this ubiquitin transfer. The TAB1/TAB2 scaffolds then recruit TAK1 (transforming growth factor-β-activated kinase). TAK1 is thus brought in proximity of the IRAKs and TAK1 gets phosphorylated by the IRAKs. The K63-linked polyubiquitin scaffolds furthermore recruit the IKKγ subunit of the IKK (IκB (inhibitor of κB) kinase, synonymous to NEMO (NF-κB essential modulator)) complex, which brings TAK1 and the IKK complex in close proximity. TAK1 then activates IKKß via phosphorylation and IKKß phosphorylates IkB. IkB is the cytoplasmatic inhibitor of NF-κB and normally inhibits NF-κB from moving into the nucleus. However, phosphorylation of IkB by IKKß leads to IkB K48 ubiquitination and subsequent degradation. Therefore NF-κB can then translocate into the nucleus and act as a transcription factor for various pro-inflammatory processes, such as IL-6, and for the expression of costimulatory molecules such as CD (cluster of differentiation) 80 and CD86, which are essential for efficient T-cell activation (Figure 1) (Janeway et al., 2017: 95 et seq., De Nardo, 2015).

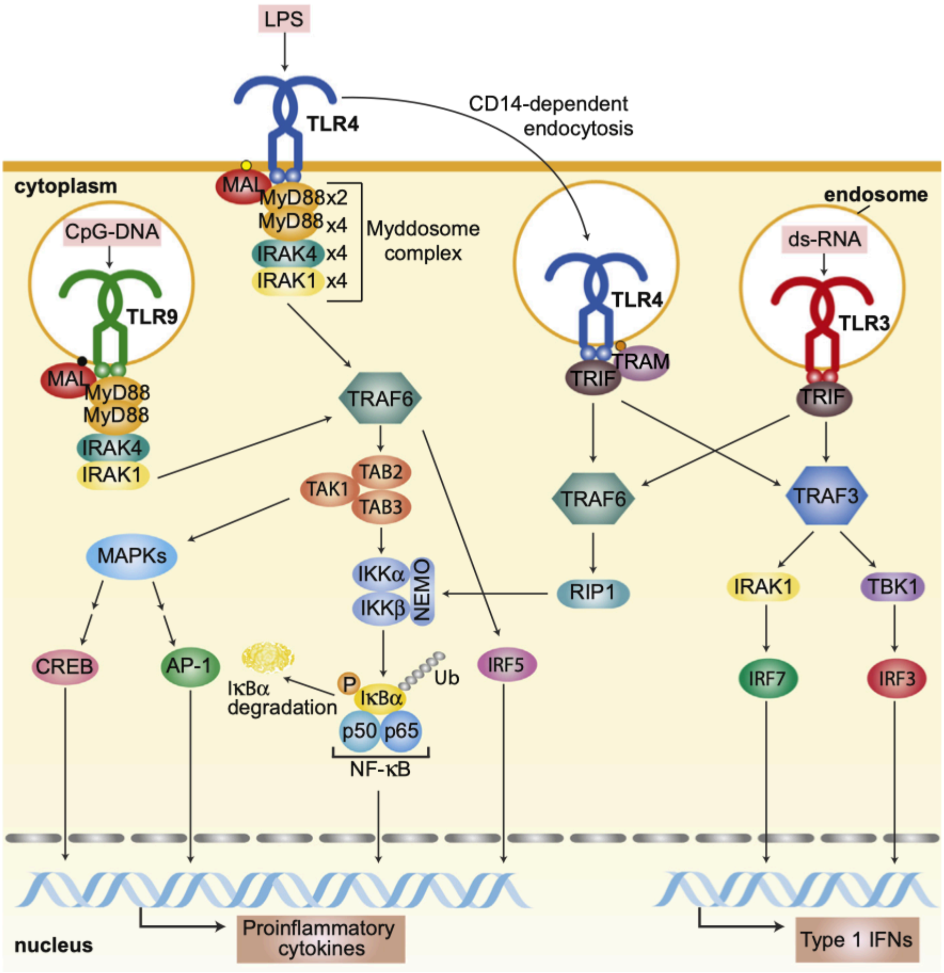

Figure 1 **Overview of TLR signalling pathways** (De Nardo, 2015). For details see text.

Activated TAK1 also activates MAPKs (mitogen-activated protein kinases) like JNK (c-Jun terminal kinase) and MAPK14 (synonymous to p38). JNK and p38 activate transcription factors of the AP1 (activator protein 1) family and CREB (cAMP response element-binding protein), which lead to the transcription of pro-inflammatory cytokines. As a second outcome besides pro-inflammatory cytokines, TLR3 and TLR4 signalling can lead to transcription of type I interferons via IRF3 and IRF7 (Figure 1) (Janeway et al., 2017: 95 et seq., De Nardo, 2015).

### 1.2.4. MyD88 and its role in innate immunity

Besides TLRs, MyD88 is also the downstream adaptor molecule for IL-1 and IL-18 receptors (Deguine and Barton, 2014). MyD88 deficiency commonly leads to immunodeficiency in both mice and humans. In a study with nine children suffering from autosomal recessive MyD88 deficiency, the main reason for even life-threatening clinical situations were recurrent pyogenic bacterial infections, primarily with *Streptococcus pneumoniae*. Interestingly, the children were otherwise healthy and did not show a tendency towards other recurrent infectious diseases (von Bernuth et al., 2008). In rats, the TLR4/MyD88 signalling pathway seems to play a role in sepsis-associated ARDS (acute respiratory distress syndrome) (Zhou et al., 2018). MyD88 is also important for healthy myeloid haematopoiesis and B-cell development (Fiedler et al., 2013). Concerning autoimmune diseases such as SLE, where sensing of self-derived nucleic acids by endosomal TLRs is aberrant, inhibiting MyD88 and the Toll-like receptor pathway could be a potential therapeutic target (Wu et al., 2015).

## 1.3. The adaptive immune system

As mentioned in section 1.1, the immune system does not only involve innate immune responses to non-self, but also adaptive, more long-term responses. The main two cell types involved in adaptive immune responses are T-cells and B-cells, which will be described briefly below.

### 1.3.1. T-cells

T-cells, like all immune cells, are derived from the hematopoietic stem cells in the bone marrow and continue to develop in the thymus (Seo and Taniuchi, 2016). Their defining feature is the TCR (T-cell receptor), accompanied by the co-receptors CD4 or CD8. CD8-positive T-cells, for example CTLs (cytotoxic killer T-cells), kill virus-infected cells and cancer cells. For this purpose, CTLs utilise mechanisms like perforin and granzyme B for cell permeabilisation, apoptosis induction via the intrinsic pathway or Fas ligands for extrinsic apoptosis induction. T-cells are primed with their cognate antigen by professional antigen-presenting cells and second signals via CD80/CD86. Subsequently, they can be activated by peptides presented via the MHC class I molecules mentioned in section 1.2.1, which are present on most nucleated cells (Mittrucker et al., 2014). CD4-positive cells, for example helper T-cells, help antigen-specific B-cells to develop into antibody-secreting plasma cells and regulate humoral immune function. CD4 T-cells are stimulated by antigens presented on MHC class II molecules (Holling et al., 2004). Several different subsets of CD4-positive T-cells exist, including helper Th1 (T-cells type 1), Th2 (helper T-cells type 2), Th17 (helper T-cells type 17), Tfh (follicular helper T-cells) and Treg (regulatory T-cells) (Zhu et al., 2010). While Th1, Th2, Th17 and Tfh cells lead to activation of their target cells, Treg cells inhibit the immune response (Janeway et al., 2017: 346 et seq.). The classical view is that Th1 cells act in the defence against intracellular parasites and tumour cells, Th2 cells against helminths and extracellular pathogens, Th17 cells against extracellular bacteria or fungi and Tfh cells help B-cells in antibody production, affinity maturation and antibody class switching (Sun and Zhang, 2014). However, further CD4 T-cell subsets exist and research is currently re-evaluating these classical definitions of T-cell subset roles.

### 1.3.2. B-cells

#### 1.3.2.1. B-cell development

B-cells mature from haematopoietic stem cells via pro-B-cells to pre-B-cells to immature B-cells in the bone marrow, which are then released into peripheral lymphoid organs (Figure 2). There, antigen-dependent differentiation occurs from immature B-cells to mature naïve B-cells. In the case of their activation via the BCR (B-cell receptor) and additional signals including those of CD4-positive T-helper cells (see 1.3.1.1.), these naïve B-cells transform into lymphoblasts and plasmablasts, producing soluble antibodies. Eventually some become memory B-cells for faster recruitment at reinfections (Janeway et al., 2017: 399 et seq.). Starting from the pre-B-cell stage, B-cells express the surface marker CD20 (Figure 2) (Blanc et al., 2011), which is nowadays commonly used for anti-CD20 therapies in malignant lymphoma (Salles et al., 2017).

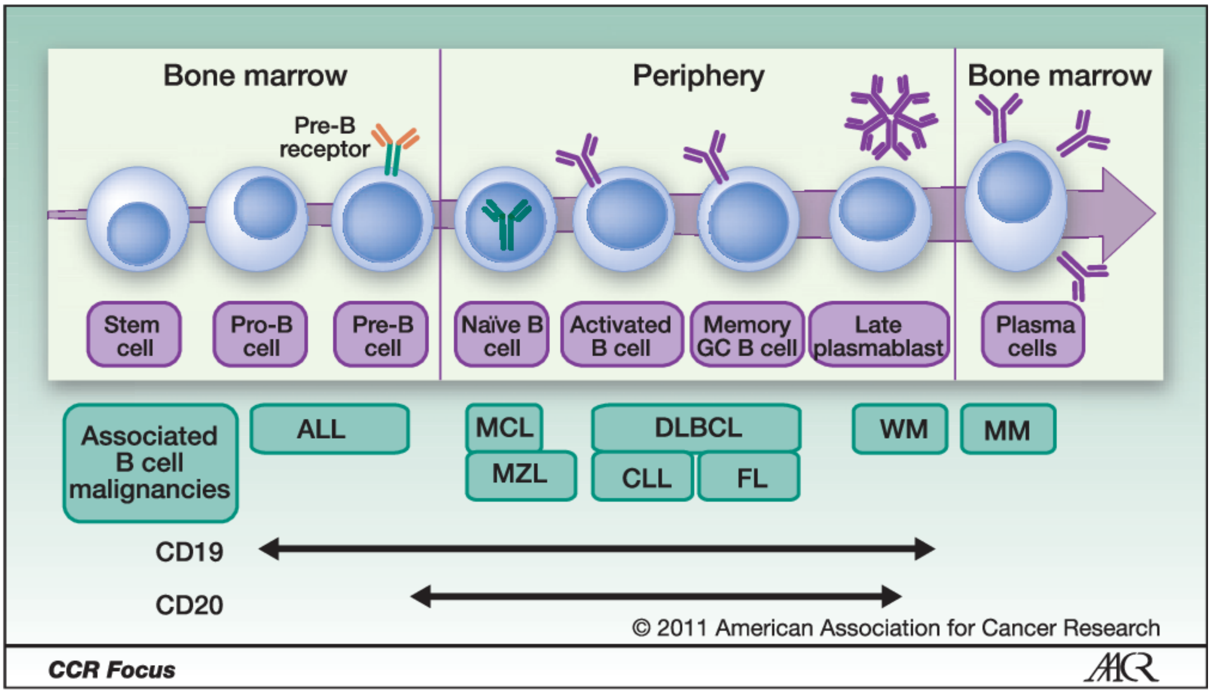

Figure 2 **Overview of B-cell development stages and associated B-cell malignancies (Blanc et al., 2011).** The expression pattern of CD19 and CD20 antigens during B-cell development is shown. The positioning of the different B-cell malignancies associated with different stages of B-cell development is abridged and illustrative only. GC = germinal center, ALL = acute lymphoblastic leukaemia, MCL = mantle cell lymphoma, MZL = marginal zone lymphoma, DLBCL = diffuse large B-cell lymphoma, CLL = chronic lymphocytic leukaemia, FL = follicular lymphoma, WM = Waldenström macroglobulinemia, MM = multiple myeloma.

Antibodies and the BCR consist of a variable antigen-binding and a constant effector region, structurally composed of two heavy chains and two light chains that each have variable and constant regions. In order to cover a wide variety of different antigens provided by pathogens, these chains are altered from a large repertoire of gene segments into many different combinations during B-cell development via the so-called VDJ-rearrangement. VDJ refers to the gene regions V, D and J that provide this repertoire. In VDJ-rearrangement, three random gene segments, one of each region respectively, are combined and the remaining DNA is removed. This process occurs at both heavy and light chain loci. Further customisation of the BCR occurs in the germinal center via somatic hypermutation (Janeway et al., 2017: 314 et seq.).

Additionally, antibodies can be classified into several Ig (immunoglobulin) classes via their constant region. While the BCR on immature B-cells belongs to the IgM class, mature naïve B-cells express both IgM and IgD. Lymphoblasts undergo a so-called class-switch from IgM to

IgG, IgA or IgE during development into plasma B-cells or memory B-cells (Janeway et al., 2017: 314 et seq.).

### 1.3.2.2. The B-cell receptor signalling pathway

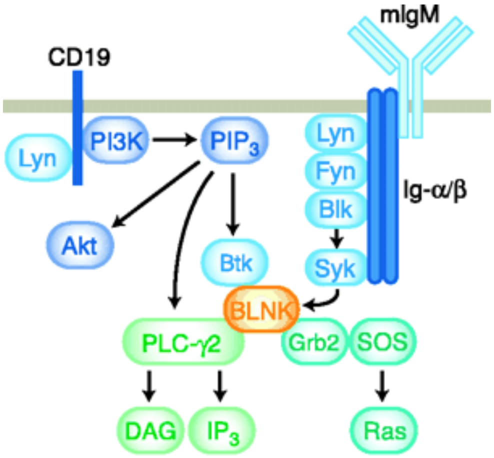

Figure 3 **Overview of the B-cell receptor signalling pathway (Gauld et al., 2002)**. For details and abbreviations see text.

The BCR, mostly consisting of an IgM immunoglobulin, intracellularly binds to a heterodimer of CD79A and CD79B, which contain so-called ITAMs (immunoreceptor tyrosine-based activation motifs). If the BCR is activated by antigen-binding, the ITAM tyrosine residues of the CD79 heterodimer become phosphorylated by LYN (Lck/Yes novel tyrosine kinase). This then leads to the recruitment of protein tyrosine kinases such as further LYN and SYK (spleen tyrosine kinase). SYK phosphorylates and thereby activates BLNK (B-cell linker protein). BLNK binds to PLC-γ2 (phospholipase C γ2) and BTK (Bruton tyrosine kinases), thereby bringing PLC-γ2 in proximity of SYK and BTK. SYK and BTK then phosphorylate tyrosine residues of PLC-γ2. PLC-γ2 subsequently produces DAG (diacylglycerol) and IP3 (inositol-1,4,5-trisphosphate) from its substrate PIP2 (phosphatidylinositol-4,5-bisphosphate), a phospholipid found in the cell membrane. DAG and IP3 act as second messengers for downstream effects such as activation of pro-survival transcription factors like NFAT (nuclear factor of activated T-cells). PLC-γ2 also activates PKC (protein kinase C) β, PKCβ phosphorylates CARD (caspase recruitment domain-containing protein) 11 and phosphorylated CARD11 recruits TAK1 and the IKK complex. As described in section 1.2.3, activation of the IKK complex then leads to the phosphorylation of IκB and recruitment of the pro-survival transcription factor NF-κB to the nucleus. LYN additionally phosphorylates CD19, a B-cell specific membrane protein, and SYK and BTK additionally phosphorylate BCAP (B-cell adaptor for phosphoinositide-3-kinase). CD19 or BCAP then bind and activate PI3K (phosphoinositide 3-kinase). PI3K is thereby brought in proximity to the membrane and transforms its substrate PIP2, found in the membrane, into the second messenger PIP3 (phosphatidylinositol-3,4,5-triphosphate). PIP3 then recruits more of the effector proteins mentioned above like BTK, PLCγ2 and PKCβ. In summary, a complex interplay of kinases leads to pro-survival stimuli following BCR stimulation (Seda and Mraz, 2015, Kurosaki, 2011). For an overview of the signalling pathways described here see Figure 3 (Gauld et al., 2002).

In the light of the recent success of BTK inhibitors in lymphoma therapy, it is of interest to note that BTK is essential for B-cell survival (Young et al., 2019). Moreover, BTK has been found to interact with the TIR domains of several TLRs, including TLR9, Fc receptors and the NLRP (NLR family pyrin domain containing) 3 inflammasome, indicating roles beyond B-cells (Weber et al., 2017).

#### 1.3.2.3. Function of CD19

As mentioned in section 1.3.2.2, CD19 is a transmembrane protein that plays an important role in BCR signalling. Since CD19 is a transmembrane protein, it can be targeted at the cell surface. This is currently being exploited in anti-CD19 therapies for malignant lymphoma that do not respond to anti-CD20 therapies – one such example is the CD3-CD19 bispecific monoclonal antibody blinatumomab (Burt et al., 2019).

Interestingly, TLR9 ligands also induce the phosphorylation of CD19 via MyD88/PYK2 (proline-rich tyrosine kinase 2)/LYN complexes, leading to PI3K recruitment and further BTK phosphorylation. One study even came to the conclusion that in B-cells, CD19 is essential for TLR9-mediated B-cell activation (Morbach et al., 2016). This could point towards a potent synergy of TLR-mediated and CD19-mediated therapy in B-cell lymphoma.

#### 1.3.2.4. Function of BAFF and APRIL

BAFF (B-cell activating factor) is a TNF (tumour necrosis factor) -like molecule and a soluble or membrane-bound ligand for the receptors TACI (transmembrane activator and calcium-modulating cyclophilin ligand interactor), BCMA (B-cell maturation antigen) and BAFF-R (BAFF receptor). TACI and BCMA can additionally bind to APRIL (a proliferation-inducing ligand) (Smulski and Eibel, 2018). The roles of individual ligands and receptors vary slightly, with TACI promoting class switching and differentiation of B-cells to plasma cells (Zhang et al., 2015) and BAFF-R promoting NF-κB signalling amongst others (Smulski and Eibel, 2018). TACI confers downstream signals via MyD88 (He et al., 2010). Overall, all ligands and receptors promote B-cell survival.

## 1.4. B-cell Lymphoma

### 1.4.1. Classification of B-cell lymphoma

Neoplasms can arise from any type of immune cell. While leukaemia usually arises from immature immune cells, lymphoma usually derives from mature lymphocytes. Historically, lymphomas were classified into HL (Hodgkin lymphomas) and NHL (Non-Hodgkin lymphomas), whereby NHL cover a wide spectrum of both B-cell and T-cell lymphomas later classified by the origin of cell type. Considering the many differentiation stages and cell types of B- and T-cells, these classifications naturally became rather complex (Jiang et al., 2017). In 2016, the WHO (World Health Organisation) classification from 2008 was revised, classifying all mature lymphoid, histiocytic and dendritic neoplasms as (1) mature B-cell neoplasms (see Table  in appendix), (2) mature T-cell and NK-Cell (Natural Killer cell) neoplasms, (3) HL, (4) PTLD (post-transplant lymphoproliferative disorders) and (5) histiocytic and dendritic cell neoplasms (Swerdlow et al., 2016). Table  (see appendix) lists all mature B-cell neoplasms as classified in the 2016 WHO classification, with DLBCL and DLBCL-like subtypes indicated.

As hinted above, the leukaemia/lymphoma differentiation is increasingly challenged with new molecular and genetic details being discovered. For example, several mature B-cell neoplasms like chronic lymphocytic leukaemia or B-cell prolymphocytic leukaemia carry the name leukaemia although the cell type they originate from is not immature. Similarly, treatment options are becoming increasingly diverse and differ substantially between subtypes.

### 1.4.2. Epidemiology of B-cell lymphoma

Approximately 90% of all lymphomas are Non-Hodgkin lymphomas, while Hodgkin lymphomas make up the rest (Shankland et al., 2012). Among NHLs, around 85% are B-cell lymphomas and 15% are T-cell lymphomas (American Cancer Society, 2018). Since the new WHO classification was published in 2016, most epidemiological data is not yet available using the new classification. Instead, CLL was classified as leukaemia, the subtypes ‘B-cell prolymphocytic leukaemia’, ‘hairy cell leukaemia’ and ‘splenic B-cell lymphoma/leukaemia’ were classified as other leukaemias and myeloma as a separate category.

Table 27 and Table 28 summarise the available epidemiological data from the US and Germany in 2014 according to the WHO 2016 classification, counting approximately 100,000 new B-cell lymphoma cases in 2014 in the US (Table 27 in appendix) and over 30,000 new cases in Germany (Table 28 in appendix). However, classification criteria were often unclear or dissenting, therefore these numbers can only be seen as an approximation. Concerning sex distribution, there is a tendency towards males across all entities in both the US and Germany. Interestingly, although the percentage of estimated total new cases is comparable between the US and Germany, death due to other NHLs makes up a larger percentage in the US than in Germany. Also of note, the median age of disease onset and death both lie above 70 years in Germany (Robert Koch Institut, 2017) and the lifetime probability of developing leukaemia or NHL in the US are both highest in the age group of 70 years and older (Siegel et al., 2014). In the light of increasingly aging populations, this underlines the necessity for new therapies to be developed.

With up to 40% of cases worldwide, DLBCL is the most common subtype of lymphomas (Li et al., 2018b, Stewart et al., 2014). While some other entities such as Burkitt lymphomas show regional differences, DLBCL is common worldwide (Shankland et al., 2012).

## 1.5. Diffuse large B-cell Lymphoma (DLBCL)

### 1.5.1. Classification of DLBCL

DLBCL per se refers to its appearance under the microscope as large, oftentimes diffuse-looking B-cells. Hence several different entities are classified as DLBCL or DLBCL-like (see Table in appendix). About 80% of cases that phenotypically resemble DLBCL fall into the category of DLBCL NOS (not otherwise specified). When classified according to the cell of origin, most DLBCL NOS cases can be classified into either the GCB (germinal center B-cell) subtype or the ABC (activated B-cell-like) subtype. GCB subtypes make up around 50% of all DLBCL NOS cases and ABC subtypes around 30%. While the GCB subtype has a 5-year survival rate of about 60%, the more aggressive ABC subtype only has a 5-year survival rate of about 30%. Concerning the ABC subtype, more than 50% of cases have mutations in molecules involved in NF-κB activation. Examples include *CD79A* or *CD79B* mutations in 20% of ABC DLBCL cases and *MYD88* mutations in 30% of ABC DLBCL cases (Beham-Schmid, 2017, Chiappella et al., 2017). Using multiple sequencing approaches, approximately 50% of DLBCL cases can be categorised into four genetically distinct subtypes that vary in their distribution among ABC DLBCL cases and GCB DLBCL cases (Figure 4). These subtypes are labelled according to some of their hallmark genetic aberrations, namely the MCD subtype (*MYD88*$^{L265P}$ and *CD79B* mutations), the BN2 subtype (*BCL6* fusions and *NOTCH2* mutations), the N1 subtype (*NOTCH1* mutations) and the EZB subtype (*EZH2* mutations and *BCL2* translocations). The MCD subtype, for which *MYD88*$^{L265P}$ is a hallmark mutation, consists almost exclusively of ABC DLBCL cases. The remaining 50% of DLBCL cases most likely belong to other, less frequent genetic subtypes (Young et al., 2019, Schmitz et al., 2018).

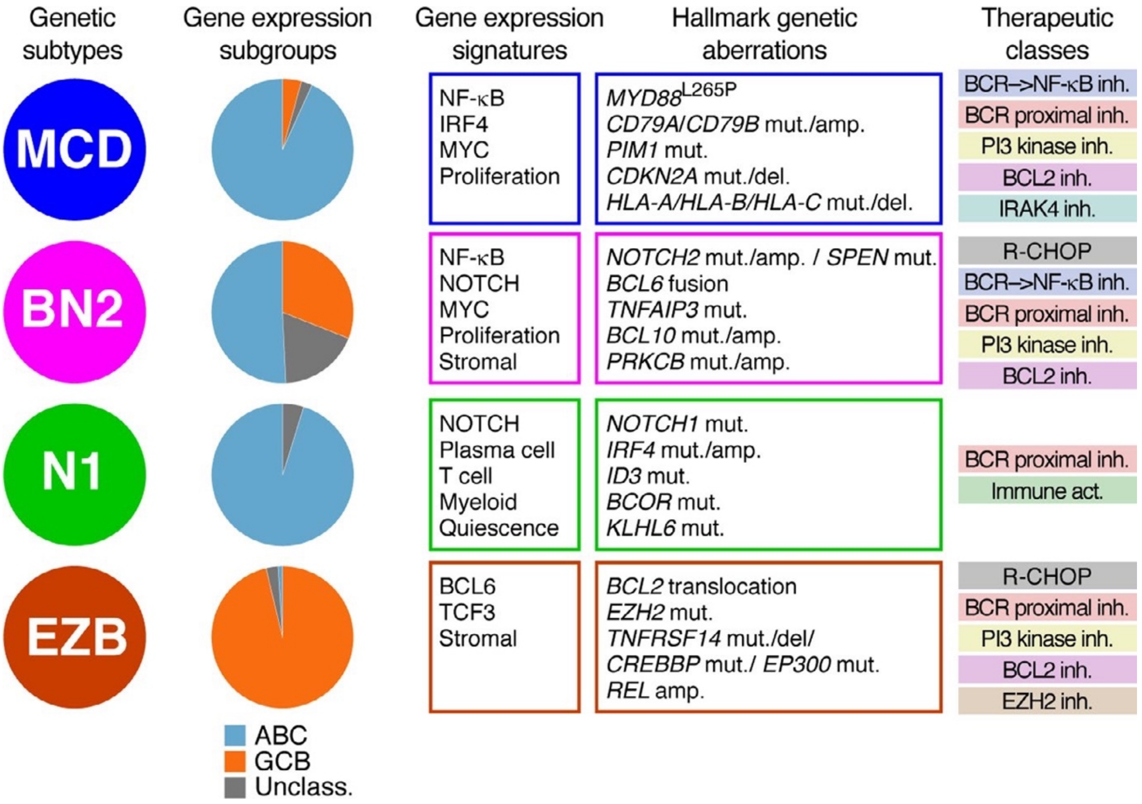

Figure 4 **Combination of different sequencing approaches revealed four distinct genetic subtypes of DLBCL (Young et al., 2019).** Approximately 50% of DLBCL cases can be categorised into four genetically distinct subtypes that vary in their distribution among ABC DLBCL cases and GCB DLBCL cases. The subtypes are labelled according to some of their hallmark genetic aberrations, namely the MCD subtype (*MYD88*$^{L265P}$ and *CD79B* mutations), the BN2 subtype (*BCL6* fusions and *NOTCH2* mutations), the N1 subtype (*NOTCH1* mutations) and the EZB subtype (*EZH2* mutations and *BCL2* translocations). inh. = inhibitors, Unclass. = unclassified, mut. = mutation, del. = deletion, amp. = amplification.

### 1.5.2. Pathophysiology of DLBCL

DLBCLs, especially DLBCL NOS, are a heterogenous group in its pathogenesis: On average, 75 to 90 mutations per DLBCL NOS were shown. Some common mutations include *TP53* (tumor protein p53) loss-of-function mutations (about 20% of cases) and rearrangements of the genes *MYC* (Myelocytomatosis) (about 10 to 15% of cases), *BCL* (B-cell lymphoma) *2* (about 20 to 30% of cases) and *BCL6* (about 30% of cases). All of these mutations prevent apoptosis or lead to increased survival of tumour cells. Rearrangement of *IGH* (immunoglobulin heavy chain), a gene whose promotor is highly active in B-cells and also leads to higher expression of other target genes such as *BCL2*, occurs in almost all DLBCL NOS cases. Around 40% of DLBCL NOS patients have extranodal disease (disease outside of lymphoid tissue), most commonly in the gastrointestinal tract, and 10 to 20% show bone marrow involvement. 20 to 25% of DLBCL NOS cases express PD-L (programmed death-ligand) 1 and 2 (see section 1.5.4) and 50 to 70% highly express the BCR on their cell surface, most commonly IgM (Li et al., 2018b). The $\mathit{MYD88}^{L265P}$ mutation is present in almost 30% of ABC cases, with some suggesting percentages as high as 39% (Ngo et al., 2011) while others report 21% (Lee et al., 2017). Amongst other effects, NF-κB signalling in ABC DLBCL drives IRF4 expression and thereby promotes plasma cell differentiation. Full differentiation of plasma cells is however often prohibited in ABC DLBCL due to the inactivation of BLIMP-1 (B lymphocyte-induced maturation protein-1) and the activation of IRF4 repressors such as BCL6, thereby promoting a state of B-cell proliferation but not terminal differentiation (Young et al., 2019). Besides genetic changes, differences in tumour microenvironment also play a role in DBLCL pathogenesis, with the presence of macrophages being beneficial and angiogenesis being unfavourable (Lenz et al., 2008).

Tonic BCR signalling, a form of BCR signalling that is present in all mature B-cells and in which the BCR transmits low-level “tonic” signals even in the absence of antigen to sustain general survival, is common in GCB DLBCL. On the contrary, ABC DLBCL is thought to rely on auto-antigen-triggered chronic active BCR signalling and signalling dependent on a supercomplex consisting of MyD88, TLR9 and the BCR (My-T-BCR). This leads to excessive downstream BCR and therefore NF-κB signalling. In the case of My-T-BCR signalling, BCRs are internalised via endocytosis and fuse with TLR9-containing lysosomes, thus allowing stimulation of TLR9 and downstream MyD88 signalling (Young et al., 2019). Interestingly, My-T-BCR signalling relies on a heterogenous genotype of CD79B with both wildtype and mutant CD79B: While BCR internalisation and thus TLR9 stimulation relies on wildtype CD79B, mutant CD79B impairs BCR internalisation. This in turn increases BCR expression on the B-cell surface, thus enhancing proximal BCR signalling, which promotes formation of the CBM (CARD11, BCL10, MALT1 (mucosa-associated lymphoid tissue lymphoma translocation protein 1)) complex necessary for downstream TLR9 signalling (Young et al., 2019). Besides apoptotic cells, excessive BCR signalling can also be triggered by certain BCRs themselves. In particular, the BCR V region $V_H$4-34 has been found to be increased in ABC DLBCL, which is remarkable given that over 15,000 different V regions are possible. Normally $V_H$4-34 BCRs lead to anergic B-cells. However, co-stimulatory TLR signalling inclines B-cells with $V_H$4-34 BCRs towards germinal center formation even more than it inclines normal, non-anergic B-cells towards germinal center formation (Young et al., 2019). Another study showed that expression of IL1R8 (interleukin-1 receptor 8), a negative regulator of the TLR pathway, was reduced in human DLBCL cell lines and correlated with decreased survival in a human cohort (no classification in subtypes undertaken) (Riva et al., 2019), indicating the importance of TLR pathways and aberrant NF-κB signalling in lymphoma. Together, these findings suggest that excessive NF-κB activation in DLBCL is triggered both by BCR signalling and TLR signalling.

### 1.5.3. Diagnostics of DLBCL

Most commonly, ABC and GCB are distinguished via immunohistochemistry using CD10, BCL6 and other markers rather than GEP (gene expression profiling) for practical reasons, since GEP requires fresh or frozen tissue (Li et al., 2018b, Beham-Schmid, 2017). With the vast emergence of different genetic profiles of DLBCL (see section 1.5.1 and 1.5.2), determination of these genetic profiles for prognostic and therapeutic planning is of growing importance. Some tools include RNA profiling and evaluation of molecules involved in BCR signalling, for example using PLA (proximity-ligation-assays) to assess MyD88-TLR9 oligomerisation. Interestingly, positive results for MyD88-TLR9 oligomerisation in PLA assays could only be found in ibrutinib-sensitive ABC DLBCL cases, suggesting PLA assays might be a good method to predict ibrutinib treatment responses (Young et al., 2019). Another option is liquid biopsy, which assesses circulating tumour DNA (Melani et al., 2019) and might also be used to test cerebral fluid for central nervous lymphoma mutations (Zorofchian et al., 2018).

Besides molecular diagnostics of DLBCL, imaging of the patient is an important part of clinical diagnostics and staging. More precisely, so-called FDG-PET-CT scans are commonly used. In FDG-PET-CT scans, CT (computer tomography) scans are combined with PET (positron emission tomography) scans and intravenously injected glucose labelled with radioactive [$^{18}$F]

(FDG, [$^{18}$F]-deoxyglucose) is used as a marker (also called tracer). Since tumours metabolise large amounts of glucose, they are subsequently often visible in these FDG-PET-CT scans. FDG-PET-CT should therefore be used for monitoring and therapeutic response assessment of FDG-avid lymphomas, meaning lymphomas that metabolise FDG and are thus positive in the FDG-PET-CT scans, while CT only should be used for non-FDG-avid lymphomas.

DLBCL is an FDG-avid lymphoma and a positive FDG-PET-CT of bone or bone marrow is sufficient to diagnose advanced stage DLBCL. However, bone marrow biopsy is recommended in case of a negative FDG-PET-CT and clinically justified suspicion (Cheson, 2015). For DLBCL, FDG-PET-CT scans are performed 6 to 8 weeks following the end of therapy, classifying response rates into CR (complete remission), PR (partial remission, > 50% reduction), SD (stable disease, < 50% reduction) and PD (progressive disease). Furthermore, metabolic response rates are classified in Deauville stages, whereby total FDG activity in lymphoma foci is below liver FDG uptake in stage 1 to 3 and above liver FDG uptake in stage 4 to 5 (Onkopedia, 2018).

In the future, the use of new PET tracers besides FDG could further advance the validity of PET scans in lymphoma diagnostics. Two examples of such new PET tracers include FLT ([$^{18}$F]-thymidine), a tracer in which thymidine (a marker for proliferation) is connected to radioactive [$^{18}$F], and Ga-68 CXCR4, a tracer in which the chemokine receptor CXCR4 (C-X-C chemokine receptor type 4) found in several lymphomas is connected to radioactive $^{68}$Gallium (Valls et al., 2016).

### 1.5.4. Current immunotherapeutic strategies in DLBCL treatment

With the current standard chemotherapy regimen R-CHOP (rituximab, cyclophosphamide, doxorubicin, vincristine and prednisone), the 5-year-survial rate of DLBCL patients is around 60 to 70%. However, the remaining 30 to 40% of DLBCL patients relapse or do not respond (Li et al., 2018b). Furthermore, ABC DLBCL cases respond worse to the R-CHOP regimen than GCB DLBCL cases (Young et al., 2019). Besides chemotherapy, options are limited to stem cell transplantation and radiotherapy. All three of them bring several side effects and urgently call for alternative or supplementary approaches. Additionally, R-CHOP is 30 times as costly as CHOP but accounts for roughly 15% improvement in cure rate compared to CHOP, thus posing a socio-economical and ethical burden especially in low-income countries (Shulman et al., 2016).

A promising alternative is the BTK inhibitor ibrutinib, which is approved by the FDA (Food and Drug Administration) and the EMA (European Medicines Agency) since 2014 for CLL, Waldenström macroglobulinemia (a type of lymphoplasmacytic lymphoma, see Table ) and some other rare entities. Ibrutinib covalently binds to the cysteine 481 of BTK, a residue whose mutation accounts for about 28% of all ibrutinib resistances. The ibrutinib response rate was higher among ABC DLBCL than among GCB DLBCL patients (37% versus 5% ORR (objective response rate), whereby ORR accounts for cases of CR and PR) and better among patients below the age of 60 years, which indicates that those tumour entities rely on BCR-driven pathways (Shaffer et al., 2012). Remarkably, lymphoma with both the *MYD88*$^{L265P}$ mutation and mutations in *CD79B*, indicative of the MCD genetic subtype that is mostly found in ABC DLBCL cases (see section 1.5.1), showed an ORR to ibrutinib of 80%. Both of these molecules are involved in downstream NF-κB activation, either via BCR signalling or via TLR signalling, suggesting that this phenotype is strongly dependent on NF-κB activation (Young et al., 2019). In one case of refractory IgA lymphoplasmacytic lymphoma featuring the *MYD88*$^{L265P}$ mutation, off-label use of ibrutinib even led to a 50% reduction in lymphadenopathy within six months (Quaglia et al., 2019). However, ibrutinib therapy still poses problems. In one study on Waldenström macroglobulinemia, ibrutinib treatment had to be discontinued in 27% of the patients mainly due to disease progression or toxicity (Gustine et al., 2018). A possible explanation for this observation is that ibrutinib treatment leads to a selection pressure that favours B-cells with a mutated cysteine 481 in BTK, which then hinders covalent binding of ibrutinib to BTK. Additionally, as with all immunomodulatory drugs, immunosuppressive effects have to be taken into consideration under therapy. For instance, *Aspergillus fumigatus* infections have been described to appear more frequently under ibrutinib treatment in DLBCL patients (Young et al., 2019).

Further small molecule inhibitors that are currently under investigation for their use in DLBCL treatment include inhibitors of kinases involved in proximal BCR signalling other than BTK. Examples of such include SYK inhibitors (Fostamatinib, terminated due to toxicity), PI3K inhibitors (Idelalisib, FDA- and EMA-approved since 2014) and LYN inhibitors (preclinical development). Additionally, there are also inhibitors against downstream effector molecules of BCR signalling such as Venetoclax, an inhibitor against the anti-apoptotic molecule BCL2 (Young et al., 2019).

Most BCR pathway inhibitors eventually develop resistance, thus synergistic targeting is becoming increasingly important to avoid clonal selection of resistant malignant cells. For example, inhibition of mTOR (mammalian target of rapamycin, a downstream effector of BCR signalling that promotes survival) paired with BTK inhibition was shown to successfully decrease MyD88 levels and block mTOR activity (Phelan et al., 2018), suggesting mTOR and TLR inhibitors synergistically decrease the formation of My-T-BCR supercomplexes. Another study showed synergistic effects of ibrutinib with the histone deacetylase inhibitor panobinostat (Mondello et al., 2018). Interestingly, it was found that panobinostat prevents STAT3 phosphorylation and thereby hinders the binding of STAT3 to the *MYD88* promotor, leading to decreased expression of MyD88 and therefore decreased MyD88-dependent NF-κB signalling. This is especially of interest as this synergistic efficacy of panobinostat and ibrutinib was found in *MYD88*$^{L265P}$ mutated ABC DLBCL cells (Mondello et al., 2018). As MyD88 dimerisation is increased in *MYD88*$^{L265P}$ mutated B-cells (Avbelj et al., 2014), molecules targeting non-BCR signalling pathways also include MyD88 dimerization inhibitors like ST2825 (Wang et al., 2019). Finally, another group of inhibitors targeting non-BCR signalling pathways are IRAK inhibitors (Ngo et al., 2011, Shaffer et al., 2012, McElroy, 2019, Gimenez et al., 2019, Young et al., 2019). Other potential therapeutic targets include the heat shock protein HSP110, which was found to stabilise MyD88 in ABC DLBCL cells (Boudesco et al., 2018).

Recent research has also identified so-called immune checkpoints, which are essential for a balanced immune response, to be dysregulated in many cancers. Immune checkpoints are essentially an interaction between the surface molecules of two cells, leading to either enhancement or inhibition of the target cell. In the case of T-cells, one of the most studied pairs of molecules are PD-1 (programmed cell death protein 1), expressed on T-cells, and PD-L1, expressed on macrophages and many tumour cells, whereby PD-L1 binding to PD-1 leads to inhibition of the T-cell. This led to the development of novel cancer therapies, including for B-cell lymphoma, that inhibit PD-L1 binding to PD-1. This inhibition ‘lifts the brakes’ on T-cells executed by PD-L1 and T-cells can carry out their normal function again, thereby promoting anti-tumour immunity (Okazaki et al., 2013, Iwai et al., 2017, Goodman et al., 2017). PD-L1 expression is detected in about 25% of DLBCL cases, mainly in the more aggressive ABC subtype (Li et al., 2018a). Interestingly, in B-cells the BCR pathway is not disconnected from PD-L1 expression: A recent study found that BCR activation leads to PD-L1 expression via a NFATc1/IL-1/JAK2/STAT3 (nuclear factor of activated T-cells c1/Interleukin-1/Janus kinase 2/ signal transducer and activator of transcription 3) axis (Li et al., 2018a). Additionally, inhibition of BCR signalling by BTK inhibitors such as ibrutinib lead to decreased NFATc1 and STAT3 activation, suggesting BCR inhibition and PD-1/PD-L1 inhibition might act synergistically in lymphoma therapy. In lymphoma mouse models such a synergistic effect of ibrutinib and PD-L1 inhibition was indeed described (Sagiv-Barfi et al., 2015).

Apart from inhibitors, other approaches currently tested are chimeric antigen receptor T-cells (CAR-T-cells) and antibodies against various B-cell surface markers including CD19, CD20 and CD22 (Li et al., 2018b). CAR-T-cells are T-cells with a modified TCR specific to a tumour antigen of the individual patient. These CAR-T-cells are injected into the patient and thereby promote anti-tumour immunity. On the other hand, antibodies against B-cell surface molecules act by inducing antibody-dependent cellular cytotoxicity and thereby cell death.

In summary, while several immunotherapeutic strategies already exist to treat DLBCL, further therapeutic strategies are needed to counteract the development of resistances and improve the efficacy of existing treatment regimens. In this light, MyD88-targeted therapies might emerge as a promising target especially in *MYD88*$^{L265P}$-mutated lymphoma patients.

## 1.6. The *MYD88*$^{L265P}$ mutation in B-cell lymphomas

### 1.6.1. Epidemiology of the *MYD88*$^{L265P}$ mutation in B-cell lymphomas

Although different gain-of-function mutations in *MYD88* have been described in B-cell lymphoma, *MYD88*$^{L265P}$ appears to be the most frequent one (Avbelj et al., 2014). Table 2 shows the frequency of MYD88$^{L265P}$ in selected B-NHL entities (Weber et al., 2018). The *MYD88*$^{L265P}$ mutation is present in almost 30% of ABC cases (Ngo et al., 2011, Lee et al., 2017) and especially frequent in WM (Waldenström macroglobulinemia), with 90% of the cases being positive (Table 2). *MYD88*$^{L265P}$ is associated with a lower 5-year-survival among DLBCL patients (Vermaat et al., 2019) and is a hallmark genetic aberration in the genetic MCD subtype of DLBCL mostly found in ABC DLBCL cases (Figure 4). It often co-occurs together with *CD79B* mutations (Young et al., 2019). *MYD88*$^{L265P}$-positive cases also show a greater disease burden in lymphoplasmacytic lymphoma in general (Fang et al., 2018) and a higher prevalence of other oncogenic mutations such as CXCL4 (C-X-C chemokine ligand type 4) in WM, a subtype of lymphoplasmacytic lymphoma (Castillo et al., 2019). Finally, *MYD88*$^{L265P}$ also seems to be an early indicator for primary central nervous system DLBCL (Nayyar et al., 2019).

Table 2 **Frequency of *MYD88*$^{L265P}$ mutation in selected B-NHLs**. Adapted from Weber et al., 2018. ABC = activated B-cell-like, MGUS = monoclonal gammopathy of undetermined significance.

| **B-NHL entity** | ***MYD88*$^{L265P}$ frequency** |
|---|---|
| Chronic lymphocytic leukaemia (CLL) | 4% |
| Mucosa-associated lymphoid tissue lymphoma (MALT) | 7 - 9% |
| Diffuse large B-cell lymphoma (DLBCL) | 6.5 - 8.2% (29% in ABC subtype) |
| Primary cutaneous large B-cell lymphoma (PCLBCL), leg type | 61% |
| Primary central nervous B-cell lymphoma (PCNBL) | 71% |
| Waldenström macroglobulinemia (WM) | 90% (54% in precursor MGUS) |

### 1.6.2. Pathophysiology of the *MYD88*$^{L265P}$ mutation in B-cell lymphomas

*MYD88*$^{L265P}$ is a gain-of-function mutation of *MYD88* that shows an amino acid exchange from leucin to proline at position 265 in the hydrophobic core of its TIR domain (Ngo et al., 2011). As described in section 1.2.2, the TIR domain of MyD88 binds to the TIR domains of the cytosolic C-terminus of Toll-like receptors via homotypic domain interaction and thereby promotes subsequent signal transduction.

As explained in section 1.5.2, internalisation of BCR-auto-antigen-complexes and their subsequent fusion with the TLR9-containing lysosomes leads to TLR9 activation. The activated TLR9 then oligomerises with MyD88 via its TIR domains for further downstream signalling (Young et al., 2019). In the case of MyD88$^{L265P}$, this oligomerisation is augmented because MyD88$^{L265P}$ can oligomerise independently of upstream TLR9 signalling. This form of independent oligomerisation is mediated by TIR-TIR interactions of MyD88$^{L265P}$. Remarkably, the oligomerisation propensity of MyD88$^{L265P}$ is highest if both mutant MyD88$^{L265P}$ and WT (wildtype) MyD88 are present within the cell due to mutated MyD88$^{L265P}$ TIR domains forming a scaffold for WT MyD88 TIR domains. This goes hand in hand with the finding that most MyD88$^{L265P}$-mutated DLBCL and WM samples are heterozygous for the mutation. It is also of interest that the L265P residue does not seem to be involved in TIR-TIR domain interactions itself, but instead mediates an increased rigidity in the region 284 to 290. This suggests an allosteric mode of action of the L265P mutation in MyD88 for augmenting TIR-mediated MyD88 oligomerisation, whereby allosteric means that the effect of L265P on oligomerisation is mediated by residues other L265P (Avbelj et al., 2014).

The MyD88 aggregates found in MyD88$^{L265P}$-mutated cells also showed increased levels of IRAK1, a downstream kinase that directly interacts with MyD88 for signal propagation by the pathway described in section 1.2.3 (Avbelj et al., 2014). Moreover, MyD88$^{L265P}$ associates downstream primarily with hyper-phosphorylated IRAK1, thus further potentiating signal propagation (Ngo et al., 2011). This supports that augmented oligomerisation in MyD88$^{L265P}$-mutated cells indeed leads to increased downstream signalling and therefore NF-κB hyperactivation. Besides the BCR (CD79A/B), TLR9 and MyD88, several other molecules such as mTOR, PLC-γ2 and the CBM complex (CARD11, BCL10, MALT1) were found to aggregate with the My-T-BCR signalling complex mentioned in section 1.5.2 (Phelan et al., 2018), making it a considerably large aggregate especially in MyD88$^{L265P}$-mutated cells. Therefore, concerning the translation of these findings to the clinical setting, increased oligomerisation of MyD88 could emerge as being an important biomarker for malignancy in B-NHL patients with the MyD88$^{L265P}$-mutation.

## 1.7. Novel mouse model for DLBCL based on the *Myd88*$^{p.L252P}$ driver mutation

Although several xenografts exist to model DLBCL *in vivo,* until recently murine transgenic lymphoma models with defined driver mutations were absent. To fill this gap in murine transgenic lymphoma models, Knittel et al. generated a mouse model featuring MyD88$^{p.L252P}$ expression (the murine analogue to MyD88$^{L265P}$) and BCL2 overexpression. *BCL2* amplifications are observed in 30 to 40% of ABC DLBCL cases and it was shown that self-reactive *MYD88*$^{L256P}$-mutated B-cells only accumulate if apoptosis is being opposed by *in vivo*, which is what *BCL2* amplifications accomplish. In the mouse model, *Bcl2* amplifications were inserted together with a gene encoding for GFP (green fluorescent protein) in the *Rosa26* locus, using the synthetic promotor CAGS (cytomegalovirus early enhancer/chicken β-actin) to further increase expression. Tissue specificity was achieved by using the Cre-Lox system, whereby one *Cd19* allele, which is B-cell specific due to the B-cell specific expression of CD19, was exchanged for a gene sequence encoding Cre recombinase. The target genes (*Myd88*$^{p.L252P}$ and *Bcl2* fused with *Gfp*) were then flanked by LoxP sites, which the Cre recombinase can bind to and thereby remove the flanked region from the genome. As a result, the wildtype *Myd88* and the *LoxP*-flanked STOP cassette upstream of the *Rosa26* locus are removed and the target genes can be expressed in B-cells selectively (Figure 5).

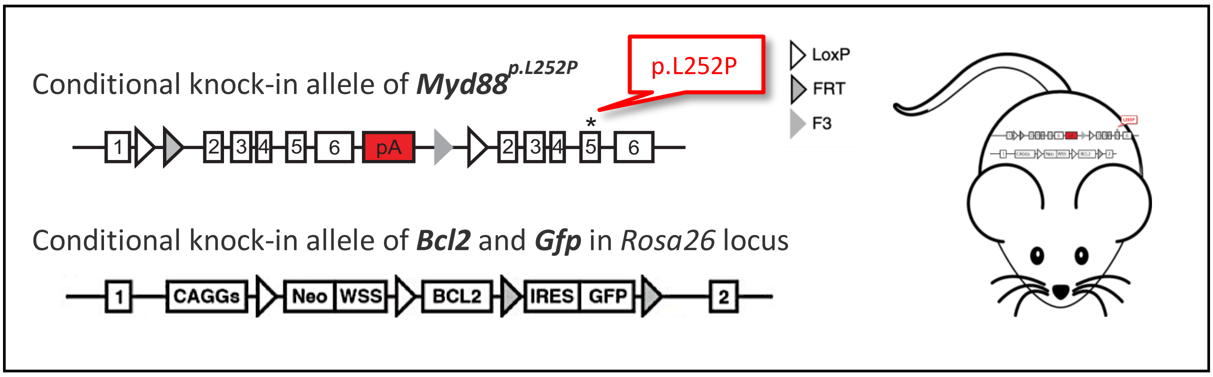

Figure 5 **Novel mouse model for DLBCL based on the *Myd88*$^{p.L252P}$ driver mutation**. B-cell specific expression of *Myd88*$^{p.L252P}$ and *Bcl2* knock-in alleles was achieved via insertion of *LoxP*-sites on the wildtype alleles and crossbreeding with *Cd19*$^{Cre}$ mice. This leads to expression of the Cre recombinase under the B-cell specific *Cd19* promotor, thereby leading to removal of the wildtype alleles and subsequent expression of the mutant allele under the natural *Myd88* promotor (for *Myd88*$^{p.L252P}$) or the synthetic promotor CAGS (for *Bcl2* IRES-linked to *Gfp*). A polyadenylation signal (pA) was added to the wildtype *MyD88* gene to prevent downstream transcription in the absence of Cre-mediated excision. The *IRES Gfp* site in the *Rosa26* locus enables constitutive fluorescent protein expression in *Bcl2* knock-in mice. pA = polyadenylation, CAGGs = synthetic CAGS (cytomegalovirus early enhancer/chicken β-actin) promotor, Neo = Neomycin resistance gene, WSS = Westphal stop sequence, IRES = intermediate ribosomal entry site, LoxP = recombination site used for Cre-mediated recombination, FRT and F3 = recombination sites used for Flp-mediated recombination (Flp-mediated recombination was used during the construction of the conditional *Myd88*$^{p.L252P}$ allele to flank antibiotic resistance genes).

Knittel et al. showed that mice expressing *Myd88*$^{p.L252P}$ instead of wildtype *Myd88* in B-cells (henceforth referred to as MC mice) displayed splenomegaly, lymphoid infiltrates in the liver and the spleen and decreased overall survival. Some developed DLBCL-like lesions that were positive for B220 and IRF4 but negative for BCL6 and CD138 in immunohistochemistry, resembling post-germinal-center (post-GC) and thus ABC DLBCL subtypes. Additionally, these DLBCL-like lesions showed increased NF-κB activation, another feature of ABC DLBCL. However, the MC mice did not show any bone marrow infiltration and only occasionally developed mono- or oligoclonal lymphoma. In comparison, mice in which the *Bcl2* amplification was added (henceforth referred to as MBC mice) mostly developed a more DLBCL-like phenotype. They died earlier and showed splenomegaly sooner than MC mice (as determined by MRI measurements). Remarkably, all MBC mice showed excessive lymphadenopathy and/or splenomegaly at death. Moreover, the DLBCL-like lesions found in

MBC mice were mostly clonal or oligoclonal, showing constitutive NF-κB activation and a Ki-67 index higher than in MC mice and similar to human ABC-DLBCL. Again, no bone marrow infiltration was detected, distinguishing the MBC phenotype from Waldenström macroglobulinemia, in which bone marrow infiltration is a mandatory feature (Knittel et al., 2016).

Overall, MC mice generally developed lymphoproliferative disease but no lymphomas, while MBC mice mostly developed a DLBCL-like phenotype, making MBC mice a valuable model to study *MYD88*$^{L265P}$-mediated DLBCL *in vivo*.

## 1.8. Open questions and aims of the study

### 1.8.1. Characterisation of the novel DLBCL mouse model

Although Knittel et al. could show that lymphoproliferation, immunohistochemical markers and NF-κB activation in liver and spleen were similar to the expected DLBCL phenotype, some markers such as greatly decreased survival in the mouse model and lacking bone marrow involvement distinguish the mouse model from human DLBCL. It is thus unclear to what extent the mouse model mimics DLBCL in other characteristics. To answer this question, this study sought to assess (1) B-cell distribution using post-mortem GFP imaging and (2) bone marrow involvement *in vivo* in the femur as measured via FDG-PET-MRI (see also 1.8.3).

### 1.8.2. Assessment of possible TLR ligand dependency of MyD88$^{p.L252P}$ *in vitro*

As outlined in section 1.5.2 and 0, My-T-BCR signalling is a complex network that is influenced by several upstream and even downstream events. It is therefore not clear whether TLR9 signalling in *MYD88*$^{L265P}$-mutated lymphomas still depends on upstream TLR9 ligands or whether its increased propensity to oligomerise already suffices for its phenotype. Both ligand dependency and ligand independency could have far-reaching consequences: In the case of ligand dependency, efforts should be focussed on exploiting the possibilities of TLR9 inhibitors and other inhibitor targets upstream of MyD88$^{L265P}$. On the other hand, ligand independency would imply that only inhibitors targeting molecules downstream of MyD88$^{L265P}$ yield therapeutic success.

To assess the question of ligand dependency of MyD88$^{L265P}$ *in vitro*, in this study survival and proliferation of murine *Myd88*$^{p.L252P}$-mutated B-cells was analysed. Additionally, since it is known that a subset ABC DLBCLs show autocrine secretion of IL-6 and IL-10 and that this autocrine secretion is diminished in *MYD88* knock-outs (Ngo et al., 2011), this study sought to analyse the supernatant of these B-cells for IL-6 and IL-10 production following *in vitro* stimulation with CpG, R848, BAFF and several other molecules (see section 2.4).

### 1.8.3. Assessment of possible TLR ligand dependency of MyD88$^{p.L252P}$ *in vivo*

To assess the question of ligand dependency of MyD88$^{L265P}$ *in vivo*, the novel DLBCL mouse model generated by Knittel et al. was used in this study to perform a longitudinal study with FDG-PET-MRI imaging whereby one group received CpG as a TLR9 ligand via intraperitoneal injection and one group received PBS (phosphate-buffered saline) for controls. Since it was not clear (1) whether FDG-PET-MRI provides enough specificity for lymphoma imaging (glucose uptake is common in many organs) and (2) whether DLBCL B-cells with increased glucose uptake in the novel DLBCL mouse model also proliferate more, additionally FLT-PET-MRI scans were performed using the tracer FLT ([$^{18}$F]-labelled thymidine) to assess proliferation. Moreover, this study analysed the serum of these cohorts for IL-6, IL-10 and IgM (BCR) levels at death (see section 2.5) since previous studies showed elevated levels of these parameters in DLBCL cell lines.

### 1.8.4. Assessment of the suitability of CD19-based PET imaging in B-cell lymphoma

As outlined in section 1.5.3, DLBCL staging via PET-CT poses its challenges with being partially unspecific and not applicable to all lymphoma entities. To improve specificity, antibody-mediated imaging was suggested as a possible alternative approach. CD20-antibody-mediated imaging might not be very successful, since 30 to 40% of DLBCL cases do not respond to rituximab (a CD20 antibody). On the other hand, CD19 is a coreceptor of the BCR expressed on all B-cells (see section 1.3.2.3) and a surface molecule that lacks selection pressure due to therapeutic approaches, making it ideal for antibody-based imaging. So far most experiments with CD19-antibody-based PET imaging were done in xenografts, meaning mice which were treated with lymphoma cell lines instead of featuring germline lymphoma mutations, with some exceptions of human case reports. However, to better understand the kinetics of CD19-antibody-based PET imaging in lymphoma patients and to assess its suitability for its deployment in human diagnostics at a large scale, it is much needed to perform further preclinical analysis with a transgenic mouse model. This for example allows the post-mortem assessment of CD19-antibody uptake to individual organs with a γ-counter parallel to PET imaging performed shortly prior to euthanasia. In this study it was assessed whether CD19-based PET-MRI imaging is also successful in the novel DLBCL mouse model generated by Knittel et al., where tissue penetration and body distribution may play a greater role than in xenograft models. If successful, it would warrant for further trials in humans and support the validity of CD19-positive results in PET images.

# 2. Materials and Methods

## 2.1. Mouse model used to mimic DLBCL

All experiments were performed using a mouse model developed by Knittel et al., which spontaneously develops a DLBCL-like phenotype (see 1.7 for details). In brief, in the mouse model the murine analogue of the *MYD88*$^{L265P}$ mutation (*Myd88*$^{p.L252P}$) and *Bcl2* amplifications were expressed exclusively in B-cells using the Cre-Lox system (henceforth called MBC mice). Additionally, the fluorescent protein GFP was expressed specifically in B-cells to track B-cell viability *in vitro* and B-cell localisation *in vivo*. B-cell specific expression was achieved by replacing one *Cd19* locus, which is specific for B-cells, with the gene encoding the Cre recombinase. This Cre recombinase was therefore expressed in B-cells only, leading to the excision of the *Myd88* wildtype alleles ahead of the mutated *Myd88* cassette and removal of the stop cassette ahead of the *Bcl2* amplifications and the *Gfp* gene in the *Rosa26* locus (see Figure 5).

For controls, mice only expressing *Bcl2* in B-cells specifically (henceforth called BC mice), mice only expressing *Myd88*$^{p.L252P}$ in B-cells specifically (henceforth called MC mice) and mice only expressing the Cre recombinase under the *Cd19* promotor (henceforth called C mice) were bred. Mice were SPF (specific pathogen free) and held under SPF conditions in barrier-free cages with enrichment at 19–22 °C and 40–60% humidity in a 12/12 h light/dark cycle with free access to standard rodent chow and autoclaved water. All animal experiments were permitted by the regional council of Tübingen under the animal experiment number IB1/17 according to §34 TierSchVersV.

## 2.2. Flow cytometry protocol used to analyse survival and proliferation of *Myd88*$^{p.L252P}$-mutated B-cells *in vitro*

To evaluate the effect of upstream TLR signals on survival and proliferation of *Myd88*$^{p.L252P}$-mutated B-cells, splenic cells were isolated (see section 2.2.1) from MC mice (featuring the *Myd88*$^{p.L252P}$ mutation) and C mice. Next, these cells were stimulated with the TLR agonists R848 (TLR7/8) or CpG (TLR9) for three days. The cells were then evaluated with flow cytometry for survival using 7AAD to stain dead cells and for proliferation using Tag-it Violet™ Proliferation and Cell Tracking Dye (BioLegend 425101).

### 2.2.1. Isolation of splenocytes

Splenocytes were isolated by first killing the mice with $CO_2$ and isolating the spleen via autopsy. Fat and vessels were removed and the spleen was cut into three to six pieces. These pieces were put into a 70 µM cell strainer and placed on a petri dish with R10 medium (RPMI 1640, consisting of 10% heat inactivated fetal calf serum (FCS), L-Glutamine, Penicillin-Streptomycin, 1:100 sodium pyruvate and 1:1000 β-Mercaptoethanol). The spleen was homogenized using the cell strainer and collected in the petri dish. Next, 10 ml of RPMI 1640 was added and the mixture was transferred to a 15 ml tube. The tube was spun for 8 minutes at 300 x g in a centrifuge cooled to 4 °C. The supernatant was removed and 5 ml erythrocyte lysis buffer (0.15 M $NH_4Cl$, 20 mM HEPES) was added, cells were resuspended and incubated for 5 minutes at room temperature. Next, 5 ml of RPMI 1640 was added and the tube was spun for 5 minutes at 300 x g in a centrifuge cooled to 4 °C. The supernatant was removed and 10 ml of cold MACS buffer (DPBS (pH 7.2), 0.5% BSA, 2 mM EDTA) was added. The mixture was poured through a 40 µM cell strainer to remove cell aggregates, collected in a 50 ml tube on ice and washed once with DPBS. Finally, the cells were counted to determine the cell concentration.

### 2.2.2. Staining with Tag-it Violet™

Tag-it Violet™ passively diffuses into the cell, where esterases cleave acetoxymethyl esters on the molecule. This then leads to the covalent binding of Tag-it Violet™ to intracellular proteins, thereby enabling its long-term retention within the cell. With every cell division, Tag-it Violet™ then gets diluted. A decrease in fluorescence is thus a readout for measuring proliferation. Since the fluorescent signal divides by half each time the cell divides, the number of mitoses per cell can be calculated.

$50 \cdot 10^6$ cells were resuspended in 5 ml DPBS in a 50 ml tube and stained with Tag-it Violet™ 1:1000 for 20 to 25 minutes at 37 °C and 5% $CO_2$. The staining reaction was stopped by adding 45 ml of RPMI 1640 warmed to 37 °C. RPMI 1640 contains FCS, which stops the reaction.

### 2.2.3. Stimulation with CpG and R848

Cells were then chilled for two to three hours and subsequently stimulated with CpG or R848 for 72 hours in a 24 well format ($10^6$ cells in 500 µl per well) at 37 °C and 5% $CO_2$. Cells were diluted to a concentration of $4 \cdot 10^6$ cells/ml and 250 µl, equal to $10^6$ cells, were added to each well. Diluted stimulants were added to a total volume of 500 µl. CpG stimulation was performed using CpG ODN 1826 (Invivogen tlrl-1826) diluted to 0.1 µM, 1 µM and 5 µM. R848 stimulation was performed using R848 (Invivogen) diluted to 0.285 µM, 2.85 µM and 14.25 µM.

### 2.2.4. Staining for flow cytometry analysis and data acquisition

After 72h of stimulation, $0.5 \cdot 10^6$ cells were stained in a 96 well plate with v-bottom, whereby 40 µl of cell suspension was mixed with 10 µl of the according mix of dyes. Survival was analysed by staining dead cells with 7-AAD (BioLegend 420403, concentration 50 µg/ml) diluted 1:100. CD19 expression was analysed by staining with Brilliant Violet 711™ anti-mouse CD19 Antibody (BioLegend 115555) diluted 1:400. IgM expression was analysed by staining with Cy™5 AffiniPure Goat Anti-Mouse IgM, µ Chain Specific (Jackson IR 115-175-075) diluted 1:1000.

Isotype controls for CD19 were performed using Brilliant Violet 711™ Rat IgG2a, κ Isotype Ctrl Antibody (BioLegend 400551) diluted 1:400. Isotype controls for IgM were performed using Cy™5 ChromPure Goat IgG, whole molecule (Jackson IR 005-170-003) diluted 1:1000. For compensation, splenocytes were left unstained or stained with 7-AAD, Brilliant Violet 711™ anti-mouse CD19 Antibody or Cy™5 AffiniPure Goat Anti-Mouse IgM. FMO controls were performed by staining splenocytes with all dyes except for one, meaning three FMO controls were done (all except 7-AAD, all except Brilliant Violet 711™ anti-mouse CD19 Antibody and all except Cy™5 AffiniPure Goat Anti-Mouse IgM). For the CD19 and IgM antibody stainings, the according mix of dyes was added and the mixture was incubated for 20 minutes on ice. Subsequently, the cells were washed and resuspended twice using DPBS. Next, 7-AAD was added to the according wells and incubated for 5 to 15 minutes on ice or at room temperature. No further washing was performed after the addition of 7-AAD. Finally, the stained cells were measured in 100 µl DPBS using a Fortessa flow cytometer. Approximately 10,000 events were recorded per sample. For an overview of the dyes used in each staining see Table 3.

Table 3 **Reagents for flow cytometry stainings**. For details see text.

| Dyes | Reagents |
|---|---|
| **Sample staining** | |
| **7-AAD + CD19 + IgM** | • 7-AAD BioLegend 420403, concentration 50 µg/ml<br>Cy™5 AffiniPure Goat Anti-Mouse IgM, µ Chain Specific (Jackson IR 115-175-075), diluted 1:1000<br>• Brilliant Violet 711™ anti-mouse CD19 Antibody (BioLegend 115555), diluted 1:400<br>• Cy™5 ChromPure Goat IgG, whole molecule (Jackson IR 005-170-003), diluted 1:1000 |
| **Isotype controls** | |
| **CD19** | • Brilliant Violet 711™ Rat IgG2a, κ Isotype Ctrl Antibody (BioLegend 400551), diluted 1:400 |
| **IgM** | • Cy™5 ChromPure Goat IgG, whole molecule (Jackson IR 005-170-003), diluted 1:1000 |
| **Compensation** | |
| **Unstained** | |
| **7-AAD** | • 7-AAD BioLegend 420403, concentration 50 µg/ml |
| **CD19** | • Brilliant Violet 711™ anti-mouse CD19 Antibody (BioLegend 115555), diluted 1:400 |
| **IgM** | • Cy™5 AffiniPure Goat Anti-Mouse IgM, µ Chain Specific (Jackson IR 115-175-075), diluted 1:1000 |
| **FMO controls** | |
| **all except 7-AAD:**<br>**CD19 + IgM** | • Brilliant Violet 711™ anti-mouse CD19 Antibody (BioLegend 115555), diluted 1:400<br>• Cy™5 AffiniPure Goat Anti-Mouse IgM, µ Chain Specific (Jackson IR 115-175-075), diluted 1:1000 |
| **all except CD-19:**<br>**7-ADD + IgM** | • 7-AAD BioLegend 420403, concentration 50 µg/ml<br>Cy™5 AffiniPure Goat Anti-Mouse IgM, µ Chain Specific (Jackson IR 115-175-075), diluted 1:1000<br>• Cy™5 AffiniPure Goat Anti-Mouse IgM, µ Chain Specific (Jackson IR 115-175-075), diluted 1:1000 |
| **all except IgM:**<br>**7-AAD + CD19** | • 7-AAD BioLegend 420403, concentration 50 µg/ml<br>Cy™5 AffiniPure Goat Anti-Mouse IgM, µ Chain Specific (Jackson IR 115-175-075), diluted 1:1000<br>• Brilliant Violet 711™ anti-mouse CD19 Antibody (BioLegend 115555), diluted 1:400 |

### 2.2.5. Data analysis of flow cytometry data

An SSC-A/FSC-A gate was used to distinguish splenocytes from debris, an FSC-H/FSC-A gate to select for singlets, a 7AAD$^-$ gate to identify cells alive and a CD19$^+$IgM$^+$ gate to identify B-cells. Then, the number of cell divisions among CD19$^+$IgM$^+$ cells was analysed using the proliferation dye Tag-it Violet™. Figure 6 shows an example of this gating strategy in an MBC mouse. In this MBC mouse there was an additional gate for GFP, as MBC and BC mice express GFP specifically in B-cells.

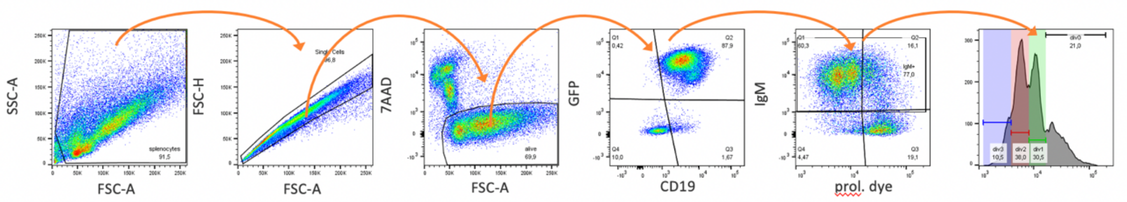

Figure 6 **Representative flow cytometry plots illustrating the gating strategy**. An SSC-A/FSC-A gate was used to distinguish splenocytes from debris, an FSC-H/FSC-A gate to select for singlets, a 7AAD$^-$ gate to identify cells alive, a CD19$^+$/GFP$^+$ gate to select for successfully activated knock-in alleles in BC/MBC genotypes, and an IgM$^+$/Tag-it Violet™ to analyse the number of divisions in CD19$^+$/GFP$^+$/IgM$^+$ positive cells. Single peaks in the histogram represent cell divisions undergone.

## 2.3. Flow cytometry analysis to assess IgM expression of B-cells

The experiments in section 3.5. were performed by isolating splenocytes as detailed in section 2.2.1. Staining was performed as detailed in section 2.2.4. Data analysis was performed as detailed in section 2.2.5, except for no analysis of the proliferation dye.

## 2.4. ELISA to assess IL-6 and IL-10 levels in splenocyte supernatant

To evaluate the effect of upstream TLR signals on *Myd88*$^{p.L252P}$-mutated B-cells, cytokine production of B-cells from MC and MBC mice upon treatment with various TLR agonists and antagonists was evaluated. In detail, IL-6 and IL-10 levels in B-cell supernatant of C, MC, BC and MBC mice five days after no treatment or treatment with chloroquine, IRS 546, IRS 869, IRS 954, CpG, R848, imiquimod, BAFF and IRS 661 were measured.

### 2.4.1. Isolation of splenocytes

Splenocytes were isolated as detailed in section 2.2.1 .

### 2.4.2. Stimulation of splenocytes

Cells were chilled for two to three hours. 250 µl of the cell suspension with a concentration of $4 \cdot 10^6$ cells/ml were then transferred into the wells of a 24 well plate and subsequently stimulated with 250 µl of the substances listed Table 4 for 5 days at 37 °C and 5% $CO_2$.

Table 4 **Reagents used for splenocyte stimulation**. For details see text.

| Stimulation | Reagent | Concentrations used | | |
|---|---|---|---|---|
| **Chloroquine** | Chloroquine (Invivogen tlrl-chq) | 10 µM | 25 mM | 100 µM |
| **IRS 546** | IRS546 control | 1 µM | 5 µM | 10 µM |
| **IRS 869** | IRS869 TLR9 inhibitor | 1 µM | 5 µM | 10 µM |
| **IRS 954** | IRS954 TLR9/7 inhibitor | 1 µM | 5 µM | 10 µM |
| **CpG** | CpG ODN 1826 (Invivogen tlrl-1826) | 0.1 µM | 1 µM | 5 µM |
| **R848** | R848 (Invivogen) | 0.285 µM | 2.85 µM | 14.25 µM |
| **Imiquimod** | Imiquimod (Invivogen tlrl-imq) | 0.5 µg/ml | 5 µg/ml | 10 µg/ml |
| **BAFF** | BAFF (BioLegend 591202) | 0.5 ng/ml | 3 ng/ml | 6 ng/ml |
| **IRS 661** | IRS661 TLR7 inhibitor | 1 µM | 5 µM | 10 µM |

### 2.4.3. ELISA

ELISA was performed using the BioLegend IL-6 ELISA MAXTM Deluxe kit (Catalog Number 431306) for IL-6 measurements and the R&D systems DuoSet® ELISA kit (Catalog Number for DY417) for IL-10 measurements.

## 2.5. ELISA to assess IL-6, IL-10 and IgM levels in serum at death

### 2.5.1. Sample collection

Serum was obtained by retrobulbar blood collection post-mortem and shortly spinning the sample to separate solid blood contents from the serum.

### 2.5.2. ELISA

ELISA was performed using the BioLegend IL-6 ELISA MAXTM Deluxe kit (Catalog Number 431306) for IL-6 measurements and the R&D systems DuoSet® ELISA kit (Catalog Number for DY417) for IL-10 measurements. For IgM measurements, Invitrogen IgM Mouse Uncoated ELISA Kit with Plates (Catalog Number 88-50470) was used.

## 2.6. Optical Imaging with GFP in MBC and BC mice

To identify locations of increased B-cell proliferation *in vivo* when *Myd88*$^{p.L252P}$ is present, we measured post-mortem GFP signal in MBC mice compared to BC mice using Hamamatsu's Optical Imaging System. When mice reached abortion criteria, they were euthanised using $CO_2$ and an autopsy was performed. Mice were pinned on black paper with styrofoam underneath to reduce background signal. Images were taken both as whole-body scans and as scans of individual organs. As mode of data acquisition, epifluorescence was selected, using a 540 nm emission filter and 500 nm excitation filter. Binning, with high values standing for increased pixel size and thus improved sensitivity while sacrificing spatial resolution, was set to eight, exposure to 2 milliseconds, and field of view to 14 cm. f/stop, representing the aperture size of the camera with high values [maximum: f/1] leading to higher light collection efficiency at the cost of decreased depth of field, was set to f/2. Image angle was set to zero, smoothing to none, and units to cm. To identify anatomical structures, a “bright field” image was overlaid with the fluorescence image. Photo adjustments of “bright field” images were set to 100% for brightness, 100% for opacity, and 1.5 for gamma (a measure for contrast). In data analysis, photon counts were standardised using average radiant efficiency $\frac{\mathrm{p\ s^{-1}\ cm^{-2}\ sr^{-1}}}{\mathrm{\mu W\ cm^{-2}}}$, which represents total photons per second per square centimetre per steradian (a measure for solid angles) in the irradiance range (measured in microwatts per square centimetre). Whole-body scans are presented using a colour range of 7.00 $e^7$ to 4.00 $e^8$ $\frac{\mathrm{p\ s^{-1}\ cm^{-2}\ sr^{-1}}}{\mathrm{\mu W\ cm^{-2}}}$.

Data acquisition and data analysis were performed using the Living Image Software. ROIs (regions of interest) were manually drawn on whole-body scans for the abdomen and cervical lymph nodes and on isolated organ scans for the spleen, the liver and inguinal lymph nodes. In whole-body scans, autofluorescent GFP signal, which is caused among others by tape, pins and skin, was excluded from any ROIs to minimise its effect on signal quantification.

## 2.7. Longitudinal study of TLR-Ligand dependency of MyD88$^{p.L252P}$ with PET-MRI

### 2.7.1. Experimental setup

To test for ligand dependency of MyD88$^{p.L252P}$ *in vivo*, MBC mice were treated with intraperitoneal injections of CpG (n = 22), a TLR9 ligand, or PBS (n = 23) as a control. After confirming the desired MBC genotype via PCR (polymerase chain reaction) of material obtained by earmarking, injections were started at an age of ten weeks. The initial five injections were carried out weekly, subsequent injections at a two-week interval. A selected cohort of eight mice each were scanned via PET-MRI in intervals of six weeks starting at week 15.

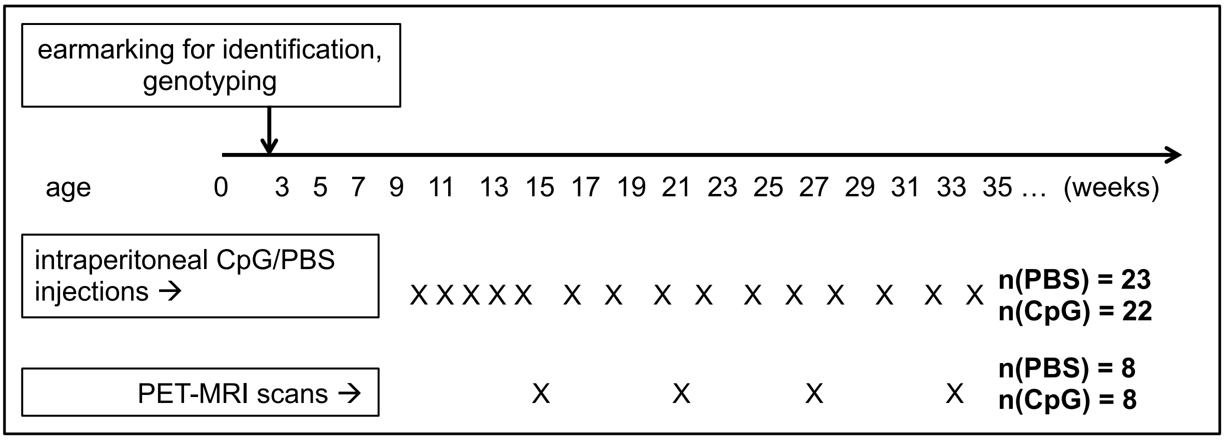

Figure 7 **Experimental setup of intraperitoneal injections and PET-MRI scans in MBC mice**. Intraperitoneal injections were performed weekly for five weeks and then bi-weekly. PET-MRI scans were performed at four time points; week 15, week 21, week 27 and week 33.

### 2.7.2. PET-MRI

Prior to the PET-MRI scan, mice received anaesthesia using isoflurane (CP-Pharma Handelsgesellschaft GmbH, Burgdorf, Germany) in pure oxygen at a concentration of 1.5% with a flow rate of 0.8 l/min. Anaesthesia depth was monitored by breath frequency. The tracer was then applied intravenously into a tail vein and incubated for one hour. Anaesthesia was maintained during this incubation time using a chamber infused with 1.5% isoflurane and a heating blanket underneath to prevent hypothermia in mice.

Following tracer application and incubation, PET (positron emission tomography) scans were performed as static scans using a dedicated Inveon small animal PET scanner with a spatial resolution of ≈1.3 mm (Siemens Preclinical Solutions, Knoxville, TN, USA) over a period of 20 minutes and reconstructed via OSEM3D. To provide anatomical orientation for the signal detected in PET scans, MRI (magnetic resonance imaging) scans were carried out using a dedicated 7T small animal MR tomograph (ClinScan, Bruker, Ettlingen, Germany) with a linearly polarized radiofrequency coil with an inner diameter of 72 mm (Clinscan, Bruker, Ettlingen, Germany) for transmission and rat whole-body volume coil (Clinscan, Bruker, Ettlingen, Germany) for reception. T2-weighted images (TE: 205 ms, TR: 3000 ms, matrix: 161 × 256, slice thickness: 0.22 mm) were obtained and no contrast agent was used. Due to efficiency reasons, TSE (turbo spin echo) imaging was used to allow for faster image collection and rat coils were used in order to place two mice in one coil per PET-MRI run. However, both of these approaches potentially limit image quality. Additionally, the placement of two mice into one rat coil could promote partial volume effects, in which a volume that is smaller than two times the resolution appears larger than it is.

For data analysis, PET and MRI images were fused, normalized using the precise injected dose and analysed using Inveon Research Workplace software (Siemens Preclinical Solutions). Tracer uptake into the selected organs was analysed by manually drawing three-dimensional ROIs on the co-registered MR images. If ROIs were not clearly defined in the MR images, PET tracer uptake patterns were used for ROI definition. Tracer uptake was reported as percentage of ID (injected dose) measured in the defined ROI (% of injected dose) and maximum becquerel per millilitre within the defined ROI (Bq/ml). Maximum Bq/ml values for the bone marrow and the spleen were standardised to the injected dose by multiplying with $\frac{injected\ dose}{average\ injected\ dose}$.

ROIs were drawn for the spleen, the inguinal lymph nodes, the bone marrow and for abdominal lymphoma. Inguinal lymph nodes were chosen as they are large enough to allow identification in the MRI. For bone marrow measurements, only maximum FDG uptake was determined because the legs of mice sometimes moved during transport between PET and MRI measurements and precise overlays were therefore not always possible. Only measuring maximum FDG uptake avoided data errors due to inclusion of surrounding FDG signal not stemming from the femoral bone marrow, such as muscle FDG signal. Abdominal lymphoma were defined as abdominal tracer uptake not explained by the liver, the heart, the kidneys, the ureter, the bladder, the spleen, the suprarenal glands or the inguinal lymph nodes. ROIs were defined using both MR images and PET tracer uptake patterns with standardised thresholds in PET images. As a control, ROIs in muscle and empty background were defined. All ROIs were drawn by one person to minimise intraindividual differences in ROI definition.

### 2.7.3. Tracers: FDG and FLT

To evaluate glucose metabolism of potential lymphoma over time, the tracer FDG was chosen. To evaluate proliferation of potential lymphoma over time, the tracer FLT was chosen. As described above, tracers were injected intravenously into the tail vein and tracer uptake was measured in a small animal PET scanner following an incubation time of one hour.

## 2.8. Novel Imaging Techniques: PET-MRI with [$^{64}$Cu]-labelled anti-CD19 antibodies

### 2.8.1. Experimental setup

Since FDG and FLT are not B-cell specific tracers, a pilot study was conducted using a B-cell specific anti-CD19 antibody generated by Sonanini et al. by radiolabelling the antibody with [$^{64}$Cu]. To detect tumours with a high likelihood, MBC mice with a higher age (n = 4, aged 56 weeks, 55 weeks, 50 weeks and 35 weeks) were chosen. As controls, BC mice (n = 2, aged 37 weeks and 34 weeks) and CD19-deficient mice (n = 1, aged 13 weeks) were chosen.

### 2.8.2. PET-MRI

The tracer (see 2.8.3) was applied intravenously into a tail vein and incubated for three days. Prior to the PET-MRI scan, mice received anaesthesia using isoflurane (CP-Pharma Handelsgesellschaft GmbH, Burgdorf, Germany) in pure oxygen at a concentration of 1.5% with a flow rate of 0.8 l/min. Anaesthesia depth was monitored by breath frequency.

PET-MRI (positron emission tomography/magnetic resonance imaging) scans were performed as static scans using a dedicated 7T small animal BioSpec (Bruker BioSpin MRI, Bruker, Ettlingen, Germany) over a period of 20 minutes and reconstructed via OSEM3D. Imaging was performed using a linearly polarized radiofrequency coil with an inner diameter of 72 mm (Bruker BioSpin MRI, Bruker, Ettlingen, Germany) for transmission and rat whole-body volume coil (Bruker BioSpin MRI, Bruker, Ettlingen, Germany) for reception. T2-weighted TurboRARE images (TE: 90.51 ms, TR: 1800 ms, FOV: 76.8 x 34.8 x 22.8 mm³, image size: 256 x 116 x 76 px, Rare factor: 40, averages: 2) were obtained and no contrast agent was used.

For data analysis, PET and MRI images were fused, normalized using the precise injected dose and analysed using Inveon Research Workplace software (Siemens Preclinical Solutions). Tracer uptake and distribution was analysed visually. Quantification was performed using a γ-counter (see 2.8.4).

### 2.8.3. Tracer: [$^{64}$Cu]-labelled anti-CD19 antibody

To image B-cells, a murine CD19 antibody was radiolabelled with [$^{64}$Cu] ([$^{64}$Cu] mCD19-NODAGA (BioXcell, *InVivo*MAb anti-mouse CD19; BE0150; Clone:1D3)). Radiolabelling was performed with 150 MBq per 500 µg antibody and 12.5 ± 0.4 MBq using 2 U (50µl) were injected intravenously using a tail vein three days prior to imaging and γ-counter quantification.

### 2.8.4. γ-counter

To determine [$^{64}$Cu] mCD19-NODAGA uptake in isolated organs (spleen, lymph nodes and potential tumours), animals were euthanised following PET-MR imaging and dissected organs were subjected to biodistribution analysis. Organ radioactivity was measured using the γ-counter Wizard$^2$ 2480 (Perkin Elmer Inc., Waltham, MA, USA) with a measuring time of 60 seconds per sample, a copper energy of 511 keV and a window of 425 to 640 keV. The fraction of injected tracer dose per gram tissue (%ID per g) was calculated by normalizing decay-corrected counts to the precise injected dose of [$^{64}$Cu] mCD19-NODAGA and sample wet weight.

## 2.9. Statistical Analysis

Statistical analysis was performed using GraphPad Prism 8.0. Experiments and analysis were not blinded for genotype or type of treatment. Sample sizes were selected according to minimal numbers needed as detailed in the according biometric report of the TVA (Tierversuchsantrag) that was permitted by the regional council of Tübingen under the animal experiment number IB1/17 according to §34 TierSchVersV. As test statistics, p-value and degrees of freedom for t-tests, Mann-Whitney U for Mann-Whitney tests and W for Wilcoxon matched-pairs signed rank tests were calculated. Degrees of freedom are a measure that states how many values are free to vary in a statistic, thereby being a distribution parameter. U counts the times that a value in one group is larger than in the other group and vice-versa and then states the smaller one of these two counts. It is useful to compare Mann-Whitney U tests done with different programs. Finally, W is the sum of signed ranks in the Wilcoxon test. If appropriate, data was tested for normal distribution using Saphiro-Wilk and Kolgomorov-Smirnov tests (see respective figure and table legends).

# 3. Results

## 3.1. MBC mice show B-cell accumulation in secondary lymphoid organs and the abdomen

So far, the B-cell distribution of the novel DLBCL model (MBC mice) remained unknown. To evaluate B-cell distribution in MBC mice compared to BC mice, we exploited the fact that MBC and BC mice both show B-cell specific expression of the *Bcl2-IRES-Gfp* transgene and thus the fluorescent protein GFP, and performed fluorescence scans of these mice using a Hamamatsu's Optical Imaging System (see section 2.6). In these scans, GFP signals indicate the presence of B-cells. Scans were done post-mortem as tissue signal penetrance of GFP is generally too low to perform kinetic scans on live animals over time. An example of these fluorescence scans can be seen in Figure 8, which shows an MBC mouse with increased GFP signal in the abdomen in the whole-body scan as well as in liver and lymph nodes in isolated organ scans.

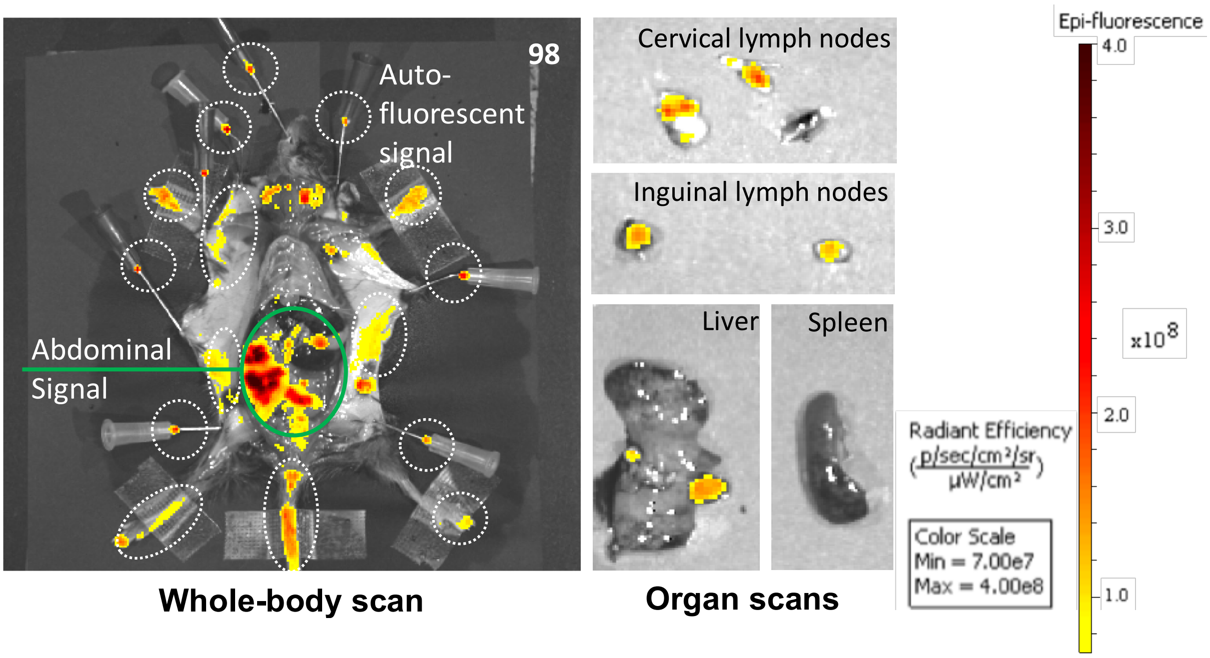

Figure 8 **Optical GFP imaging allows analysis of B-cell distribution in MBC mice**. Whole-body scans and isolated organ scans of exemplary MBC mouse, signal represents B-cells as B-cells express GFP in this mouse model. Higher GFP intensity is indicated by a switch form yellow to dark red. Colour scale on right side shows average radiant efficiency, a standardised measure for epifluorescence, ranging from 7.00 $e^7$ to 4.00 $e^8 \frac{p\,s^{-1}\,cm^{-2}\,sr^{-1}}{\mu W\,cm^{-2}}$. One representative of 6 repeats in MBC cohort. GFP = green fluorescent protein.

Compared to BC mice, MBC mice showed increased overall GFP signal (Figure 50 in appendix). Intriguingly, there was higher signal detected in the abdominal tract of MBC mice compared to BC mice. In five out of eight MBC mice this strong signal, indicative of an invasion of GFP-positive cells into the abdomen, lead to identification of solid tumours by autopsy (mice 98, 35, 48, 123 and 125 in Figure 50, see appendix), while in only one out of eleven BC mice solid tumours were identified (ZK5wBC1 in in Figure 50, see appendix). In four BC mice (ZK5mBC1, ZK5wBC1, ZK14mBC1 and m1 in Figure 50, see appendix) an intense signal was caused by the bladder, probably due to fluorescent agents in the urine, which does not represent a true abdominal signal. These mice were excluded from further analysis of abdominal signal.

The epifluorescent signal was quantified and standardised using average radiant efficiency ($\frac{\mathrm{p\ s^{-1}\ cm^{-2}\ sr^{-1}}}{\mathrm{\mu W\ cm^{-2}}}$), which counts total photons per second per square centimetre per steradian (a measure for solid angels) in the irradiance range (measured in microwatts per square centimetre) (see section 2.6). It again revealed that GFP signal in MBC mice is higher in the abdomen ($p = 0.0002$, multiple t-tests), in cervical lymph nodes ($p = 0.0340$, multiple t-tests), in inguinal lymph nodes ($p=0.0140$, multiple t-tests), in the spleen ($p = 0.0002$, multiple t-tests) and in the liver ($p = 0.0039$, multiple t-tests) (see Figure 9 and Table 5). When comparing standard deviations, the variance in signal was higher in MBC mice in all organs except the abdomen (Table 5).

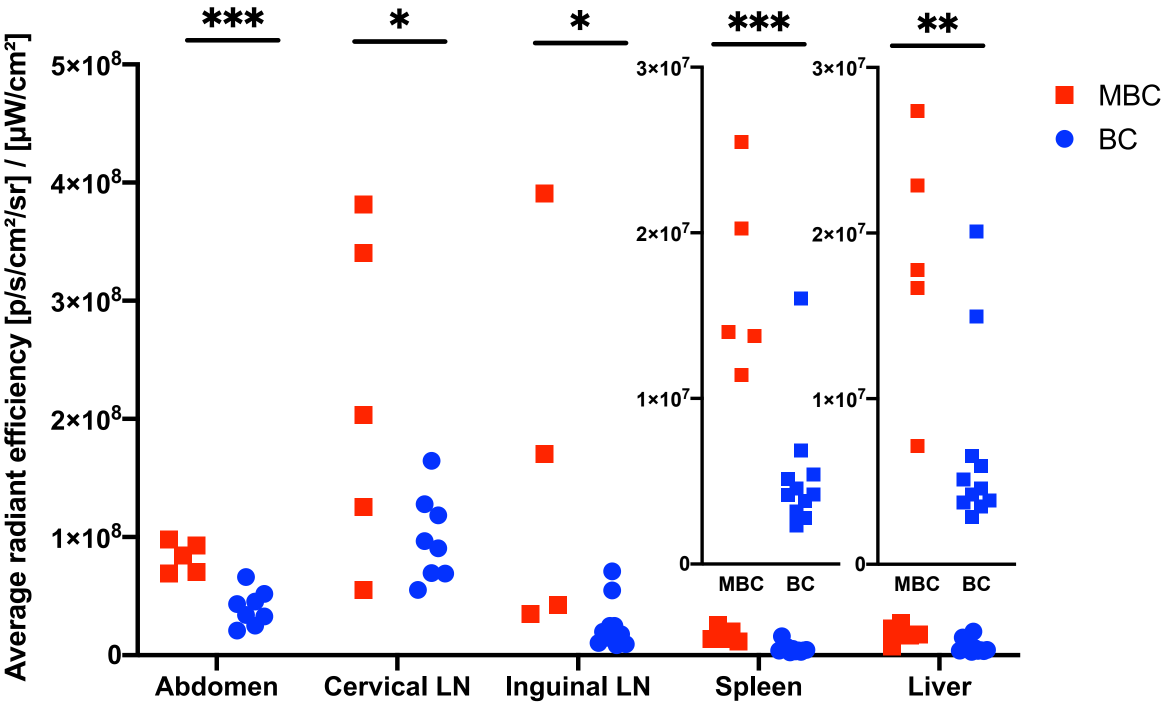

Figure 9 **MBC mice show B-cell accumulation in secondary lymphoid organs and the abdomen**. Each dot represents one animal. Statistical analysis was performed using multiple t-tests corrected via Holm-Sidak (see Table 5), data was normally distributed via Saphiro-Wilk and Kolgomorov-Smirnov. * = $p < 0.05$, ** = $p < 0.01$, *** = $p < 0.001$, **** = $p < 0.0001$, ns = not significant.

Table 5 **MBC mice show B-cell accumulation in secondary lymphoid organs and the abdomen**. Mean and SD values represent average radiant efficiency and thus B-cell density of specified organs. Statistically significant results are marked. Statistical analysis was performed using multiple t-tests, thereby calculating adjusted p-values to account for multiple testing. Adjusted p-value refers to difference between MBC and BC. SD = standard deviation, N = sample size, Df = degrees of freedom, LN = lymph nodes.

| | MBC genotype | | | BC genotype | | | | | |
|---|---|---|---|---|---|---|---|---|---|
| Organ | Mean av. radiant efficiency | SD | N | Mean av. radiant efficiency | SD | N | Adjusted p-value | Df | Mode of acquisition |
| **Abdomen** | 8.29E+07 | 1.29E+07 | 5 | 4.00E+07 | 1.48E+07 | 8 | ***0.0012*** | 11 | whole-body scan |
| **Cervical LN** | 2.21E+08 | 1.39E+08 | 5 | 9.90E+07 | 3.64E+07 | 8 | ***0.0340*** | 11 | combined |
| **Inguinal LN** | 1.60E+08 | 1.66E+08 | 4 | 2.49E+07 | 1.99E+07 | 11 | ***0.0284*** | 13 | isolated organ scan |
| **Spleen** | 1.70E+07 | 5.76E+06 | 5 | 5.32E+06 | 3.77E+06 | 11 | ***0.0012*** | 14 | isolated organ scan |
| **Liver** | 1.84E+07 | 7.59E+06 | 5 | 6.86E+06 | 5.51E+06 | 11 | ***0.0115*** | 14 | isolated organ scan |

## 3.2. TLR stimulation increases survival, proliferation and IL-6 production of *Myd88*$^{p.L252P}$-mutated B-cells *in vitro*

### 3.2.1. TLR stimulation leads to increased survival and proliferation of *Myd88*$^{p.L252P}$-mutated B-cells *in vitro*

As illustrated above, MBC mice showed high B-cell accumulation in secondary lymphoid organs and the abdomen *in vivo*, which might indicate uncontrolled B-cell infiltration and proliferation compared to BC mice that lack the *Myd88*$^{p.L252P}$ mutation. Since MyD88 is a downstream molecule in the Toll-like receptor pathway, we wanted to evaluate the effect of upstream TLR signals on survival and proliferation of *Myd88*$^{p.L252P}$-mutated B-cells. Therefore, splenic cells were isolated from MC mice (featuring the *Myd88*$^{p.L252P}$ mutation) and C mice for controls and stimulated with the TLR agonists R848 (TLR7/8) and CpG (TLR9) for three days. With flow cytometry, the cells were evaluated for survival using 7AAD to stain dead cells and for proliferation using Tag-it Violet™ Proliferation and Cell Tracking Dye. B-cells were identified using CD19 and IgM antibodies (see section 2.2.5).

Splenocytes from MC mice showed an increased fraction of CD19$^+$IgM$^+$ cells that were 7AAD$^-$ , indicate of higher survival than B-cells from C mice lacking the *Myd88*$^{p.L252P}$ mutation (Figure

51 in appendix and Table 5). Furthermore, this increase in CD19$^+$IgM$^+$7AAD$^-$ cells seems to be dependent on the concentration of the stimulant, as the increase is statistically significant upon R848 treatment at 0.285 µM and 2.85 µM, but not 14.25 µM, and upon CpG treatment at 1 µM and 5 µM, but not 0.1 µM.

Table 5 **Survival of B-cells upon *in vitro* TLR stimulation is higher in *Myd88$^{p.L252P}$*-mutated mice**. Mean and SD values represent the percentage of CD19/IgM positive B-cells that are alive following *in vitro* stimulation of TLR7 via R848 or TLR9 via CpG. Statistically significant results are marked. Statistical analysis was performed using Mann-Whitney tests, p-value refers to difference between MC and C. SD = standard deviation, N = sample size, U = Mann-Whitney U.

| | **MC genotype** | | | **C genotype** | | | | |
|---|---|---|---|---|---|---|---|---|
| Treatment | Mean | SD | N | Mean | SD | N | P-value | U |
| **Untreated** | 8.05 | 3.69 | 14 | 7.46 | 3.95 | 7 | 0.4430 | 38 |
| **R848 0.285 µM** | 31.86 | 12.93 | 8 | 23.74 | 4.88 | 5 | ***0.0289*** | 9 |
| **R848 2.85 µM** | 36.03 | 11.34 | 14 | 25.89 | 7.64 | 5 | ***0.0159*** | 17 |
| **R848 14.25 µM** | 35.95 | 13.17 | 8 | 25.64 | 8.03 | 5 | 0.1520 | 15 |
| **CpG 1826 0.10 µM** | 43.54 | 12.74 | 7 | 33.38 | 9.80 | 7 | 0.2593 | 15 |
| **CpG 1826 1.00 µM** | 52.17 | 11.40 | 12 | 38.96 | 12.06 | 7 | ***0.0283*** | 16 |
| **CpG 1826 5.00 µM** | 51.13 | 12.31 | 8 | 35.21 | 12.88 | 7 | ***0.0401*** | 10 |

Proliferation was assessed by staining cells with the fluorescent proliferation dye Tag-it Violet™, which covalently binds to the cell membrane, leading to dilution of the proliferation dye with every cell division. A decrease in fluorescence is thus a readout for measuring proliferation. Using this method, we observed that the percentage of B-cells with the highest fluorescent signal of Tag-it Violet™, indicative of having undergone no division, was lower in MC mice in untreated conditions and at all concentrations of R848 and CpG tested (see Figure 52 (appendix), Table 29 (appendix) and Table 7). This indicates that besides increased survival, *Myd88$^{p.L252P}$* also enhances B-cell proliferation.

Table 6 **Proliferation of B-cells upon *in vitro* TLR stimulation is higher in *Myd88*$^{p.L252P}$-mutated mice.** Mean and SD values represent percentage of undivided cells (div0) in each treatment group. Statistically significant results are marked. Statistical analysis was performed using Mann-Whitney tests, p-value refers to difference between MC and C. SD = standard deviation, N = sample size, U = Mann-Whitney U.

| | **MC genotype** | | | **C genotype** | | | | |
|---|---|---|---|---|---|---|---|---|
| Treatment | Mean | SD | N | Mean | SD | N | P-value | U |
| **Untreated** | 86.20 | 12.14 | 12 | 96.58 | 3.02 | 5 | ***0.0194*** | 8 |
| **R848 0.285 µM** | 37.80 | 14.03 | 6 | 71.90 | 29.74 | 3 | ***0.0303*** | 3 |
| **R848 2.85 µM** | 19.43 | 9.09 | 12 | 68.73 | 29.59 | 3 | ***0.0003*** | 0 |
| **R848 14.25 µM** | 22.90 | 8.09 | 6 | 70.40 | 31.82 | 3 | ***0.0043*** | 0 |
| **CpG 1826 0.10 µM** | 11.31 | 10.73 | 6 | 43.36 | 29.77 | 5 | ***0.0303*** | 3 |
| **CpG 1826 1.00 µM** | 6.31 | 4.36 | 11 | 35.26 | 21.66 | 5 | ***0.0009*** | 1 |
| **CpG 1826 5.00 µM** | 5.93 | 2.03 | 6 | 35.44 | 22.40 | 5 | ***0.0043*** | 0 |

### 3.2.2. TLR stimulation leads to increased levels of IL-6 in *Myd88*$^{p.L252P}$-mutated B-cells *in vitro*

As human *MYD88*$^{L265P}$-mutated DLBCL cells secrete increased levels of IL-6 and IL-10 *in vitro* (see section 1.8.2), we were interested in whether murine *Myd88*$^{p.L252P}$-mutated cells also secreted increased levels of IL-6 and IL-10 upon TLR stimulation *in vitro.* We stimulated B-cells isolated from mouse spleens with various TLR agonists and antagonists for 5 days at different concentrations (see section 2.4 2). Upon treatment with CpG, R848 or BAFF, IL-6 but not IL-10 was higher in cell supernatant of *Myd88*$^{p.L252P}$-mutated B-cells (MC genotype) compared to non-mutated B-cells (C genotype) (see Figure 53, Table 30, Figure 54 and Table 31 in appendix). Treatment with IRS 546, originally used as a control, inhibited the IL-10 response in MC mice but not the IL-6 response. Other substances tested did not yield significant differences (chloroquine, imiquimod, IRS 661, IRS869 and IRS 954, see Table 30 and Table 31 in appendix). Similarly, supernatant from MBC B-cells did not show any differences in IL-6 and IL-10 secretion upon TLR stimulation compared to BC mice (see Figure 55, Table 32, Figure 56 and Table 33 in appendix). When comparing standard deviations across all stimulations, supernatant of B-cells from MBC mice showed more variance in IL-6 (p = 0.0175, see Figure 55 and Table 32) and IL-10 (p = 0.0016, Figure 56 and Table 33) levels than supernatant of B-cells from BC mice.

## 3.3. Longitudinal study supports TLR-Ligand dependency of MyD88$^{p.L252P}$ *in vivo*

### 3.3.1. MBC mice injected with CpG show decreased overall survival

Since *in vitro* TLR ligand stimulation of B-cells from *Myd88*$^{p.L252P}$ mutated mice lead to increased B-cell survival and proliferation (see section 3.2.1), we were interested to investigate if *Myd88*$^{p.L252P}$ also enhanced disease progression towards DLBCL *in vivo.* Therefore, we used the MBC mouse model described in section 1.7 to model DLBCL and injected MBC mice with intraperitoneal CpG or PBS injections bi-weekly. Measuring survival in both groups, we observed that MBC mice treated with intraperitoneal CpG injections show decreased survival and decreased age at death compared to mice treated with intraperitoneal PBS injections (Figure 10).

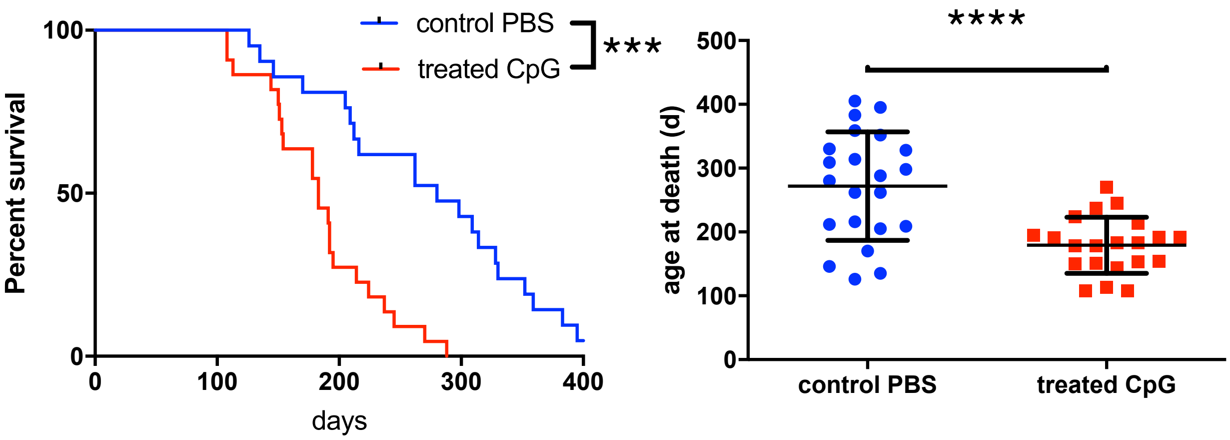

Figure 10 **MBC mice treated with CpG show decreased survival and age at death.** When treating MBC mice, which develop a DLBCL-like phenotype, with intraperitoneal CpG or PBS injections bi-weekly, CpG-treated MBC mice show a decrease in survival ($p = 0.0009$ (Chi square = 11.11), n(PBS) = 21, n(CpG) = 22) and age of death ($p < 0.0001$ (df = 41), PBS: n = 21, mean = 272.00, SD = 84.94, CpG: n = 22, mean = 179.20, SD = 43.94). Each dot in the right graph represents one animal. Statistical analysis was performed using the Gehan-Breslow-Wilcoxon test for survival and an unpaired t-test for age at death. * = $p < 0.05$, ** = $p < 0.01$, *** = $p < 0.001$, **** = $p < 0.0001$, ns = not significant.

### 3.3.2. Autopsy reveals increased levels of splenomegaly and hepatomegaly in CpG-treated MBC mice

To evaluate potential causes of death, an autopsy was performed upon death. Autopsy revealed that CpG stimulation lead to a relative risk of 1.65 (95% CI = 0.99 – 3.482, for absolute numbers see Table 8) to display splenomegaly and a relative risk of 2.273 (95% CI = 1.072 – 7.803, for absolute numbers see Table 9) to display hepatomegaly at death. The relative risk to display ascites at death was 0.750 (95% CI = 0.204 – 3.164, for absolute numbers see Table 10) and the relative risk to display intestinal tumours at death upon CpG stimulation was 0.445 (95% CI = 0.174 – 1.063, for absolute numbers see Table 11). Among CpG-treated MBC mice, spleen weight at death was higher in mice that displayed intestinal tumours than in mice without intestinal tumours ($p = 0.0114$, df = 6, CpG-treated MBC mice with intestinal tumour: $n = 4$, mean = 0.6575, SD = 0.1517, CpG-treated MBC mice without intestinal tumour: $n = 4$, mean = 0.3100, SD = 0.1197). A stratification of the occurrence of splenomegaly, hepatomegaly, intestinal tumours and ascites at death by the age at death did not reveal any patterns (see Figure 57 in appendix).

Table 8 **Splenomegaly in CpG-treated and PBS-treated MBC mice.** Numbers refer to the number of mice in the given category.

| | Splenomegaly | No splenomegaly | Total |
|---|---|---|---|
| CpG | 11 | 1 | 12 |
| PBS | 5 | 4 | 9 |
| Total | 16 | 5 | 21 |

Table 9 **Hepatomegaly in CpG-treated and PBS-treated MBC mice.** Numbers refer to the number of mice in the given category.

| | Hepatomegaly | No hepatomegaly | Total |
|---|---|---|---|
| CpG | 10 | 1 | 11 |
| PBS | 2 | 3 | 5 |
| Total | 12 | 4 | 16 |

Table 10 **Ascites in CpG-treated and PBS-treated MBC mice**. Numbers refer to the number of MBC mice in the given category.

| | Ascites | No ascites | Total |
|---|---|---|---|
| CpG | 3 | 7 | 10 |
| PBS | 2 | 3 | 5 |
| Total | 5 | 10 | 15 |

Table 11 **Intestinal tumours in CpG-treated and PBS-treated MBC mice.** Numbers refer to the number of MBC mice in the given category.

| | Intestinal tumour | No intestinal tumour | Total |
|---|---|---|---|
| CpG | 4 | 8 | 12 |
| PBS | 6 | 2 | 8 |
| Total | 10 | 10 | 20 |

### 3.3.3. CpG stimulation leads to extensive splenomegaly and lymphadenopathy

To gain insights on the disease progression of MBC mice following *in vivo* treatment with CpG or PBS, we performed MRI measurements at four time points (aged 15 weeks, 21 weeks, 27 weeks and 33 weeks) to investigate the volume of lymphoid organs in these MBC mice over time (see section 2.7). For this purpose, we manually drew three-dimensional regions of interest (ROIs) on the MR images around the spleen and the inguinal lymph nodes to measure their volume (examples shown in Figure 11 and Figure 12). Wildtype mice were scanned for reference and calibration. MRI measurements of spleen volume revealed that CpG injections lead to splenomegaly (Figure 13, Table 12). Of note, mice with large spleens at any measurement time point died soon after. Additionally, CpG mice seem to have a peak in spleen volume at week 21.

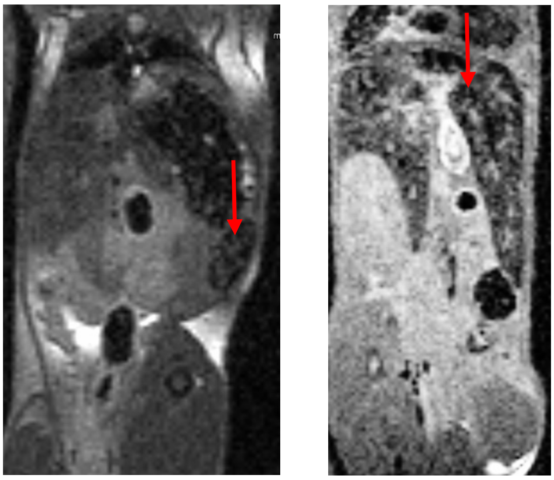

Figure 11 **MRI measurements can determine spleen size, examples**. Using MRI measurements, spleen size can be evaluated *in vivo*. An example of a normal spleen (left, wildtype mouse at 27 weeks of age) and an enlarged spleen (right, CpG-treated MBC mouse 107 at 27 weeks of age) are given. Red arrows indicate spleens.

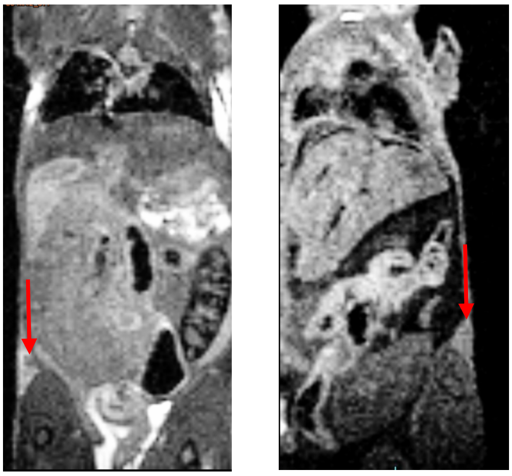

Figure 12 **MRI measurements can determine inguinal lymph node size, examples**. Using MRI measurements, inguinal lymph node size can be evaluated *in vivo*. An example of a normal inguinal lymph node (left, PBS-treated MBC mouse 98 at 15 weeks of age) and an enlarged inguinal lymph node (right, CpG-treated MBC mouse 110 at 15 weeks of age) are given. Red arrows indicate lymph nodes.

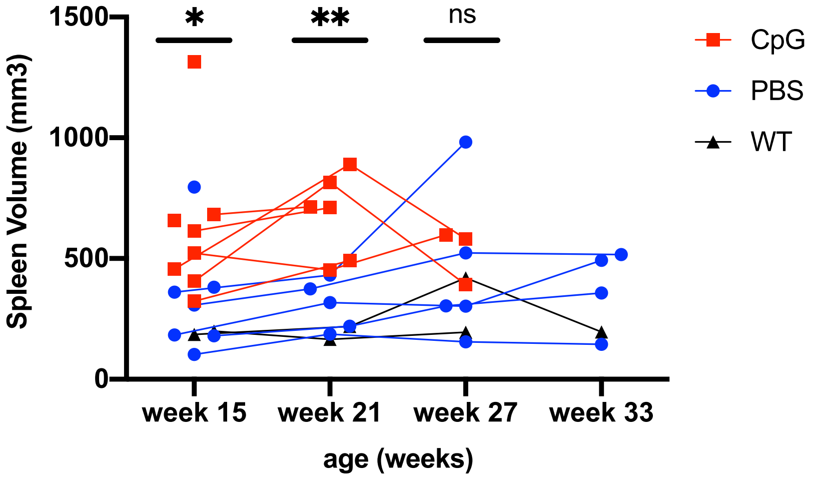

Figure 13a **CpG-treated MBC mice show splenomegaly**. WT = wild type mice. Each dot represents one animal. Statistical analysis was performed using Mann-Whitney tests, see Table 12. * = $p < 0.05$, ** = $p < 0.01$, *** = $p < 0.001$, **** = $p < 0.0001$, ns = not significant. P-values refer to the comparison between CpG and PBS treatment groups. Connecting lines identify identical animals measured at different time points.

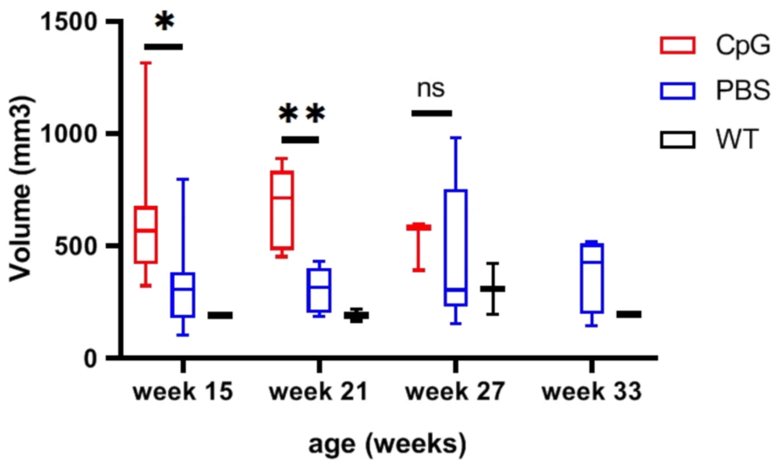

Figure 14b **CpG-treated MBC mice show splenomegaly, summary data**. WT = wild type mice. Statistical analysis was performed using Mann-Whitney tests, see Table 12. * = $p < 0.05$, ** = $p < 0.01$, *** = $p < 0.001$, **** = $p < 0.0001$, ns = not significant. P-values refer to the comparison between CpG and PBS treatment groups. Box plot whiskers indicate minimum and maximum.

Table 12 **CpG-treated MBC mice show splenomegaly**. Mean and SD values represent spleen volume in $mm^3$ as measured via MRI. Statistically significant results are marked. Statistical analysis was performed using Mann-Whitney tests, p-value refers to difference between MBC mice with CpG treatment and MBC mice with PBS (control) treatment at the age indicated. SD = standard deviation, N = sample size, U = Mann-Whitney U.

| | **CpG-treated MBC mice** | | **PBS-treated MBC mice** | | | | **WT mice** | |
|---|---|---|---|---|---|---|---|---|
| Age (weeks) | Spleen volume ($mm^3$) | N | Spleen volume ($mm^3$) | N | P-value | U | Spleen volume ($mm^3$) | N |
| **15** | 622 ± 307 | 8 | 330 ± 230 | 7 | ***0.0289*** | 9 | 192 ± 10 | 2 |
| **21** | 680 ± 174 | 6 | 306 ± 103 | 5 | ***0.0043*** | 0 | 191 ± 38 | 2 |
| **27** | 523 ± 114 | 3 | 453 ± 323 | 5 | 0.3929 | 4 | 308 ± 159 | 2 |
| **33** | / | 0 | 378 ± 170 | 4 | / | / | 196 ± 0 | 1 |

Besides spleen volume, inguinal lymph nodes were also enlarged (Figure 15, Table 13). Remarkably, all inguinal lymph nodes of CpG-challenged mice were larger than those of PBS-challenged mice, with the exception of one PBS mouse at week 15. Again, similar to spleen volumes, mice with large inguinal lymph nodes at any measurement time point died soon afterwards. One CpG stimulated mouse (mouse 112) even showed a 6.64-fold increase in inguinal lymph node volume from week 15 to week 21 and also died soon afterwards at the age of 22 weeks, indicating that rapid volume increase of lymphoid organs is a marker for disease progression. The value of mouse 112 at week 21 was included in the statistical data analysis since no error in data collection and no specific biological cause that would justify excluding the value as an outlier was found.

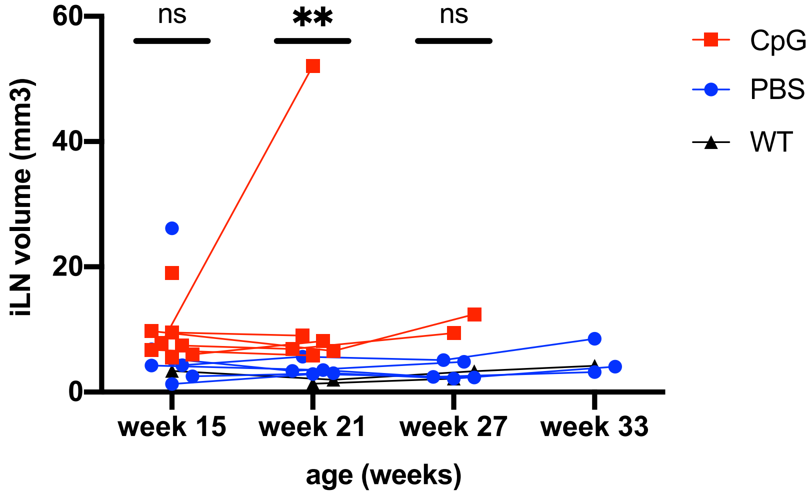

Figure 15a **CpG-treated MBC mice show lymphadenopathy.** WT = wild type mice. Each dot represents one animal. One mouse was still alive at week 27, but measurement was not possible due to technical reasons, thus no value is shown at week 27. Statistical analysis was performed using unpaired Mann-Whitney tests, see Table 13. * = $p < 0.05$, ** = $p < 0.01$, *** = $p < 0.001$, **** = $p < 0.0001$, ns = not significant. P-values refer to the comparison between CpG and PBS treatment groups. Connecting lines identify identical animals measured at different time points.

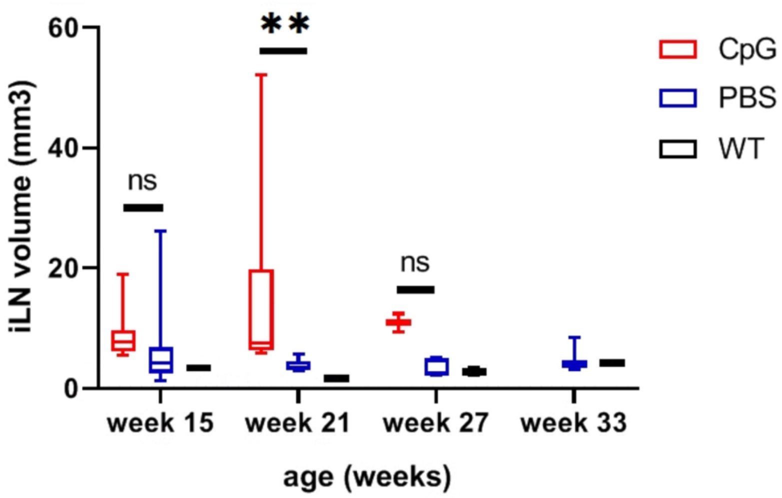

Figure 16b **CpG-treated MBC mice show lymphadenopathy, summary data.** WT = wild type mice. Statistical analysis was performed using unpaired Mann-Whitney tests, see Table 13. * = $p < 0.05$, ** = $p < 0.01$, *** = $p < 0.001$, **** = $p < 0.0001$, ns = not significant. P-values refer to the comparison between CpG and PBS treatment groups. Box plot whiskers indicate minimum and maximum.

Table 13 **CpG-treated MBC mice show lymphadenopathy**. Mean and SD values represent inguinal lymph node (iLN) volume in mm$^3$ as measured via MRI. Statistically significant results are marked. Statistical analysis was performed using Mann-Whitney tests, p-value refers to difference between MBC mice with CpG treatment and MBC mice with PBS (control) treatment at the age indicated. SD = standard deviation, N = sample size, U = Mann-Whitney U.

| | **CpG-treated MBC mice** | | **PBS-treated MBC mice** | | | | **WT mice** | |
|---|---|---|---|---|---|---|---|---|
| Age (weeks) | iLN volume (mm$^3$) | N | iLN volume (mm$^3$) | N | P-value | U | iLN volume (mm$^3$) | N |
| **15** | 9 ± 4 | 8 | 7 ± 9 | 7 | 0.054 | 11 | 3 ± 0 | 2 |
| **21** | 15 ± 18 | 6 | 4 ± 1 | 5 | ***0.0043*** | 0 | 2 ± 0 | 2 |
| **27** | 11 ± 2 | 2 | 3 ± 1 | 5 | 0.095 | 0 | 2 ± 1 | 2 |
| **33** | / | 0 | 5 ± 3 | 3 | / | / | 4 ± 0 | 1 |

### 3.3.4. CpG stimulation leads to increased glucose uptake in inguinal lymph nodes

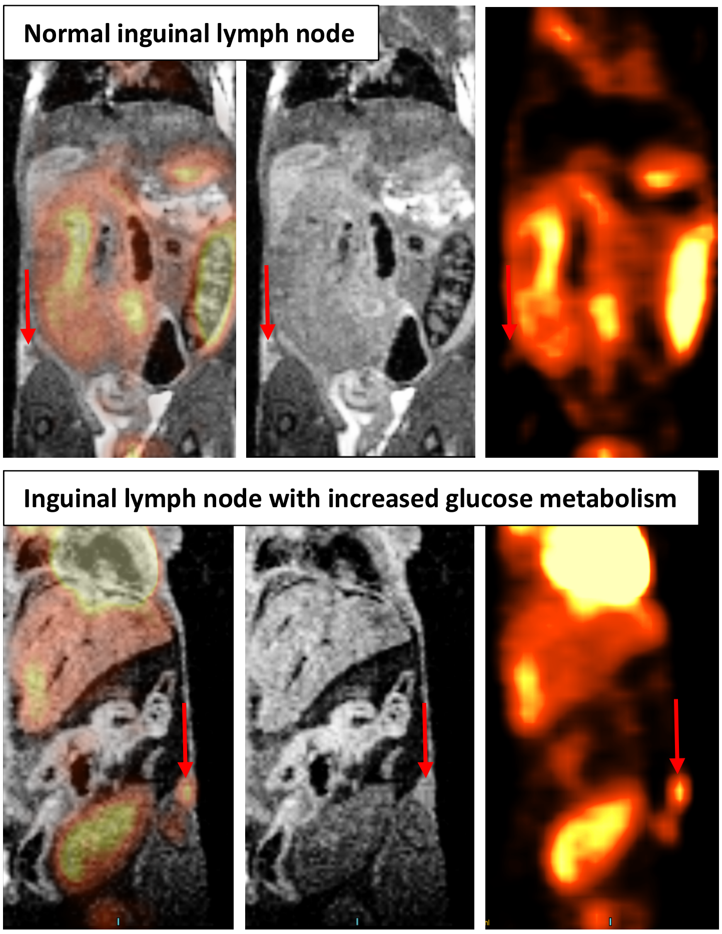

Figure 17 **PET-MRI measurements can determine glucose metabolism of inguinal lymph nodes, examples**. Using PET-MRI measurements, glucose metabolism of inguinal lymph nodes can be evaluated *in vivo*. An example of a normal inguinal lymph node (top, PBS-treated MBC mouse 98 at 15 weeks of age) and an inguinal lymph node with increased glucose metabolism (bottom, CpG-treated MBC mouse 110 at 15 weeks of age) are given. Red arrows indicate lymph nodes.

To gain further insights into the disease progression of DLBCL *in vivo*, we assessed glucose metabolism by co-registering FDG-PET images with the MR images described above. For the FDG-PET measurements, we injected the mice intravenously with the tracer FDG and used a dedicated Inveon small animal PET scanner with a spatial resolution of ≈1.3 mm (Siemens Preclinical Solutions, Knoxville, TN, USA) to track glucose metabolism *in vivo* (see section 2.7). An example can be seen in Figure 17.

FDG-PET-MRI measurements of inguinal lymph nodes revealed that CpG injections lead to increased glucose uptake to inguinal lymph nodes (Figure 18, Table 14). With that, FDG signal in inguinal lymph nodes shows a similar pattern to inguinal lymph node size, which was also higher in the CpG group (Figure 15, Table 13). For example, similar to its increase in inguinal lymph node size the CpG-stimulated mouse 112 (highest value at week 21, see Figure 18) showed a 65.77-fold increase in FDG uptake to inguinal lymph nodes from week 15 to week 21 and died soon afterwards.

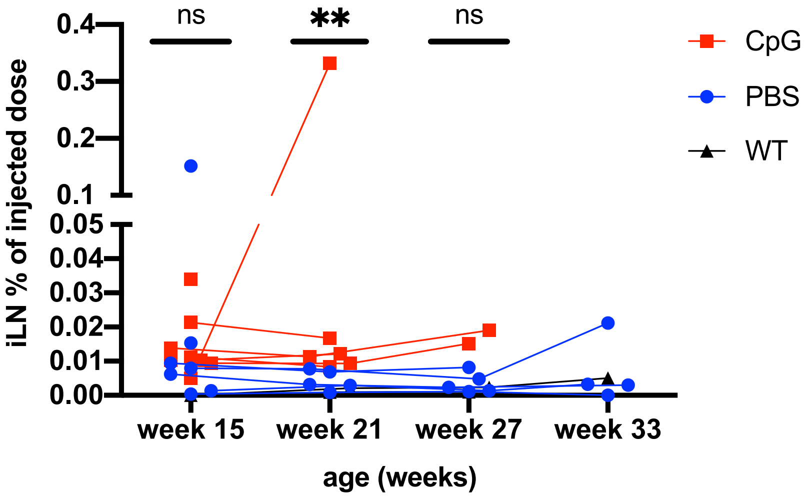

Figure 18a **CpG-treated MBC mice show increased glucose metabolism in inguinal lymph nodes.** CpG stimulation of MBC mice leads to an increased percentage uptake of FDG tracer in inguinal lymph nodes (iLN) at the age of 21 weeks. One CpG mouse was still alive at week 27, but measurement was not possible due to technical reasons, thus no value is shown at week 27. Each dot represents one animal. WT = wild type mice. Statistical analysis was performed using unpaired Mann-Whitney tests, see Table 14. * = p < 0.05, ** = p < 0.01, *** = p < 0.001, **** = p < 0.0001, ns = not significant. P-values refer to the comparison between CpG and PBS treatment groups. Connecting lines identify identical animals measured at different time points.

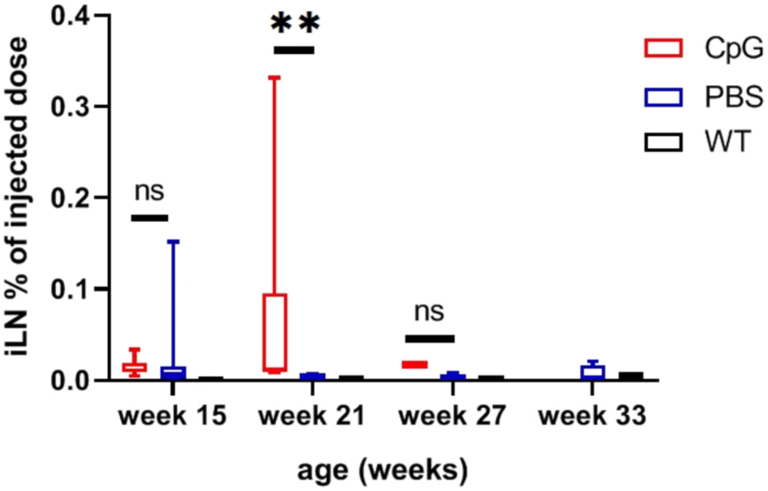

Figure 19b **CpG-treated MBC mice show increased glucose metabolism in inguinal lymph nodes, summary data.** CpG stimulation of MBC mice leads to an increased percentage uptake of FDG tracer in inguinal lymph nodes (iLN) at the age of 21 weeks. WT = wild type mice. Statistical analysis was performed using unpaired Mann-Whitney tests, see Table 14. * = p < 0.05, ** = p < 0.01, *** = p < 0.001, **** = p < 0.0001, ns = not significant. P-values refer to the comparison between CpG and PBS treatment groups. Box plot whiskers indicate minimum and maximum.

Table 14 **CpG-treated MBC mice show increased glucose metabolism in inguinal lymph nodes.** Mean and SD values represent percentage of injected dose (ID) of FDG measured in inguinal lymph nodes (iLN). Statistically significant results are marked. Statistical analysis was performed using Mann-Whitney tests, p-value refers to difference between MBC mice with CpG treatment and MBC mice with PBS (control) treatment at the age indicated. SD = standard deviation, N = sample size, U = Mann-Whitney U.

| | **CpG-treated MBC mice** | | **PBS-treated MBC mice** | | | | **WT mice** | |
|---|---|---|---|---|---|---|---|---|
| Age (weeks) | % of ID in iLN | N | % of ID in iLN | N | P-value | U | % of ID in iLN | N |
| **15** | 0.0144 ± 0.0091 | 8 | 0.0274 ± 0.0550 | 7 | 0.2810 | 18 | 0.0000 ± 0.0000 | 1 |
| **21** | 0.0648 ± 0.1306 | 6 | 0.0043 ± 0.0029 | 5 | ***0.0043*** | 0 | 0.0015 ± 0.0008 | 2 |
| **27** | 0.0171 ± 0.0026 | 2 | 0.0035 ± 0.0030 | 5 | 0.0952 | 0 | 0.0017 ± 0.0009 | 2 |
| **33** | 0 ± 0 | 0 | 0.0069 ± 0.0096 | 4 | / | / | 0.0000 ± 0.0000 | 1 |

Since increased total uptake of glucose to iLNs of CpG-injected mice might be due to increased organ volumes in CpG-injected mice, it was also of interest to look at maximum intensity of FDG signal in iLNs. Local maximum intensities might indicate proliferative centers of malignant cells, which require more energy generated by glycolysis. Maximum intensity in a defined volume, measured as radioactivity in becquerel per ml, can be seen as an equivalent to the maximum concentration of glucose per ml in a defined volume. Maximum Bq/ml after FDG injection in inguinal lymph nodes (Figure 17, Table 15) again shows a similar pattern to inguinal lymph node volume (Figure 15, Table 13) and percentage of FDG uptake (Figure 18, Table 14), further supporting the thesis that CpG injections increase the metabolism of lymph nodes *in vivo*.

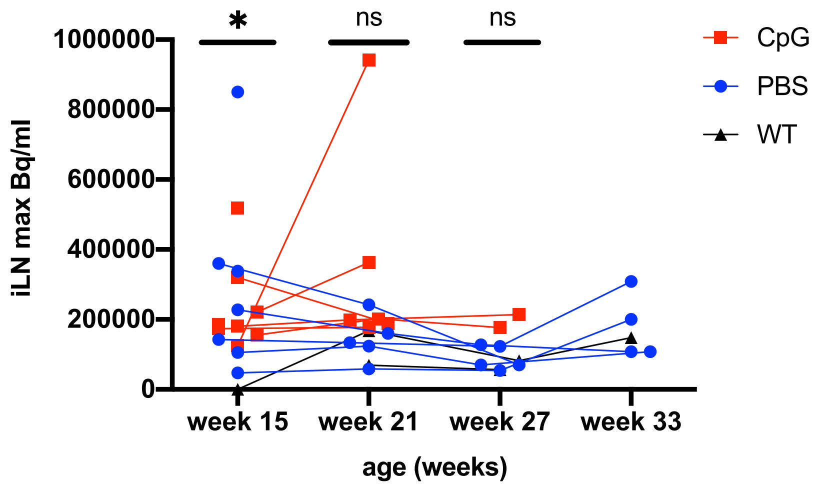

Figure 20a **CpG-treated MBC mice show increased maximum glucose metabolism in inguinal lymph nodes, illustrated as a line diagram.** CpG stimulation leads to increased maximum activity in inguinal lymph nodes (iLN), measured in becquerel per ml, at age of 15 weeks. One CpG mouse was still alive at week 27, but measurement was not possible due to technical reasons, thus no value is shown at week 27. Each dot represents one animal. WT = wild type mice. Statistical analysis was performed using unpaired Mann-Whitney tests, see Table 15. * = $p < 0.05$, ** = $p < 0.01$, *** = $p < 0.001$, **** = $p < 0.0001$, ns = not significant. P-values refer to the comparison between CpG and PBS treatment groups. Connecting lines identify identical animals measured at different time points.

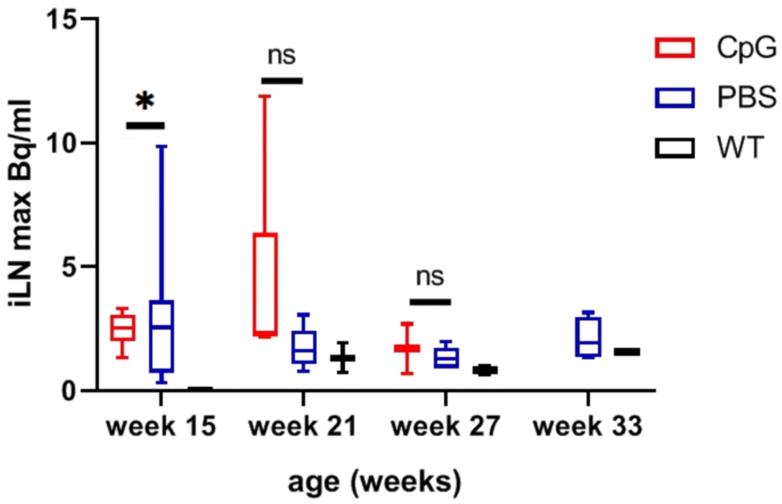

Figure 21b **CpG-treated MBC mice show increased maximum glucose metabolism in inguinal lymph nodes, summary data.** CpG stimulation leads to increased maximum activity in inguinal lymph nodes (iLN), measured in becquerel per ml, at age of 15 weeks. WT = wild type mice. Statistical analysis was performed using unpaired Mann-Whitney tests, see Table 15. * = p < 0.05, ** = p < 0.01, *** = p < 0.001, **** = p < 0.0001, ns = not significant. P-values refer to the comparison between CpG and PBS treatment groups. Box plot whiskers indicate minimum and maximum.

Table 15 **CpG-treated MBC mice show increased maximum glucose metabolism in inguinal lymph nodes**. Mean and SD values represent maximum FDG uptake to inguinal lymph node (iLN) measured in maximum becquerel per millilitre (max Bq/ml). Statistically significant results are marked. Statistical analysis was performed using Mann-Whitney tests, p-value refers to difference between MBC mice with CpG treatment and MBC mice with PBS (control) treatment at the age indicated. SD = standard deviation, N = sample size, U = Mann-Whitney U.

| | **CpG-treated MBC mice** | | **PBS-treated MBC mice** | | | | **WT mice** | |
|---|---|---|---|---|---|---|---|---|
| Age (weeks) | Max Bq/ml in iLN | N | Max Bq/ml in iLN | N | P-value | U | Max Bq/ml in iLN | N |
| **15** | 235125 ± 128483 | 8 | 296029 ± 270435 | 7 | ***0.0401*** | 10 | 0 ± 0 | 1 |
| **21** | 345500 ± 300240 | 6 | 143720 ± 66431 | 5 | 0.0519 | 4 | 118750 ± 69650 | 2 |
| **27** | 195500 ± 26163 | 2 | 89100 ± 33895 | 5 | 0.0952 | 0 | 69500 ± 18243 | 2 |
| **33** | 0 ± 0 | 0 | 181250 ± 95573 | 4 | / | / | 148000 ± 0 | 1 |

### 3.3.5. CpG stimulation might lead to increased glucose uptake in the spleen

Since the spleen is another lymphoid organ relevant for DLBCL disease course, glucose metabolism in the spleen of CpG-treated and PBS-treated MBC mice was also assessed using the PET-MRI measurements described for the measurement of inguinal lymph node glucose metabolism in section 3.3.4. Examples of a normally sized spleen with lower glucose uptake and an enlarged spleen with higher glucose uptake can be seen in Figure 22, respectively.

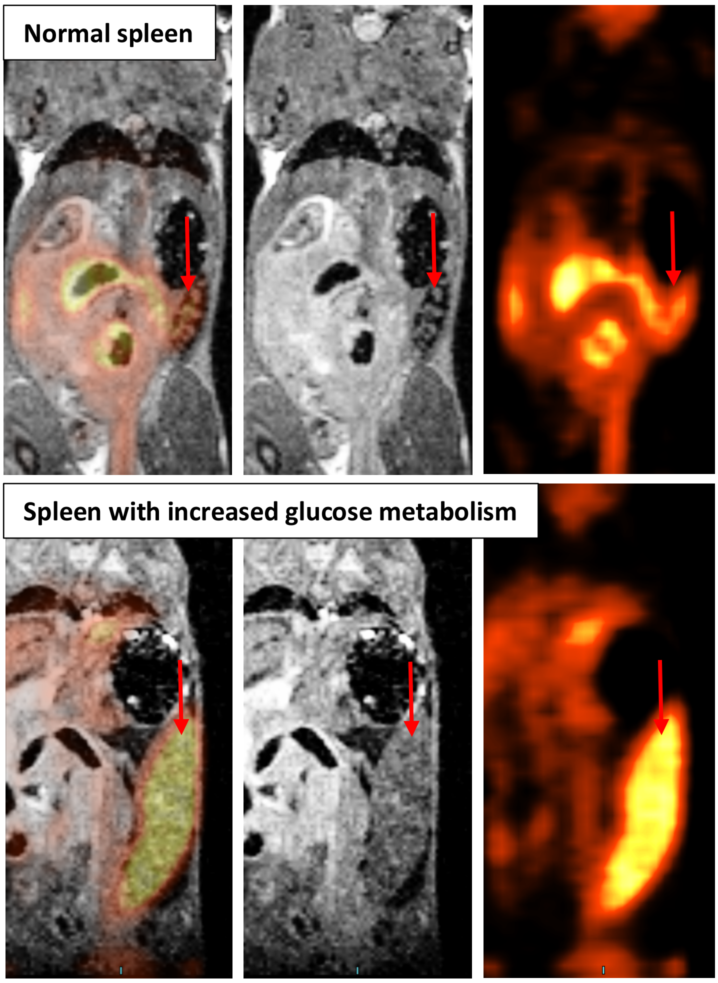

Figure 22 **PET-MRI measurements can determine glucose metabolism in the spleen, examples**. Using PET-MRI measurements, glucose metabolism in the spleen can be evaluated *in vivo*. An example of a spleen with low glucose uptake (top, PBS-treated MBC mouse 66 at 15 weeks of age) and a spleen with increased glucose uptake (bottom, CpG-treated MBC mouse 110 at 15 weeks of age) are given. Red arrows indicate spleens.

Although not statistically significant, the values of some mice suggest that CpG treatment might increase total uptake of FDG into the spleen: The highest value at week 15 was from a CpG-treated mouse and the highest three values at week 21 were recorded for CpG-treated mice as well (Figure 23). Additionally, mice of either treatment died soon after showing high values of total FDG uptake into the spleen, suggesting a putative relevance of glucose metabolism in the spleen to DLBCL disease progression in MBC mice that waits to be confirmed. Interestingly, regarding maximum glucose metabolism values in the spleen, several CpG-treated mice seem to have lower values than PBS-treated mice (Figure 25, Table 17). Potentially this indicates that CpG-treated mice have proliferation centers elsewhere such as in inguinal lymph nodes (see section 3.3.4).

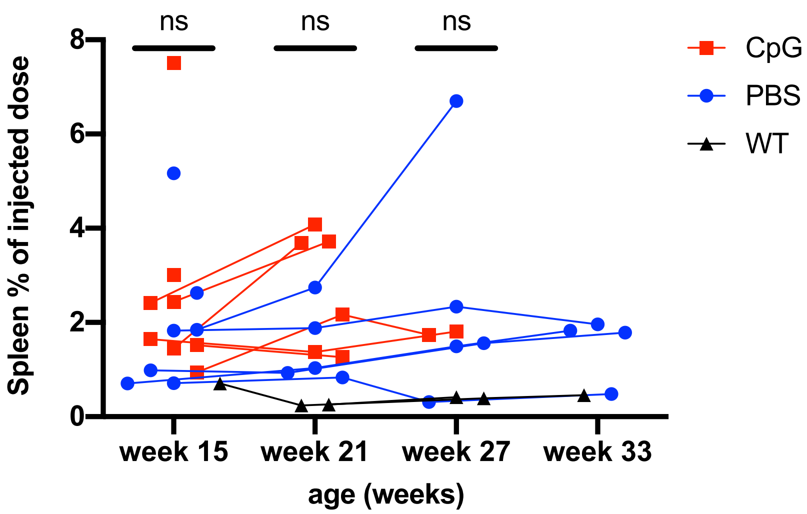

Figure 23a **CpG treatment in MBC mice might increase glucose metabolism in the spleen.** One CpG mouse was still alive at week 27, but measurement was not possible due to technical reasons, thus no value is shown at week 27. Each dot represents one animal. WT = wild type mice. Statistical analysis was performed using unpaired Mann-Whitney tests, see Table 16. * = p < 0.05, ** = p < 0.01, *** = p < 0.001, **** = p < 0.0001, ns = not significant. P-values refer to the comparison between CpG and PBS treatment groups. Connecting lines identify identical animals measured at different time points.

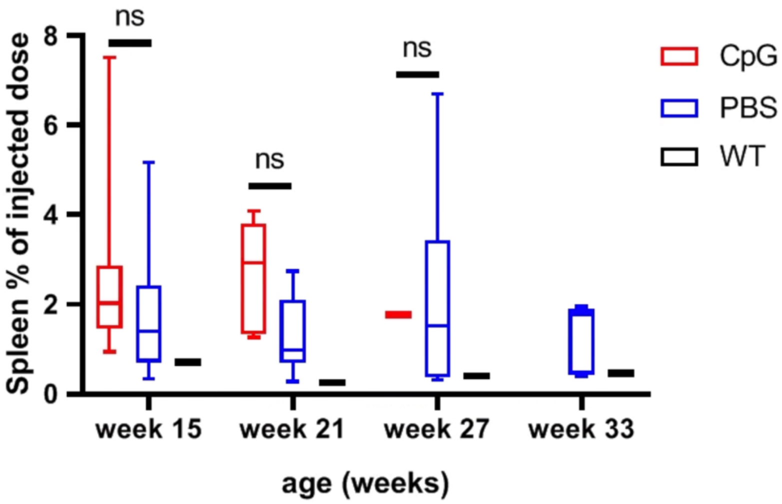

Figure 24b **CpG treatment in MBC mice might increase glucose metabolism in the spleen, summary data.** WT = wild type mice. Statistical analysis was performed using unpaired Mann-Whitney tests, see Table 16. * = p < 0.05, ** = p < 0.01, *** = p < 0.001, **** = p < 0.0001, ns = not significant. P-values refer to the comparison between CpG and PBS treatment groups. Box plot whiskers indicate minimum and maximum.

Table 16 **CpG treatment in MBC mice might increase glucose metabolism in the spleen**. Mean and SD values represent percentage of injected dose (ID) of FDG measured in the spleen. Statistical analysis was performed using Mann-Whitney tests, p-value refers to difference between MBC mice with CpG treatment and MBC mice with PBS (control) treatment at the age indicated. SD = standard deviation, N = sample size, U = Mann-Whitney U.

| | **CpG-treated MBC mice** | | **PBS-treated MBC mice** | | | | **WT mice** | |
|---|---|---|---|---|---|---|---|---|
| Age (weeks) | % of ID in spleen | N | % of ID in spleen | N | P-value | U | % of ID in spleen | N |
| **15** | 2.6150 ± 2.0860 | 8 | 1.7748 ± 1.5676 | 8 | 0.5358 | 22 | 0.7066 ± 0 | 1 |
| **21** | 2.7157 ± 1.2692 | 6 | 1.2823 ± 0.8830 | 6 | 0.0823 | 5 | 0.2489 ± 0.0129 | 2 |
| **27** | 1.7718 ± 0.0537 | 2 | 2.1320 ± 2.3651 | 6 | 0.8571 | 4 | 0.4024 ± 0.0174 | 2 |
| **33** | 0 ± 0 | 0 | 1.2882 ± 0.7835 | 5 | / | / | 0.4589 ± 0 | 1 |

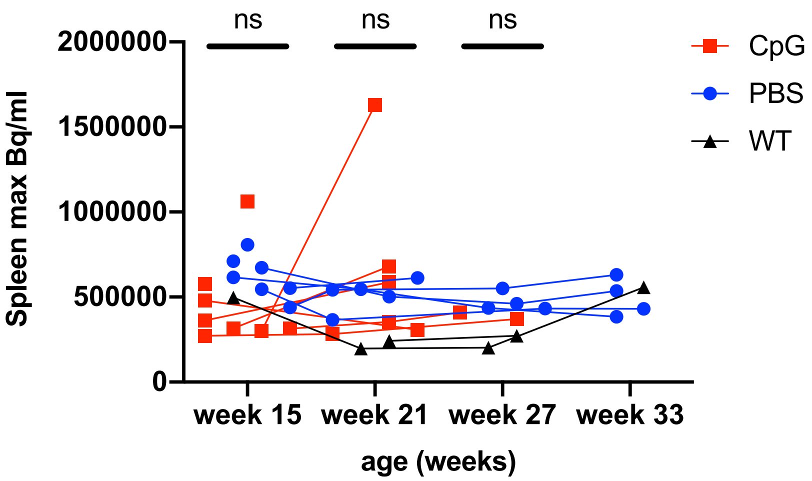

Figure 25a **Maximum glucose metabolism in the spleen might be lower in CpG-treated MBC mice.** Maximum glucose metabolism, measured in becquerel per ml, is not statistically different between CpG- and PBS-treated MBC mice. However, several CpG-treated mice seem to have lower values of maximum glucose metabolism in the spleen than PBS-treated mice, suggesting CpG treatment might lead to proliferation centers being elsewhere than in the spleen (see text). One CpG and one PBS mouse were still alive at week 27, but measurement was not possible due to technical reasons, thus no value is shown at week 27. Each dot represents one animal. WT = wild type mice. Statistical analysis was performed using unpaired Mann-Whitney tests, see Table 17. * = p < 0.05, ** = p < 0.01, *** = p < 0.001, **** = p < 0.0001, ns = not significant. P-values refer to the comparison between CpG and PBS treatment groups. Connecting lines identify identical animals measured at different time points.

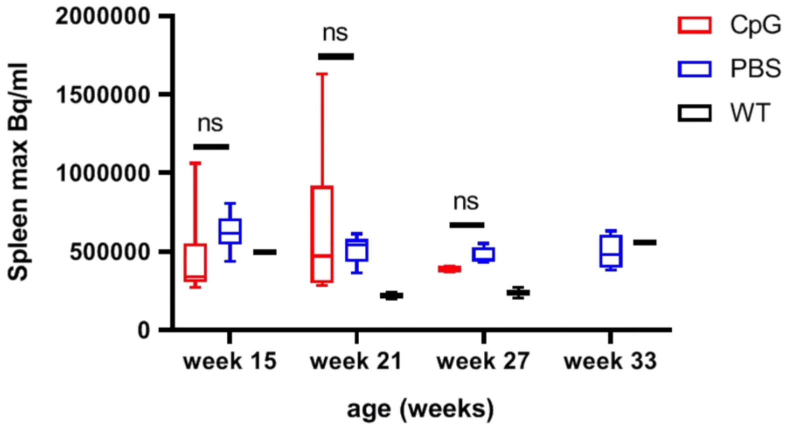

Figure 26b **Maximum glucose metabolism in the spleen might be lower in CpG-treated MBC mice, summary data.** Maximum glucose metabolism, measured in becquerel per ml, is not statistically different between CpG- and PBS-treated MBC mice. However, several CpG-treated mice seem to have lower values of maximum glucose metabolism in the spleen than PBS-treated mice, suggesting CpG treatment might lead to proliferation centers being elsewhere than in the spleen (see text). WT = wild type mice. Statistical analysis was performed using unpaired Mann-Whitney tests, see Table 17. * = p < 0.05, ** = p < 0.01, *** = p < 0.001, **** = p < 0.0001, ns = not significant. P-values refer to the comparison between CpG and PBS treatment groups. Box plot whiskers indicate minimum and maximum.

Table 17 **Maximum glucose metabolism in the spleen might be lower in CpG-treated MBC mice.** Mean and SD values represent maximum FDG uptake to the spleen measured in maximum becquerel per millilitre (max Bq/ml). Statistical analysis was performed using Mann-Whitney tests, p-value refers to difference between MBC mice with CpG treatment and MBC mice with PBS (control) treatment at the age indicated. SD = standard deviation, N = sample size, U = Mann-Whitney U.

| | **CpG-treated MBC mice** | | **PBS-treated MBC mice** | | | | **WT mice** | |
|---|---|---|---|---|---|---|---|---|
| Age (weeks) | Max Bq/ml in spleen | N | Max Bq/ml in spleen | N | P-value | U | Max Bq/ml in spleen | N |
| **15** | 460125 ± 263733 | 8 | 620429 ± 121685 | 7 | 0.0541 | 11 | 498000 ± 0 | 1 |
| **21** | 640167 ± 510811 | 6 | 513600 ± 91341 | 5 | 0.9307 | 14 | 220000 ± 32527 | 2 |
| **27** | 389500 ± 27577 | 2 | 470000 ± 54790 | 4 | 0.1333 | 0 | 238000 ± 49497 | 2 |
| **33** | 0 ± 0 | 0 | 495000 ± 110230 | 4 | / | / | 558000 ± 0 | 1 |

### 3.3.6. CpG stimulation triggers splenic cell proliferation

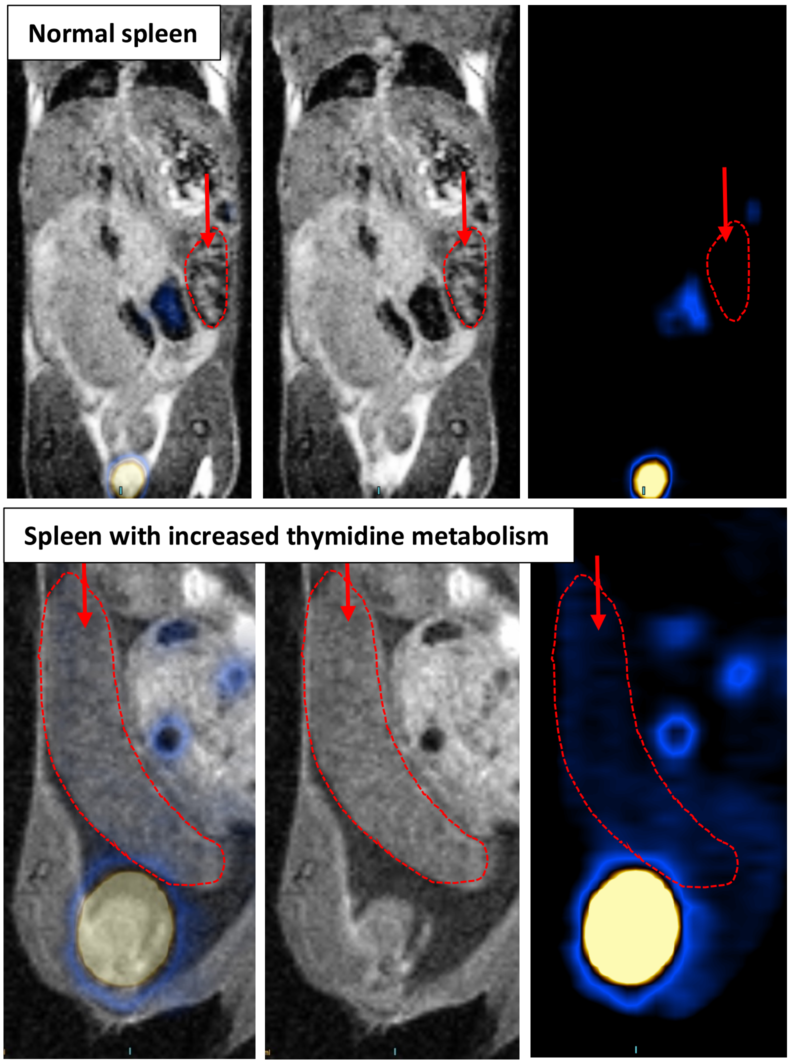

Figure 27 **PET-MRI measurements can determine proliferation in the spleen, examples**. Using PET-MRI measurements, thymidine metabolism in the spleen can be evaluated *in vivo*. An example of a spleen with low thymidine uptake (top, PBS-treated MBC mouse 98 at 15 weeks of age) and a spleen with increased thymidine uptake (bottom, CpG-treated MBC mouse 110 at 15 weeks of age) are given. Red arrows indicate spleens. Yellow signal on the bottom represents the bladder.

Tumours typically do not only show increased glycolysis but also increased proliferation. To evaluate proliferation in MBC mice upon CpG treatment *in vivo*, we performed PET scans using the tracer FLT ([$^{18}$F]-thymidine), which tracks thymidine metabolism and thereby proliferation. The mice were intravenously injected with the tracer and PET scans were performed using a dedicated Inveon small animal PET scanner with a spatial resolution of ≈ 1.3 mm (Siemens Preclinical Solutions, Knoxville, TN, USA). For anatomical orientation, the PET images were co-registered with MR images as described in 3.3.4. An example can be seen in Figure 27.

FLT-PET-MRI measurements revealed that CpG injections lead to increased thymidine uptake and thus proliferation in the spleen as measured by the percentage of injected dose in the spleen (Figure 28, Table 18) and maximum Bq/ml in the spleen (Figure 30, Table 19). This suggests that CpG treatment leads to increased proliferation in the spleen of MBC mice. High FLT values in the spleen also correlated with other disease Parameters on an individual basis: Mouse 110, which had the highest percentage of injected dose FLT in the spleen at week 15 (Figure 28), also showed signs of a liver tumour in FDG-PET-MRI scans (Figure 44) and died before the next measurement at week 21. Mouse 112, which had the second-highest value for % of injected FLT dose in the spleen at week 21 (Figure 18), had the highest inguinal lymph node volume (Figure 15) and also died before the next measurement at week 27. However, when aggravating factors such as signs of liver tumour or increased inguinal lymph node volume were absent, some mice even survived high percentages of injected FLT dose in the spleen: Mouse 108 had the highest value of % of injected FLT dose in the spleen at week 21 (Figure 28), but no signs of liver tumour, average inguinal lymph node volume and did not die until after week 27. Although it is possible that CpG injection alone was detrimental, it appears that CpG-treated MBC mice not only succumbed earlier as a result of being treated but also showed signs of concomitant advanced lymphoproliferative disease contributing to death.

Another observation was that at week 21, the percentage of injected dose in the spleen seems to peak in both CpG and PBS mice (Figure 28). Similar trends could be seen with spleen volume (Figure 13) and maximum Bq/ml FLT in the spleen (Figure 30). This might suggest that in MBC mice the spleen is especially relevant for DLBCL progression at the age of around 21 weeks.

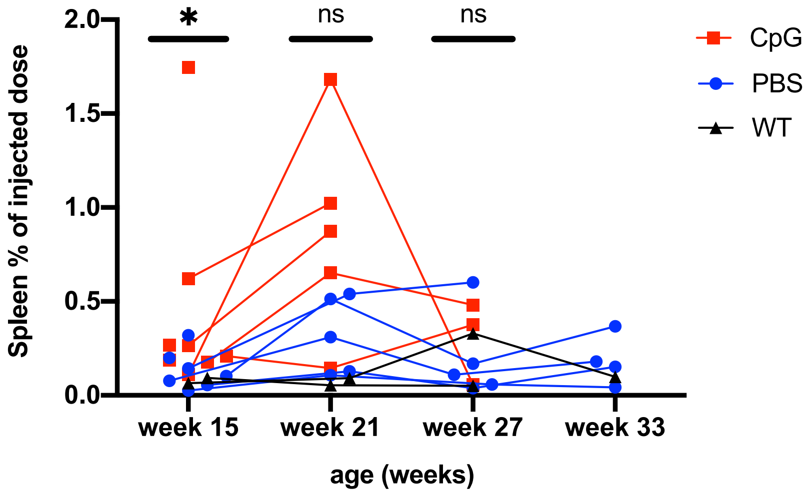

Figure 28a **CpG-treated MBC mice show increased proliferation in the spleen.** Each dot represents one animal. WT = wild type mice. Statistical analysis was performed using unpaired Mann-Whitney tests, see Table 18. * = $p < 0.05$, ** = $p < 0.01$, *** = $p < 0.001$, **** = $p < 0.0001$, ns = not significant. P-values refer to the comparison between CpG and PBS treatment groups. Connecting lines identify identical animals measured at different time points.

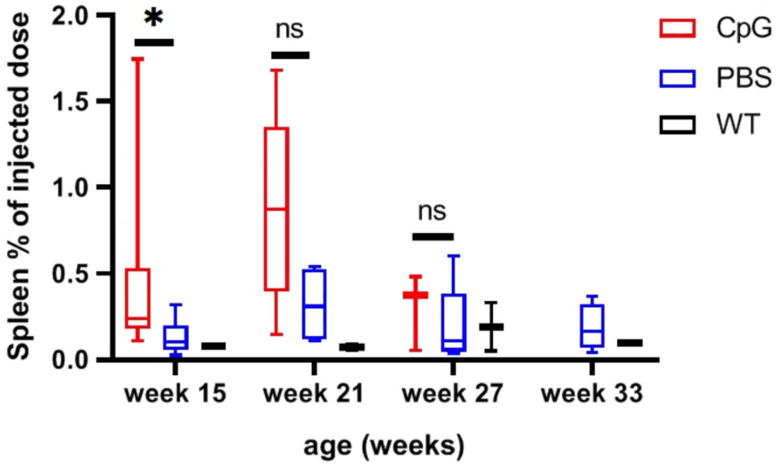

Figure 29b **CpG-treated MBC mice show increased proliferation in the spleen, summary data.** WT = wild type mice. Statistical analysis was performed using unpaired Mann-Whitney tests, see Table 18. * = p < 0.05, ** = p < 0.01, *** = p < 0.001, **** = p < 0.0001, ns = not significant. P-values refer to the comparison between CpG and PBS treatment groups. Box plot whiskers indicate minimum and maximum.

Table 18 **CpG-treated MBC mice show increased proliferation in the spleen**. Mean and SD values represent percentage of injected dose (ID) of FLT measured in the spleen. Statistical analysis was performed using Mann-Whitney tests, p-value refers to difference between MBC mice with CpG treatment and MBC mice with PBS (control) treatment at the age indicated. SD = standard deviation, N = sample size, U = Mann-Whitney U.

| | **CpG-treated MBC mice** | | **PBS-treated MBC mice** | | | | **WT mice** | |
|---|---|---|---|---|---|---|---|---|
| Age (weeks) | % of ID in spleen | N | % of ID in spleen | N | P-value | U | % of ID in spleen | N |
| **15** | 0.6249 ± 0.3700 | 8 | 0.3908 ± 0.0659 | 7 | ***0.0401*** | 10 | 0.4180 ± 0.0694 | 2 |
| **21** | 1.1130 ± 0.6140 | 5 | 0.9845 ± 0.4670 | 5 | 0.0556 | 3 | 0.3310 ± 0.1189 | 2 |
| **27** | 0.5706 ± 0.2681 | 3 | 0.3758 ± 0.1583 | 5 | 0.7857 | 6 | 0.3876 ± 0.1952 | 2 |
| **33** | 0 ± 0 | 0 | 0.4617 ± 0.1945 | 4 | / | / | 0.4318 ± 0 | 1 |

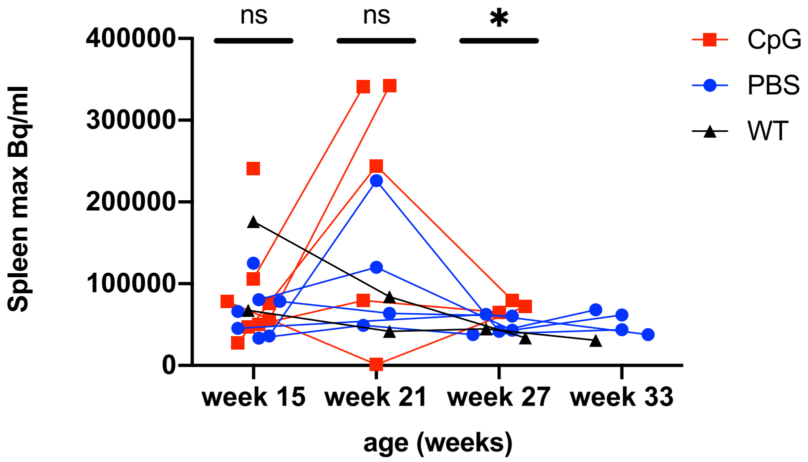

Figure 30a **CpG-treated MBC mice show increased maximum proliferation in the spleen.** Maximum FLT uptake, measured in becquerel per ml, is higher in the CpG-treated MBC mice at week 27. Additionally, maximum FLT uptake to the spleen shows a peak at week 21. Each dot represents one animal. WT = wild type mice. Statistical analysis was performed using unpaired Mann-Whitney tests, see Table 19. * = p < 0.05, ** = p < 0.01, *** = p < 0.001, **** = p < 0.0001, ns = not significant. P-values refer to the comparison between CpG and PBS treatment groups. Connecting lines identify identical animals measured at different time points.

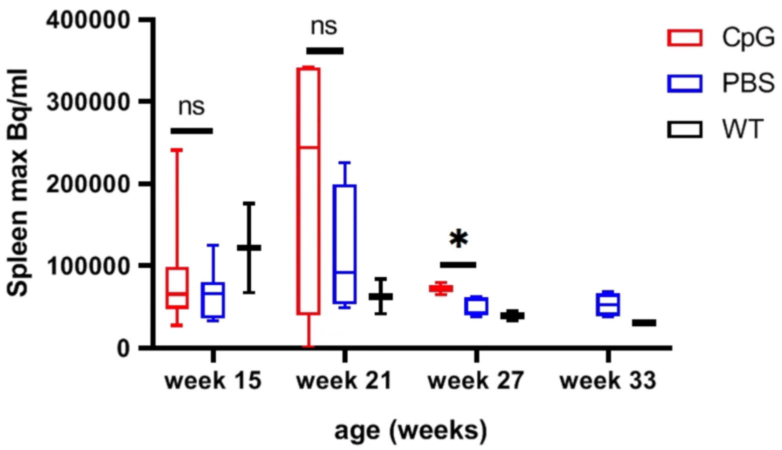

Figure 31b **CpG-treated MBC mice show increased maximum proliferation in the spleen, summary data.** Maximum FLT uptake, measured in becquerel per ml, is higher in the CpG-treated MBC mice at week 27. Additionally, maximum FLT uptake to the spleen shows a peak at week 21. WT = wild type mice. Statistical analysis was performed using unpaired Mann-Whitney tests, see Table 19. * = $p < 0.05$, ** = $p < 0.01$, *** = $p < 0.001$, **** = $p < 0.0001$, ns = not significant. P-values refer to the comparison between CpG and PBS treatment groups. Box plot whiskers indicate minimum and maximum.

Table 19 **CpG-treated MBC mice show increased maximum proliferation in the spleen.** Mean and SD values represent maximum FLT uptake to the spleen measured in maximum becquerel per millilitre (max Bq/ml). Statistical analysis was performed using Mann-Whitney tests, p-value refers to difference between MBC mice with CpG treatment and MBC mice with PBS (control) treatment at the age indicated. SD = standard deviation, N = sample size, U = Mann-Whitney U.

| | **CpG-treated MBC mice** | | **PBS-treated MBC mice** | | | | **WT mice** | |
|---|---|---|---|---|---|---|---|---|
| Age (weeks) | Max Bq/ml in spleen | N | Max Bq/ml in spleen | N | P-value | U | Max Bq/ml in spleen | N |
| **15** | 85212 ± 67326 | 8 | 66529 ± 32136 | 7 | 0.8665 | 26 | 121750 ± 76721 | 2 |
| **21** | 201494 ± 154990 | 5 | 114800 ± 80153 | 4 | 0.4127 | 6 | 62950 ± 29769 | 2 |
| **27** | 72333 ± 7353 | 3 | 49100 ± 11452 | 5 | ***0.0357*** | 0 | 39300 ± 7778 | 2 |
| **33** | 0 ± 0 | 0 | 52825 ± 14332 | 4 | / | / | 30700 ± 0 | 1 |

### 3.3.7. CpG stimulation does not increase proliferation in the bone marrow

In DLBCL diagnostics, both bone marrow biopsy and bone marrow evaluation via FDG-PET-MRI play an important role in DLBCL staging (see section 1.5.3). Thus, we evaluated whether bone marrow involvement in MBC mice differed between CpG-treated and PBS-treated MBC mice by performing FDG PET-MRI measurements of the femoral bone marrow (Figure 32).

Overall, no notable pattern or difference was detectable between the groups. In particular, the values for maximum Bq/ml in the femur's bone marrow did not differ between CpG-injected mice and PBS-injected mice (Figure 33, Table 20), suggesting that CpG does not affect bone marrow involvement in MBC mice.

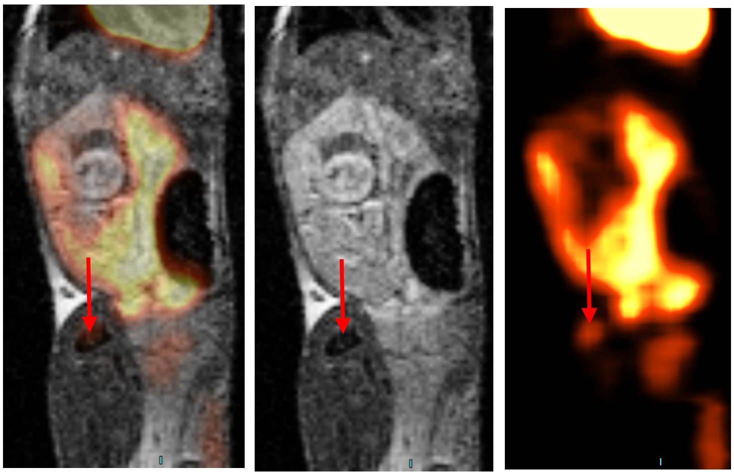

Figure 32 **PET-MRI measurements can determine glucose metabolism in the bone marrow, example**. Using PET-MRI measurements, glucose metabolism in the bone marrow of the femur can be evaluated *in vivo*. An example of a femur is given (PBS-treated MBC mouse 73 at 15 weeks of age). Red arrows indicate the femur.

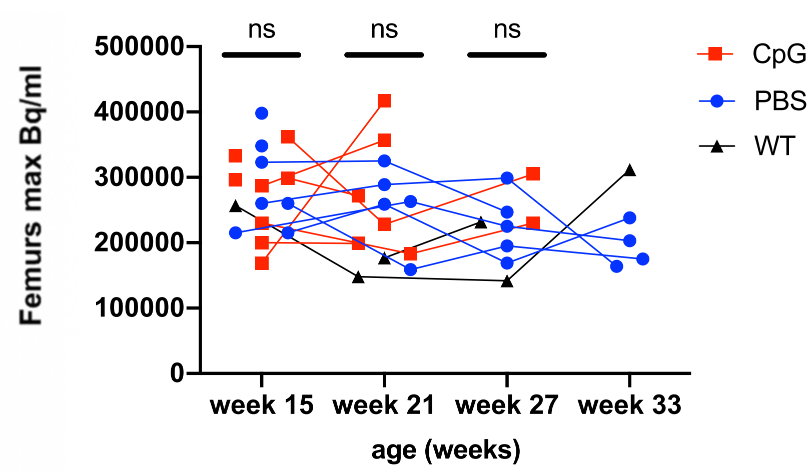

Figure 33a **CpG-treated MBC mice do not show increased glucose metabolism in the bone marrow.** Maximum FDG uptake in the femurs' bone marrow, measured in maximum becquerel per millilitre (max Bq/ml) and standardised to average injected dose, did not differ between CpG and PBS stimulated mice. One CpG mouse was still alive at week 27, but measurement was not possible due to technical reasons, thus no value is shown at week 27. Each dot represents one animal. WT = wild type mice. Statistical analysis was performed using unpaired Mann-Whitney tests, see Table 20. * = p < 0.05, ** = p < 0.01, *** = p < 0.001, **** = p < 0.0001, ns = not significant. P-values refer to the comparison between CpG and PBS treatment groups. Connecting lines identify identical animals measured at different time points.

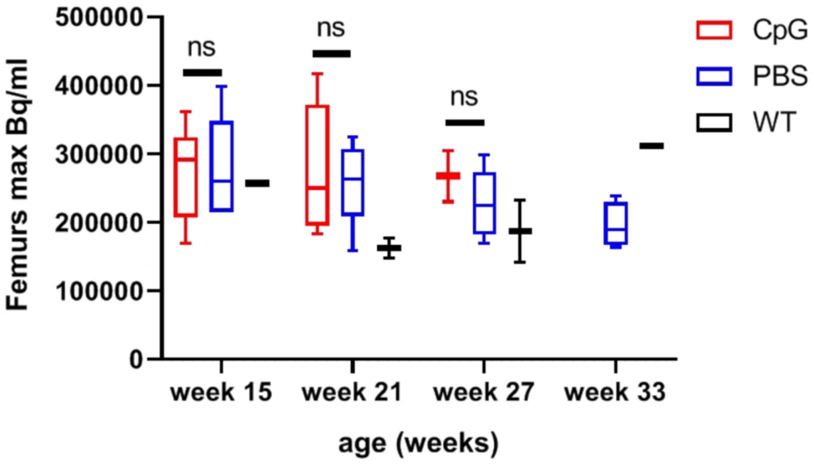

Figure 34b **CpG-treated MBC mice do not show increased glucose metabolism in the bone marrow, summary data.** Maximum FDG uptake in the femurs' bone marrow, measured in maximum becquerel per millilitre (max Bq/ml) and standardised to average injected dose, did not differ between CpG and PBS stimulated mice. WT = wild type mice. Statistical analysis was performed using unpaired Mann-Whitney tests, see Table 20. * = p < 0.05, ** = p < 0.01, *** = p < 0.001, **** = p < 0.0001,

ns = not significant. P-values refer to the comparison between CpG and PBS treatment groups. Box plot whiskers indicate minimum and maximum.

Table 20 **CpG-treated MBC mice do not show increased glucose metabolism in the bone marrow.** Mean and SD values represent maximum FLT uptake to the femurs measured in maximum becquerel per millilitre (max Bq/ml). Statistical analysis was performed using Mann-Whitney tests, p-value refers to difference between MBC mice with CpG treatment and MBC mice with PBS (control) treatment at the age indicated. SD = standard deviation, N = sample size, U = Mann-Whitney U.

| | **CpG-treated MBC mice** | | **PBS-treated MBC mice** | | | | **WT mice** | |
|---|---|---|---|---|---|---|---|---|
| Age (weeks) | Max Bq/ml in femurs | N | Max Bq/ml in femurs | N | P-value | U | Max Bq/ml in femurs | N |
| **15** | 272000 ± 66449 | 8 | 288428 ± 69701 | 7 | 0.7584 | 25 | 257000 ± 0 | 1 |
| **21** | 276000 ± 93102 | 6 | 259000 ± 61790 | 5 | 0.9307 | 14 | 162500 ± 20506 | 2 |
| **27** | 267500 ± 53033 | 2 | 227000 ± 49940 | 5 | 0.3810 | 2 | 187000 ± 63640 | 2 |
| **33** | 0 ± 0 | 0 | 195000 ± 33035 | 4 | / | / | 312000 ± 0 | 1 |

### 3.3.8. FDG-PET-MRI measurements allow case studies of intestinal tumours in MBC mice

The finding of increased B-cell density in the abdomen of MBC mice compared to those of BC mice when reaching abortion criteria (see section 3.1) suggests the presence of lymphoma in the intestine in MBC mice. It was thus of interest whether intestinal tumours could be found in PET-MRI measurements of MBC mice since this would point towards increased abdominal lymphomagenesis in MBC mice and therefore potentially increased abdominal lymphomagenesis in DLBCL patients with the *MYD88*$^{L265P}$ mutation.

FDG-PET-MRI allowed identification of intestinal tumours (abdominal FDG signal not due to spleen, liver, heart, kidney, ureters, bladder or adrenal glands) in several MBC mice (see Figure 36 and examples in Figure 58, Figure 59, Figure 60, Figure 61 and Figure 62 in appendix). Despite continuous bowel loop movement over time, it was possible to track lymphoma in one mouse over all four time points (see Figure 36) and in another mouse over two time points (see Figure 61 in appendix). Potentially, this was due to the increased infiltrative growth of the lymphoma mass, limiting bowel movement. WT mice did not show any intestinal tumours (see Figure 35).

For FLT-PET data, we did not find any significant uptake to the intestinal area and most trace was already within the urinary tract, suggesting that the incubation time of one hour might have been too long for FLT as to be able to detect FLT uptake to the intestine.

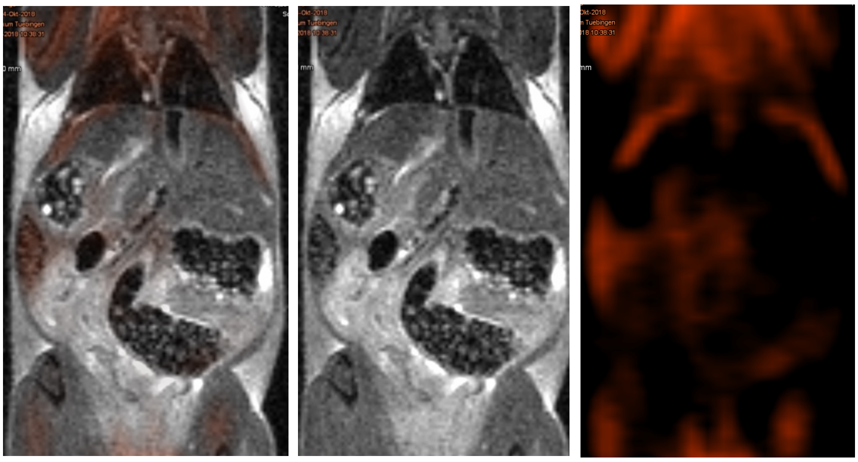

Figure 35 **Wildtype mice do not show increased abdominal FDG signal or intestinal tumours, example.** Example taken from wildtype mouse at the age of 33 weeks. Even at this age no areas of increased FDG signal can be seen in the abdominal area.

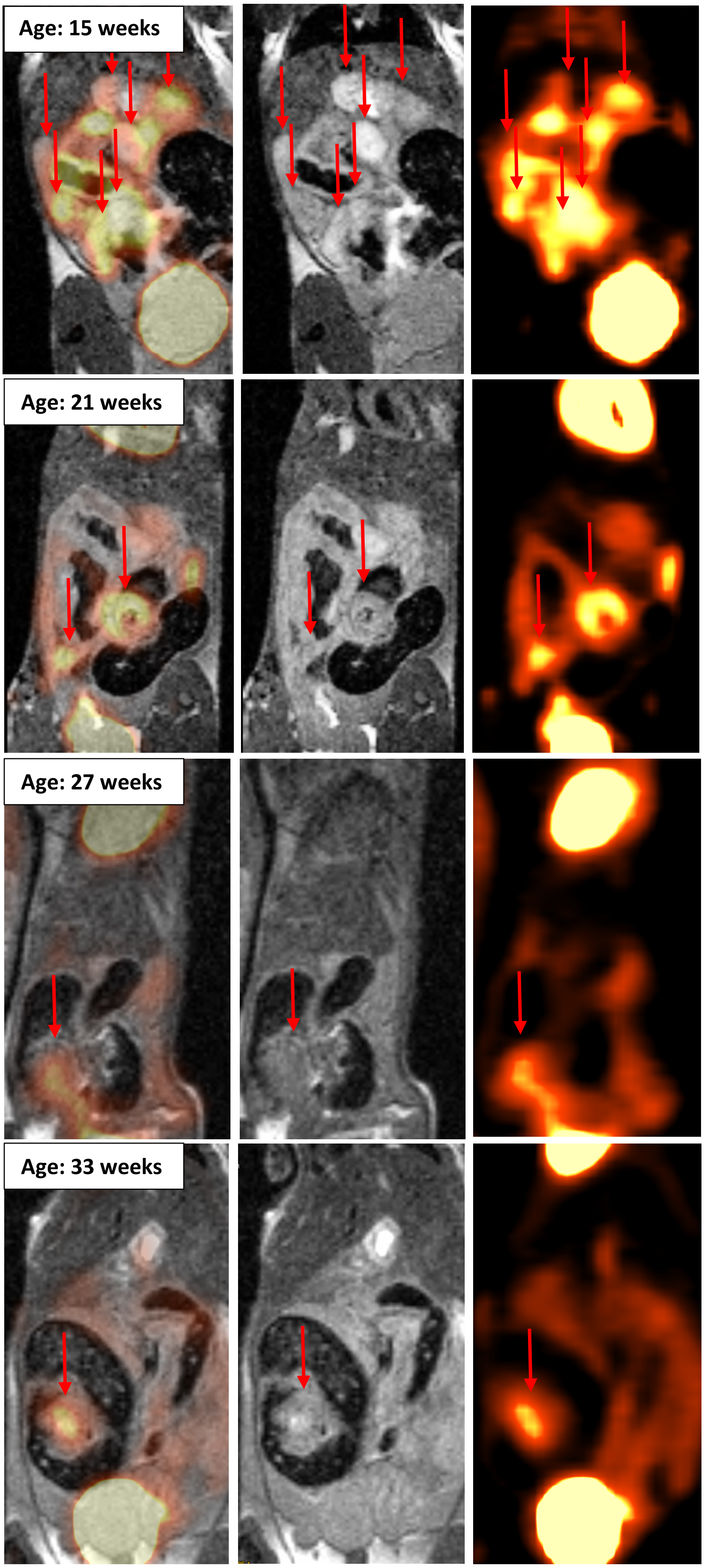

Figure 36 **Example of intestinal tumours in a MBC mouse across 4 time points.** Images of mouse 73 (PBS-treated) at the age of 15, 21, 27 and 33 weeks shows high FDG-PET signal around several bowel loops. Red arrows indicate protruding intestinal tumours.

### 3.3.9. FDG-PET-MRI quantification suggests CpG does not increase intestinal tumour growth

Since qualitative data of intestinal tumours in MBC mice on a case to case basis showed intestinal tumours being present in MBC mice but not in WT mice (see section 3.3.8), we were interested in whether a quantification of these intestinal tumours would show differences between PBS-treated and CpG-treated MBC mice. The attempt of quantification shown in this section was performed by drawing ROIs around increased abdominal FDG-PET signal not stemming from the spleen, the liver, the kidneys, the ureters, the bladder, the heart or the adrenal glands. If no such signal was found, no ROIs were drawn and thus any values in the following graphs equal zero. However, these mice might still have intestinal tumours that are too small (below 1 mm) or too diffuse to detect via FDG-PET or that do not take up FDG due to necrosis or for other reasons.

As already mentioned in section 3.3.8, all WT mice did not show any increased abdominal FDG signal while MBC mice did show increased abdominal FDG signal. Conversely, the percentage of CpG-treated MBC mice with increased abdominal FDG signal was lower than the percentage of PBS-treated MBC mice with increased abdominal FDG signal at all time points measured (see Table 21). The greatest difference was observed at the age of 15 weeks, where only two out of eight CpG-treated MBC mice (25%) but all seven PBS-treated MBC mice (100%) showed increased abdominal FDG signal (see Table 21). At the age of 15 weeks, PBS-treated MBC mice showed a higher volume of increased abdominal FDG signal ($p = 0.0003$, see Figure 37 and Table 22) and a higher percentage of injected FDG dose taken up to areas of increased abdominal FDG signal ($p = 0.0003$, see and Table 23) compared to CpG-treated MBC mice. Except for one PBS-treated mouse, the volume of increased abdominal FDG signal seems to decrease in PBS-treated MBC mice but increase in CpG-treated MBC mice over time (Figure 37). A similar trend can be seen in the percentage of injected FDG dose taken up to areas of increased abdominal FDG signal ( Figure 39). Finally, if areas of increased abdominal FDG signal were detected, maximum becquerel per ml in these areas did not differ between PBS-treated and CpG-treated MBC mice). As explained in section 3.3.4, maximum becquerel per ml can be seen as an equivalent to maximum concentration of glucose per ml.

Table 21 **A higher percentage of PBS-treated MBC mice show areas of increased abdominal FDG signal**. Given is the percentage of mice in which areas of increased abdominal FDG-PET signal not stemming from the spleen, the liver, the kidneys, the ureters, the bladder, the heart or the adrenal glands were detected. WT mice did not show any increased abdominal FDG signal (n(week 15) =1, n(week 21) = 2, n(week 27) = 2, n(week 33) = 1) and are thus not shown in the table.

| | **MBC genotype – CpG treatment** | | **MBC genotype – PBS (control) treatment** | |
|---|---|---|---|---|
| Age (weeks) | Percentage of mice with increased abdominal FDG signal | N | Percentage of mice with increased abdominal FDG signal | N |
| **15** | 25% | 8 | 100% | 7 |
| **21** | 50% | 6 | 80% | 5 |
| **27** | 50% | 2 | 80% | 5 |
| **33** | 0% | 0 | 75% | 4 |

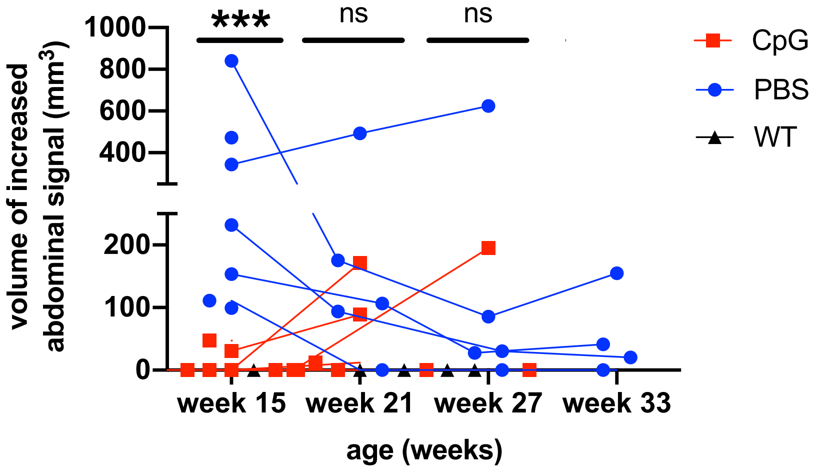

Figure 37a **The volume of increased abdominal FDG signal might be higher in PBS-treated MBC mice**. Each dot represents one animal. WT = wild type mice. Statistical analysis was performed using unpaired Mann-Whitney tests, see Table 22. * = $p < 0.05$, ** = $p < 0.01$, *** = $p < 0.001$, **** = $p < 0.0001$, ns = not significant. P-values refer to the comparison between CpG and PBS treatment groups. Connecting lines identify identical animals measured at different time points.

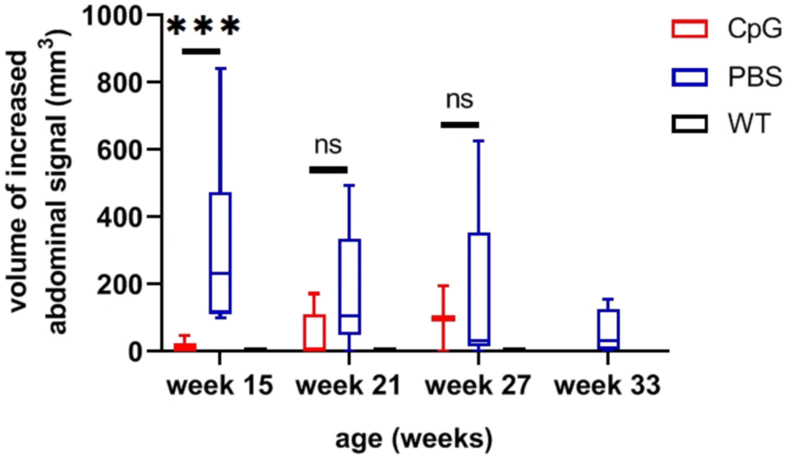

Figure 38b **The volume of increased abdominal FDG signal might be higher in PBS-treated MBC mice, summary data**. WT = wild type mice. Statistical analysis was performed using unpaired Mann-Whitney tests, see Table 22. * = $p < 0.05$, ** = $p < 0.01$, *** = $p < 0.001$, **** = $p < 0.0001$, ns = not significant. P-values refer to the comparison between CpG and PBS treatment groups. Box plot whiskers indicate minimum and maximum.

Table 22 **The volume of increased abdominal FDG signal might be higher in PBS-treated MBC mice**. Mean and SD values represent the volume of increased abdominal FDG signal measured in mm$^3$. Statistical analysis was performed using Mann-Whitney tests, p-value refers to difference between MBC mice with CpG treatment and MBC mice with PBS (control) treatment at the age indicated. SD = standard deviation, N = sample size, U = Mann-Whitney U. WT mice did not show any increased abdominal FDG signal (n(week 15) =1, n(week 21) = 2, n(week 27) = 2, n(week 33) = 1) and are thus not shown in the table.

| | **CpG-treated MBC mice** | | **PBS-treated MBC mice** | | | |
|---|---|---|---|---|---|---|
| Age (weeks) | Volume of increased abdominal FDG signal (mm$^3$) | N | Volume of increased abdominal FDG signal (mm$^3$) | N | P-value | U |
| **15** | 10 ± 19 | 8 | 322 ± 265 | 7 | ***0.0003*** | 0 |
| **21** | 45 ± 71 | 6 | 174 ± 189 | 5 | 0.1342 | 6.5 |
| **27** | 98 ± 138 | 2 | 154 ± 265 | 5 | 0.9524 | 4.5 |
| **33** | 0 ± 0 | 0 | 54 ± 69 | 4 | / | / |

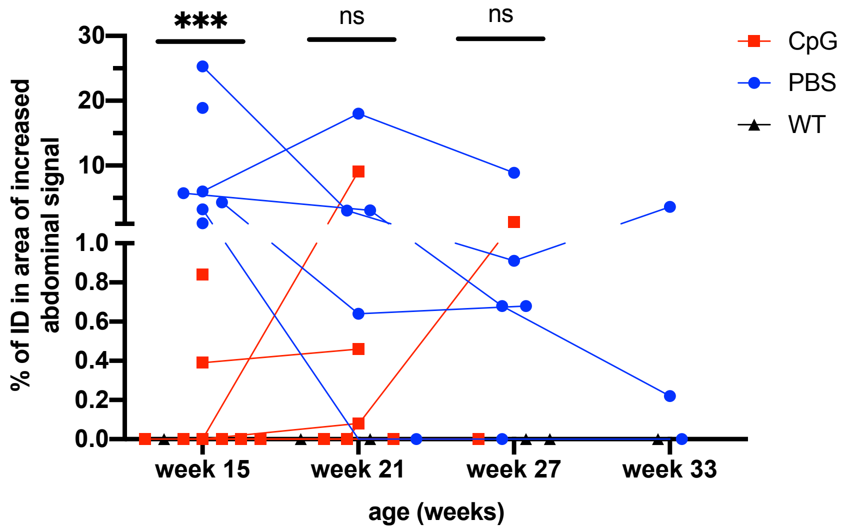

Figure 39a **PBS-treated MBC mice might take up more FDG to the abdomen than CpG-treated MBC mice.** Each dot represents one animal. WT = wild type mice. Statistical analysis was performed using unpaired Mann-Whitney tests, see Table 23. * = $p < 0.05$, ** = $p < 0.01$, *** = $p < 0.001$, **** = $p < 0.0001$, ns = not significant. P-values refer to the comparison between CpG and PBS treatment groups. Connecting lines identify identical animals measured at different time points.

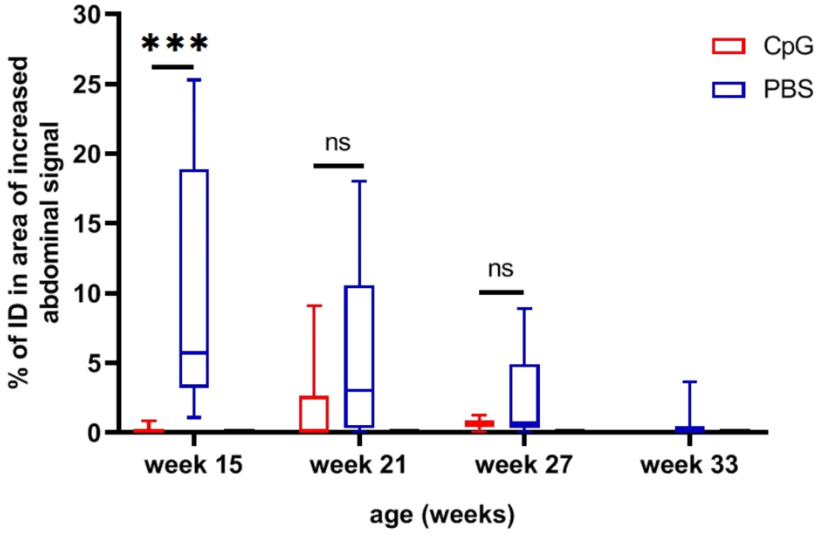

Figure 40b **PBS-treated MBC mice might take up more FDG to the abdomen than CpG-treated MBC mice, summary data.** WT = wild type mice. Statistical analysis was performed using unpaired Mann-Whitney tests, see Table 23. * = $p < 0.05$, ** = $p < 0.01$, *** = $p < 0.001$, **** = $p < 0.0001$, ns = not significant. P-values refer to the comparison between CpG and PBS treatment groups. Box plot whiskers indicate minimum and maximum.

Table 23 **PBS-treated mice might take up more FDG to the abdomen than CpG-treated MBC mice.** Mean and SD values represent the percentage of injected dose (ID) of FDG in areas of increased abdominal FDG signal (see text). Statistical analysis was performed using Mann-Whitney tests, p-value refers to difference between MBC mice with CpG treatment and MBC mice with PBS (control) treatment at the age indicated. SD = standard deviation, N = sample size, U = Mann-Whitney U. WT mice did not show any increased abdominal FDG signal (n(week 15) =1, n(week 21) = 2, n(week 27) = 2, n(week 33) = 1) and are thus not shown in the table.

| | **CpG-treated MBC mice** | | **PBS-treated MBC mice** | | | |
|---|---|---|---|---|---|---|
| Age (weeks) | ID in area of increased abdominal FDG signal (%) | N | ID in area of increased abdominal FDG signal (%) | N | P-value | U |
| **15** | 0.1538 ± 0.3091 | 8 | 9.2229 ± 9.1335 | 7 | ***0.0003*** | 0 |
| **21** | 1.6067 ± 3.6753 | 6 | 4.9560 ± 7.4338 | 5 | 0.1905 | 7.5 |
| **27** | 0.6350 ± 0.8980 | 2 | 2.2320 ± 3.7375 | 5 | 0.9999 | 4.5 |
| **33** | 0 ± 0 | 0 | 1.2800 ± 2.0295 | 3 | / | / |

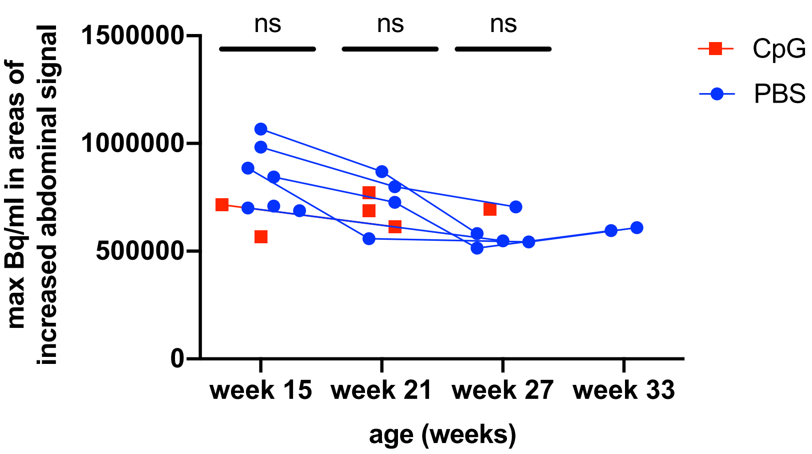

Figure 41a **Maximum glucose metabolism in areas of increased abdominal FDG signal does not differ between PBS-treated and CpG-treated MBC mice.** If areas of increased abdominal FDG signal were detected, maximum becquerel per millilitre (max Bq/ml) measured in these areas did not differ between PBS-treated and CpG-treated MBC mice. Mice in which no increased abdominal FDG signal was detected were excluded. Each dot represents one animal. Statistical analysis was performed using unpaired Mann-Whitney tests, see Table 24. * = p < 0.05, ** = p < 0.01, *** = p < 0.001, **** = p < 0.0001, ns = not significant. P-values refer to the comparison between CpG and PBS treatment groups. Connecting lines identify identical animals measured at different time points.

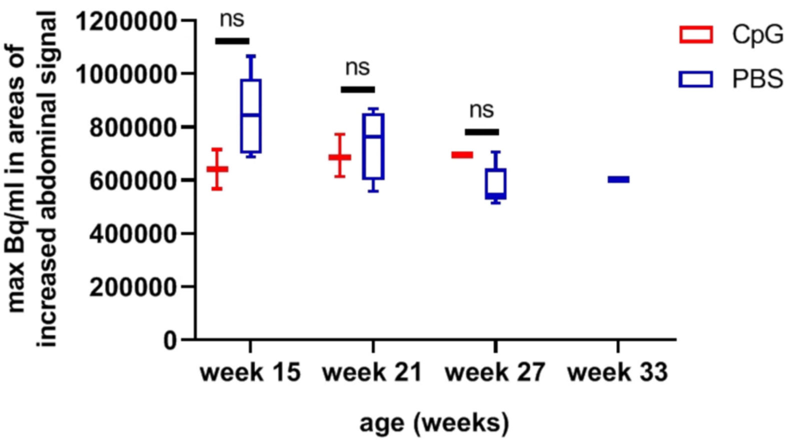

Figure 42b **Maximum glucose metabolism in areas of increased abdominal FDG signal does not differ between PBS-treated and CpG-treated MBC mice, summary data.** If areas of increased abdominal FDG signal were detected, maximum becquerel per millilitre (max Bq/ml) measured in these areas did not differ between PBS-treated and CpG-treated MBC mice. Mice in which no increased abdominal FDG signal was detected were excluded. Statistical analysis was performed using unpaired Mann-

Whitney tests, see Table 24. * = p < 0.05, ** = p < 0.01, *** = p < 0.001, **** = p < 0.0001, ns = not significant. P-values refer to the comparison between CpG and PBS treatment groups. Box plot whiskers indicate minimum and maximum.

Table 24 **Maximum glucose metabolism in areas of increased abdominal FDG signal does not differ between PBS-treated and CpG-treated MBC mice.** Mean and SD values represent the maximum becquerel per millilitre (max Bq/ml) in areas of increased abdominal FDG signal (see text). Mice in which no increased abdominal FDG signal was detected were excluded. Statistical analysis was performed using Mann-Whitney tests, p-value refers to difference between MBC mice with CpG treatment and MBC mice with PBS (control) treatment at the age indicated. SD = standard deviation, N = sample size, U = Mann-Whitney U. WT mice did not show any increased abdominal FDG signal (n(week 15) =1, n(week 21) = 2, n(week 27) = 2, n(week 33) = 1) and are thus not shown in the table.

| | **CpG-treated MBC mice** | | **PBS-treated MBC mice** | | | |
|---|---|---|---|---|---|---|
| Age (weeks) | Max Bq/ml in areas of increased abdominal FDG signal | N | Max Bq/ml in areas of increased abdominal FDG signal | N | P-value | U |
| **15** | 641877 ± 104645 | 2 | 839737 ± 148968 | 7 | 0.3333 | 3 |
| **21** | 690759 ± 79644 | 3 | 738598 ± 133340 | 4 | 0.6286 | 4 |
| **27** | 694359 ± 0 | 1 | 578446 ± 75169 | 5 | / | / |
| **33** | 0 ± 0 | 0 | 602263 ± 9809 | 2 | / | / |

In summary, FDG-PET-MRI data supports that intestinal tumours are present in MBC mice but not in WT mice. PBS-treated mice seem to have a higher volume of increased abdominal FDG signal and a higher percentage of total injected FDG dose taken up by these areas at the age of 15 weeks. With increasing age, volume of and ID taken up by these areas might be increasing in CpG-treated MBC mice but decreasing in PBS-treated MBC mice. However, the technical limitations of intestinal tumour identification in FDG-PET-MRI images mentioned above potentially limit the validity of these results.

### 3.3.10. FDG-PET-MRI measurements suggest liver lymphoma in CpG-treated MBC mice

Besides lymph nodes and the spleen, the liver is another peripheral lymphoid organ where B-cells differentiate and proliferate in germinal centers. In FDG-PET-MRI measurements, two out of 15 MBC mice (eight CpG-treated MBC mice, seven PBS-treated MBC mice) showed increased signal in the liver, suggesting the presence of a liver tumour (Figure 43, Figure 44). Notably both of these mice were from the CpG-treated cohort. Additionally, mouse 110 (Figure 43, see also Figure 22 for image of spleen) had the highest percentage of injected dose in the spleen and died after the first measurement at week 15 (death days before the next measurement at week 21). Mouse 109 (Figure 43) died at week 25 after the second measurement at week 21. WT mice (n = 2) and PBS-treated MBC mice (n = 7) did not show any increased FDG signal in the liver.

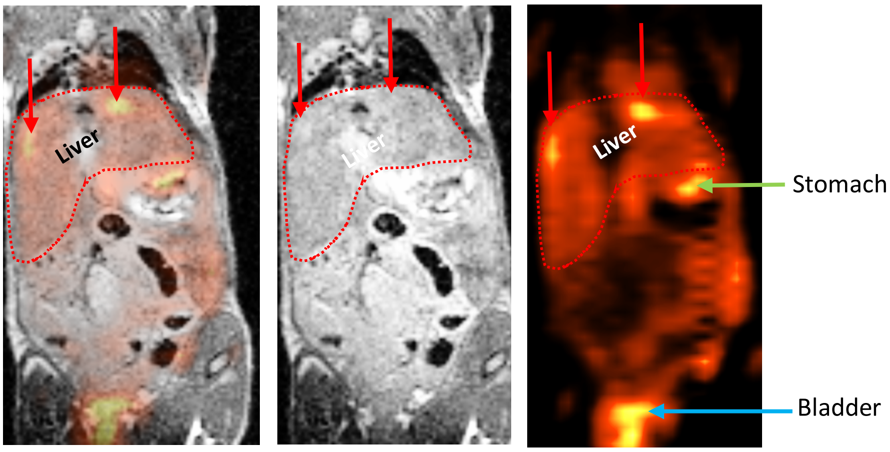

Figure 43 **Example of CpG-treated MBC mouse with potential liver tumour**. FDG-PET-MRI measurements showed increased FDG-PET signal in the liver of the CpG-treated MBC mouse 109 at the age of 15 weeks, suggesting a liver tumour. Red arrows indicate potential tumours in the liver.

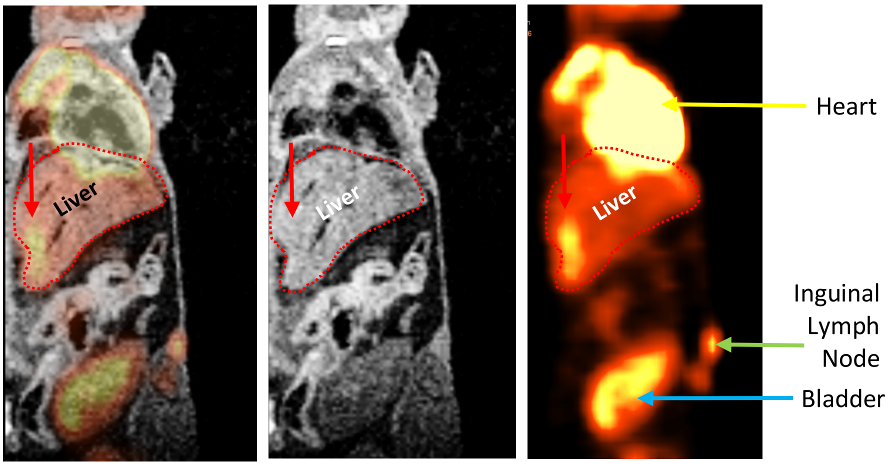

Figure 44 **Example of CpG-treated MBC mouse with potential liver tumour**. FDG-PET-MRI measurements showed increased FDG-PET signal in the liver of the CpG-treated MBC mouse 110 at the age of 15 weeks, suggesting a liver tumour. Red arrows indicate potential tumours in the liver.

### 3.3.11. CpG stimulation does not increase serum IL-6, IL-10 and IgM levels of MBC mice *in vivo*

In section 3.2.2, it was shown that IL-6 levels in the supernatant of murine *Myd88*$^{p.L252P}$-mutated B-cells were increased upon TLR stimulation *in vitro*. Additionally, IgM, representing the B-cell receptor, is frequently overexpressed on and increasingly secreted by DLBCL cells (see section 1.5.2). We were thus interested in whether IL-6, IL-10 and IgM levels would be affected by the *in vivo* TLR stimulation with CpG in our cohort of MBC mice from section 3.3. Therefore, we tested sera at the time of death for IL-6, IL-10 and IgM levels using ELISA. Data from PBS-treated and untreated MBC mice were pooled and are henceforth referred to as non-stimulated MBC mice.

We found that levels of IL-6, IL-10 and IgM in sera of *in vivo* CpG-treated MBC mice did not differ from non-stimulated MBC mice at the time of death (see Figure 45 and Table 25).

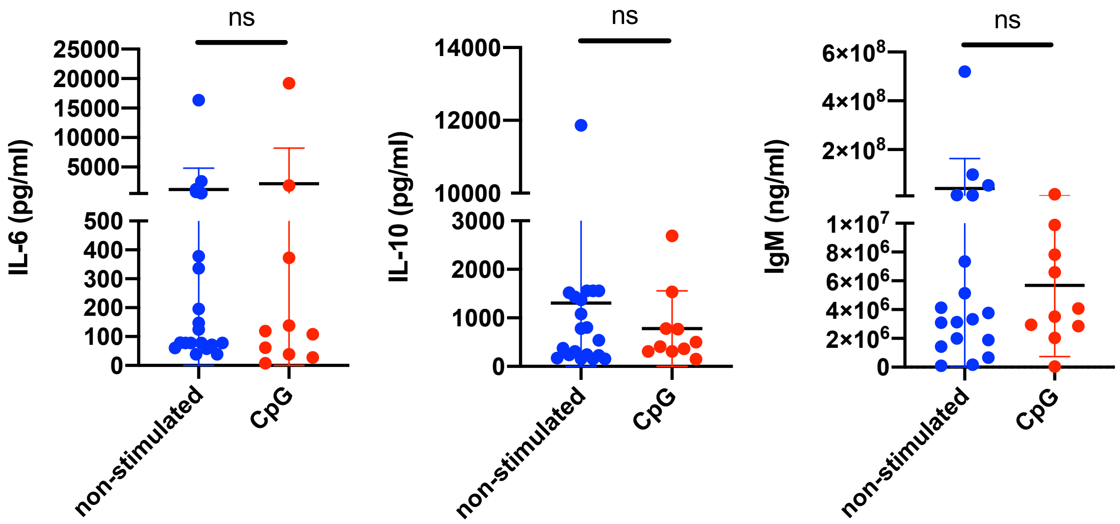

Figure 45 **CpG stimulation does not increase serum IL-6, IL-10 and IgM levels of MBC mice *in vivo***. Serum IL-6, IL-10 and IgM levels in MBC mice at the time of death were not increased upon TLR stimulation with CpG, as measured using ELISA. For statistics see Table 25. Each dot represents one animal. ns = not significant. Bars shown represent mean and SD.

Table 25 **CpG stimulation does not increase serum IL-6, IL-10 and IgM levels of MBC mice *in vivo***. Mean and SD values represent serum IL-6, IL-10 and IgM levels in MBC mice with the treatment indicated at the time of death, as measured using ELISA. Statistical analysis was performed using Mann-Whitney tests, p-value refers to difference between MBC mice with CpG treatment and non-stimulated MBC mice (PBS treatment and no treatment pooled). SD = standard deviation, N = sample size, U = Mann-Whitney U.

| | **MBC genotype – CpG treatment** | | | **MBC genotype – PBS and no treatment pooled** | | | | |
|---|---|---|---|---|---|---|---|---|
| Parameter | Mean | SD | N | Mean | SD | N | P-value | U |
| **IL-6 (pg/ml)** | 2194 | 6001 | 10 | 1171 | 3628 | 20 | 0.6105 | 88 |
| **Il-10 (pg/ml)** | 782 | 778 | 10 | 1305 | 2548 | 20 | 0.8876 | 96.50 |
| **IgM (ng/ml)** | 5.68E+06 | 4.93E+06 | 10 | 4.08E+07 | 1.22E+08 | 18 | 0.9999 | 90 |

When cytokine levels were stratified according to the presence of ascites or intestinal tumours at death as identified via autopsy, no differences were found (see Figure 63, Figure 64, Figure 65, Figure 66, Table 34, Table 35, Table 36 and Table 37 in appendix). In those MBC mice that developed ascites (seven out of 30), cytokine levels were additionally measured in ascitic fluid. Although not statistically significant, compared to serum levels IL-6 levels were higher in ascitic fluid in four out of six mice and IL-10 levels were higher in ascitic fluid in five out of six mice (see Figure 67, Table 38, Table 39 and Table 40 in appendix).

In summary, CpG stimulation *in vivo* does lead to increased serum cytokine levels at death. However, cytokines might be elevated locally at tumour sites such as the intestine or at time points before death. Additionally, half-life and stability of the cytokines measured might not be long enough to be detectable post mortem, as *in vivo* stimulation was only performed weekly in the first five weeks, followed by bi-weekly injections, and serum only collected several hours after death. Finally, bystander release of CpG by APCs (Brahmakshatriya, 2017 #2) and other TLR9-positive cells such as NK-cells might camouflage any differences.

## 3.4. Proof of principle: *in vivo* imaging of MyD88$^{p.L252P}$ -dependent intestinal lymphoma with [$^{64}$Cu]-labelled anti-CD19-antibodies is possible

Since glucose is an omnipresent molecule in mammals, PET-MRI measurements using FDG as a marker can never be fully specific to imaging tumour mass. Other markers, such as FLT to image proliferation or [$^{68}$Ga]-RGD (peptide with Arg-Gly-Asp sequence) to image angiogenesis, also rely on indirect ways of measuring tumour emergence and tumour growth. To improve the specificity of PET imaging, current developments include focussing on surface molecules of tumour cells. In the case of B-cell lymphoma, a CD19-based antibody radiolabelled with [$^{64}$Cu] was developed to image B-cells. Since our mouse model expresses MyD88$^{p.L252P}$ and BCL2 only in cells where the *Cd19* promotor is active, we tested whether imaging of Myd88$^{p.L252P}$-dependent intestinal lymphoma with [$^{64}$Cu]-labelled anti-CD19-antibodies is possible. Autopsy results of MBC mice stratified by age suggested that intestinal tumours were more frequent in MBC mice with higher age (Figure 57 in appendix), thus older MBC mice were chosen for this experiment (aged 56 weeks, 55 weeks, 50 weeks and 35 weeks). Additionally, a higher-resolution MRI was used.

Intestinal tumour mass could be identified in one out of four MBC mice in the MR and verified as being B-cell positive in the PET (see example in Figure 46). No abdominal tumours were found in BC mice (n = 2) or CD19-deficient mice used as a negative control for the imaging (n = 1).

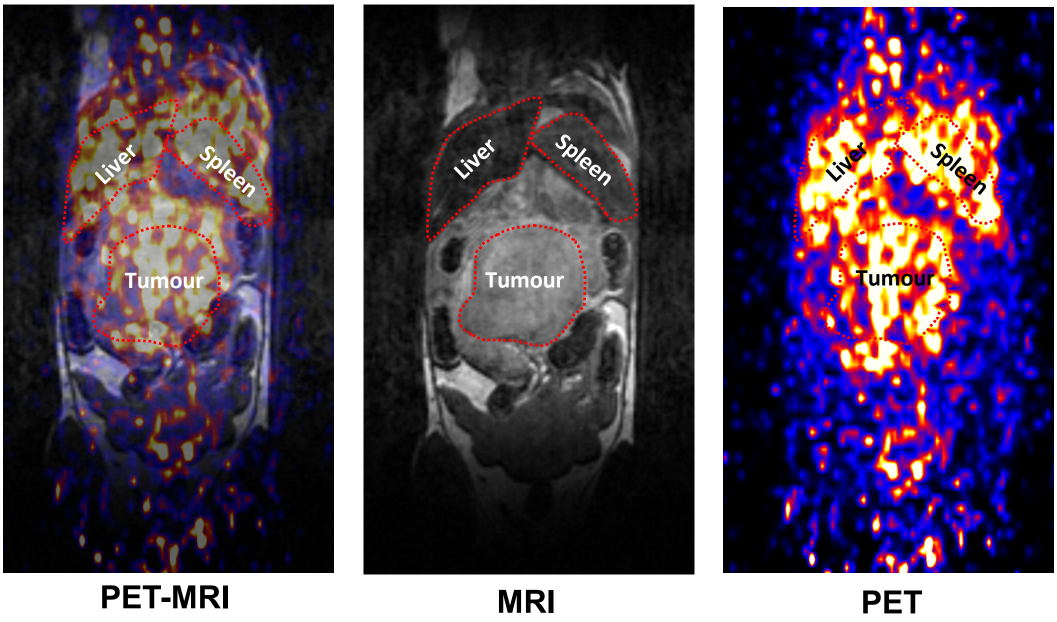

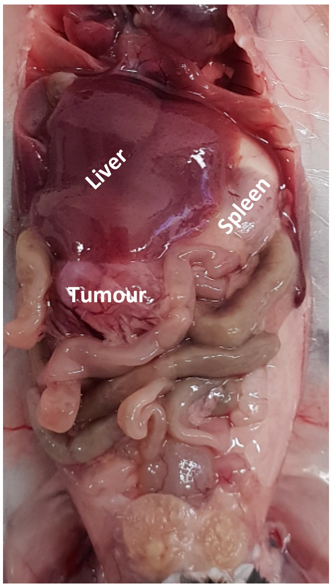

Figure 46 **[$^{64}$Cu]-labelled anti-CD19-antibody-based PET-MRI can detect MyD88$^{p.L252P}$-dependent intestinal tumours in MBC mice *in vivo*, example**. PET-MRI with [$^{64}$Cu]-labelled anti-CD19-antibodies detects B-cells in the liver, the spleen and a large intestinal tumour in this MBC mouse aged 56 weeks. The tumour finding was confirmed by autopsy following the PET-MRI imaging (see photograph on the left).

Following the PET-MRI, mice were euthanised and an autopsy was performed to isolate individual organs and potential tumours. Uptake of [$^{64}$Cu]-labelled anti-CD19-antibodies to individual organs and potential tumours was then measured using a γ-counter. Intestinal tumour mass could be identified in three out of four MBC mice in the autopsy and verified as being B-cell positive in the γ-counter (Figure 47). Uptake of [$^{64}$Cu]-labelled anti-CD19-antibodies to total lymphoid tissue was higher in all MBC mice compared to BC mice, whereby total lymphoid tissue was defined as potential intestinal tumours plus cervical and inguinal lymph nodes if identifiable.

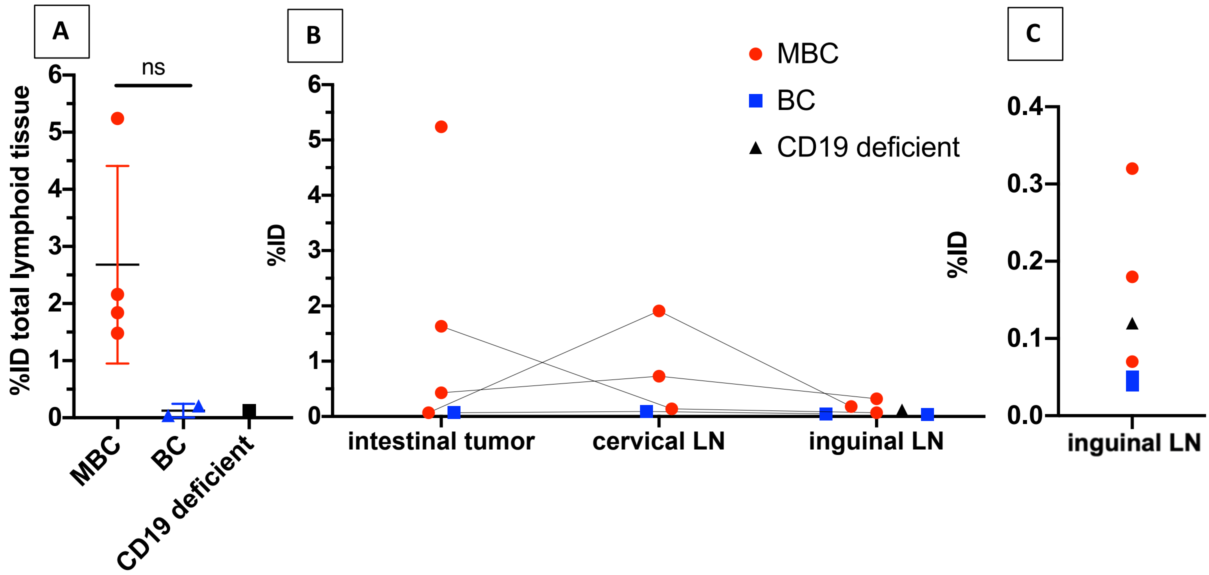

Figure 47 **Uptake of CD19-antibodies into total lymphoid tissue was higher in MBC mice than in BC mice**. A: Uptake of [$^{64}$Cu]-labelled anti-CD19-antibodies (as determined via γ-counter) into total lymphoid tissue, defined as potential intestinal tumours plus cervical and inguinal lymph nodes if identifiable. The percentage of injected dose (% ID) taken up into total lymphoid tissue was higher in all MBC mice compared to BC mice, although not statistically significant (p = 0.1333, U = 0, MBC: n = 4, mean = 2.680, SD = 1.729, BC: n = 2, mean = 0.1250, SD = 0.1202, CD19-deficient: n = 1, mean = 0.1200, SD = 0). B: Percentage of injected dose (% ID) taken up by individual organs. The mouse with highest % ID in abdominal tumour mass did not show any identifiable lymph nodes. LN = lymph nodes. Each dot represents one animal. ns = not significant. Bars shown represent mean and SD. Connecting lines identify identical animals measured at different time points. C: For inguinal lymph nodes, a graph with a smaller scale was added to better illustrate the inter-individual differences.

## 3.5. Case study: B-cells of intestinal tumour in MBC mouse show increased IgM expression

Having shown that MBC mice develop intestinal tumours (see section 3.3.8 and 3.3.9) and knowing that IgM is frequently overexpressed on DLBCL cells (see section 1.5.2), we were interested in whether intestinal tumours would also show increased IgM expression. IgM serves as the B-cell receptor and increased expression would allow more B-cell receptor stimulation and thus more downstream pro-survival signals in these B-cells.

In a case study of one MBC mouse with an intestinal tumour, we found that IgM expression (as determined via the MFI (mean fluorescence intensity) of IgM) was indeed increased on the B-cells of its intestinal tumour compared to its spleen (Figure 36, Figure 37). Additionally, its cervical lymph nodes were enlarged and also had a higher MFI of IgM than its spleen. The MFI of IgM in its spleen was lower than the MFI of IgM in the spleen of a control BC mouse.

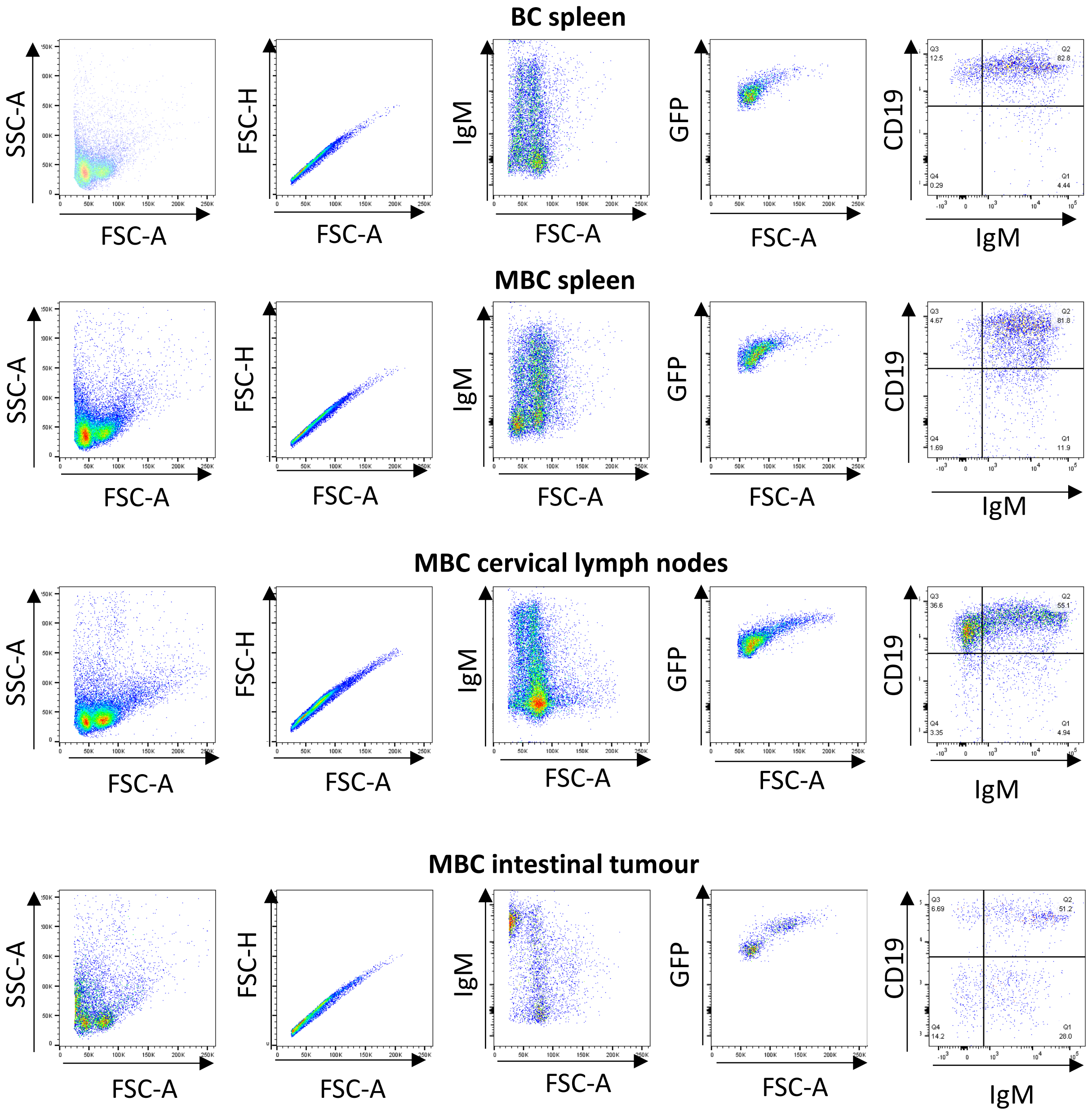

Figure 48 **Gating strategy to evaluate IgM expression of B-cells in different tissues of BC and MBC mice.** All biological replicates are shown (BC: n = 1, MBC: n = 1). The third column shows all IgM positive cells, the fifth column only GFP-positive cells. GFP-positive cells represent B-cells since BC and MBC mice were genetically modified to express GFP exclusively in B-cells using the CD19 promotor (see section 2.1).

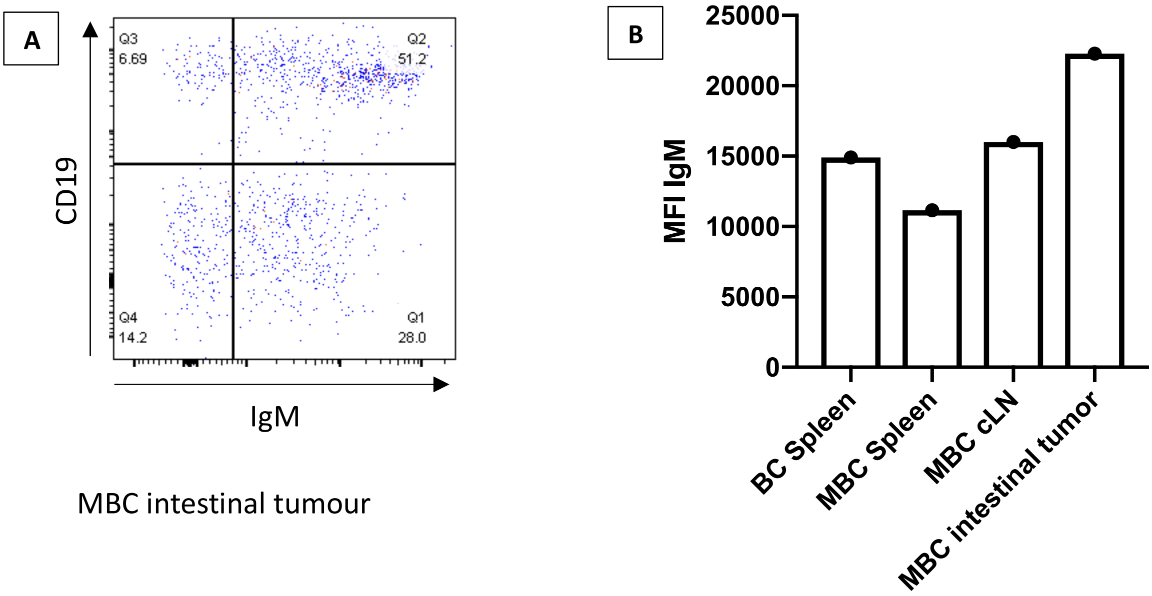

MBC intestinal tumour

Figure 49 **B-cells from an intestinal tumour of a MBC mouse show increased IgM expression.** Left: Gating result from Figure 48 for the intestinal tumour of the MBC mouse. Right: B-cells from the intestinal tumour of the MBC mouse show increased IgM expression compared to its spleen, its cervical lymph nodes (cLN) and the spleen of the BC mouse. All biological replicates are shown (BC: n = 1, MBC: n = 1). MFI IgM values represent means fluorescence intensity of IgM as determined via FACS.

Overall, this case study suggests that *Myd88*$^{p.L252P}$-mutated B-cells of intestinal tumours have a higher IgM expression than those of other locations, which might point towards a higher malignancy of the former.

# 4. Discussion

This study sought to better characterise the novel DLBCL mouse model (MBC mice) generated by Knittel et al. and assess if B-cells with the *MYD88*$^{L265P}$ mutation still depend on upstream TLR signals, which would make TLR inhibitors an attractive target for lymphoma therapies. For this purpose, the distribution of B-cells within MBC mice was assessed using *in vivo* GFP scans and metabolism and proliferation in MBC mice upon TLR stimulation was assessed using PET-MR imaging. IgM expression as well as IL-6 and IL-10 production of B-cells upon TLR stimulation was analysed *in vitro* and *in vivo* using ELISA. Additionally, an evaluation of CD19-antibody-based PET-MR imaging in these mice was performed in a proof-of-concept approach. In the following section, implications and limitations of the data collected shall be addressed.

## 4.1. MBC mice show B-cell accumulation in secondary lymphoid organs and the abdomen

### 4.1.1. Implications of data and future experimental approaches

As shown in section 3.1, compared to BC mice MBC mice showed a higher GFP signal, representative of B-cell counts, in the abdomen and in lymphoid organs at death. This supports the conclusion that *Myd88*$^{p.L252P}$ promotes abdominal tumours in mesenterial lymph nodes as well as massive B-cell infiltration in peripheral lymphoid organs.

The finding of increased abdominal B-cell accumulation in MBC mice compared to BC mice is interesting, as the abdomen is commonly not seen as one of the main lymphoid organs. However, the intestinal tract is in fact the largest single immunologic organ of the body, containing over 40% of all lymphocytes (Shea-Donohue, 2018) and gut-associated lymphoid tissues like Peyer's patches, which harbor T- and B-lymphocytes as well as dendritic cells and innate lymphocytes (Diehl et al., 2013). My findings suggest that *Myd88*$^{p.L252P}$ is involved in a pathway for B-cell proliferation exclusive to or especially prominent in the abdomen. One such mechanism could be the stimulation of MyD88-dependent receptors by components of the microbiota, such as bacterial or viral DNA, flagellin or LPS. A dependency of tumour growth on MyD88 was already shown in colorectal cancer (Koliaraki et al., 2019, Holtorf et al., 2018, Zhu et al., 2020), a tumour highly exposed to microbial components. The development of spontaneous colitis, an autoimmune disease of the gut, was shown to depend on microbiota-derived signals and MyD88-dependent pathways in intestinal epithelial cells (El Abbas et al., 2020). Additionally, commensal bacteria transmit signals via MyD88 to regulate gene expression of a variety of genes encoding for antimicrobial peptides, cytokines and chemokines in intestinal epithelial cells (Takahashi et al., 2020). A study of gnotobiotic piglets showed that infection of the gut with *S. typhimurium* lead to increased transcription of MyD88 in the piglets' intestines and colonisation with *E. coli* Nissle 1917 lead to increased transcription of TLR9 in the piglet's intestines (Splichal et al., 2019). This suggests that the microbial landscape is tightly connected to MyD88-related and TLR9-related activity in the gut. Concerning systemic effects of the microbiome on the immune system, it is known that peptidoglycans from intestinal microbiota even enter the blood stream and increase the basal activation of neutrophils (Janeway et al., 2017). This suggests that microbiota-derived TLR ligands could potentially also enter the bloodstream and then stimulate *Myd88*$^{p.L252P}$-dependent tumour cells elsewhere. Besides ligands provided by microbiota, other ligands could also increase MyD88 activation in the gut. For example, intestinal epithelial cells can produce BAFF and APRIl, both ligands of the MyD88-dependent receptor TACI (He et al., 2010). Interestingly, the gastrointestinal tract is reported to be the most common site of primary disease in DLBCL patients (Li et al., 2018b). Together, these data suggest that the gut, potentially the microbiota, could play a role in *Myd88*$^{p.L252P}$-dependent lymphomagenesis. This role is currently evaluated in a follow-up study using gnotobiotic MBC mice, in which colonisation of the gut with microbiota is absent. These gnotobiotic MBC mice were transplanted with different microbiota and subsequent tumour growth was assessed.

The higher variance of GFP signal found in lymph nodes, the spleen and the liver of MBC mice (see section 3.1) might be due to technical issues such as autofluorescence but could also point towards stronger interindividual differences in MBC mice. Potentially the latter indicates a higher variance of MBC mice in B-cell density in potential homing or proliferation clusters compared to BC mice. In that way it would be similar to the higher variance in IL-6 and IL-10 levels observed in B-cell supernatant of MBC mice compared to BC mice following treatment with TLR agonists and antagonists *in vitro* (see section 3.2.2). Both IL-6 and IL-10 levels are increased in human *MYD88*$^{L265P}$-mutated DLBCL *in vitro* (Ngo et al., 2011). Interestingly, the increased variance of GFP signal was not found in the abdomen although tumours were exclusively found in MBC mice. One could speculate that BC represents a healthier status with less variance in location of B-cell infiltration. In contrast, MBC could lead to higher B-cell infiltration but to different secondary lymphoid organs in different MBC mice. This could explain a higher variance of GFP signal in specified organs among MBC mice.

To evaluate this explanation, it would be necessary to identify potential factors leading to one or the other organ preference for B-cell infiltration or proliferation. One such factor could be age at the time of death, as the location of B-cell infiltration might vary dynamically depending on age or the stage of disease. This is supported by the apparent peak at the age of 21 weeks observed in the percentage of injected FLT dose in the spleen, spleen volume and maximum Bq/ml FLT in the spleen (see section 3.3.6). On the other hand, tumours in elder mice might simply be larger due to the tumour having had more time to grow. To evaluate if the primary location of B-cell infiltration depends on age, it would be necessary to scan for B-cells *in vivo* by for example using B-cell specific antibody-based imaging at several time points over the lifespan of MBC mice. Another possibility would be to euthanise a cohort of MBC mice for each time point and then evaluate B-cell distribution cross-sectionally by using FACS analysis or microscopic analysis of organs. However, in this approach individual mice cannot be evaluated over time. Finally, another factor leading to increased variation in B-cell distribution of MBC mice could be the presence of autoreactive BCRs on the cell surface of MBC B-cells: In this case, the amount of antigen that stimulates these autoreactive BCRs could vary in different organs. In summary, factors influencing the location of B-cell infiltration in MBC mice should be reviewed.

### 4.1.2. Limitations of data and improvement strategies

Optical imaging is based on the detection of weak light by a highly sensitive high-resolution CCD camera. The advantages of optical imaging in research include its high sensitivity and that it is easy to handle, established and cheap. Additionally, it allows for the study of protein-protein interactions, does not use ionizing radiation and can be used *in vivo* and *ex vivo*. However, optical imaging is limited by its low penetration depth and its restricted quantification possibilities (signal is quantified per area unit and not per volume unit). Moreover, nude mice should be used to reduce autofluorescent signals caused by skin pigmentation. Finally, the generation of transgenic mouse models expressing fluorescent proteins is costly and takes time (Hoffman and Yang, 2006).

In our setting, data could only be collected post-mortem after removing skin and fat covering the organs due to the low tissue penetrance of GFP signal and the high autofluorescence of materials such as skin, fur or tape during GFP imaging. One way to overcome this problem could be the use of NIRF (near-infrared fluorescence) optical imaging, which has a penetration depth of up to several centimetres and a higher sensitivity than regular fluorescence (Lowik et al., 2009). The NIRF protein iRFP is a near-infrared fluorescent protein with an excitation wavelength of 690 nm and an emission wavelength of 713 nm (Tran et al., 2014). Hence, iRFP emission is of higher wavelength and lower energy than GFP emission. iRFP emission is thus less likely to be absorbed by the surrounding tissue and therefore has a higher tissue penetrance. This would allow fluorescence scans over the lifespan of mice and additionally decrease the autofluorescent signal (Hock et al., 2017). To evaluate B-cell distribution during the lifespan of each MBC mouse individually, a potential strategy could thus be to develop an MBC mouse model with B-cell specific expression of near-infrared fluorescent proteins like iRFP.

Another possibility to reduce autofluorescence is optical imaging with bioluminescent proteins instead of fluorescent proteins, as bioluminescence does not occur in normal cells (Mezzanotte et al., 2017). For example, in our setting mice that express B-cell specific luciferase instead of GFP could be used to image B-cells. However, for bioluminescent imaging it is necessary to inject the luciferase’s substrate intravenously prior to imaging, thus requiring animals that are alive and under anaesthesia.

Concerning variation among MBC mice, another factor leading to increased variation of B-cell infiltration in MBC mice could be genetic variation among individual MBC mice due to genetic instability and chance. In the future, it should thus be investigated if any accumulation of further mutations known from human DLBCL occurred in MBC mice such as mutations in *CD79* or *BCL6*. However, as both M, B and C alleles were originally generated on a *C57BL/6N* background, this explanation for interindividual variation is not fully satisfying.

## 4.2. *In vitro* and *in vivo* work support TLR ligand dependency of MyD88$^{p.L252P}$

### 4.2.1. Implications of data and future experimental approaches

As shown in section 3.2 and 3.3, TLR stimulation of cells or mice with the *Myd88*$^{p.L252P}$ mutation lead to increased survival and proliferation *in vitro* as well as lymphomagenesis and abdominal tumours *in vivo*. This suggests that malignant B-cell proliferation and thus disease progression due to MyD88$^{p.L252P}$ is indeed triggered by upstream signals. Additionally, we found that *in vivo* serum IL-6, IL-10 and IgM levels were not increased at death, potentially pointing towards a tumour microenvironment that is not accessible for evaluation via the blood stream. If such a tumour microenvironment with elevated cytokines exists could be evaluated in future experiments by comparing blood stream cytokine levels to cytokine levels in tumours.

These findings are in line with the proposed pathophysiology of MyD88$^{L265P}$-dependent lymphoma (Phelan et al., 2018, Ngo et al., 2011) and the TLR ligand dependency found in other B-cell lymphomas such as chronic lymphatic leukaemia (CLL) (Ghamlouch et al., 2014, Jahrsdorfer et al., 2005). One report found the opposite, arguing that the inhibition of TLR9 and other UNC93B1-dependent TLRs paradoxically increase the accumulation of MyD88$^{L265P}$ in B-cells (Wang et al., 2016). This controversy remains yet to be resolved. However, the study used a *Rag1*$^{-}$/$^{-}$ mouse model that lacks both B- and T-cells is thus potentially inferior to the MBC mouse model in which MyD88$^{L265P}$ is expressed endogenously in B-cells and T-cells are present. A recent study using NOD/SCID/IL-2RγKO (NSG) immunodeficient mice found that linking CpG to an inhibitor of STAT3, a transcription factor that binds to the *Myd88* promotor, led to inhibition of genes downstream of MyD88 but induction of genes critical for antigen-processing and -presentation as well as Th1 cell activation (Zhao et al., 2018). This gene signature led to the development of CD8 and CD4 T-cells specific to lymphoma cells that protected mice from a tumour re-challenge. Again, the use of immunodeficient mice might limit the transferability of the data. However, this finding suggests that although CpG stimulation likely promotes proliferation of *MYD88*$^{L265P}$-mutated B-cells, CpG might also stimulate macrophages and antigen-presenting cells that then promote an anti-tumour T-cell response. Indeed, a recent study found that TLR9 stimulation reduced brain metastasis in several tumour mouse models by activating the microglia, which are resident macrophages in the brain (Benbenishty et al., 2019). Differences between B-cell lymphomas in responsiveness to CpG might be a result of varying tumour microenvironments between different B-cell lymphoma (Ben Abdelwahed et al., 2013).

#### 4.2.1.1. Possible explanation for pathogenesis of MyD88-mediated lymphomagenesis

One implication of TLR ligand dependency of B-cell lymphomas is that there might be naturally present TLR ligands within the organism that lead to TLR stimulation, thus promoting lymphomagenesis. Potential TLR ligands could be derived from nucleic acids from apoptotic cells, neutrophil extracellular traps or the intestinal microbiota. Additionally, TLR ligands could be derived from specific infections, such as Helicobacter pylori infection that is associated with MALT (mucosa-associated lymphoid tissue) lymphoma and Hepatitis C infection that is associated with SMZL (splenic marginal zone lymphoma), both lymphomas that show *MYD88* mutations (Young et al., 2019). Other potential endogenous TLR ligands could be microRNAs derived from small extracellular vesicles (exosomes): For plasmacytoid dendritic cell (pDC) activation in SLE patients, it was shown that these exosome-derived microRNAs increased INFα secretion of pDCs via TLR7 (Salvi et al., 2018). Besides RNA, mitochondrial DNA might also serve as a TLR9 stimulant, as was shown in one study on macrophages (Zhang et al., 2014). However, for mitochondrial DNA to be found in the endosome, normally cellular damage or apoptosis must have occurred previously.

Future experiments should address these TLR ligands for their potential to modulate B-cell lymphomas, as in many cases it cannot be distinguished whether any stimulatory effects are due to the specific TLR ligands or due to general inflammation. This might shed light on novel preventive countermeasures against B-cell lymphoma, such as microbiota screening and subsequent modulation as well as screening for and subsequent modulation of specific TLR ligands.

#### 4.2.1.2. TLR ligand dependency links B-cell lymphoma to autoimmune diseases

In the light of different naturally present TLR ligands, it is interesting that many autoimmune diseases apparently also rely on TLR ligands for B-cell proliferation. TLR-MyD88 signalling has been shown to play a role in a variety of autoimmune diseases, including SLE, Sjögren's Syndrome and multiple sclerosis (Zheng et al., 2019, Young et al., 2019, Kiripolsky et al., 2019).

SLE is a disease in which endogenous TLR ligands like the TLR7 ligand Sm/ribonucleoprotein (Sm/RNP) potentiate the disease progression. Autoreactive BCRs in SLE patients bind to Sm/RNP, leading to B-cell activation and subsequent antibody formation against Sm/RNP, which is crucial for the development of SLE (Akatsu et al., 2016). When these autoantibodies against Sm/RNP are complexed with their RNA-containing ligand Sm/RNP, they can be endocytosed via Fc-receptors and subsequently complex with endosomal RNA-sensing TLRs (Akatsu et al., 2016). In this way, autoantibodies against Sm/RNP could introduce large amounts of RNA that in turn again stimulate RNA-sensing TLRs like TLR7. A similar pathway of autoantibody-mediated TLR stimulation that then furthers the development of MyD88-TLR-BCR complexes described by Phelan et al. (2018) could be imagined for B-cell lymphoma. DLBCL is indeed associated with increased levels of antinuclear antibodies, another autoreactive antibody (Lang et al., 2018). Interestingly, SLE is also associated with an increased risk of developing haematological malignancies like DLBCL (Dias and Isenberg, 2011), again pointing towards parallels in the pathogenesis of SLE and lymphomas. Besides dysregulated stimulation, another pathophysiological pathway could be dysregulated inhibition. For SLE, the inhibitory co-receptor CD72 on B-cells recognises Sm/RNP and inhibits the B-cell response to Sm/RNP (Akatsu et al., 2016). It thereby prevents B-cell activation by Sm/RNP and successive antibody formation against Sm/RNP. Again, a similar dysregulated inhibition could be imagined for B-cell lymphoma.

It is known that TLR stimulation of anergic B-cells inclines them towards forming germinal centers (Young et al., 2019). Yet in SLE TLR9 responses of B-cells are impaired and disease is worsened by B-cell specific TLR9 knockouts (Dieudonne et al., 2019, Tilstra et al., 2020). This suggests that the quality and quantity of TLR signalling might determine whether B-cell proliferative processes are heading towards autoimmunity or malignancy. Interestingly, B-cells from SLE patients show upregulated levels of TLR9 expression (Mortezagholi et al., 2016), suggesting some form of counter regulation of SLE B-cells against its impaired TLR9 responses. In inflammatory bowel disease, another autoimmune disease, TLR9 on B-cells is also upregulated and correlates with disease severity (Berkowitz et al., 2013). For DLBCL, increased NF-κB activation due to MyD88$^{L265P}$ might help overcome the anergic status of B-cells with self-reactive BCRs, which might then lead to the inhibition of apoptosis during normal B-cell development.

Similar to the suppression of MyD88$^{L265P}$-driven lymphoma upon IRAK4 inhibition (Kelly et al., 2015), IRAK4 deficiency attenuates the disease phenotype in SLE (Murphy et al., 2017), suggesting a potential turning point between autoimmunity and malignancy in proliferative B-cells occurs upstream of IRAK signalling. In other autoimmune diseases such as cryoglobulinemia vasculitis, TLR9 stimulation of B-cells led to upregulation of co-cultured type 1 effector T-cells and downregulation of regulatory T-cells *in vitro* (Comarmond et al., 2019), suggesting a complex interplay with other immune cells might be at work following TLR9 stimulation of B-cells.

In summary, while BCR signal dependency is well established in both B-cell lymphoma and autoimmune diseases (Young et al., 2019), evidence points towards TLR signalling as being an additional, potentially distinguishing, factor in their pathogenesis. Forthcoming studies should address to what extent TLR signalling leads to differing effects on B-cells in models prone to B-cell lymphoma such as the MBC mice used in this study compared to models prone to autoimmune diseases such as SLE models.

#### 4.2.1.3. Possible treatment via inhibitors

Since ligand dependency of DLBCL disease progression implies aggravation by stimulants and alleviation by inhibitors, inhibitors of the MyD88-associated pathway are a promising therapeutic target. An example of such a small molecule inhibitor is ibrutinib, a BTK inhibitor. BTK is part of the BCR pathway but was also found to be a downstream target of MyD88$^{L265P}$ (Yang et al., 2013). BTK inhibition has revolutionised lymphoma therapy in recent years and has also led to novel insights into the role of MyD88 in lymphoma: Ibrutinib-sensitive lymphoma form a MyD88-TLR9-BCR multiprotein supercomplex, which co-localises with mTOR (mammalian target of rapamycin) to endolysosomes. This then leads to increased NF-κB and mTOR signalling (Phelan et al., 2018). Following the large success of the BTK inhibitor ibrutinib, second-generation drugs are already under development. Acalabrutinib for example was developed to reduce side effects of ibrutinib such as bleeding (Owen et al., 2020, Series et al., 2019). Ibrutinib might even improve autoimmune disease outcome: BTK for example interacts with NLRP3, a Nod-like receptor involved in inflammasome hyperactivation of patients with the autoinflammatory Muckle-Wells syndrome (Liu et al., 2017). In one study of three patients with Waldenström macroglobulinemia and anti-MAG neuropathy, a rare autoimmune variant of peripheral neuropathy, ibrutinib led to subjective and objective clinical improvements (Castellani et al., 2020).

Another attractive target for inhibitors are IRAKs, kinases downstream of MyD88 (see section 1.5.4). IRAK inhibitors were found to be protective against NEC (necrotizing enterocolitis) in a NEC rat model (Hou et al., 2018) and are also investigated for their use in rheumatoid arthritis (Wiese et al., 2020). Therapeutic responses in a melanoma mouse model (Srivastava et al., 2012) and breast cancer cell lines (Rahemi et al., 2019) were augmented when co-administered with IRAK-1,-4 inhibitors. Interestingly, IRAK inhibitors might even have as far-reaching effects as counteracting resistance of tumours to radiotherapy (Liu et al., 2019) and alleviating autoimmune diseases like SLE (Murphy et al., 2017). However, development of IRAK inhibitors for clinical use proves to be difficult and is mostly still in pre-clinical stages (Chen et al., 2020, Scarneo et al., 2020). For DLBCL, the MBC mouse model used in this study might thus provide a much needed platform for preclinical testing of IRAK inhibitors in the treatment of DLBCL and should therefore be performed in the future.

Finally, another potential inhibitory approach would be the use of iODNs (inhibitory oligodeoxynucleotides), which are TLR7/9 receptor antagonists (Lenert et al., 2003, Avalos and Ploegh, 2011). However, manufacturing of an efficient iODN proves to be difficult and is still in preclinical assessment (Rommler et al., 2015, An et al., 2020).

On a side note, hydroxychloroquine has recently been shown to act on B-cells via TLR9 inhibition (Torigoe et al., 2018). Hydroxychloroquine is a long-standing drug used to treat autoimmune diseases, prevent malaria (Ben-Zvi et al., 2012) and lately also COVID-19 (Agrawal et al., 2020). However, it might not be applicable for general lymphoma therapy due to its many side effects, including loss of vision (Yusuf et al., 2017).

In summary, several approaches to TLR9 inhibition therapy for lymphomas and other diseases currently exist. Our finding of TLR dependency of MyD88$^{p.L252P}$ supports that these should be followed up on and might also, if not especially, be a well-suited therapy for MyD88$^{L265P}$-dependent B-cell lymphoma. However, as mentioned in section 4.2.1, TLR inhibition could also be harmful (Wang et al., 2016) and TLR9 stimulation beneficial if effects downstream of

MyD88 are blocked (Zhao et al., 2018). Any clinical trials therefore require to be performed with extra caution.

### 4.2.2. Limitations of data and improvement strategies

#### 4.2.2.1. Differences in survival led to unequal cohort sizes over time

On a general note, one limitation of the data is that due to the differences in survival it was not possible to always compare equal numbers of animals between the CpG-treated MBC mice and the PBS-treated MBC mice. In future experiments, this could be alleviated by including earlier measurement time points before the age of 15 weeks, at which a higher number of both cohorts is still alive.

#### 4.2.2.2. Additional control groups could help differentiate MyD88$^{p.L252P}$-mediated effects from general immunostimulatory effects of CpG

It is well known that CpG acts as a general immune stimulant on many different kinds of cells (Ben Abdelwahed et al., 2013, Campbell, 2017). CpG might thus have *in vivo* effects in MBC mice that are not dependent on MyD88$^{p.L252P}$, which on its own could for example already account for the lower survival and age at death observed in CpG-treated MBC mice compared to PBS-treated MBC mice. On the other hand, immunostimulatory effects of CpG could also be protective against lymphoma progression (Wang et al., 2016, Zhao et al., 2018) or lead to upregulation of therapeutic targets on B-cells such as CD20 (Mankai et al., 2009). Possibly this explains the lower percentages of number of mice with increased abdominal signal in the CpG-treated MBC cohort (section 3.3.9), as CpG-treated MBC mice might benefit from the general immunostimulatory properties of CpG before even developing abdominal tumours. This is especially true since CpG injections were administered interperitoneally and could thus have acted as a local immune stimulant.

It is therefore of interest to perform experiments comparing lymphomagenesis in CpG-treated MBC mice with lymphomagenesis in CpG-treated BC mice. This would allow for assessing the effect of MyD88$^{p.L252P}$ in a controlled TLR9-stimulated setting. Additionally, the difference in lymphomagenesis between CpG-treated MBC mice and PBS-treated MBC mice should be compared to the difference in lymphomagenesis between CpG-treated BC mice and PBS-treated BC mice. Such an elaborate experimental series may take time and funds to realize but may help to quantify more specifically how much the MyD88$^{p.L252P}$ alone potentiates the effect of TLR9 stimulation on lymphomagenesis independent of general immunostimulatory effects of CpG.

In summary, two additional control groups should be added in future experimental settings: CpG-treated BC mice and PBS-treated BC mice. On a side note, numbers of mice per group might need to increase if smaller effect sizes are to be expected.

#### 4.2.2.3. Additional groups could help differentiate CpG-mediated effects from TLR9-mediated effects

It is known that MyD88$^{L265P}$ lowers the threshold of TLR9 *in vitro* by formation of the Myddosome (Avbelj et al., 2014). A lowering of the threshold of TLR9 means that the affinity and the avidity of TLR9 and therefore the necessary amount of TLR9 ligand to evoke a downstream signal is lower. However, controlled evaluation of a threshold *in vivo* proves to be difficult as many endogenous ligands of TLR9 potentially exist in the organism (see section 4.2.1.1). Thus stimulation of TLR9 with CpG only provides an additional ligand. To answer the question of whether the threshold of TLR9 in MyD88$^{L265P}$-mutated B-cells is lowered *in vivo*, a potential experimental approach would be to compare lymphomagenesis in MBC mice to lymphomagenesis in MBC mice with a B-cell specific TLR9 knockout, in which all ligand-induced effects would thus be eliminated. Additionally, it would be valuable to also compare these groups to MBC mice with B-cell specific TLR7 or TLR8 knockouts, as these TLRs are also located within the endosome. A combined knockout could also be achieved by generating MBC mice with an Unc93b3d knockout, as Unc93b3d is a chaperone protein necessary for the formation of endosomal TLRs.

Another limitation of CpG stimulation instead of TLR9 knockouts is that the Myddosome includes the cytoplasmic domains of TLR9, which on its own could already be enough to promote lymphomagenesis independent of ligands binding to TLR9. To evaluate this question, it would be of interest to compare lymphomagenesis in MBC mice in which as many endogenous TLR9 ligands as possible are eliminated to lymphomagenesis in MBC mice with a TLR9 knockout. One possibility to eliminate as many endogenous TLR9 ligands as possible would be the use of gnotobiotic MBC mice. However, the use of gnotobiotic mice would still not eliminate TLR9 ligands stemming for example from necrotic or apoptotic cells. Another option is to treat these MBC mice with TLR9 inhibitors, yet as explained in section 4.2.1.3, this might lead to other off-target effects that cannot be controlled for. A third, very neat possibility would be to generate an MBC mouse model in which the ligand-binding domain of TLR9 is dysfunctional. However, generation of such a mouse model is costly and takes time. In summary, evaluation of this question *in vivo* remains problematic.

#### 4.2.2.4. Validity of PET-MRI measurements

##### 4.2.2.4.1. Limitations of FDG-PET measurements

FDG is a well-established tracer in the clinics and part of several cancer screening and follow-up programs (Kandathil et al., 2018, Gandy et al., 2019, Groheux et al., 2013). Although successfully used for evaluation of gastrointestinal cancer in humans (Kitajima et al., 2017), the PET resolution of one to two millimetres remains a limiting factor when evaluating abdominal tumours in mice.

Additionally, specificity of FDG to assess tumour mass is limited. As mentioned in section 3.3.9, the gastrointestinal tract is an active site of glucose metabolism and thus FDG uptake. The urinary tract - including the kidneys, the ureter and the bladder - shows high FDG signal due to its elimination function. Moreover, the adrenal glands, the heart, the liver and the spleen all take up glucose and therefore FDG. Finally, inflammation at any location could lead to increased glucose uptake. All these factors complicate distinction of tumour mass from unspecific FDG uptake. Consequently, interpretation requires caution and calls for consecutive imaging of the same animals as this facilitates the identification of tumours due to the de novo appearance of FDG positive signals.

The problem of non-specificity could potentially also be addressed by labelling glucose with another isotope like [$^{124}$I], a radiotracer that has a longer half-life. This would allow for prolonged incubation time and thereby more time for non-specifically bound tracer to be eliminated (Thunemann et al., 2017). For comparison: The half-life of [$^{124}$I] is 4.2 days (Cascini et al., 2014) and that of [$^{64}$Cu] is 12.7 hours (Anderson and Ferdani, 2009), while the half-life of [$^{18}$F] is 109.8 minutes (Cascini et al., 2014).

In summary, resolution of FDG-PET images and specificity of FDG to tumour mass limit data use and validity in preclinical settings. Future developments for preclinical imaging in mice should focus on improving resolution and developing tracers that bind to tumour cell attributes more specifically.

#### 4.2.2.4.2. Limitations of FLT-PET measurements

FLT is a promising alternative tracer to FDG for gastrointestinal cancer, as thymidine has less non-specific targets to bind to (Nakajo et al., 2017). However, FLT uptake is generally lower compared to FDG uptake (Nakajo et al., 2017), an observation that is consistent with the uptake we observed in our experiments. Possibly uptake could be improved in our setting by shortening the incubation time of FLT, as plenty of tracer was detected within the urinary tract, suggesting most of the tracer had already been excreted at the time of PET imaging. This might also explain why detection of abdominal tumours in FLT-PET measurements was not possible in our experimental setting.

#### 4.2.2.4.3. Limitations of MRI measurements

MR imaging greatly improves the value of PET imaging as it enables an anatomical mapping of the PET signal. However, optimum resolution in the MRI is key to obtaining valuable data since structures are difficult to distinguish in the PET. Due to efficiency reasons, we used TSE imaging to allow for faster image collection and a coil developed for the imaging of rats in order to simultaneously fit two mice on one PET-MRI image. However, both of these approaches potentially limit image quality. Additionally, the placement of two mice into one rat coil could promote partial volume effects, in which a volume that is smaller than two times the resolution appears larger than it is. To obtain optimum image quality, the use of TSE should thus be limited and designated mouse coils should be used. Finally, image quality in future experiments could also be improved by applying intravenous MRI contrast agents such as Omniscan® prior to performing the MRI measurements.

#### 4.2.2.4.4. [$^{64}$Cu]-labelled anti-CD19 Imaging could predict therapeutic response rates of CD19-mediated DLBCL treatments

As already explained above, there is a great interest in finding tumour-specific imaging tracers that lack non-specific binding sites. One such tracer was recently developed for B-cell lymphomas using CD19, a surface marker found on B-cells. As mentioned in section 3.4, this tracer is a CD19-based antibody radiolabelled with [$^{64}$Cu] and is currently already in experimental clinical use. In the light of the recently developed bispecific therapeutic antibody blinatumomab, which links CD19 to CD3 to evoke a T-cell response (Burt et al., 2019), CD19-based imaging could help predict response rates in B-cell lymphoma patients. It could also be advantageous in comparison to CD20-based PET imaging (Zettlitz et al., 2019), as patients already treated with CD20 antibodies like rituximab might have downregulated CD20. In our experiments we could show that *in vivo* imaging of MyD88$^{p.L252P}$-dependent intestinal lymphoma with [$^{64}$Cu]-labelled anti-CD19-antibodies is possible.

While the resolution of [$^{64}$Cu]-labelled anti-CD19-antibodies is precise enough for most clinical settings in humans, it is a clear limitation of [$^{64}$Cu]-labelled anti-CD19-antibody-based imaging in preclinical settings such as the imaging of our mouse model. Other preclinical mouse models rely on subcutaneous cell-line-based tumours instead of real genetic modifications in murine B-cells, in which correct borders of abdominal and other organs do not have to be identified. However, these models limit the transferability of the data to human settings. Hence, for [$^{64}$Cu]-labelled anti-CD19-antibody-based imaging to be most useful for preclinical settings, resolution has to be optimised. One approach could be decreasing the size of the CD19-antibody by for example generating nanobodies, as this would potentially ameliorate tissue penetration.

#### 4.2.2.5. Transferability of mouse model to human setting

Lastly, the MBC mouse model comes with some limitations concerning its transferability to the human setting.

In MBC mice, MyD88$^{p.L252P}$ is expressed in all B-cells from birth on. In human B-cell lymphoma, *MYD88*$^{L265P}$ mutations have not been described in childhood B-cell malignancies (Cairo and Beishuizen, 2019). The mutation is rather acquired later in life in single B-cells that then expand to clones. Therefore, ideally a mouse model that expresses MyD88$^{p.L252P}$ only in a fraction of all B-cells and only after a certain age would be of interest. Potentially this could be realised by using the R26R-Confetti mouse system that was originally developed by Livet and colleagues (Livet et al., 2007). Different mutually incompatible LoxP cassettes would have to be engineered around the *Myd88/Myd88*$^{p.L252P}$ locus in MBC mice that then at random cut out *Myd88* or *Myd88*$^{p.L252P}$. To further improve the transferability of the MBC mouse model, the *Myd88*$^{p.L252P}$ mutation should only be expressed after the mice reached a certain age. This could be achieved by making the Cre recombinase at the CD19 locus inducible, for example by using tamoxifen-inducible or acyclovir-inducible systems. This would allow for the activation of the mutation at an advanced age. But even then the *Myd88*$^{p.L252P}$ mutation would arise in every B-cell and not sporadically as in the patient. However, in practicable terms, the current model embodies an adequate representation.

Secondly, due to one CD19 promotor being replaced by the Cre recombinase, MBC mice might exhibit lower CD19 expression. This might also limit the transferability of [$^{64}$Cu]-labelled anti-CD19-antibody-based imaging data in MBC mice to humans. To assess if CD19 expression is lowered on B-cells of MBC mice, the CD19 expression of their B-cells could be compared to the CD19 expression of B-cells from mice that feature the *Myd88*$^{p.L252P}$ mutation and the *Bcl2* mutation but no insertion of a Cre recombinase in the *Cd19* locus.

Another factor potentially limiting the transferability of the mouse model to the human setting is the observed increased variance in TLR ligand dependency of MBC mice compared to BC mice (see section 3.2.1 and 4.1.1). It is possible that the increased variance is due to a synergy between *Myd88*$^{p.L252P}$ and *Bcl2*, as the same difference in variance was not observed between MC and C mice. In terms of transferability, increased variance means that either disease based on *Myd88*$^{p.L252P}$ and *Bcl2* has a high variation in phenotypes or the mouse model does not represent the disease well. In either case, factors that lead to this variation would have to be identified.

Lastly, as Knittel et al. already noted, it is not clear as to why the MBC mice develop a ABC DLBCL phenotype instead of a Waldenström macroglobulinemia phenotype (Knittel et al., 2016). This could be expected since Waldenström macroglobulinemia exhibits the highest prevalence of the *MYD88*$^{L265P}$ mutation with 90% of cases being positive in comparison to only 6.5 to 29% of cases in DLBCL (see section 1.6.1). As Knittel et al. previously suggested, this might be due to the different genomic landscapes of these two B-cell malignancies that are not accounted for in this MBC mouse model.

### 4.3. Outlook: Further approaches may be necessary to fully target lymphomagenesis in DLBCL and related lymphoid malignancies

Finally, while this study supports that MyD88$^{L265P}$ plays an important role in B-cell lymphomagenesis, there may be further factors necessary to fully target MyD88$^{L265P}$-related lymphomagenesis. For example, while MyD88$^{L265P}$ leads to the development of non-clonal, low-grade B-cell lymphoproliferative disorders, secondary genetic lesions are necessary for its transformation to DLBCL (Sewastianik et al., 2019, Landau et al., 2013). Secondary genetic lesions might include well-known lesions such as mutations in *CD79B* but also recent discoveries like activating lesions in *LUBAC* (linear ubiquitin chain assembly complex*)* (Jo et al., 2020), *TBL1XR1* (TBL1X Receptor 1) mutations (Wang et al., 2020) or *CXCR4*$^{S338X}$ (Gustine et al., 2019). In this sense MyD88$^{L265P}$ might be similar to the CD79B mutant isoforms frequently observed in B-cell malignancies, as these isoforms cannot initiate BCR signalling de novo but instead potentiate ongoing BCR signalling (Young et al., 2019). Other potential factors that could play a role are decreased immune surveillance at sites of inflammation (King et al., 2019). The level of malignancy might also depend on IgM expression, as suggested in section 3.5. This is supported by the circumstance that the more severe ABC-DLBCL subtype expresses an IgM-BCR, a rather unspecific BCR, in around 80% of cases while the GCB-DLBCL subtype does so in only about 34% (Young et al., 2019). Increased expression of these rather unspecific IgM-BCRs would also support that autoreactive BCRs are involved in DLBCL pathogenesis (see section 4.2.1.2). Possibly TLR ligands could act in tandem with BCR antigens to promote the emergence of single B-cells and these B-cells could then in turn expand to clonal tumours.

That being said, there could also be novel therapeutic approaches to MyD88$^{L265P}$-induced lymphomagenesis using downstream molecules as targets. One such example is SYK, which is increasingly activated by MyD88$^{L265P}$ (Munshi et al., 2020). Anti-IL-10 antibodies could alleviate disease aggravation since IL-10, a cytokine whose expression can be induced by MyD88 signalling, potentially induces PD-L1 expression on B-cells via the JAK2/STAT3 signalling pathway (Li et al., 2018a). Similarly, IL-6 signalling is elevated in DLBCL cells and could potentially be targeted therapeutically with IL-6 receptor inhibitors (Hashwah et al., 2019). On the other hand, there may be protective molecules such as KLHL14 (Kelch Like Family Member 14), whose loss mediates BTK inhibitor resistance and promotes assembly of the Myddosome (Choi et al., 2020). Similarly SPOP hinders the Myddosome assembly by promoting nondegradative ubiquitination of MyD88 (Jin et al., 2019, Guillamot et al., 2019).

## 4.4. Concluding remarks

In this study we could replicate that MBC mice, harbouring *Bcl2* amplifications and the genetic lesion *Myd88*$^{p.L252P}$, exhibit increased lymphoproliferation in lymph nodes and the spleen. Additionally, the evidence collected points towards an increased presence of intestinal tumours in MBC mice. Finally, we could show that upstream signals such as TLR9 stimulation seem to enhance lymphoproliferation and tumourigenesis in MBC mice.

In the future, potential endogenous TLR ligands such as microbiota-derived ligands that could promote lymphomagenesis should be investigated. Additionally, the nature of the observed intestinal lymphomas should be examined. This might lead to a better understanding of MyD88$^{p.L252P}$-induced effects during lymphomagenesis und thereby to better therapeutic approaches.

# 5. Summary (English)

With up to 40% of cases worldwide, diffuse large B-cell lymphoma (DLBCL) is the most common subtype of lymphoma (Li et al., 2018b, Stewart et al., 2014). The more aggressive activated B-cell like (ABC) subtype of DLBCL only has a 5-year survival rate of about 30% and more than 50% of ABC DLBCL cases have mutations in molecules involved in NF-κB activation. One of these mutations is the *MYD88*$^{L265P}$ mutation, which is present in almost 30% of ABC DLBCL cases. MyD88 is an adaptor molecule of Toll-like receptors (TLR) and its downstream effectors include many pro-survival and pro-proliferation signals, such as NF-κB hyperactivation. It is thus of interest to better understand and subsequently exploit the *MYD88*$^{L265P}$ mutation for therapeutic purposes, such as Toll-like receptor inhibition.

In this study, it was assessed if B-cells with the *MYD88*$^{L265P}$ mutation still depend on upstream TLR signals, which would make TLR inhibitors an attractive target for therapies, or if MyD88$^{L265P}$ is independent of upstream signals. For this purpose, a mouse model that mimics human DLBCL with B-cell specific expression of *Myd88*$^{p.L252P}$, *Bcl2* amplifications and *Gfp* was used and PET-MR imaging with radioactive glucose to assess glucose metabolism and radioactive thymidine to assess proliferation was performed in these mice. Additionally, the distribution of B-cells within the DLBCL mouse model was assessed using *in vivo* GFP scans. IgM expression as well as IL-6 and IL-10 production of B-cells in these mice was analysed *in vitro* and *in vivo* using ELISA. Finally, an evaluation of CD19-antibody-based PET-MR imaging in these transgenic DLBCL mice was performed in a proof-of-concept approach.

We found that the effect of MyD88$^{L265P}$ is indeed exacerbated by upstream TLR signals, supporting further research to be done on TLR(9) inhibitors. Secondly, we could show that in MyD88$^{L265P}$-mutated mice, more B-cells accumulate in the abdomen than in unmutated mice, suggesting potential TLR ligands, for example from the microbiota, to be present in the abdomen. Cytokine levels and IgM expression did not differ between mutated and unmutated B-cells *in vitro* and *in vivo*. Finally, we could demonstrate that CD19-antibody-based PET-MR imaging of lymphomas in our transgenic DLBCL mouse model is possible. This supports that CD19-based PET imaging is indeed possible for *MYD88*$^{L265P}$-mutated lymphoma and could help to improve diagnostics and treatment monitoring of *MYD88*$^{L265P}$-mutated lymphoma. Collectively, this study supports that *MYD88*$^{L265P}$ is an important driver of DLBCL.

# 6. Summary (German)

Mit bis zu 40% aller Fälle weltweit ist das Diffus-großzellige B-Zell-Lymphom (DLBCL) der häufigste Subtyp unter den Lymphomen (Li et al., 2018b, Stewart et al., 2014). Der aggressivere aktivierte B-Zell-ähnliche (ABC) Subtyp des DLBCL hat eine 5-Jahres-Überlebensrate von nur 30% und mehr als 50% der ABC DLBCL Fälle haben Mutationen in Molekülen, die in der Aktivierung von NF-κB beteiligt sind. Eine dieser Mutationen ist die *MYD88*$^{L265P}$ Mutation, welche in beinahe 30% der ABC DLBCL Fälle vorhanden ist. MyD88 ist ein Adaptormolekül des TLR (Toll-like Rezeptor) und seine nachfolgenden Effektormoleküle beinhalten viele überlebensfördernde und proliferationsfördernde Signale, wie beispielsweise NF-κB-Hyperaktivierung. Es ist daher von Interesse, die *MYD88*$^{L265P}$-Mutation besser zu verstehen und anschließend für therapeutische Zwecke zu nutzen, wie beispielsweise durch Hemmung der Toll-like-Rezeptoren.

In dieser Studie wurde untersucht, ob *MYD88*$^{L265P}$-mutierte B-Zellen weiterhin von übergeordneten TLR-Signalen abhängig sind, was TLR-Inhibitoren zu einem attraktiven Ziel für Therapien machen würde, oder ob MyD88$^{L265P}$ unabhängig von übergeordneten Signalen ist. Zu diesem Zweck wurde ein Mausmodell verwendet, welches humanes DLBCL durch B-Zell-spezifische Expression von *Myd88*$^{p.L252P}$, *Bcl2*-Amplifikationen und *Gfp* imitiert und PET-MR Bildgebung mit radioaktiv markierter Glukose zur Glukosestoffwechselanalyse sowie mit radioaktiv markiertem Thymidin zur Proliferationsanalyse durchgeführt. Zusätzlich wurde durch *in vivo* GFP Scans untersucht, wie sich die B-Zellen im verwendeten Mausmodell verteilten. Die Expression von IgM sowie die Produktion von IL-6 und IL-10 wurde im Mausmodell *in vitro* und *in vivo* mithilfe von ELISA analysiert. Schließlich wurde als proof-of-concept eine Evaluation von CD19-Antikörper-basierter PET-MR-Bildgebung in diesen transgenetischen DLBCL-Mäusen durchgeführt.

Es konnte gezeigt werden, dass MyD88$^{L265P}$ unabhängig von übergeordneten TLR-Signalen ist, was daher weitere Studien zu TLR(9)-Inhibitoren befürwortet. Zweitens konnte gezeigt werden, dass in MyD88$^{L265P}$-mutierten Mäusen mehr B-Zellen im Abdomen akkumulieren als in nicht-mutierten Mäusen. Dies deutet auf die potentielle Anwesenheit von TLR-Liganden im Abdomen hin, beispielsweise durch Mikrobiota. Zytokinlevel und die Expression von IgM unterschieden sich nicht zwischen mutierten und nicht-mutierten B-Zellen *in vitro* und *in vivo*.

Abschließend konnte gezeigt werden, dass CD19-Antikörper-basierte PET-MR Bildgebung von Lymphomherden im verwendeten transgenetischen DLBCL-Mausmodell möglich ist. Dies bestätigt, dass CD19-basierte PET-Bildgebung von *MYD88*$^{L265P}$-mutierten Lymphomen möglich ist und dass sie helfen könnte, Diagnostik und Therapiemonitoring von *MYD88*$^{L265P}$-mutierten Lymphomen zu verbessern. Zusammenfassend bekräftigt diese Studie, dass *MYD88*$^{L265P}$ eine treibende Kraft des DLBCL ist.

# List of Publications

At the time of writing, no publications based on this dissertation project have been submitted.

# Bibliography

AGRAWAL, S., GOEL, A. D. & GUPTA, N. 2020. Emerging prophylaxis strategies against COVID-19. *Monaldi Arch Chest Dis,* 90.

AKATSU, C., SHINAGAWA, K., NUMOTO, N., LIU, Z., UCAR, A. K., ASLAM, M., PHOON, S., ADACHI, T., FURUKAWA, K., ITO, N. & TSUBATA, T. 2016. CD72 negatively regulates B lymphocyte responses to the lupus-related endogenous toll-like receptor 7 ligand Sm/RNP. *J Exp Med,* 213**,** 2691-2706.

AKIRA, S. & TAKEDA, K. 2004. Toll-like receptor signalling. *Nat Rev Immunol,* 4**,** 499-511.

AMERICAN CANCER SOCIETY 2018. Types of B-cell Lymphoma. URL: https://www.cancer.org/cancer/non-hodgkin-lymphoma/about/b-cell-lymphoma.html#references, last accessed: 08.05.2020.

AN, B., ZHU, S., LI, T., WU, J., ZANG, G., LV, X., QIAO, Y., HUANG, J., SHAO, Y., CUI, J., LIU, Y. J. & CHEN, J. 2020. A Dual TLR7/TLR9 Inhibitor HJ901 Inhibits ABC-DLBCL Expressing the MyD88 L265P Mutation. *Front Cell Dev Biol,* 8**,** 262.

ANDERSON, C. J. & FERDANI, R. 2009. Copper-64 radiopharmaceuticals for PET imaging of cancer: advances in preclinical and clinical research. *Cancer Biother Radiopharm,* 24**,** 379-93.

AVALOS, A. M. & PLOEGH, H. L. 2011. Competition by inhibitory oligonucleotides prevents binding of CpG to C-terminal TLR9. *Eur J Immunol,* 41**,** 2820-7.

AVBELJ, M., WOLZ, O. O., FEKONJA, O., BENCINA, M., REPIC, M., MAVRI, J., KRUGER, J., SCHARFE, C., DELMIRO GARCIA, M., PANTER, G., KOHLBACHER, O., WEBER, A. N. & JERALA, R. 2014. Activation of lymphoma-associated MyD88 mutations via allostery-induced TIR-domain oligomerization. *Blood,* 124**,** 3896-904.

BEHAM-SCHMID, C. 2017. Aggressive lymphoma 2016: revision of the WHO classification. *Memo,* 10**,** 248-254.

BEN-ZVI, I., KIVITY, S., LANGEVITZ, P. & SHOENFELD, Y. 2012. Hydroxychloroquine: from malaria to autoimmunity. *Clin Rev Allergy Immunol,* 42**,** 145-53.

BEN ABDELWAHED, R., COSETTE, J., DONNOU, S., CROZET, L., OUAKRIM, H., FRIDMAN, W. H., SAUTES-FRIDMAN, C., MAHJOUB, A. & FISSON, S. 2013. Lymphoma B-cell responsiveness to CpG-DNA depends on the tumor microenvironment. *J Exp Clin Cancer Res,* 32**,** 18.

BENBENISHTY, A., GADRICH, M., COTTARELLI, A., LUBART, A., KAIN, D., AMER, M., SHAASHUA, L., GLASNER, A., EREZ, N., AGALLIU, D., MAYO, L., BEN-ELIYAHU, S. & BLINDER, P. 2019. Prophylactic TLR9 stimulation reduces brain metastasis through microglia activation. *PLoS Biol,* 17**,** e2006859.

BERKOWITZ, D., PERI, R., LAVY, A. & KESSEL, A. 2013. Increased Toll-like receptor 9 expression by B cells from inflammatory bowel disease patients. *Hum Immunol,* 74**,** 1519-23.

BLANC, V., BOUSSEAU, A., CARON, A., CARREZ, C., LUTZ, R. J. & LAMBERT, J. M. 2011. SAR3419: an anti-CD19-Maytansinoid Immunoconjugate for the treatment of B-cell malignancies. *Clin Cancer Res,* 17**,** 6448-58.

BOUDESCO, C., VERHOEYEN, E., MARTIN, L., CHASSAGNE-CLEMENT, C., SALMI, L., MHAIDLY, R., PANGAULT, C., FEST, T., RAMLA, S., JARDIN, F., WOLZ, O. O., WEBER, A. N. R., GARRIDO, C. & JEGO, G. 2018. HSP110 sustains chronic NF-kappaB signaling in activated B-cell diffuse large B-cell lymphoma through MyD88 stabilization. *Blood,* 132**,** 510-520.

BRAHMAKSHATRIYA, V., KUANG, Y., DEVARAJAN, P., XIA, J., ZHANG, W., VONG, A. M. & SWAIN, S. L. 2017. IL-6 Production by TLR-Activated APC Broadly Enhances Aged Cognate CD4 Helper and B Cell Antibody Responses In Vivo. *J Immunol,* 198**,** 2819-2833.

BRUBAKER, S. W., BONHAM, K. S., ZANONI, I. & KAGAN, J. C. 2015. Innate immune pattern recognition: a cell biological perspective. *Annu Rev Immunol,* 33**,** 257-90.

BURT, R., WARCEL, D. & FIELDING, A. K. 2019. Blinatumomab, a bispecific B-cell and T-cell engaging antibody, in the treatment of B-cell malignancies. *Hum Vaccin Immunother,* 15**,** 594-602.

CAIRO, M. S. & BEISHUIZEN, A. 2019. Childhood, adolescent and young adult non-Hodgkin lymphoma: current perspectives. *Br J Haematol,* 185**,** 1021-1042.

CAMPBELL, J. D. 2017. Development of the CpG Adjuvant 1018: A Case Study. *Methods Mol Biol,* 1494**,** 15-27.

CARLSSON, E., DING, J. L. & BYRNE, B. 2016. SARM modulates MyD88-mediated TLR activation through BB-loop dependent TIR-TIR interactions. *Biochim Biophys Acta,* 1863**,** 244-53.

CASCINI, G. L., NICCOLI ASABELLA, A., NOTARISTEFANO, A., RESTUCCIA, A., FERRARI, C., RUBINI, D., ALTINI, C. & RUBINI, G. 2014. 124 Iodine: a longer-life positron emitter isotope-new opportunities in molecular imaging. *Biomed Res Int,* 2014**,** 672094.

CASTELLANI, F., VISENTIN, A., CAMPAGNOLO, M., SALVALAGGIO, A., CACCIAVILLANI, M., CANDIOTTO, C., BERTORELLE, R., TRENTIN, L. & BRIANI, C. 2020. The Bruton tyrosine kinase inhibitor ibrutinib improves anti-MAG antibody polyneuropathy. *Neurol Neuroimmunol Neuroinflamm,* 7.

CASTILLO, J. J., MORENO, D. F., ARBELAEZ, M. I., HUNTER, Z. R. & TREON, S. P. 2019. CXCR4 mutations affect presentation and outcomes in patients with Waldenstrom macroglobulinemia: A systematic review. *Expert Rev Hematol***,** 1-9.

CHEN, Y., BAI, G., NING, Y., CAI, S., ZHANG, T., SONG, P., ZHOU, J., DUAN, W., DING, J., XIE, H. & ZHANG, H. 2020. Design and synthesis of Imidazo[1,2-b]pyridazine IRAK4 inhibitors for the treatment of mutant MYD88 L265P diffuse large B-cell lymphoma. *Eur J Med Chem,* 190**,** 112092.

CHESON, B. D. 2015. Staging and response assessment in lymphomas: the new Lugano classification. *Chin Clin Oncol,* 4**,** 5.

CHIAPPELLA, A., SANTAMBROGIO, E., CASTELLINO, A., NICOLOSI, M. & VITOLO, U. 2017. Integrating novel drugs to chemoimmunotherapy in diffuse large B-cell lymphoma. *Expert Rev Hematol,* 10**,** 697-705.

CHOI, J., PHELAN, J. D., WRIGHT, G. W., HAUPL, B., HUANG, D. W., SHAFFER, A. L., 3RD, YOUNG, R. M., WANG, Z., ZHAO, H., YU, X., OELLERICH, T. & STAUDT, L. M. 2020. Regulation of B cell receptor-dependent NF-kappaB signaling by the tumor suppressor KLHL14. *Proc Natl Acad Sci U S A,* 117**,** 6092-6102.

COMARMOND, C., LORIN, V., MARQUES, C., MACIEJEWSKI-DUVAL, A., JOHER, N., PLANCHAIS, C., TOUZOT, M., BIARD, L., HIEU, T., QUINIOU, V., DESBOIS, A. C., ROSENZWAJG, M., KLATZMANN, D., CACOUB, P., MOUQUET, H. & SAADOUN, D. 2019. TLR9 signalling in HCV-associated atypical memory B cells triggers Th1 and rheumatoid factor autoantibody responses. *J Hepatol,* 71**,** 908-919.

DE NARDO, D. 2015. Toll-like receptors: Activation, signalling and transcriptional modulation. *Cytokine,* 74**,** 181-9.

DEGUINE, J. & BARTON, G. M. 2014. MyD88: a central player in innate immune signaling. *F1000Prime Rep,* 6**,** 97.

DIAS, C. & ISENBERG, D. A. 2011. Susceptibility of patients with rheumatic diseases to B-cell non-Hodgkin lymphoma. *Nat Rev Rheumatol,* 7**,** 360-8.

DIEHL, G. E., LONGMAN, R. S., ZHANG, J. X., BREART, B., GALAN, C., CUESTA, A., SCHWAB, S. R. & LITTMAN, D. R. 2013. Microbiota restricts trafficking of bacteria to mesenteric lymph nodes by CX(3)CR1(hi) cells. *Nature,* 494**,** 116-20.

DIEUDONNE, Y., GIES, V., GUFFROY, A., KEIME, C., BIRD, A. K., LIESVELD, J., BARNAS, J. L., POINDRON, V., DOUIRI, N., SOULAS-SPRAUEL, P., MARTIN, T., MEFFRE, E., ANOLIK, J. H. & KORGANOW, A. S. 2019. Transitional B cells in quiescent SLE: An early checkpoint imprinted by IFN. *J Autoimmun,* 102**,** 150-158.

EL ABBAS, S., RADERMECKER, C., BAI, Q., BEGUIN, C., SCHYNS, J., MEUNIER, M., PIROTTIN, D., DESMET, C. J., MEUWIS, M. A., ART, T., LOUIS, E., TAM, S. Y., TSAI, M., BUREAU, F., GALLI, S. J. & MARICHAL, T. 2020. Epithelial RABGEF1 deficiency promotes intestinal inflammation by dysregulating intrinsic MYD88-dependent innate signaling. *Mucosal Immunol,* 13**,** 96-109.

FANG, H., KAPOOR, P., GONSALVES, W. I., FREDERICK, L. A., VISWANATHA, D., HOWARD, M. T., HE, R., MORICE, W. G., 2ND, MCPHAIL, E. D., GREIPP, P. T., ANSELL, S. M., KYLE, R. A., GERTZ, M. A., PALUDO, J., ABEYKOON, J. & KING, R. L. 2018. Defining Lymphoplasmacytic Lymphoma: Does MYD88L265P Define a Pathologically Distinct Entity Among Patients With an IgM Paraprotein and Bone Marrow-Based Low-Grade B-Cell Lymphomas With Plasmacytic Differentiation? *Am J Clin Pathol,* 150**,** 168-176.

FIEDLER, K., KOKAI, E., BRESCH, S. & BRUNNER, C. 2013. MyD88 is involved in myeloid as well as lymphoid hematopoiesis independent of the presence of a pathogen. *Am J Blood Res,* 3**,** 124-40.

GANDY, N., ARSHAD, M. A., PARK, W. E., ROCKALL, A. G. & BARWICK, T. D. 2019. FDG-PET Imaging in Cervical Cancer. *Semin Nucl Med,* 49**,** 461-470.

GAULD, S. B., DAL PORTO, J. M. & CAMBIER, J. C. 2002. B cell antigen receptor signaling: roles in cell development and disease. *Science,* 296**,** 1641-2.

GHAMLOUCH, H., OULED-HADDOU, H., GUYART, A., REGNIER, A., TRUDEL, S., CLAISSE, J. F., FUENTES, V., ROYER, B., MAROLLEAU, J. P. & GUBLER, B. 2014. TLR9 Ligand (CpG Oligodeoxynucleotide) Induces CLL B-Cells to Differentiate into CD20(+) Antibody-Secreting Cells. *Front Immunol,* 5**,** 292.

GIMENEZ, N., SCHULZ, R., HIGASHI, M., AYMERICH, M., VILLAMOR, N., DELGADO, J., JUAN, M., LOPEZ-GUERRA, M., CAMPO, E., ROSICH, L., SEIFFERT, M. & COLOMER, D. 2019. Targeting IRAK4 disrupts inflammatory pathways and delays tumor development in chronic lymphocytic leukemia. *Leukemia*.

GOODMAN, A., PATEL, S. P. & KURZROCK, R. 2017. PD-1-PD-L1 immune-checkpoint blockade in B-cell lymphomas. *Nat Rev Clin Oncol,* 14**,** 203-220.

GROHEUX, D., ESPIE, M., GIACCHETTI, S. & HINDIE, E. 2013. Performance of FDG PET/CT in the clinical management of breast cancer. *Radiology,* 266**,** 388-405.

GUILLAMOT, M., OUAZIA, D., DOLGALEV, I., YEUNG, S. T., KOURTIS, N., DAI, Y., CORRIGAN, K., ZEA-REDONDO, L., SARAF, A., FLORENS, L., WASHBURN, M. P., TIKHONOVA, A. N., MALUMBRES, M., GONG, Y., TSIRIGOS, A., PARK, C., BARBIERI, C., KHANNA, K. M., BUSINO, L. & AIFANTIS, I. 2019. The E3 ubiquitin ligase SPOP controls resolution of systemic inflammation by triggering MYD88 degradation. *Nat Immunol,* 20**,** 1196-1207.

GUSTINE, J. N., MEID, K., DUBEAU, T., SEVERNS, P., HUNTER, Z. R., GUANG, Y., XU, L., TREON, S. P. & CASTILLO, J. J. 2018. Ibrutinib discontinuation in Waldenstrom macroglobulinemia: Etiologies, outcomes, and IgM rebound. *Am J Hematol,* 93**,** 511-517.

GUSTINE, J. N., XU, L., TSAKMAKLIS, N., DEMOS, M. G., KOFIDES, A., CHEN, J. G., LIU, X., MUNSHI, M., GUERRERA, M. L., CHAN, G. G., PATTERSON, C. J., KEEZER, A., MEID, K., DUBEAU, T., YANG, G., HUNTER, Z. R., TREON, S. P. & CASTILLO, J. J. 2019. CXCR4 (S338X) clonality is an important determinant of ibrutinib outcomes in patients with Waldenstrom macroglobulinemia. *Blood Adv,* 3**,** 2800-2803.

HASHWAH, H., BERTRAM, K., STIRM, K., STELLING, A., WU, C. T., KASSER, S., MANZ, M. G., THEOCHARIDES, A. P., TZANKOV, A. & MULLER, A. 2019. The IL-6 signaling complex is a critical driver, negative prognostic factor, and therapeutic target in diffuse large B-cell lymphoma. *EMBO Mol Med,* 11**,** e10576.

HE, B., SANTAMARIA, R., XU, W., COLS, M., CHEN, K., PUGA, I., SHAN, M., XIONG, H., BUSSEL, J. B., CHIU, A., PUEL, A., REICHENBACH, J., MARODI, L., DOFFINGER, R., VASCONCELOS, J., ISSEKUTZ, A., KRAUSE, J., DAVIES, G., LI, X., GRIMBACHER, B., PLEBANI, A., MEFFRE, E., PICARD, C., CUNNINGHAM-RUNDLES, C., CASANOVA, J. L. & CERUTTI, A. 2010. The transmembrane activator TACI triggers immunoglobulin class switching by activating B cells through the adaptor MyD88. *Nat Immunol,* 11**,** 836-45.

HOCK, A. K., CHEUNG, E. C., HUMPTON, T. J., MONTEVERDE, T., PAULUS-HOCK, V., LEE, P., MCGHEE, E., SCOPELLITI, A., MURPHY, D. J., STRATHDEE, D., BLYTH, K. & VOUSDEN, K. H. 2017. Development of an inducible mouse model of iRFP713 to track recombinase activity and tumour development in vivo. *Sci Rep,* 7**,** 1837.

HOFFMAN, R. M. & YANG, M. 2006. Whole-body imaging with fluorescent proteins. *Nat Protoc,* 1**,** 1429-38.

HOLLING, T. M., SCHOOTEN, E. & VAN DEN ELSEN, P. J. 2004. Function and regulation of MHC class II molecules in T-lymphocytes: of mice and men. *Hum Immunol,* 65**,** 282-90.

HOLTORF, A., CONRAD, A., HOLZMANN, B. & JANSSEN, K. P. 2018. Cell-type specific MyD88 signaling is required for intestinal tumor initiation and progression to malignancy. *Oncoimmunology,* 7**,** e1466770.

HOU, Y., LU, X. & ZHANG, Y. 2018. IRAK Inhibitor Protects the Intestinal Tract of Necrotizing Enterocolitis by Inhibiting the Toll-Like Receptor (TLR) Inflammatory Signaling Pathway in Rats. *Med Sci Monit,* 24**,** 3366-3373.

IWAI, Y., HAMANISHI, J., CHAMOTO, K. & HONJO, T. 2017. Cancer immunotherapies targeting the PD-1 signaling pathway. *J Biomed Sci,* 24**,** 26.

JAHRSDORFER, B., MUHLENHOFF, L., BLACKWELL, S. E., WAGNER, M., POECK, H., HARTMANN, E., JOX, R., GIESE, T., EMMERICH, B., ENDRES, S., WEINER, G. J. & HARTMANN, G. 2005. B-cell lymphomas differ in their responsiveness to CpG oligodeoxynucleotides. *Clin Cancer Res,* 11**,** 1490-9.

JANEWAY, C., MURPHY, K. M. & WEAVER, C. 2017. *Janeway's immunobiology,* New York London, Garland Science Taylor & Francis Group.

JANEWAY, C. A., JR. 1989. Approaching the asymptote? Evolution and revolution in immunology. *Cold Spring Harb Symp Quant Biol,* 54 Pt 1**,** 1-13.

JIANG, M., BENNANI, N. N. & FELDMAN, A. L. 2017. Lymphoma classification update: B-cell non-Hodgkin lymphomas. *Expert Rev Hematol,* 10**,** 405-415.

JIN, X., SHI, Q., LI, Q., ZHOU, L., WANG, J., JIANG, L., ZHAO, X., FENG, K., LIN, T., LIN, Z., ZHUANG, H., YANG, J., HU, C., ZHANG, L., SHEN, L., LU, Y., ZHU, J., WANG, H., QI, H., MENG, X., XI, Y., PAN, J., FANG, S., TIAN, H., ZHOU, C., ZHANG, P., GAO, K., ZHAO, S. M., LI, Y., GONG, Z. & WANG, C. 2019. CRL3-SPOP ubiquitin ligase complex suppresses the growth of diffuse large B-cell lymphoma by negatively regulating the MyD88/NF-kappaB signaling. *Leukemia*.

JO, T., NISHIKORI, M., KOGURE, Y., ARIMA, H., SASAKI, K., SASAKI, Y., NAKAGAWA, T., IWAI, F., MOMOSE, S., SHIRAISHI, A., KIYONARI, H., KAGAYA, N., ONUKI, T., SHIN-YA, K., YOSHIDA, M., KATAOKA, K., OGAWA, S., IWAI, K. & TAKAORI-KONDO, A. 2020. LUBAC accelerates B-cell lymphomagenesis by conferring B cells resistance to genotoxic stress. *Blood*.

KANDATHIL, A., KAY, F. U., BUTT, Y. M., WACHSMANN, J. W. & SUBRAMANIAM, R. M. 2018. Role of FDG PET/CT in the Eighth Edition of TNM Staging of Non-Small Cell Lung Cancer. *Radiographics,* 38**,** 2134-2149.

KELLY, P. N., ROMERO, D. L., YANG, Y., SHAFFER, A. L., 3RD, CHAUDHARY, D., ROBINSON, S., MIAO, W., RUI, L., WESTLIN, W. F., KAPELLER, R. & STAUDT, L. M. 2015. Selective interleukin-1 receptor-associated kinase 4 inhibitors for the treatment of autoimmune disorders and lymphoid malignancy. *J Exp Med,* 212**,** 2189-201.

KING, R. L., GOODLAD, J. R., CALAMINICI, M., DOTLIC, S., MONTES-MORENO, S., OSCHLIES, I., PONZONI, M., TRAVERSE-GLEHEN, A., OTT, G. & FERRY, J. A. 2019. Lymphomas arising in immune-privileged sites: insights into biology, diagnosis, and pathogenesis. *Virchows Arch*.

KIRIPOLSKY, J., ROMANO, R. A., KASPEREK, E. M., YU, G. & KRAMER, J. M. 2019. Activation of Myd88-Dependent TLRs Mediates Local and Systemic Inflammation in a Mouse Model of Primary Sjogren's Syndrome. *Front Immunol,* 10**,** 2963.

KITAJIMA, K., NAKAJO, M., KAIDA, H., MINAMIMOTO, R., HIRATA, K., TSURUSAKI, M., DOI, H., UENO, Y., SOFUE, K., TAMAKI, Y. & YAMAKADO, K. 2017. Present and future roles of FDG-PET/CT imaging in the management of gastrointestinal cancer: an update. *Nagoya J Med Sci,* 79**,** 527-543.

KNITTEL, G., LIEDGENS, P., KOROVKINA, D., SEEGER, J. M., AL-BALDAWI, Y., AL-MAARRI, M., FRITZ, C., VLANTIS, K., BEZHANOVA, S., SCHEEL, A. H., WOLZ, O. O., REIMANN, M., MOLLER, P., LOPEZ, C., SCHLESNER, M., LOHNEIS, P., WEBER, A. N., TRUMPER, L., GERMAN INTERNATIONAL CANCER GENOME CONSORTIUM MOLECULAR MECHANISMS IN MALIGNANT LYMPHOMA BY SEQUENCING PROJECT, C., STAUDT, L. M., ORTMANN, M., PASPARAKIS, M., SIEBERT, R., SCHMITT, C. A., KLATT, A. R., WUNDERLICH, F. T., SCHAFER, S. C., PERSIGEHL, T., MONTESINOS-RONGEN, M., ODENTHAL, M., BUTTNER, R., FRENZEL, L. P., KASHKAR, H. & REINHARDT, H. C. 2016. B-cell-specific conditional expression of Myd88p.L252P leads to the development of diffuse large B-cell lymphoma in mice. *Blood,* 127**,** 2732-41.

KOLIARAKI, V., CHALKIDI, N., HENRIQUES, A., TZAFERIS, C., POLYKRATIS, A., WAISMAN, A., MULLER, W., HACKAM, D. J., PASPARAKIS, M. & KOLLIAS, G. 2019. Innate Sensing through Mesenchymal TLR4/MyD88 Signals Promotes Spontaneous Intestinal Tumorigenesis. *Cell Rep,* 26**,** 536-545 e4.

KUROSAKI, T. 2011. Regulation of BCR signaling. *Mol Immunol,* 48**,** 1287-91.

LANDAU, D. A., CARTER, S. L., STOJANOV, P., MCKENNA, A., STEVENSON, K., LAWRENCE, M. S., SOUGNEZ, C., STEWART, C., SIVACHENKO, A., WANG, L., WAN, Y., ZHANG, W., SHUKLA, S. A., VARTANOV, A., FERNANDES, S. M., SAKSENA, G., CIBULSKIS, K., TESAR, B., GABRIEL, S., HACOHEN, N., MEYERSON, M., LANDER, E. S., NEUBERG, D., BROWN, J. R., GETZ, G. & WU, C. J. 2013. Evolution and impact of subclonal mutations in chronic lymphocytic leukemia. *Cell,* 152**,** 714-26.

LANG, J., MA, K., GUO, J., ZHANG, J., WANG, Q. & SUN, H. 2018. Clinical significance of elevated antinuclear antibodies in patients with diffuse large B-cell lymphoma: A single center study. *J Cancer Res Ther,* 14**,** 213-219.

LEE, J. H., JEONG, H., CHOI, J. W., OH, H. & KIM, Y. S. 2017. Clinicopathologic significance of MYD88 L265P mutation in diffuse large B-cell lymphoma: a meta-analysis. *Sci Rep,* 7**,** 1785.

LENERT, P., YI, A. K., KRIEG, A. M., STUNZ, L. L. & ASHMAN, R. F. 2003. Inhibitory oligonucleotides block the induction of AP-1 transcription factor by stimulatory CpG oligonucleotides in B cells. *Antisense Nucleic Acid Drug Dev,* 13**,** 143-50.

LENZ, G., WRIGHT, G., DAVE, S. S., XIAO, W., POWELL, J., ZHAO, H., XU, W., TAN, B., GOLDSCHMIDT, N., IQBAL, J., VOSE, J., BAST, M., FU, K., WEISENBURGER, D. D., GREINER, T. C., ARMITAGE, J. O., KYLE, A., MAY, L., GASCOYNE, R. D., CONNORS, J. M., TROEN, G., HOLTE, H., KVALOY, S., DIERICKX, D., VERHOEF, G., DELABIE, J., SMELAND, E. B., JARES, P., MARTINEZ, A., LOPEZ-GUILLERMO, A., MONTSERRAT, E., CAMPO, E., BRAZIEL, R. M., MILLER, T. P., RIMSZA, L. M., COOK, J. R., POHLMAN, B., SWEETENHAM, J., TUBBS, R. R., FISHER, R. I., HARTMANN, E., ROSENWALD, A., OTT, G., MULLER-HERMELINK, H. K., WRENCH, D., LISTER, T. A., JAFFE, E. S., WILSON, W. H., CHAN, W. C., STAUDT, L. M. & LYMPHOMA/LEUKEMIA MOLECULAR PROFILING, P. 2008. Stromal gene signatures in large-B-cell lymphomas. *N Engl J Med,* 359**,** 2313-23.

LI, L., ZHANG, J., CHEN, J., XU-MONETTE, Z. Y., MIAO, Y., XIAO, M., YOUNG, K. H., WANG, S., MEDEIROS, L. J., WANG, M., FORD, R. J. & PHAM, L. V. 2018a. B-cell receptor-mediated NFATc1 activation induces IL-10/STAT3/PD-L1 signaling in diffuse large B-cell lymphoma. *Blood,* 132**,** 1805-1817.

LI, S., YOUNG, K. H. & MEDEIROS, L. J. 2018b. Diffuse large B-cell lymphoma. *Pathology,* 50**,** 74-87.

LIU, P. H., SHAH, R. B., LI, Y., ARORA, A., UNG, P. M., RAMAN, R., GORBATENKO, A., KOZONO, S., ZHOU, X. Z., BRECHIN, V., BARBARO, J. M., THOMPSON, R., WHITE, R. M., AGUIRRE-GHISO, J. A., HEYMACH, J. V., LU, K. P., SILVA, J. M., PANAGEAS, K. S., SCHLESSINGER, A., MAKI, R. G., SKINNER, H. D., DE STANCHINA, E. & SIDI, S. 2019. An IRAK1-PIN1 signalling axis drives intrinsic tumour resistance to radiation therapy. *Nat Cell Biol*.

LIU, X., PICHULIK, T., WOLZ, O. O., DANG, T. M., STUTZ, A., DILLEN, C., DELMIRO GARCIA, M., KRAUS, H., DICKHOFER, S., DAIBER, E., MUNZENMAYER, L., WAHL, S., RIEBER, N., KUMMERLE-DESCHNER, J., YAZDI, A., FRANZ-WACHTEL, M., MACEK, B., RADSAK, M., VOGEL, S., SCHULTE, B., WALZ, J. S., HARTL, D., LATZ, E., STILGENBAUER, S., GRIMBACHER, B., MILLER, L., BRUNNER, C., WOLZ, C. & WEBER, A. N. R. 2017. Human NACHT, LRR, and PYD domain-containing protein 3 (NLRP3) inflammasome activity is regulated by and potentially targetable through Bruton tyrosine kinase. *J Allergy Clin Immunol,* 140**,** 1054-1067 e10.

LIVET, J., WEISSMAN, T. A., KANG, H., DRAFT, R. W., LU, J., BENNIS, R. A., SANES, J. R. & LICHTMAN, J. W. 2007. Transgenic strategies for combinatorial expression of fluorescent proteins in the nervous system. *Nature,* 450**,** 56-62.

LOWIK, C. W., KAIJZEL, E., QUE, I., VAHRMEIJER, A., KUPPEN, P., MIEOG, J. & VAN DE VELDE, C. 2009. Whole body optical imaging in small animals and its translation to the clinic: intra-operative optical imaging guided surgery. *Eur J Cancer,* 45 Suppl 1**,** 391-3.

MANKAI, A., BUHE, V., HAMMADI, M., YOUINOU, P., GHEDIRA, I., BERTHOU, C. & BORDRON, A. 2009. Improvement of rituximab efficiency in chronic lymphocytic leukemia by

CpG-mediated upregulation of CD20 expression independently of PU.1. *Ann N Y Acad Sci,* 1173**,** 721-8.

MATZINGER, P. 2002. The danger model: a renewed sense of self. *Science,* 296**,** 301-5.

MCELROY, W. T. 2019. Interleukin-1 receptor-associated kinase 4 (IRAK4) inhibitors: an updated patent review (2016-2018). *Expert Opin Ther Pat,* 29**,** 243-259.

MELANI, C., WILSON, W. H. & ROSCHEWSKI, M. 2019. Liquid biopsy in non-Hodgkin's lymphoma. *Hematol Oncol,* 37 Suppl 1**,** 70-74.

MEZZANOTTE, L., VAN 'T ROOT, M., KARATAS, H., GOUN, E. A. & LOWIK, C. 2017. In Vivo Molecular Bioluminescence Imaging: New Tools and Applications. *Trends Biotechnol,* 35**,** 640-652.

MITTRUCKER, H. W., VISEKRUNA, A. & HUBER, M. 2014. Heterogeneity in the differentiation and function of CD8(+) T cells. *Arch Immunol Ther Exp (Warsz),* 62**,** 449-58.

MONDELLO, P., BREA, E. J., DE STANCHINA, E., TOSKA, E., CHANG, A. Y., FENNELL, M., SESHAN, V., GARIPPA, R., SCHEINBERG, D. A., BASELGA, J., WENDEL, H. G. & YOUNES, A. 2018. Panobinostat acts synergistically with ibrutinib in diffuse large B cell lymphoma cells with MyD88 L265 mutations. *JCI Insight,* 3.

MORBACH, H., SCHICKEL, J. N., CUNNINGHAM-RUNDLES, C., CONLEY, M. E., REISLI, I., FRANCO, J. L. & MEFFRE, E. 2016. CD19 controls Toll-like receptor 9 responses in human B cells. *J Allergy Clin Immunol,* 137**,** 889-98 e6.

MORTEZAGHOLI, S., BABALOO, Z., RAHIMZADEH, P., GHAEDI, M., NAMDARI, H., ASSAR, S., AZIMI MOHAMADABADI, M. & SALEHI, E. 2016. Evaluation of PBMC Distribution and TLR9 Expression in Patients with Systemic Lupus Erythematosus. *Iran J Allergy Asthma Immunol,* 15**,** 229-36.

MUNSHI, M., LIU, X., CHEN, J. G., XU, L., TSAKMAKLIS, N., DEMOS, M. G., KOFIDES, A., GUERRERA, M. L., JIMENEZ, C., CHAN, G. G., HUNTER, Z. R., PALOMBA, M. L., ARGYROPOULOS, K. V., MEID, K., KEEZER, A., GUSTINE, J., DUBEAU, T., CASTILLO, J. J., PATTERSON, C. J., WANG, J., BUHRLAGE, S. J., GRAY, N. S., TREON, S. P. & YANG, G. 2020. SYK is activated by mutated MYD88 and drives pro-survival signaling in MYD88 driven B-cell lymphomas. *Blood Cancer J,* 10**,** 12.

MURPHY, M., PATTABIRAMAN, G., MANAVALAN, T. T. & MEDVEDEV, A. E. 2017. Deficiency in IRAK4 activity attenuates manifestations of murine Lupus. *Eur J Immunol,* 47**,** 880-891.

NAKAJO, M., KAJIYA, Y., JINGUJI, M., NAKABEPPU, Y., NAKAJO, M., NIHARA, T. & YOSHIURA, T. 2017. Current clinical status of (18)F-FLT PET or PET/CT in digestive and abdominal organ oncology. *Abdom Radiol (NY),* 42**,** 951-961.

NAYYAR, N., WHITE, M. D., GILL, C. M., LASTRAPES, M., BERTALAN, M., KAPLAN, A., D'ANDREA, M. R., BIHUN, I., KANEB, A., DIETRICH, J., FERRY, J. A., MARTINEZ-LAGE, M., GIOBBIE-HURDER, A., BORGER, D. R., RODRIGUEZ, F. J., FROSCH, M. P., BATCHELOR, E., HOANG, K., KUTER, B., FORTIN, S., HOLDHOFF, M., CAHILL, D. P., CARTER, S., BRASTIANOS, P. K. & BATCHELOR, T. T. 2019. MYD88 L265P mutation and CDKN2A loss are early mutational events in primary central nervous system diffuse large B-cell lymphomas. *Blood Adv,* 3**,** 375-383.

NGO, V. N., YOUNG, R. M., SCHMITZ, R., JHAVAR, S., XIAO, W., LIM, K. H., KOHLHAMMER, H., XU, W., YANG, Y., ZHAO, H., SHAFFER, A. L., ROMESSER, P., WRIGHT, G., POWELL, J., ROSENWALD, A., MULLER-HERMELINK, H. K., OTT, G., GASCOYNE, R. D., CONNORS, J. M., RIMSZA, L. M., CAMPO, E., JAFFE, E. S., DELABIE, J., SMELAND, E. B., FISHER, R. I., BRAZIEL, R. M., TUBBS, R. R., COOK, J. R., WEISENBURGER, D. D., CHAN, W. C. &

STAUDT, L. M. 2011. Oncogenically active MYD88 mutations in human lymphoma. *Nature,* 470**,** 115-9.

OKAZAKI, T., CHIKUMA, S., IWAI, Y., FAGARASAN, S. & HONJO, T. 2013. A rheostat for immune responses: the unique properties of PD-1 and their advantages for clinical application. *Nat Immunol,* 14**,** 1212-8.

ONKOPEDIA 2018. Diffuses großzelliges B-Zell-Lymphom. URL: https://www.onkopedia.com/de/onkopedia/guidelines/diffuses-grosszelliges-b-zell-lymphom/@@guideline/html/index.html, last accessed: 09.05.2020.

OWEN, R. G., MCCARTHY, H., RULE, S., D'SA, S., THOMAS, S. K., TOURNILHAC, O., FORCONI, F., KERSTEN, M. J., ZINZANI, P. L., IYENGAR, S., KOTHARI, J., MINNEMA, M. C., KASTRITIS, E., AURRAN-SCHLEINITZ, T., CHESON, B. D., WALTER, H., GREENWALD, D., CHEN, D. Y., FRIGAULT, M. M., HAMDY, A., IZUMI, R., PATEL, P., WEI, H., LEE, S. K., MITTAG, D. & FURMAN, R. R. 2020. Acalabrutinib monotherapy in patients with Waldenstrom macroglobulinemia: a single-arm, multicentre, phase 2 study. *Lancet Haematol,* 7**,** e112-e121.

PATIDAR, A., SELVARAJ, S., SARODE, A., CHAUHAN, P., CHATTOPADHYAY, D. & SAHA, B. 2018. DAMP-TLR-cytokine axis dictates the fate of tumor. *Cytokine,* 104**,** 114-123.

PHELAN, J. D., YOUNG, R. M., WEBSTER, D. E., ROULLAND, S., WRIGHT, G. W., KASBEKAR, M., SHAFFER, A. L., 3RD, CERIBELLI, M., WANG, J. Q., SCHMITZ, R., NAKAGAWA, M., BACHY, E., HUANG, D. W., JI, Y., CHEN, L., YANG, Y., ZHAO, H., YU, X., XU, W., PALISOC, M. M., VALADEZ, R. R., DAVIES-HILL, T., WILSON, W. H., CHAN, W. C., JAFFE, E. S., GASCOYNE, R. D., CAMPO, E., ROSENWALD, A., OTT, G., DELABIE, J., RIMSZA, L. M., RODRIGUEZ, F. J., ESTEPHAN, F., HOLDHOFF, M., KRUHLAK, M. J., HEWITT, S. M., THOMAS, C. J., PITTALUGA, S., OELLERICH, T. & STAUDT, L. M. 2018. A multiprotein supercomplex controlling oncogenic signalling in lymphoma. *Nature,* 560**,** 387-391.

QUAGLIA, F. M., RIGOLIN, G. M., SACCENTI, E., NEGRINI, M., VOLTA, E., DABUSTI, M., CICCONE, M., URSO, A., LAUDISI, M. & CUNEO, A. 2019. Response to Ibrutinib of a Refractory IgA Lymphoplasmacytic Lymphoma Carrying the MYD88 L265P Gene Mutation. *Mediterr J Hematol Infect Dis,* 11**,** e2019057.

RAHEMI, S., NEMATOLLAHI-MAHANI, S. N., RAJAIE, A. & FALLAH, H. 2019. Inhibitor of Interleukin-1 Receptor-associated Kinases 1/4, Can Increase the Sensitivity of Breast Cancer Cells to Methotrexate. *Int J Mol Cell Med,* 8**,** 200-209.

RIVA, F., PONZONI, M., SUPINO, D., BERTILACCIO, M. T. S., POLENTARUTTI, N., MASSARA, M., PASQUALINI, F., CARRIERO, R., INNOCENZI, A., ANSELMO, A., VELIZ-RODRIGUEZ, T., SIMONETTI, G., ANDERS, H. J., CALIGARIS-CAPPIO, F., MANTOVANI, A., MUZIO, M. & GARLANDA, C. 2019. IL1R8 Deficiency Drives Autoimmunity-Associated Lymphoma Development. *Cancer Immunol Res,* 7**,** 874-885.

ROBERT KOCH INSTITUT 2017. Krebs in Deutschland für 2013/2014. Robert Koch-Institut.

ROH, J. S. & SOHN, D. H. 2018. Damage-Associated Molecular Patterns in Inflammatory Diseases. *Immune Netw,* 18**,** e27.

ROMMLER, F., HAMMEL, M., WALDHUBER, A., MULLER, T., JURK, M., UHLMANN, E., WAGNER, H., VOLLMER, J. & MIETHKE, T. 2015. Guanine-modified inhibitory oligonucleotides efficiently impair TLR7- and TLR9-mediated immune responses of human immune cells. *PLoS One,* 10**,** e0116703.

SAGIV-BARFI, I., KOHRT, H. E., CZERWINSKI, D. K., NG, P. P., CHANG, B. Y. & LEVY, R. 2015. Therapeutic antitumor immunity by checkpoint blockade is enhanced by ibrutinib, an inhibitor of both BTK and ITK. *Proc Natl Acad Sci U S A,* 112**,** E966-72.

SALLES, G., BARRETT, M., FOA, R., MAURER, J., O'BRIEN, S., VALENTE, N., WENGER, M. & MALONEY, D. G. 2017. Rituximab in B-Cell Hematologic Malignancies: A Review of 20 Years of Clinical Experience. *Adv Ther,* 34**,** 2232-2273.

SALVI, V., GIANELLO, V., BUSATTO, S., BERGESE, P., ANDREOLI, L., D'ORO, U., ZINGONI, A., TINCANI, A., SOZZANI, S. & BOSISIO, D. 2018. Exosome-delivered microRNAs promote IFN-alpha secretion by human plasmacytoid DCs via TLR7. *JCI Insight,* 3.

SCARNEO, S. A., HUGHES, P. F., YANG, K. W., CARLSON, D. A., GURBANI, D., WESTOVER, K. D. & HAYSTEAD, T. A. J. 2020. A highly selective inhibitor of interleukin-1 receptor-associated kinases 1/4 (IRAK-1/4) delineates the distinct signaling roles of IRAK-1/4 and the TAK1 kinase. *J Biol Chem,* 295**,** 1565-1574.

SCHMITZ, R., WRIGHT, G. W., HUANG, D. W., JOHNSON, C. A., PHELAN, J. D., WANG, J. Q., ROULLAND, S., KASBEKAR, M., YOUNG, R. M., SHAFFER, A. L., HODSON, D. J., XIAO, W., YU, X., YANG, Y., ZHAO, H., XU, W., LIU, X., ZHOU, B., DU, W., CHAN, W. C., JAFFE, E. S., GASCOYNE, R. D., CONNORS, J. M., CAMPO, E., LOPEZ-GUILLERMO, A., ROSENWALD, A., OTT, G., DELABIE, J., RIMSZA, L. M., TAY KUANG WEI, K., ZELENETZ, A. D., LEONARD, J. P., BARTLETT, N. L., TRAN, B., SHETTY, J., ZHAO, Y., SOPPET, D. R., PITTALUGA, S., WILSON, W. H. & STAUDT, L. M. 2018. Genetics and Pathogenesis of Diffuse Large B-Cell Lymphoma. *N Engl J Med,* 378**,** 1396-1407.

SEDA, V. & MRAZ, M. 2015. B-cell receptor signalling and its crosstalk with other pathways in normal and malignant cells. *Eur J Haematol,* 94**,** 193-205.

SEO, W. & TANIUCHI, I. 2016. Transcriptional regulation of early T-cell development in the thymus. *Eur J Immunol,* 46**,** 531-8.

SERIES, J., GARCIA, C., LEVADE, M., VIAUD, J., SIE, P., YSEBAERT, L. & PAYRASTRE, B. 2019. Differences and similarities in the effects of ibrutinib and acalabrutinib on platelet functions. *Haematologica,* 104**,** 2292-2299.

SEWASTIANIK, T., GUERRERA, M. L., ADLER, K., DENNIS, P. S., WRIGHT, K., SHANMUGAM, V., HUANG, Y., TANTON, H., JIANG, M., KOFIDES, A., DEMOS, M. G., DALGARNO, A., PATEL, N. A., NAG, A., PINKUS, G. S., YANG, G., HUNTER, Z. R., JAROLIM, P., MUNSHI, N. C., TREON, S. P. & CARRASCO, R. D. 2019. Human MYD88L265P is insufficient by itself to drive neoplastic transformation in mature mouse B cells. *Blood Adv,* 3**,** 3360-3374.

SHAFFER, A. L., 3RD, YOUNG, R. M. & STAUDT, L. M. 2012. Pathogenesis of human B cell lymphomas. *Annu Rev Immunol,* 30**,** 565-610.

SHANKLAND, K. R., ARMITAGE, J. O. & HANCOCK, B. W. 2012. Non-Hodgkin lymphoma. *Lancet,* 380**,** 848-57.

SHEA-DONOHUE, T. 2018. Gut Barrier: Adaptive Immunity. *In:* SAID, H. M. (ed.) *Physiology of the gastrointestinal tract.* Academic press.

SHULMAN, L. N., WAGNER, C. M., BARR, R., LOPES, G., LONGO, G., ROBERTSON, J., FORTE, G., TORODE, J. & MAGRINI, N. 2016. Proposing Essential Medicines to Treat Cancer: Methodologies, Processes, and Outcomes. *J Clin Oncol,* 34**,** 69-75.

SIEGEL, R., MA, J., ZOU, Z. & JEMAL, A. 2014. Cancer statistics, 2014. *CA Cancer J Clin,* 64**,** 9-29.

SMULSKI, C. R. & EIBEL, H. 2018. BAFF and BAFF-Receptor in B Cell Selection and Survival. *Front Immunol,* 9**,** 2285.

SPLICHAL, I., DONOVAN, S. M., JENISTOVA, V., SPLICHALOVA, I., SALMONOVA, H., VLKOVA, E., NEUZIL BUNESOVA, V., SINKORA, M., KILLER, J., SKRIVANOVA, E. & SPLICHALOVA, A. 2019. High Mobility Group Box 1 and TLR4 Signaling Pathway in Gnotobiotic Piglets

Colonized/Infected with L. amylovorus, L. mucosae, E. coli Nissle 1917 and S. Typhimurium. *Int J Mol Sci,* 20.

SRIVASTAVA, R., GENG, D., LIU, Y., ZHENG, L., LI, Z., JOSEPH, M. A., MCKENNA, C., BANSAL, N., OCHOA, A. & DAVILA, E. 2012. Augmentation of therapeutic responses in melanoma by inhibition of IRAK-1,-4. *Cancer Res,* 72**,** 6209-16.

STEWART, B. W., CANCER, I. A. F. R. O. & WELTGESUNDHEITSORGANISATION 2014. *World cancer report 2014,* Lyon, International Agency for Research in Cancer.

SUN, B. & ZHANG, Y. 2014. Overview of orchestration of CD4+ T cell subsets in immune responses. *Adv Exp Med Biol,* 841**,** 1-13.

SWERDLOW, S. H., CAMPO, E., PILERI, S. A., HARRIS, N. L., STEIN, H., SIEBERT, R., ADVANI, R., GHIELMINI, M., SALLES, G. A., ZELENETZ, A. D. & JAFFE, E. S. 2016. The 2016 revision of the World Health Organization classification of lymphoid neoplasms. *Blood,* 127**,** 2375-90.

TAKAHASHI, K., SUGI, Y., NAKANO, K., KOBAYAKAWA, T., NAKANISHI, Y., TSUDA, M., HOSONO, A. & KAMINOGAWA, S. 2020. Regulation of Gene Expression through Gut Microbiota-Dependent DNA Methylation in Colonic Epithelial Cells. *Immunohorizons,* 4**,** 178-190.

THUNEMANN, M., SCHORG, B. F., FEIL, S., LIN, Y., VOELKL, J., GOLLA, M., VACHAVIOLOS, A., KOHLHOFER, U., QUINTANILLA-MARTINEZ, L., OLBRICH, M., EHRLICHMANN, W., REISCHL, G., GRIESSINGER, C. M., LANGER, H. F., GAWAZ, M., LANG, F., SCHAFERS, M., KNEILLING, M., PICHLER, B. J. & FEIL, R. 2017. Cre/lox-assisted non-invasive in vivo tracking of specific cell populations by positron emission tomography. *Nat Commun,* 8**,** 444.

TILSTRA, J. S., JOHN, S., GORDON, R. A., LEIBLER, C., KASHGARIAN, M., BASTACKY, S., NICKERSON, K. M. & SHLOMCHIK, M. J. 2020. B cell-intrinsic TLR9 expression is protective in murine lupus. *J Clin Invest*.

TORIGOE, M., SAKATA, K., ISHII, A., IWATA, S., NAKAYAMADA, S. & TANAKA, Y. 2018. Hydroxychloroquine efficiently suppresses inflammatory responses of human class-switched memory B cells via Toll-like receptor 9 inhibition. *Clin Immunol,* 195**,** 1-7.

TRAN, M. T., TANAKA, J., HAMADA, M., SUGIYAMA, Y., SAKAGUCHI, S., NAKAMURA, M., TAKAHASHI, S. & MIWA, Y. 2014. In vivo image analysis using iRFP transgenic mice. *Exp Anim,* 63**,** 311-9.

VALLS, L., BADVE, C., AVRIL, S., HERRMANN, K., FAULHABER, P., O'DONNELL, J. & AVRIL, N. 2016. FDG-PET imaging in hematological malignancies. *Blood Rev,* 30**,** 317-31.

VERMAAT, J. S., SOMERS, S. F., DE WREEDE, L. C., KRAAN, W., DE GROEN, R. A. L., SCHRADER, A. M. R., KERVER, E. D., SCHEEPSTRA, C. G., BEERENSCHOT, H., DEENIK, W., WEGMAN, J., BROERS, R., DE BOER, J. D., NIJLAND, M., VAN WEZEL, T., VEELKEN, H., SPAARGAREN, M., CLEVEN, A. H., KERSTEN, M. J. & PALS, S. T. 2019. MYD88 mutations identify a molecular subgroup of diffuse large B-cell lymphoma with an unfavourable prognosis. *Haematologica*.

VON BERNUTH, H., PICARD, C., JIN, Z., PANKLA, R., XIAO, H., KU, C. L., CHRABIEH, M., MUSTAPHA, I. B., GHANDIL, P., CAMCIOGLU, Y., VASCONCELOS, J., SIRVENT, N., GUEDES, M., VITOR, A. B., HERRERO-MATA, M. J., AROSTEGUI, J. I., RODRIGO, C., ALSINA, L., RUIZ-ORTIZ, E., JUAN, M., FORTUNY, C., YAGUE, J., ANTON, J., PASCAL, M., CHANG, H. H., JANNIERE, L., ROSE, Y., GARTY, B. Z., CHAPEL, H., ISSEKUTZ, A., MARODI, L., RODRIGUEZ-GALLEGO, C., BANCHEREAU, J., ABEL, L., LI, X., CHAUSSABEL, D., PUEL, A. & CASANOVA, J. L. 2008. Pyogenic bacterial infections in humans with MyD88 deficiency. *Science,* 321**,** 691-6.

WANG, J. Q., BEUTLER, B., GOODNOW, C. C. & HORIKAWA, K. 2016. Inhibiting TLR9 and other UNC93B1-dependent TLRs paradoxically increases accumulation of MYD88L265P plasmablasts in vivo. *Blood,* 128**,** 1604-8.

WANG, X., TAN, Y., HUANG, Z., HUANG, N., GAO, M., ZHOU, F., HU, J. & FENG, W. 2019. Disrupting myddosome assembly in diffuse large Bcell lymphoma cells using the MYD88 dimerization inhibitor ST2825. *Oncol Rep*.

WANG, X., XU, X., CAI, W., BAO, H., HUANG, H., LIU, Y., YANG, X., RUAN, C., WU, D., SHEN, H. & CHEN, S. 2020. TBL1XR1 mutation predicts poor outcome in primary testicular diffuse large B-cell lymphoma patients. *Biomark Res,* 8**,** 10.

WEBER, A. N. R., BITTNER, Z., LIU, X., DANG, T. M., RADSAK, M. P. & BRUNNER, C. 2017. Bruton's Tyrosine Kinase: An Emerging Key Player in Innate Immunity. *Front Immunol,* 8**,** 1454.

WEBER, A. N. R., CARDONA GLORIA, Y., CINAR, O., REINHARDT, H. C., PEZZUTTO, A. & WOLZ, O. O. 2018. Oncogenic MYD88 mutations in lymphoma: novel insights and therapeutic possibilities. *Cancer Immunol Immunother*.

WIESE, M. D., MANNING-BENNETT, A. T. & ABUHELWA, A. Y. 2020. Investigational IRAK-4 inhibitors for the treatment of rheumatoid arthritis. *Expert Opin Investig Drugs,* 29**,** 475-482.

WILLARD-MACK, C. L. 2006. Normal structure, function, and histology of lymph nodes. *Toxicol Pathol,* 34**,** 409-24.

WU, Y. W., TANG, W. & ZUO, J. P. 2015. Toll-like receptors: potential targets for lupus treatment. *Acta Pharmacol Sin,* 36**,** 1395-407.

YANG, G., ZHOU, Y., LIU, X., XU, L., CAO, Y., MANNING, R. J., PATTERSON, C. J., BUHRLAGE, S. J., GRAY, N., TAI, Y. T., ANDERSON, K. C., HUNTER, Z. R. & TREON, S. P. 2013. A mutation in MYD88 (L265P) supports the survival of lymphoplasmacytic cells by activation of Bruton tyrosine kinase in Waldenstrom macroglobulinemia. *Blood,* 122**,** 1222-32.

YOUNG, R. M., PHELAN, J. D., WILSON, W. H. & STAUDT, L. M. 2019. Pathogenic B-cell receptor signaling in lymphoid malignancies: New insights to improve treatment. *Immunol Rev,* 291**,** 190-213.

YUSUF, I. H., SHARMA, S., LUQMANI, R. & DOWNES, S. M. 2017. Hydroxychloroquine retinopathy. *Eye (Lond),* 31**,** 828-845.

ZETTLITZ, K. A., TAVARE, R., TSAI, W. K., YAMADA, R. E., HA, N. S., COLLINS, J., VAN DAM, R. M., TIMMERMAN, J. M. & WU, A. M. 2019. (18)F-labeled anti-human CD20 cys-diabody for same-day immunoPET in a model of aggressive B cell lymphoma in human CD20 transgenic mice. *Eur J Nucl Med Mol Imaging,* 46**,** 489-500.

ZHANG, J. Z., LIU, Z., LIU, J., REN, J. X. & SUN, T. S. 2014. Mitochondrial DNA induces inflammation and increases TLR9/NF-kappaB expression in lung tissue. *Int J Mol Med,* 33**,** 817-24.

ZHANG, Y., LI, J., ZHANG, Y. M., ZHANG, X. M. & TAO, J. 2015. Effect of TACI signaling on humoral immunity and autoimmune diseases. *J Immunol Res,* 2015**,** 247426.

ZHAO, X., ZHANG, Z., MOREIRA, D., SU, Y. L., WON, H., ADAMUS, T., DONG, Z., LIANG, Y., YIN, H. H., SWIDERSKI, P., PILLAI, R. K., KWAK, L., FORMAN, S. & KORTYLEWSKI, M. 2018. B Cell Lymphoma Immunotherapy Using TLR9-Targeted Oligonucleotide STAT3 Inhibitors. *Mol Ther,* 26**,** 695-707.

ZHENG, C., CHEN, J., CHU, F., ZHU, J. & JIN, T. 2019. Inflammatory Role of TLR-MyD88 Signaling in Multiple Sclerosis. *Front Mol Neurosci,* 12**,** 314.

ZHOU, S., WANG, G. & ZHANG, W. 2018. Effect of TLR4/MyD88 signaling pathway on sepsis-associated acute respiratory distress syndrome in rats, via regulation of macrophage activation and inflammatory response. *Exp Ther Med,* 15**,** 3376-3384.

ZHU, G., CHENG, Z., HUANG, Y., ZHENG, W., YANG, S., LIN, C. & YE, J. 2020. MyD88 mediates colorectal cancer cell proliferation, migration and invasion via NFkappaB/AP1 signaling pathway. *Int J Mol Med,* 45**,** 131-140.

ZHU, J., YAMANE, H. & PAUL, W. E. 2010. Differentiation of effector CD4 T cell populations (*). *Annu Rev Immunol,* 28**,** 445-89.

ZOROFCHIAN, S., LU, G., ZHU, J. J., DUOSE, D. Y., WINDHAM, J., ESQUENAZI, Y. & BALLESTER, L. Y. 2018. Detection of the MYD88 p.L265P Mutation in the CSF of a Patient With Secondary Central Nervous System Lymphoma. *Front Oncol,* 8**,** 382.

# Appendix

Table 26 **2016 WHO classification of mature B-cell lymphoma.** Adapted from Swerdlow et al., 2016. Entities marked with a star (*) were changed in comparison to the 2008 WHO classification. Provisional entities are listed in italics. Superscript numbers stand for DLBCL subtypes (1), large B-cell lymphoma subtypes (2) and borderline cases (3) (as described in Li et al., 2018b). Irf4 = Interferon regulatory factor 4, DLBCL = diffuse large B-cell lymphoma, NOS = not otherwise specified, EBV = Epstein-Barr virus, ALK = anaplastic lymphoma kinase, HHV8 = human herpesvirus 8, MYC = myelocytoma (a cancer of myelocytes, a type of bone marrow cell), BCL2 = B-cell lymphoma 2, BCL6 = B-cell lymphoma 6.

| | |
|---|---|
| **1** | Chronic lymphocytic leukaemia/small lymphocytic lymphoma |
| **2** | Monoclonal B-cell lymphocytosis* |
| **3** | B-cell prolymphocytic leukaemia |
| **4** | Splenic marginal zone lymphoma |
| **5** | Hairy cell leukaemia |
| ***6*** | *Splenic B-cell lymphoma/leukaemia, unclassifiable*<br>• *Splenic diffuse red pulp small B-cell lymphoma*<br>• *Hairy cell leukaemia-variant* |
| **7** | Lymphoplasmacytic lymphoma<br>• Waldenström macroglobulinemia |
| **8** | Monoclonal gammopathy of undetermined significance (MGUS), IgM* |
| **9** | µ heavy-chain disease |
| **10** | γ heavy-chain disease |
| **11** | α heavy-chain disease |
| **12** | Monoclonal gammopathy of undetermined significance (MGUS), IgG/A* |
| **13** | Plasma cell myeloma |
| **14** | Solitary plasmacytoma of bone |
| **15** | Extraosseous plasmacytoma |
| **16** | Monoclonal immunoglobulin deposition diseases* |
| **17** | Extranodal marginal zone lymphoma of mucosa-associated lymphoid tissue (MALT lymphoma) |
| **18** | Nodal marginal zone lymphoma<br>• *Paediatric nodal marginal zone lymphoma* |
| **19** | Follicular lymphoma<br>• In situ follicular neoplasia*<br>• Duodenal-type follicular lymphoma* |
| **20** | Paediatric-type follicular lymphoma* |
| ***21*** | *Large B-cell lymphoma with IRF4 rearrangement** |
| **22** | Primary cutaneous follicle center lymphoma |
| **23** | Mantle cell lymphoma<br>• In situ mantle cell neoplasia* |
| **$24^{1}$** | Diffuse large B-cell lymphoma (DLBCL), NOS<br>• Germinal center B-cell type* (GCB subtype)<br>• Activated B-cell type* (ABC subtype) |
| **$25^{1}$** | T-cell/histiocyte-rich large B-cell lymphoma |
| **$26^{1}$** | Primary DLBCL of the central nervous system (CNS) |
| **$27^{1}$** | Primary cutaneous DLBCL, leg type |
| **$28^{1}$** | EBV$^{+}$ DLBCL, NOS* |
| ***29*** | *EBV$^{+}$ mucocutaneous ulcer** |
| **$30^{2}$** | DLBCL associated with chronic inflammation |
| **$31^{2}$** | Lymphomatoid granulomatosis |
| **$32^{2}$** | Primary mediastinal (thymic) large B-cell lymphoma |

| | |
|---|---|
| **33**[2] | Intravascular large B-cell lymphoma |
| **34**[2] | ALK$^+$ large B-cell lymphoma |
| **35**[2] | Plasmablastic lymphoma |
| **36**[2] | Primary effusion lymphoma |
| ***37***[2] | *HHV8$^+$ DLBCL, NOS** |
| **38** | Burkitt lymphoma |
| ***39*** | *Burkitt-like lymphoma with 11q aberration** |
| **40**[3] | High-grade B-cell lymphoma, with *MYC* and *BCL2* and/or *BCL6* rearrangements* |
| **41**[3] | High-grade B-cell lymphoma, NOS* |
| **42**[3] | B-cell lymphoma, unclassifiable, with features intermediate between DLBCL and classical Hodgkin lymphoma |

Table 27 **Incidence and mortality of NHL in the US in 2014.** Adapted from Siegel et al., 2014. Subtypes as described in Table 2 are given in brackets. Numbers of B-cell lymphoma were estimated according to an approximation of the percentage of B-cell lymphoma among all lymphoma cases (American Cancer Society, 2018).

| | **Estimated new cases, 2014** | | | | | | **Estimated deaths, 2014** | | | | | |
|---|---|---|---|---|---|---|---|---|---|---|---|---|
| **Subtype** | **both sexes** | **% of total cases** | **male** | **%** | **female** | **%** | **both sexes** | **% of total cases** | **male** | **%** | **female** | **%** |
| Chronic lymphocytic leukaemia [1] | 15.720 | 14% | 9,100 | 58% | 6,620 | 42% | 4,600 | 14% | 2,800 | 61% | 1,800 | 39% |
| Other leukaemia (not ALL, CLL, AML or CML) [3, 5, 6] | 5,800 | 5% | 3,200 | 55% | 2,600 | 45% | 6,780 | 5% | 3,870 | 57% | 2,910 | 43% |
| Myeloma [13] | 24,050 | 21% | 13,500 | 56% | 10,550 | 44% | 11,090 | 21% | 6,110 | 55% | 4,980 | 45% |
| Other Non-Hodgkin lymphoma | 70,800 | 61% | 38,270 | 54% | 32,530 | 46% | 18,990 | 61% | 10,470 | 55% | 8,520 | 45% |
| **Total cases** | **116,370** | | **64,070** | | **52,300** | | **41,460** | | **23,250** | | **18,210** | |
| **Approximate of B-cell lymphoma (*0.85)** | **98,915** | | **54,460** | | **44,455** | | **35,241** | | **19,763** | | **15,479** | |

Table 28 **Incidence and mortality of NHL in Germany in 2014.** Adapted from Robert-Koch-Institute, 2017. Subtypes as described in Table 2 are given in brackets. The Robert-Koch Institute (RKI) includes all leukaemic entities in one category, but gives a percentage of CLL cases, thus CLL cases were calculated as an approximate. Numbers of B-cell lymphoma were estimated according to an approximation of the percentage of B-cell lymphoma among all lymphoma cases (American Cancer Society, 2018).

| | **Estimated new cases, 2014** | | | | | | **Estimated deaths, 2014** | | | | | |
|---|---|---|---|---|---|---|---|---|---|---|---|---|
| **Subtype** | **both sexes** | **% of total cases** | **male** | **%** | **female** | **%** | **both sexes** | **% of total cases** | **male** | **%** | **female** | **%** |
| Chronic lymphocytic leukaemia [1] (approximate: all leukaemia forms * 0,4) | 5.480 | 19% | 3.056 | 56% | 2.424 | 44% | 3.097 | 23% | 1.667 | 54% | 1.430 | 46% |
| Myeloma [13] | 6.510 | 22% | 3.550 | 55% | 2.960 | 45% | 3.981 | 29% | 2.071 | 52% | 1.910 | 48% |
| Other Non-Hodgkin lymphoma | 17.040 | 59% | 9.160 | 54% | 7.880 | 46% | 6.509 | 48% | 3.560 | 55% | 2.949 | 45% |
| **Total cases** | **29.030** | | **15.766** | | **13.264** | | **13.587** | | **7.298** | | **6.289** | |
| **Approximate of B-cell lymphoma (*0.85)** | **24.676** | | **98.915** | | **98.915** | | **98.915** | | **98.915** | | **98.915** | |

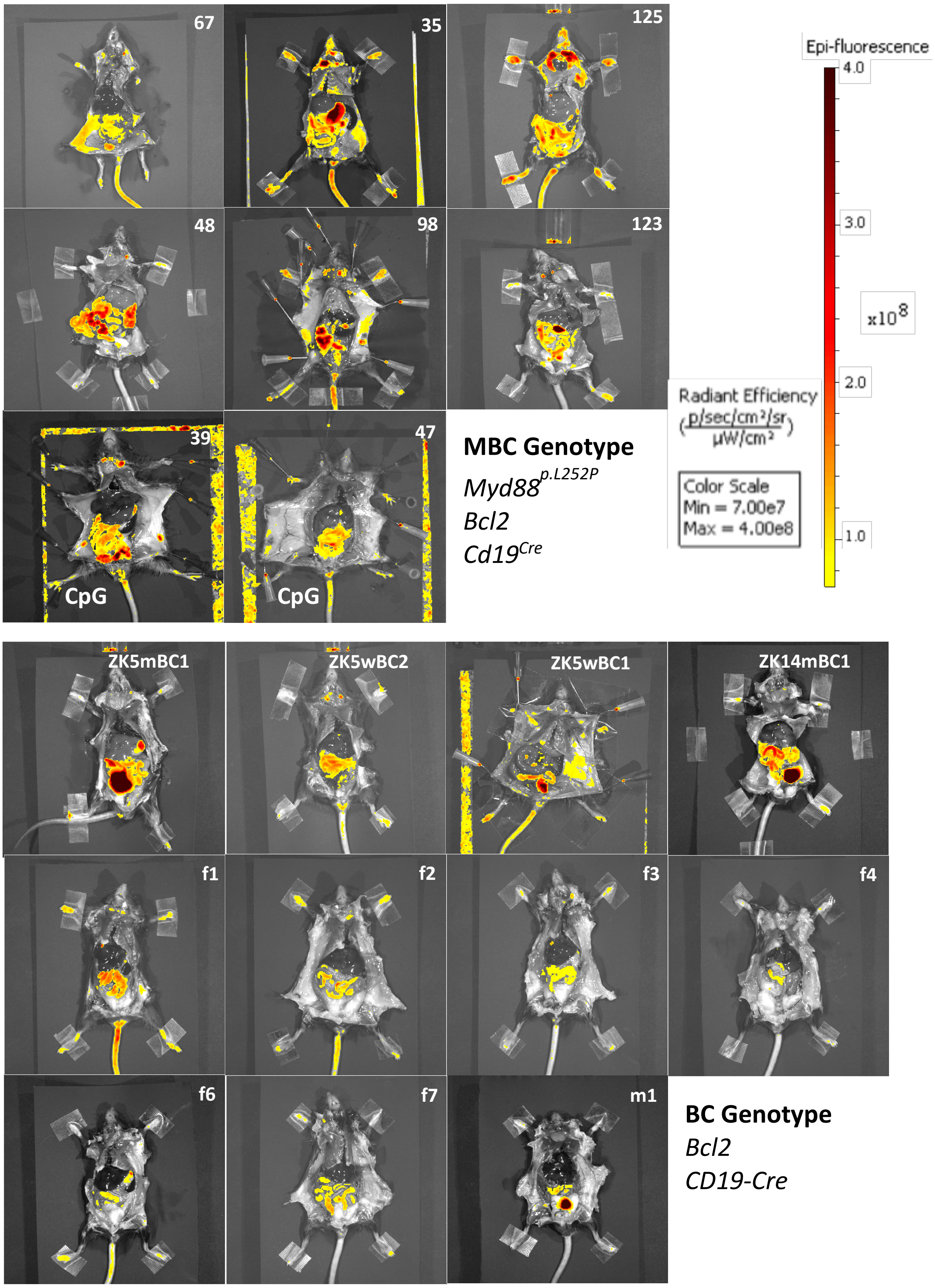

Figure 50 **MBC mice show B-cell accumulation in secondary lymphoid organs and abdominal tract**. B-cell distribution in MBC mice vs BC mice shown as visual data of whole-body scans. Colour scale on left side shows average radiant efficiency, a standardised measure for epifluorescence, ranging from 7.00 e$^{7}$ to 4.00 e$^{8}$ $\frac{p\,s^{-1}\,cm^{-2}\,sr^{-1}}{\mu W\,cm^{-2}}$. Mouse 39 and 47 were stimulated with CpG and excluded from further analysis of B-cell distribution but shown as an example for CpG stimulated MBC mice used in later experiments (see 3.3.). Mouse 67 showed degraded organs at imaging time point and was excluded from further analysis. In 4 BC mice (ZK5mBC1, ZK5wBC1, ZK14mBC1 and m1) an intense signal was caused by the bladder, probably due

to fluorescent agents in the urine, which does not represent a true abdominal signal. These mice were excluded from further analysis of abdominal signal.

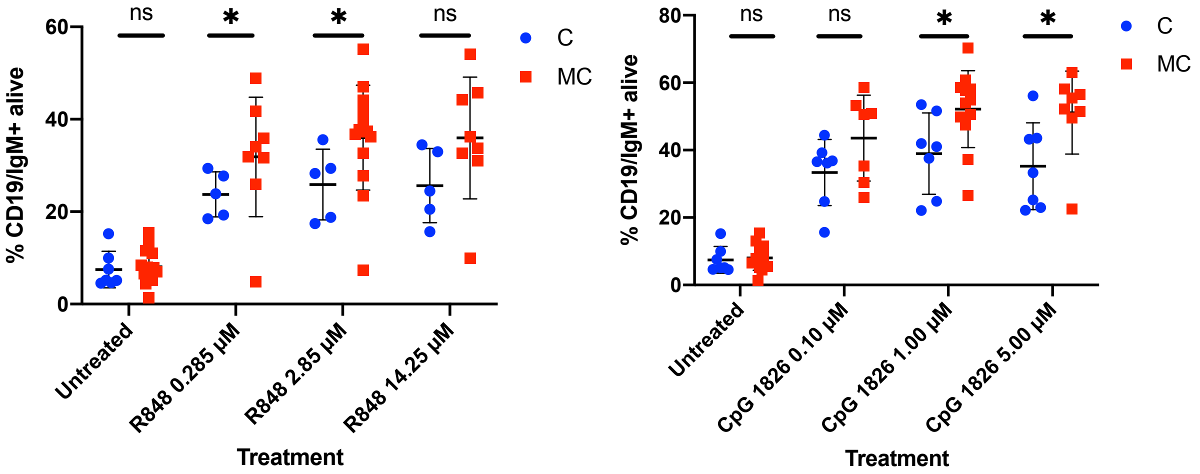

Figure 51 **Survival of B-cells upon *in vitro* TLR stimulation is higher in MC mice than in C mice.** Cells were isolated from spleens and stimulated for 3 days. Each dot represents one animal. Statistical analysis was performed using Mann-Whitney tests, see Table 5. * = $p < 0.05$, ** = $p < 0.01$, *** = $p < 0.001$, **** = $p < 0.0001$, ns = not significant.

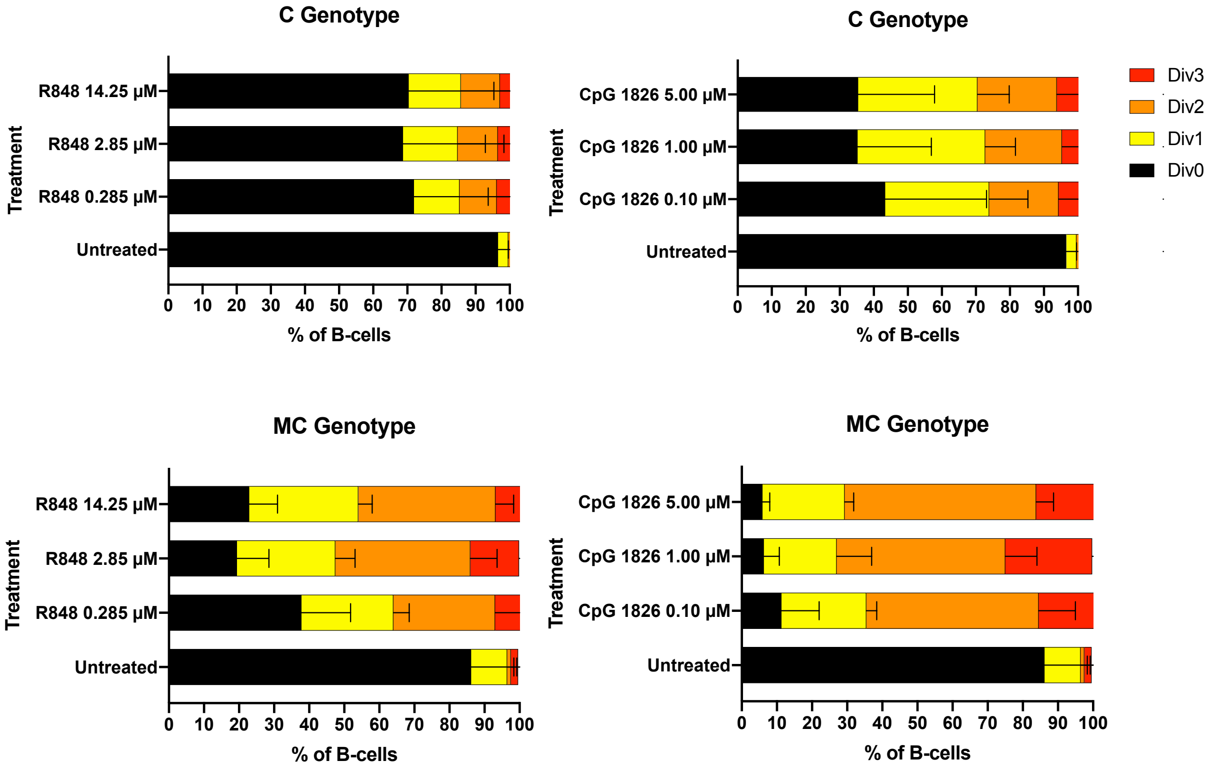

Figure 52 **Proliferation of B-cells upon *in vitro* TLR stimulation is higher in *Myd88*$^{p.L252P}$-mutated mice.** Cells were isolated from spleens of MC and C mice and stimulated *in vitro* for 3 days with CpG and R848 at various concentrations. Using the proliferation dye Tag-it Violet$^{\text{TM}}$ that dilutes itself following B-cell division, the number of B-cell divisions was calculated. Stimulated B-cells from MC mice, as identified via CD19$^+$IgM$^+$ positivity, show higher proliferation than B-cells from C mice. Div0 = no mitosis, Div1 = 1 mitosis, Div2 = 2 mitoses, Div3 = 3 mitoses. For statistics see Table 7 and Table 29.

Table 29 **Proliferation of B-cells upon *in vitro* TLR stimulation is higher in *Myd88*$^{p.L252P}$-mutated mice**. Div0 = no mitosis, Div1 = 1 mitosis, Div2 = 2 mitoses, Div3 = 3 mitoses, SD = standard deviation, N = sample size.

| | **MC** | | | | | | | | | | | |
|---|---|---|---|---|---|---|---|---|---|---|---|---|
| | **Div0** | | | **Div1** | | | **Div2** | | | **Div3** | | |
| | Mean | SD | N | Mean | SD | N | Mean | SD | N | Mean | SD | N |
| **Untreated** | 86.20 | 12.14 | 12 | 10.28 | 7.76 | 12 | 1.07 | 1.65 | 12 | 2.06 | 4.46 | 12 |
| **R848 0.285 µM** | 37.80 | 14.03 | 6 | 26.20 | 4.54 | 6 | 29.02 | 7.77 | 6 | 7.31 | 3.00 | 6 |
| **R848 2.85 µM** | 19.43 | 9.09 | 12 | 28.03 | 5.64 | 12 | 38.51 | 7.60 | 12 | 13.89 | 6.69 | 12 |
| **R848 14.25 µM** | 22.90 | 8.09 | 6 | 31.13 | 3.95 | 6 | 39.10 | 5.15 | 6 | 7.26 | 2.07 | 6 |
| **CpG 1826 0.10 µM** | 11.31 | 10.73 | 6 | 24.17 | 2.95 | 6 | 49.03 | 10.47 | 6 | 15.67 | 4.84 | 6 |
| **CpG 1826 1.00 µM** | 6.31 | 4.36 | 11 | 20.71 | 9.93 | 11 | 48.03 | 8.97 | 11 | 24.71 | 13.11 | 11 |
| **CpG 1826 5.00 µM** | 5.93 | 2.03 | 6 | 23.37 | 2.59 | 6 | 54.52 | 4.96 | 6 | 16.30 | 4.43 | 6 |

| | **C** | | | | | | | | | | | |
|---|---|---|---|---|---|---|---|---|---|---|---|---|
| | **Div0** | | | **Div1** | | | **Div2** | | | **Div3** | | |
| | Mean | SD | N | Mean | SD | N | Mean | SD | N | Mean | SD | N |
| **Untreated** | 96.58 | 3.02 | 5 | 3.02 | 2.34 | 5 | 0.54 | 0.91 | 5 | 0.14 | 0.19 | 5 |
| **R848 0.285 µM** | 71.90 | 29.74 | 3 | 13.39 | 8.38 | 3 | 10.91 | 15.61 | 3 | 4.21 | 6.84 | 3 |
| **R848 2.85 µM** | 68.73 | 29.59 | 3 | 15.99 | 8.16 | 3 | 11.82 | 16.81 | 3 | 3.87 | 6.35 | 3 |
| **R848 14.25 µM** | 70.40 | 31.82 | 3 | 15.30 | 9.65 | 3 | 11.43 | 17.56 | 3 | 3.32 | 5.44 | 3 |
| **CpG 1826 0.10 µM** | 43.36 | 29.77 | 5 | 30.58 | 11.39 | 5 | 20.34 | 17.38 | 5 | 5.87 | 8.59 | 5 |
| **CpG 1826 1.00 µM** | 35.26 | 21.66 | 5 | 37.48 | 8.91 | 5 | 22.54 | 14.98 | 5 | 4.90 | 6.15 | 5 |
| **CpG 1826 5.00 µM** | 35.44 | 22.40 | 5 | 35.02 | 9.37 | 5 | 23.36 | 15.19 | 5 | 6.40 | 7.48 | 5 |

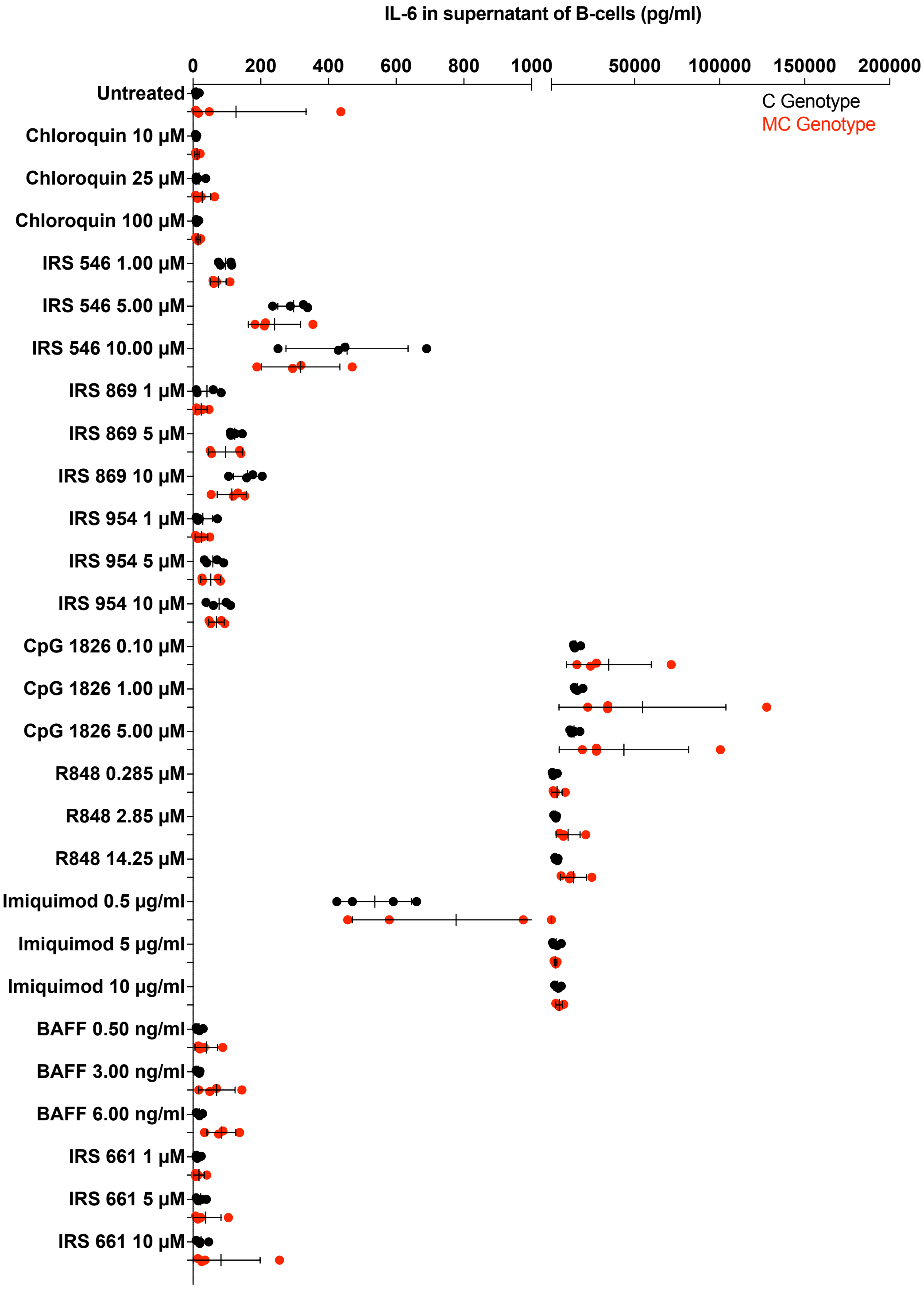

Figure 53 **MC mice show higher IL-6 levels in supernatant of B-cells than C mice following treatment with CpG, R848 or BAFF.** B-cells were treated for 5 days with the various TLR agonists and potential antagonists indicated. IL-6 levels were higher in MC mice following treatment with CpG 1826 1.00 µM ($p = 0.0286$), CpG 1826 5.00 µM ($p = 0.0286$), R848 2.85 µM ($p = 0.0286$), R848 14.25 µM ($p = 0.0286$) and BAFF 6.00 mg/ml ($p = 0.0286$). Supernatant of B-cells from MC mice did not show more variance in IL-6 levels than supernatant of B-cells from C mice when comparing standard deviations ($p = 0.0681$ (df = 54), n = 28, MC: mean = 4788 pg/ml, SD = 121100 pg/ml; C: mean = 516 pg/ml, SD = 855 pg/ml). Shown are the individual values, mean and standard deviation. For detailed statistics see Table 30.

Table 30 **MC mice show higher IL-6 levels in supernatant of B-cells than C mice following treatment with CpG, R848 or BAFF.** B-cells were treated for 5 days with the various TLR agonists and potential antagonists indicated. IL-6 levels were higher in MC mice following treatment with CpG 1826 1.00 µM (p = 0.0286), CpG 1826 5.00 µM (p = 0.0286), R848 2.85 µM (p = 0.0286), R848 14.25 µM (p = 0.0286) and BAFF 6.00 mg/ml (p = 0.0286). Supernatant of B-cells from MC mice did not show more variance in IL-6 levels than supernatant of B-cells from C mice when comparing standard deviations (p = 0.0681 (df = 54), n = 28, MC: mean = 4788 pg/ml, SD = 121100 pg/ml; C: mean = 516 pg/ml, SD = 855 pg/ml). Statistically significant results are marked. Statistical analysis was performed using Mann-Whitney tests, p-value refers to difference between MC and C. SD = standard deviation, N = sample size, U = Mann-Whitney U.

| | MC | | | C | | | | |
|---|---|---|---|---|---|---|---|---|
| | Mean (pg/ml) | SD (pg/ml) | N | Mean (pg/ml) | SD (pg/ml) | N | P-value | U |
| **Untreated** | 127.00 | 207.09 | 4 | 11.10 | 4.87 | 4 | 0.3714 | 5 |
| **Chloroquine 10 µM** | 11.80 | 6.24 | 4 | 9.30 | 1.38 | 4 | 0.9714 | 8 |
| **Chloroquine 25 µM** | 27.24 | 25.39 | 4 | 17.61 | 13.87 | 4 | 0.8857 | 7 |
| **Chloroquine 100 µM** | 14.74 | 6.14 | 4 | 11.61 | 3.74 | 4 | 0.6857 | 6 |
| **IRS 546 1.00 µM** | 74.92 | 23.05 | 4 | 95.39 | 20.30 | 4 | 0.1143 | 2 |
| **IRS 546 5.00 µM** | 240.61 | 77.02 | 4 | 296.75 | 46.44 | 4 | 0.3429 | 4 |
| **IRS 546 10.00 µM** | 317.96 | 116.04 | 4 | 454.99 | 180.37 | 4 | 0.4857 | 5 |
| **IRS 869 1 µM** | 24.58 | 17.47 | 4 | 41.14 | 36.56 | 4 | 0.6857 | 6 |
| **IRS 869 5 µM** | 96.07 | 50.41 | 4 | 123.29 | 16.43 | 4 | 0.6857 | 6 |
| **IRS 869 10 µM** | 114.48 | 42.77 | 4 | 161.07 | 41.83 | 4 | 0.2000 | 3 |
| **IRS 954 1 µM** | 25.07 | 18.45 | 4 | 28.66 | 29.24 | 4 | 0.8857 | 7 |
| **IRS 954 5 µM** | 52.37 | 29.43 | 4 | 58.73 | 26.68 | 4 | 0.6857 | 6 |
| **IRS 954 10 µM** | 69.43 | 23.05 | 4 | 77.04 | 33.35 | 4 | 0.6857 | 6 |
| **CpG 1826 0.10 µM** | 34811.73 | 24967.66 | 4 | 15386.89 | 1975.84 | 4 | 0.0571 | 1 |
| **CpG 1826 1.00 µM** | 54611.84 | 49061.07 | 4 | 16381.72 | 2265.30 | 4 | ***0.0286*** | 0 |
| **CpG 1826 5.00 µM** | 43702.96 | 38043.01 | 4 | 14318.96 | 2593.12 | 4 | ***0.0286*** | 0 |
| **R848 0.285 µM** | 4411.08 | 3243.10 | 4 | 2530.21 | 1347.77 | 4 | 0.3429 | 4 |
| **R848 2.85 µM** | 10888.87 | 7034.26 | 4 | 3380.34 | 746.39 | 4 | ***0.0286*** | 0 |
| **R848 14.25 µM** | 13969.17 | 7686.38 | 4 | 4019.41 | 910.85 | 4 | ***0.0286*** | 0 |
| **Imiquimod 0.5 µg/ml** | 776.88 | 306.72 | 4 | 536.95 | 108.20 | 4 | 0.4857 | 5 |
| **Imiquimod 5 µg/ml** | 3503.67 | 768.16 | 4 | 3817.14 | 2323.96 | 4 | >0.9999 | 8 |
| **Imiquimod 10 µg/ml** | 5655.69 | 1996.20 | 4 | 4784.39 | 1674.47 | 4 | 0.6857 | 6 |
| **BAFF 0.50 ng/ml** | 39.32 | 33.27 | 4 | 17.65 | 9.40 | 4 | 0.2000 | 3 |
| **BAFF 3.00 ng/ml** | 70.07 | 53.92 | 4 | 15.66 | 5.00 | 4 | 0.1143 | 2 |
| **BAFF 6.00 ng/ml** | 83.84 | 42.72 | 4 | 18.09 | 7.90 | 4 | ***0.0286*** | 0 |
| **IRS 661 1 µM** | 17.72 | 15.57 | 4 | 13.88 | 7.24 | 4 | 0.8857 | 7 |
| **IRS 661 5 µM** | 37.29 | 45.19 | 4 | 22.45 | 13.41 | 4 | 0.8857 | 7 |
| **IRS 661 10 µM** | 82.78 | 115.42 | 4 | 23.83 | 15.70 | 4 | 0.4857 | 5 |

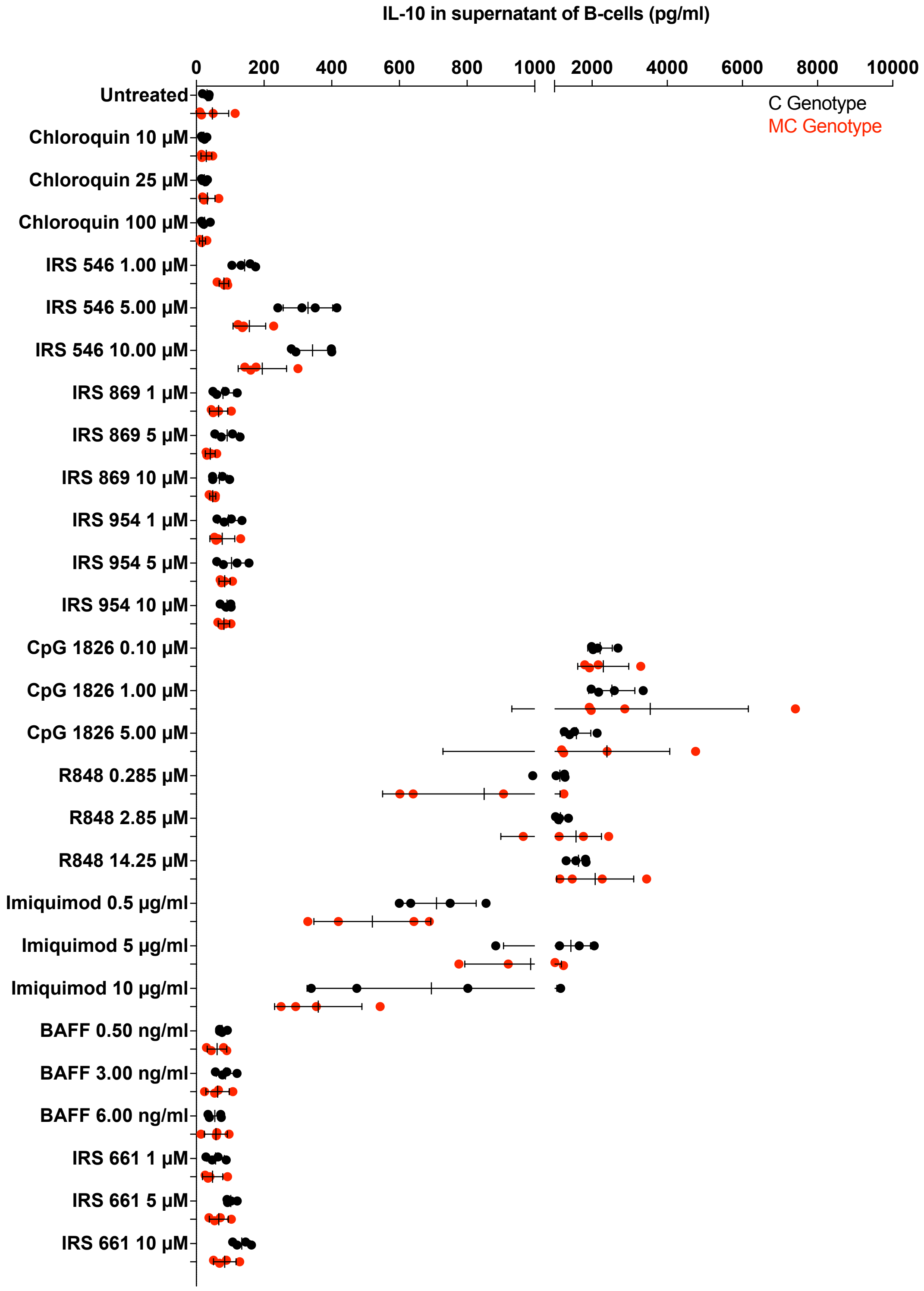

Figure 54 **MC mice show lower IL-10 levels in supernatant of B-cells than C mice following treatment with IRS 546.** B-cells were treated for 5 days with the various TLR agonists and potential antagonists indicated. IL-10 levels were higher in MC mice following treatment with IRS 546 1.00 µM (p = 0.0286) and IRS 546 5.00 µM (p = 0.0286). Supernatant of B-cells from MC mice did not show more variance in IL-10 levels than supernatant of B-cells from C mice when comparing standard deviations (p = 0.1634 (df = 54), n = 28, MC: mean = 285 pg/ml, SD = 593 pg/ml; C: mean = 121 pg/ml, SD = 169 pg/ml). Shown are the individual values, mean and standard deviation. For detailed statistics see Table 31.

Table 31 **MC mice show lower IL-10 levels in supernatant of B-cells than C mice following treatment with IRS 546.** B-cells were treated for 5 days with the various TLR agonists and potential antagonists indicated. IL-10 levels were higher in MC mice following treatment with IRS 546 1.00 µM (p = 0.0286) and IRS 546 5.00 µM (p = 0.0286). Supernatant of B-cells from MC mice did not show more variance in IL-10 levels than supernatant of B-cells from C mice when comparing standard deviations (p = 0.1634 (df = 54), n = 28, MC: mean = 285 pg/ml, SD = 593 pg/ml; C: mean = 121 pg/ml, SD = 169 pg/ml). Statistically significant results are marked. Statistical analysis was performed using Mann-Whitney tests, p-value refers to difference between MC and C. SD = standard deviation, N = sample size, U = Mann-Whitney U.

| | MC | | | C | | | | |
|---|---|---|---|---|---|---|---|---|
| | Mean | SD | N | Mean | SD | N | P-value | U |
| **Untreated** | 47.57 | 47.94 | 4 | 31.79 | 9.14 | 4 | >0,9999 | 0 |
| **Chloroquine 10 µM** | 29.72 | 16.23 | 4 | 22.34 | 6.93 | 4 | 0.7714 | 7 |
| **Chloroquine 25 µM** | 32.87 | 22.46 | 4 | 23.57 | 8.02 | 4 | 0.6857 | 6 |
| **Chloroquine 100 µM** | 18.22 | 8.99 | 4 | 24.41 | 11.66 | 4 | 0.3143 | 4 |
| **IRS 546 1.00 µM** | 81.69 | 14.18 | 4 | 142.95 | 30.98 | 4 | ***0.0286*** | 0 |
| **IRS 546 5.00 µM** | 156.84 | 48.17 | 4 | 329.79 | 73.05 | 4 | ***0.0286*** | 0 |
| **IRS 546 10.00 µM** | 195.15 | 71.33 | 4 | 343.47 | 65.21 | 4 | 0.1143 | 2 |
| **IRS 869 1 µM** | 65.87 | 26.85 | 4 | 78.96 | 31.87 | 4 | 0.6857 | 6 |
| **IRS 869 5 µM** | 41.16 | 14.37 | 4 | 91.11 | 33.29 | 4 | 0.0571 | 1 |
| **IRS 869 10 µM** | 48.58 | 8.95 | 4 | 67.95 | 24.43 | 4 | 0.3429 | 4 |
| **IRS 954 1 µM** | 76.68 | 36.64 | 4 | 95.22 | 31.54 | 4 | 0.3429 | 4 |
| **IRS 954 5 µM** | 83.57 | 16.30 | 4 | 104.06 | 42.42 | 4 | 0.6857 | 6 |
| **IRS 954 10 µM** | 81.66 | 16.66 | 4 | 90.71 | 15.20 | 4 | 0.4857 | 5 |
| **CpG 1826 0.10 µM** | 2299.16 | 679.01 | 4 | 2213.45 | 324.60 | 4 | 0.8857 | 7 |
| **CpG 1826 1.00 µM** | 3546.75 | 2614.25 | 4 | 2526.59 | 613.66 | 4 | >0,9999 | 8 |
| **CpG 1826 5.00 µM** | 2398.08 | 1668.99 | 4 | 1582.83 | 384.32 | 4 | >0,9999 | 8 |
| **R848 0.285 µM** | 850.48 | 300.25 | 4 | 1145.97 | 147.36 | 4 | 0.1143 | 2 |
| **R848 2.85 µM** | 1575.13 | 675.10 | 4 | 1159.93 | 147.41 | 4 | 0.6857 | 6 |
| **R848 14.25 µM** | 2083.41 | 1026.78 | 4 | 1637.83 | 251.33 | 4 | 0.8857 | 7 |
| **Imiquimod 0.5 µg/ml** | 520.16 | 172.91 | 4 | 709.88 | 116.93 | 4 | 0.3429 | 4 |
| **Imiquimod 5 µg/ml** | 987.77 | 194.26 | 4 | 1434.81 | 527.22 | 4 | 0.3429 | 4 |
| **Imiquimod 10 µg/ml** | 360.49 | 129.04 | 4 | 694.66 | 367.25 | 4 | 0.2000 | 3 |
| **BAFF 0.50 ng/ml** | 61.25 | 28.76 | 4 | 76.21 | 10.75 | 4 | 0.6857 | 6 |
| **BAFF 3.00 ng/ml** | 62.96 | 34.62 | 4 | 86.05 | 26.78 | 4 | 0.3429 | 4 |
| **BAFF 6.00 ng/ml** | 57.79 | 34.05 | 4 | 54.74 | 21.02 | 4 | >0,9999 | 8 |
| **IRS 661 1 µM** | 48.20 | 29.97 | 4 | 56.94 | 25.52 | 4 | 0.6857 | 6 |
| **IRS 661 5 µM** | 66.36 | 28.19 | 4 | 101.65 | 13.90 | 4 | 0.2000 | 3 |
| **IRS 661 10 µM** | 84.07 | 33.19 | 4 | 134.05 | 25.06 | 4 | 0.1143 | 2 |

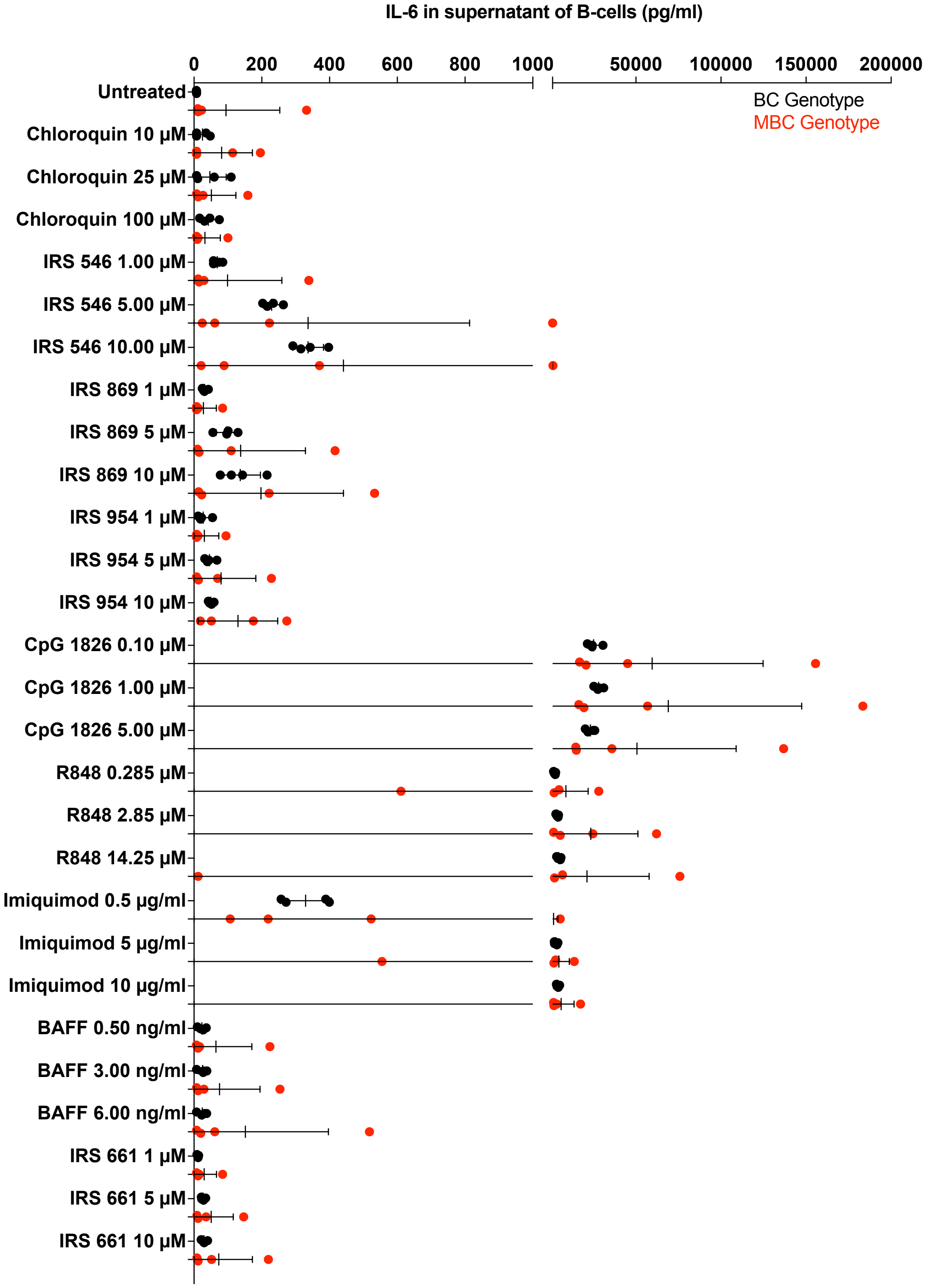

Figure 55 **IL-6 levels in supernatant of B-cells do not differ between MBC and BC mice, but MBC mice show a higher variance.** B-cells were treated for 5 days with the various TLR agonists and potential antagonists indicated. Supernatant of B-cells from MBC mice showed more variance in IL-6 levels than supernatant of B-cells from BC mice, when comparing standard deviations (p = 0.0175 (df = 54), n = 28, MBC: mean = 10661 pg/ml, SD = 21939 pg/ml; BC: mean = 490 pg/ml, SD = 960 pg/ml). Shown are the individual values, mean and standard deviation. For detailed statistics see Table 32.

Table 32 **IL-6 levels in supernatant of B-cells do not differ between MBC and BC mice, but MBC mice show a higher variance.** B-cells were treated for 5 days with the various TLR agonists and potential antagonists indicated. Supernatant of B-cells from MBC mice showed more variance in IL-6 levels than supernatant of B-cells from BC mice, when comparing standard deviations (p = 0.0175 (df = 54), n = 28, MBC: mean = 10661 pg/ml, SD = 21939 pg/ml; BC: mean = 490 pg/ml, SD = 960 pg/ml). Statistically significant results are marked. Statistical analysis was performed using Mann-Whitney tests, p-value refers to difference between MBC and BC. SD = standard deviation, N = sample size, U = Mann-Whitney U.

| | MBC | | | BC | | | | |
|---|---|---|---|---|---|---|---|---|
| | Mean | SD | N | Mean | SD | N | P-value | U |
| **Untreated** | 94.42 | 158.85 | 4 | 7.54 | 0.53 | 4 | ***0.0286*** | 0 |
| **Chloroquine 10 µM** | 81.36 | 91.30 | 4 | 24.88 | 20.33 | 4 | 0.6571 | 6 |
| **Chloroquine 25 µM** | 51.38 | 72.34 | 4 | 47.04 | 48.06 | 4 | 0.9714 | 8 |
| **Chloroquine 100 µM** | 32.41 | 45.22 | 4 | 42.17 | 24.86 | 4 | 0.3429 | 4 |
| **IRS 546 1.00 µM** | 98.85 | 160.34 | 4 | 68.56 | 13.51 | 4 | 0.3429 | 4 |
| **IRS 546 5.00 µM** | 337.05 | 476.20 | 4 | 229.26 | 26.32 | 4 | 0.6857 | 6 |
| **IRS 546 10.00 µM** | 441.31 | 582.08 | 4 | 336.91 | 45.24 | 4 | 0.8857 | 7 |
| **IRS 869 1 µM** | 27.96 | 37.68 | 4 | 31.34 | 7.78 | 4 | 0.3143 | 4 |
| **IRS 869 5 µM** | 137.57 | 191.29 | 4 | 95.87 | 30.37 | 4 | 0.8857 | 7 |
| **IRS 869 10 µM** | 197.76 | 243.24 | 4 | 136.76 | 59.08 | 4 | >0,9999 | 8 |
| **IRS 954 1 µM** | 30.52 | 42.78 | 4 | 27.17 | 18.81 | 4 | 0.3429 | 4 |
| **IRS 954 5 µM** | 79.79 | 102.96 | 4 | 45.64 | 15.53 | 4 | >0,9999 | 8 |
| **IRS 954 10 µM** | 129.74 | 117.44 | 4 | 49.85 | 7.28 | 4 | 0.6857 | 6 |
| **CpG 1826 0.10 µM** | 59611.60 | 65230.40 | 4 | 25212.18 | 3857.70 | 4 | >0,9999 | 8 |
| **CpG 1826 1.00 µM** | 69040.14 | 78409.96 | 4 | 28056.91 | 2392.57 | 4 | >0,9999 | 8 |
| **CpG 1826 5.00 µM** | 50583.28 | 58323.10 | 4 | 23226.67 | 2625.65 | 4 | >0,9999 | 8 |
| **R848 0.285 µM** | 8913.83 | 12969.74 | 4 | 2295.02 | 597.91 | 4 | 0.8857 | 7 |
| **R848 2.85 µM** | 23494.26 | 27650.86 | 4 | 3826.92 | 700.92 | 4 | 0.3429 | 4 |
| **R848 14.25 µM** | 21247.58 | 36565.00 | 4 | 4790.87 | 1237.21 | 4 | >0,9999 | 8 |
| **Imiquimod 0.5 µg/ml** | 1584.93 | 2610.08 | 4 | 329.28 | 75.20 | 4 | >0.9999 | 8 |
| **Imiquimod 5 µg/ml** | 4769.04 | 6118.04 | 4 | 3022.16 | 1024.60 | 4 | 0.6857 | 6 |
| **Imiquimod 10 µg/ml** | 6081.81 | 7632.92 | 4 | 4122.69 | 842.60 | 4 | 0.4857 | 5 |
| **BAFF 0.50 ng/ml** | 64.80 | 106.11 | 4 | 23.12 | 11.23 | 4 | 0.6857 | 6 |
| **BAFF 3.00 ng/ml** | 75.69 | 119.08 | 4 | 25.26 | 12.55 | 4 | 0.9714 | 8 |
| **BAFF 6.00 ng/ml** | 151.74 | 245.15 | 4 | 24.61 | 12.68 | 4 | 0.7714 | 7 |
| **IRS 661 1 µM** | 29.86 | 36.50 | 4 | 11.49 | 2.02 | 4 | 0.6857 | 6 |
| **IRS 661 5 µM** | 50.55 | 65.16 | 4 | 26.84 | 6.01 | 4 | >0,9999 | 8 |
| **IRS 661 10 µM** | 73.02 | 99.71 | 4 | 29.65 | 7.92 | 4 | >0.9999 | 8 |

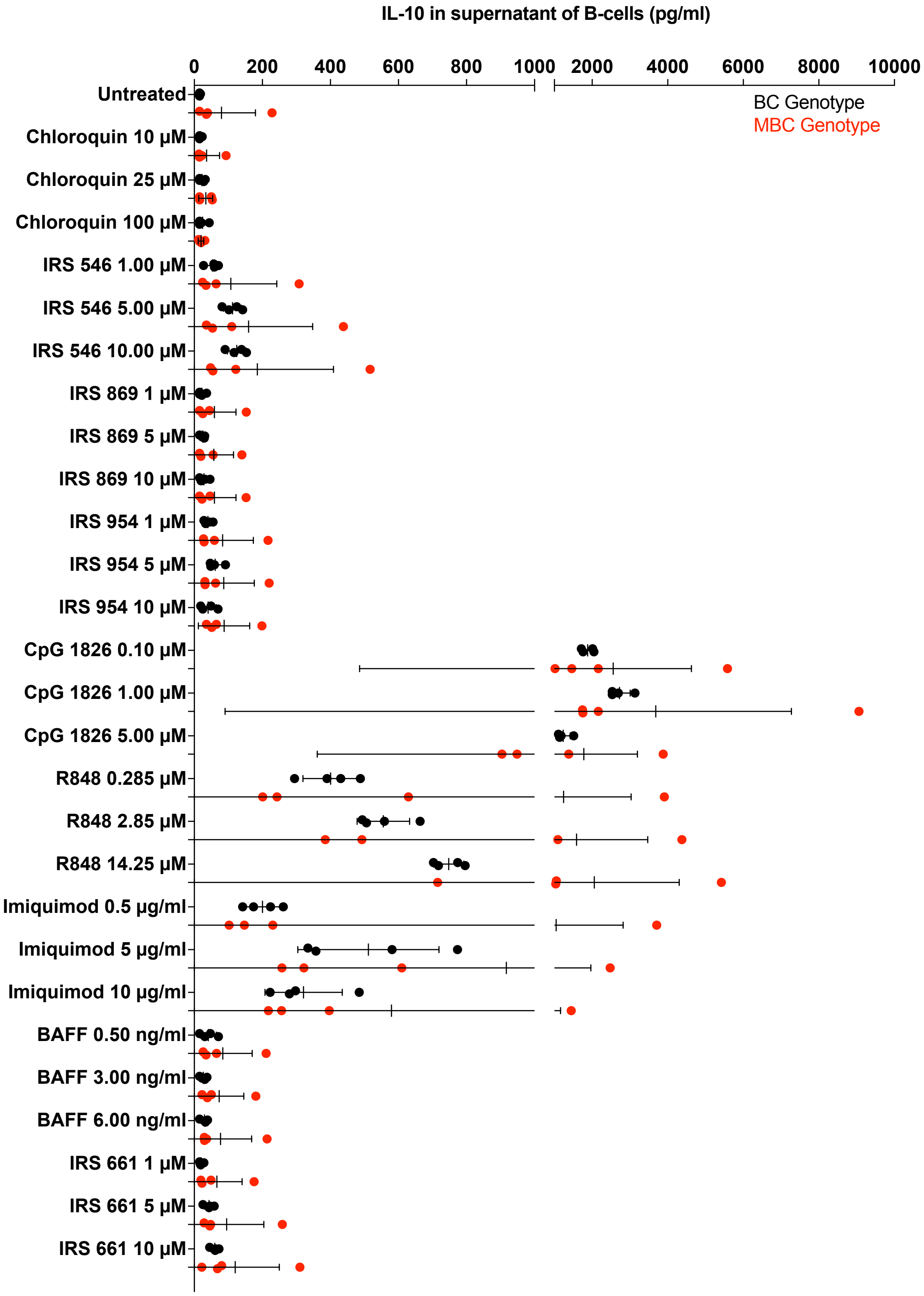

Figure 56 **IL-10 levels in supernatant of B-cells do not differ between MBC and BC mice, but MBC mice show a higher variance.** B-cells were treated for 5 days with the various TLR agonists and potential antagonists indicated. Supernatant of B-cells from MBC mice showed more variance in IL-10 levels than supernatant of B-cells from BC mice, when comparing standard deviations (p = 0.0016 (df = 54), n = 28, MBC: mean = 648 pg/ml, SD = 944 pg/ml; BC: mean = 53 pg/ml, SD = 73 pg/ml). Shown are the individual values, mean and standard deviation. For detailed statistics see Table 33.

Table 33 **IL-10 levels in supernatant of B-cells do not differ between MBC and BC mice, but MBC mice show a higher variance.** B-cells were treated for 5 days with the various TLR agonists and potential antagonists indicated. Supernatant of B-cells from MBC mice showed more variance in IL-10 levels than supernatant of B-cells from BC mice, when comparing standard deviations (p = 0.0016 (df = 54), n = 28, MBC: mean = 648 pg/ml, SD = 944 pg/ml; BC: mean = 53 pg/ml, SD = 73 pg/ml). Statistically significant results are marked. Statistical analysis was performed using Mann-Whitney tests, p-value refers to difference between MBC and BC. SD = standard deviation, N = sample size, U = Mann-Whitney U.

| | MBC | | | BC | | | | |
|---|---|---|---|---|---|---|---|---|
| | Mean | SD | N | Mean | SD | N | P-value | U |
| **Untreated** | 79.67 | 99.95 | 4 | 16.19 | 1.17 | 4 | 0.1429 | 3 |
| **Chloroquine 10 µM** | 36.29 | 38.23 | 4 | 17.49 | 3.77 | 4 | >0,9999 | 8 |
| **Chloroquine 25 µM** | 33.67 | 20.52 | 4 | 22.76 | 8.45 | 4 | 0.4857 | 5 |
| **Chloroquine 100 µM** | 19.71 | 8.23 | 4 | 24.15 | 13.60 | 4 | 0.6286 | 6 |
| **IRS 546 1.00 µM** | 107.67 | 134.67 | 4 | 53.56 | 18.63 | 4 | >0,9999 | 8 |
| **IRS 546 5.00 µM** | 159.52 | 188.58 | 4 | 112.49 | 26.44 | 4 | 0.6857 | 6 |
| **IRS 546 10.00 µM** | 185.35 | 223.65 | 4 | 124.79 | 27.25 | 4 | 0.6857 | 6 |
| **IRS 869 1 µM** | 59.36 | 63.40 | 4 | 22.41 | 9.77 | 4 | 0.3143 | 4 |
| **IRS 869 5 µM** | 57.48 | 57.72 | 4 | 24.81 | 6.92 | 4 | 0.6857 | 6 |
| **IRS 869 10 µM** | 59.31 | 63.44 | 4 | 28.26 | 13.65 | 4 | 0.4857 | 5 |
| **IRS 954 1 µM** | 83.05 | 90.43 | 4 | 40.25 | 12.08 | 4 | 0.8857 | 7 |
| **IRS 954 5 µM** | 86.39 | 90.26 | 4 | 61.48 | 20.94 | 4 | 0.8857 | 7 |
| **IRS 954 10 µM** | 87.56 | 75.23 | 4 | 40.56 | 23.57 | 4 | 0.3429 | 4 |
| **CpG 1826 0.10 µM** | 2557.04 | 2070.89 | 4 | 1883.75 | 171.76 | 4 | >0,9999 | 8 |
| **CpG 1826 1.00 µM** | 3682.09 | 3591.69 | 4 | 2724.87 | 284.61 | 4 | 0.3429 | 4 |
| **CpG 1826 5.00 µM** | 1780.15 | 1418.91 | 4 | 1234.69 | 188.59 | 4 | 0.8857 | 7 |
| **R848 0.285 µM** | 1246.28 | 1787.12 | 4 | 401.00 | 81.35 | 4 | >0,9999 | 8 |
| **R848 2.85 µM** | 1587.50 | 1885.79 | 4 | 555.66 | 77.23 | 4 | >0,9999 | 8 |
| **R848 14.25 µM** | 2057.55 | 2246.79 | 4 | 747.67 | 44.50 | 4 | 0.2000 | 3 |
| **Imiquimod 0.5 µg/ml** | 1047.40 | 1775.18 | 4 | 200.59 | 52.90 | 4 | >0.9999 | 8 |
| **Imiquimod 5 µg/ml** | 917.28 | 1052.34 | 4 | 511.69 | 207.37 | 4 | 0.8857 | 7 |
| **Imiquimod 10 µg/ml** | 579.87 | 584.00 | 4 | 321.26 | 113.74 | 4 | >0.9999 | 8 |
| **BAFF 0.50 ng/ml** | 84.09 | 86.38 | 4 | 41.32 | 23.74 | 4 | 0.6857 | 6 |
| **BAFF 3.00 ng/ml** | 72.93 | 72.75 | 4 | 26.87 | 9.39 | 4 | 0.2000 | 3 |
| **BAFF 6.00 ng/ml** | 77.34 | 91.21 | 4 | 29.79 | 9.96 | 4 | 0.8857 | 7 |
| **IRS 661 1 µM** | 66.69 | 73.88 | 4 | 19.88 | 5.66 | 4 | 0.1143 | 2 |
| **IRS 661 5 µM** | 95.25 | 109.43 | 4 | 43.46 | 13.78 | 4 | 0.6857 | 6 |
| **IRS 661 10 µM** | 120.43 | 129.30 | 4 | 60.46 | 11.37 | 4 | 0.4857 | 5 |

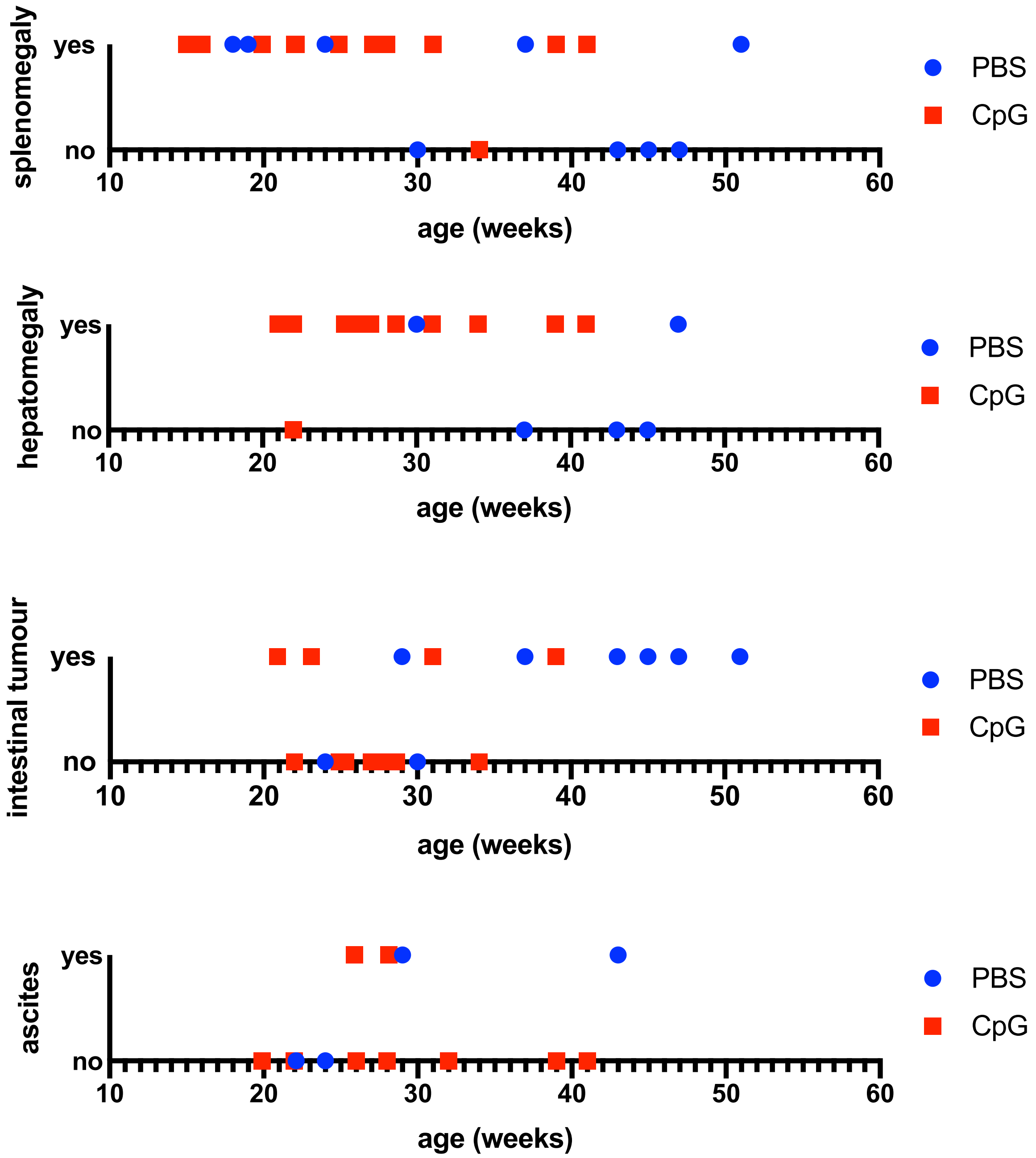

Figure 57 **Stratification of the occurrence of splenomegaly, hepatomegaly, intestinal tumours and ascites in MBC mice at death by the age at death did not reveal any patterns**. Autopsy results at death of MBC mice treated either with PBS (control) or CpG are shown. Stratification was performed by age at death and the identification of splenomegaly, hepatomegaly, intestinal tumours and ascites at death.

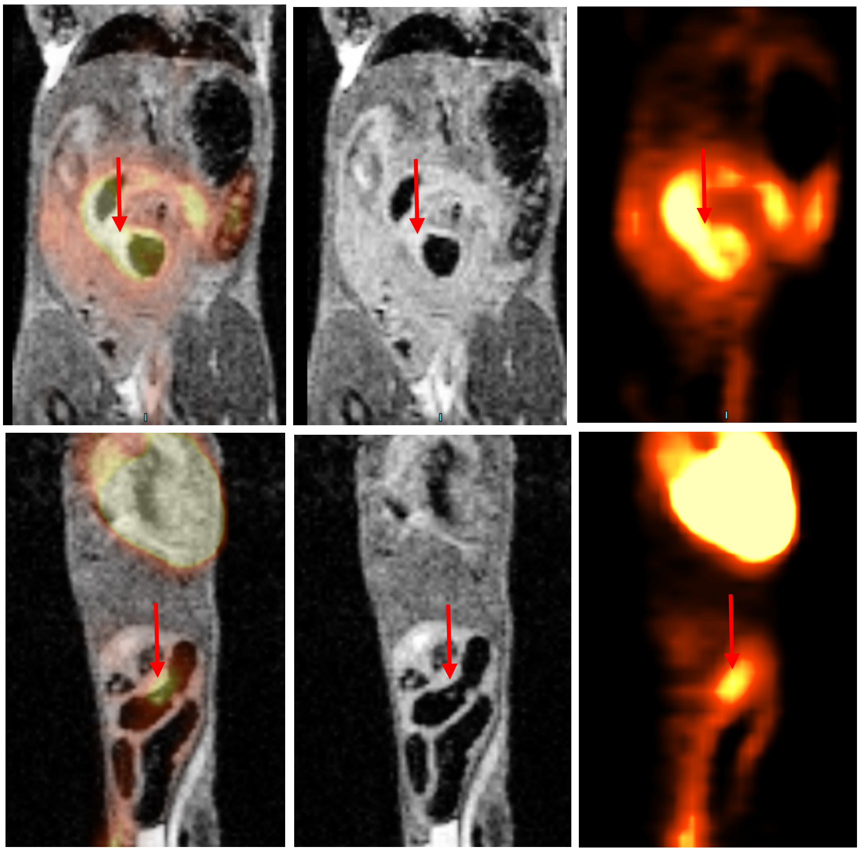

Figure 59 **MBC mice show intestinal tumours, example.** Images of mouse 66 (PBS-treated) at the age of 15 weeks shows high FDG-PET signal around several bowel loops. Red arrows indicate protruding intestinal tumours.

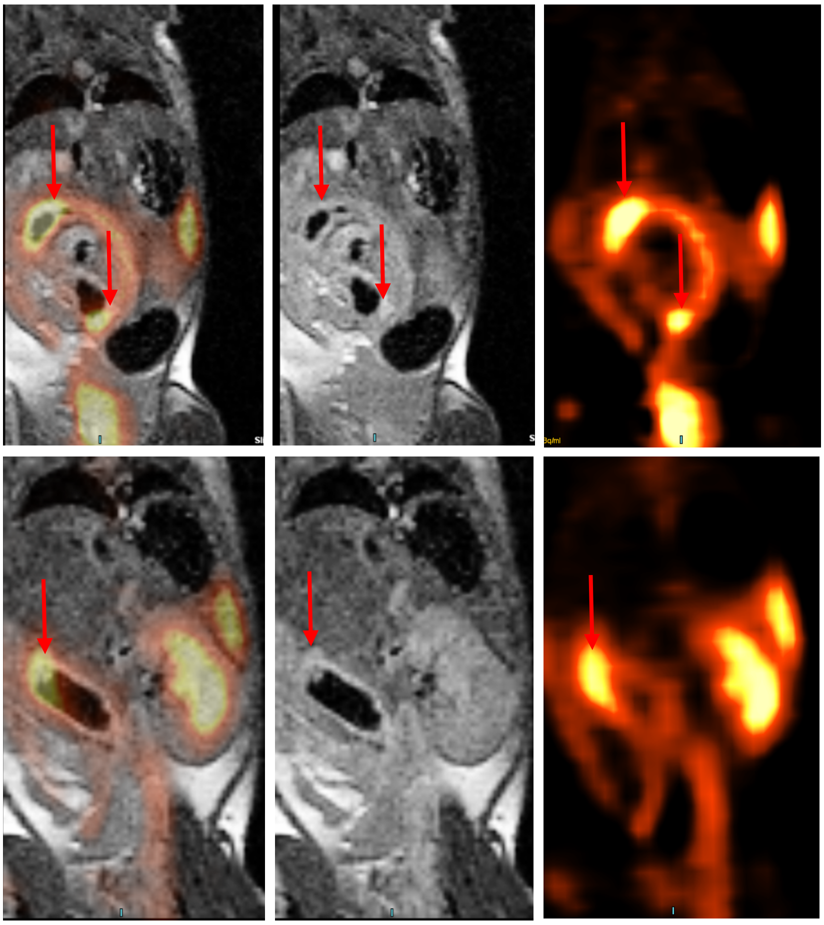

Figure 58 **MBC mice show intestinal tumours, example.** Images of mouse 83 (PBS-treated) at the age of 15 weeks shows high FDG-PET signal around several bowel loops. Red arrows indicate protruding intestinal tumours.

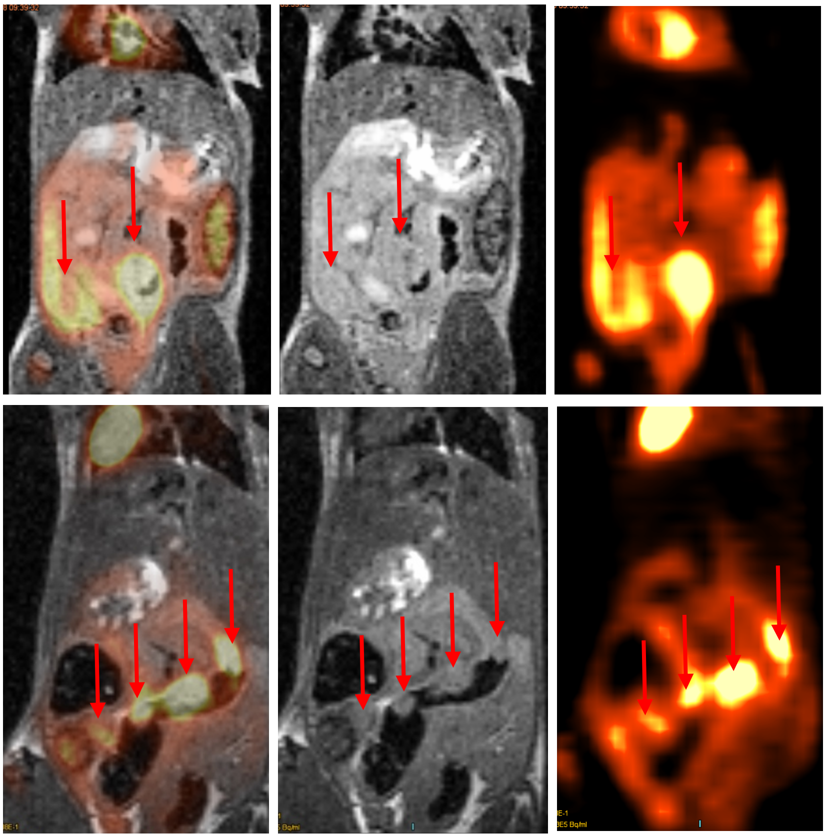

Figure 61 **MBC mice show intestinal tumours, example.** Images of mouse 67 (PBS-treated) at the age of 15 weeks (top) and 21 weeks (bottom) shows high FDG-PET signal around several bowel loops. Red arrows indicate protruding intestinal tumours.

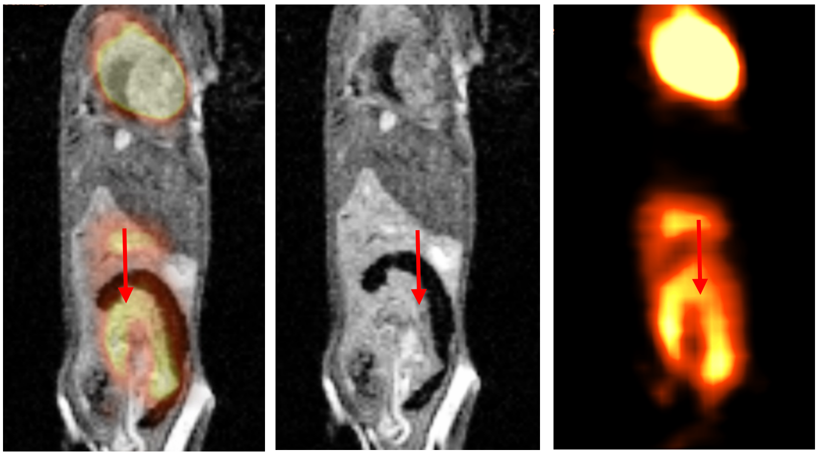

Figure 60 **MBC mice show intestinal tumours, example.** Images of mouse 98 (PBS-treated) at the age of 15 weeks shows high FDG-PET signal around several bowel loops. Red arrows indicate protruding intestinal tumours.

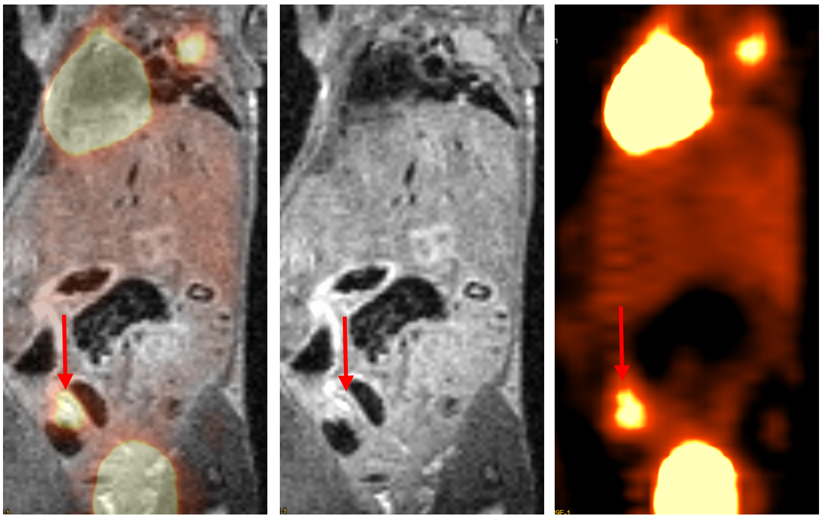

Figure 62 **MBC mice show intestinal tumours, example.** Images of mouse 109 (CpG-treated) at the age of 15 weeks shows high FDG-PET signal around several bowel loops. Red arrows indicate protruding intestinal tumours.

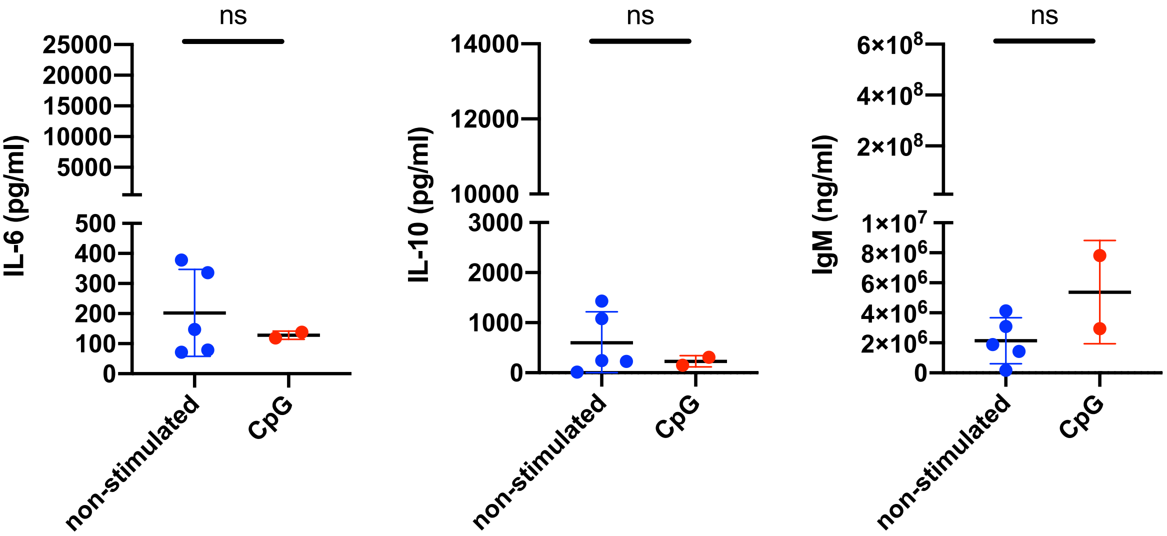

Figure 63 **Cytokine levels in serum at death did not differ between CpG-treated and non-stimulated MBC mice with ascites**. Treatment groups are indicated. Non-stimulated refers to pooled values from PBS-treated MBC mice and untreated MBC mice. For statistics see Table 34. Each dot represents one animal. ns = not significant. Bars shown represent mean and SD.

Table 34 **Cytokine levels in serum at death did not differ between CpG-treated and non-stimulated MBC mice with ascites**. Mean and SD values represent serum IL-6, IL-10 and IgM levels in MBC mice with the treatment indicated at the time of death, as measured using ELISA. Statistical analysis was performed using Mann-Whitney tests, p-value refers to difference between MBC mice with CpG treatment and non-stimulated MBC mice (PBS treatment and no treatment pooled). SD = standard deviation, N = sample size, U = Mann-Whitney U.

| | **MBC genotype – CpG treatment** | | | **MBC genotype – PBS and no treatment pooled** | | | | |
|---|---|---|---|---|---|---|---|---|
| Parameter | Mean | SD | N | Mean | SD | N | P-value | U |
| **IL-6 (pg/ml)** | 14 | 129 | 2 | 203 | 145 | 5 | 0.8571 | 4 |
| **Il-10 (pg/ml)** | 228 | 112 | 2 | 599 | 619 | 5 | 0.8571 | 4 |
| **IgM (ng/ml)** | 5.38E+06 | 3.44E+06 | 2 | 2.14E+06 | 1.53E+06 | 5 | 0.3810 | 2 |

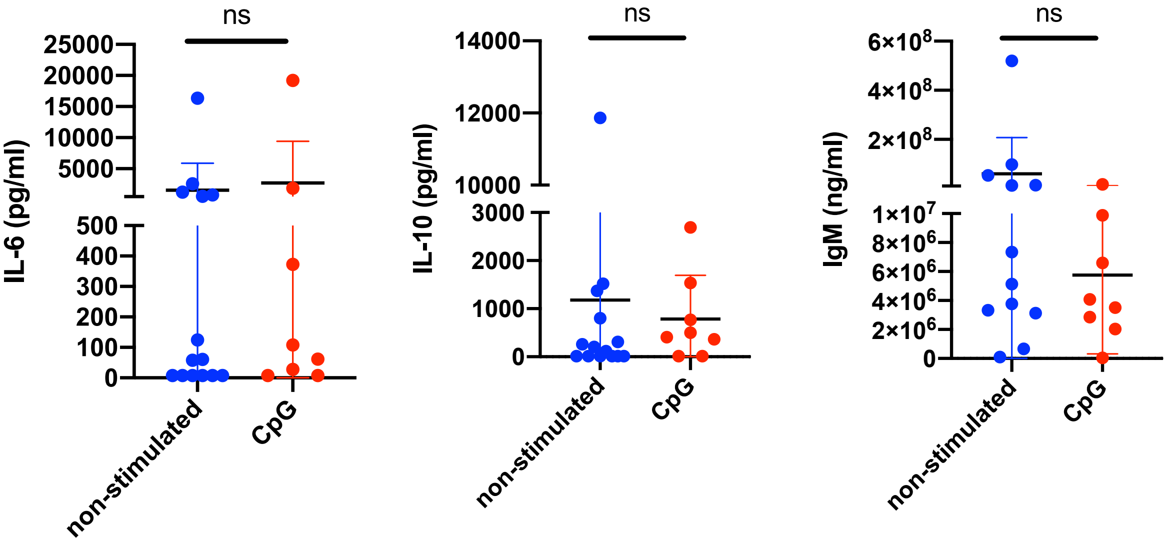

Figure 64 **Cytokine levels in serum at death did not differ between CpG-treated and non-stimulated MBC mice without ascites**. Treatment groups are indicated. Non-stimulated refers to pooled values from PBS-treated MBC mice and untreated MBC mice. For statistics see Table 35. Each dot represents one animal. ns = not significant. Bars shown represent mean and SD.

Table 35 **Cytokine levels in serum at death did not differ between CpG-treated and non-stimulated MBC mice without ascites**. Mean and SD values represent serum IL-6, IL-10 and IgM levels in MBC mice with the treatment indicated at the time of death, as measured using ELISA. Statistical analysis was performed using Mann-Whitney tests, p-value refers to difference between MBC mice with CpG treatment and non-stimulated MBC mice (PBS treatment and no treatment pooled). SD = standard deviation, N = sample size, U = Mann-Whitney U.

| | **MBC genotype – CpG treatment** | | | **MBC genotype – PBS and no treatment pooled** | | | | |
|---|---|---|---|---|---|---|---|---|
| Parameter | Mean | SD | N | Mean | SD | N | P-value | U |
| **IL-6 (pg/ml)** | 2706 | 6693 | 8 | 1562 | 4323 | 14 | 0.6425 | 49 |
| **Il-10 (pg/ml)** | 788 | 909 | 8 | 1182 | 3116 | 14 | 0.2798 | 40 |
| **IgM (ng/ml)** | 5.75E+06 | 5.44E+06 | 8 | 6.02E+07 | 1.48E+08 | 12 | 0.3431 | 35 |

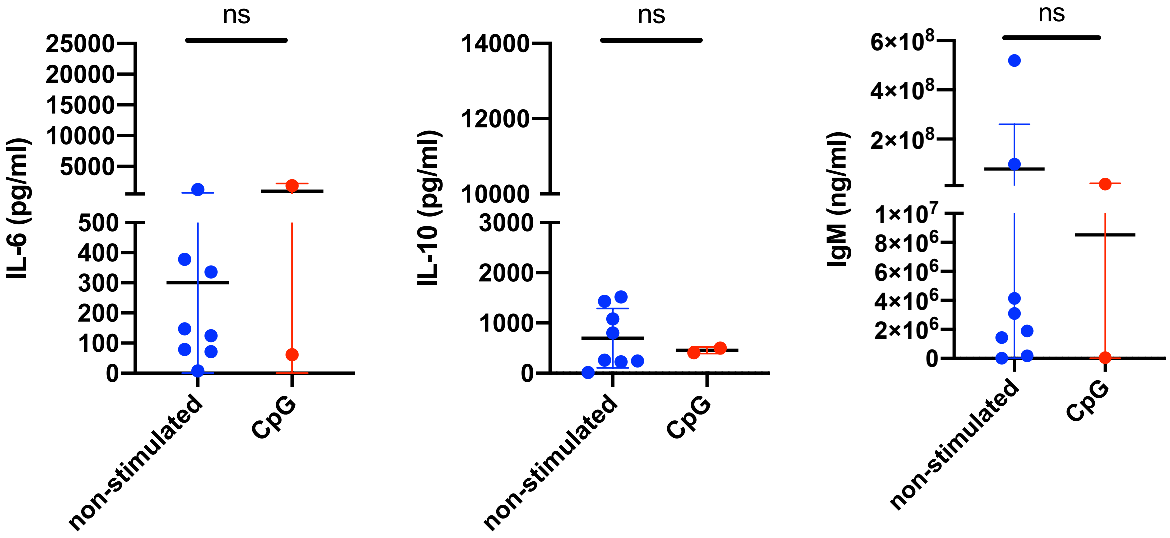

Figure 65 **Cytokine levels in serum at death did not differ between CpG-treated and non-stimulated MBC mice with intestinal tumours**. Treatment groups are indicated. Non-stimulated refers to pooled values from PBS-treated MBC mice and untreated MBC mice. For statistics see Table 36. Each dot represents one animal. ns = not significant. Bars shown represent mean and SD.

Table 36 **Cytokine levels in serum at death did not differ between CpG-treated and non-stimulated MBC mice with intestinal tumours**. Mean and SD values represent serum IL-6, IL-10 and IgM levels in MBC mice with the treatment indicated at the time of death, as measured using ELISA. Statistical analysis was performed using Mann-Whitney tests, p-value refers to difference between MBC mice with CpG treatment and non-stimulated MBC mice (PBS treatment and no treatment pooled). SD = standard deviation, N = sample size, U = Mann-Whitney U.

| | **MBC genotype – CpG treatment** | | | **MBC genotype – PBS and no treatment pooled** | | | | |
|---|---|---|---|---|---|---|---|---|
| Parameter | Mean | SD | N | Mean | SD | N | P-value | U |
| **IL-6 (pg/ml)** | 964 | 1276 | 2 | 300 | 408 | 8 | 0.8889 | 7 |
| **Il-10 (pg/ml)** | 456 | 66 | 2 | 697 | 592 | 8 | >0.9999 | 8 |
| **IgM (ng/ml)** | 8.52E+06 | 1.20E+07 | 2 | 7.86E+07 | 1.82E+08 | 8 | 0.8889 | 7 |

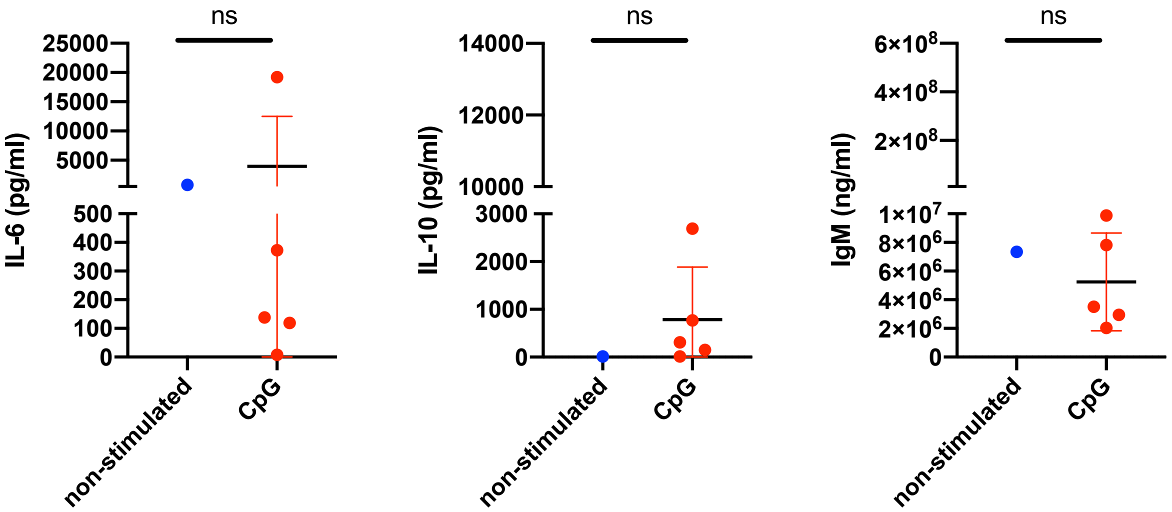

Figure 66 **Cytokine levels in serum at death did not differ between CpG-treated and non-stimulated MBC mice without intestinal tumours**. Treatment groups are indicated. Non-stimulated refers to pooled values from PBS-treated MBC mice and untreated MBC mice. For statistics see Table 37. Each dot represents one animal. ns = not significant. Bars shown represent mean and SD.

Table 37 **Cytokine levels in serum at death did not differ between CpG-treated and non-stimulated MBC mice without intestinal tumours**. Mean and SD values represent serum IL-6, IL-10 and IgM levels in MBC mice with the treatment indicated at the time of death, as measured using ELISA. Statistical analysis was performed using Mann-Whitney tests, p-value refers to difference between MBC mice with CpG treatment and non-stimulated MBC mice (PBS treatment and no treatment pooled). SD = standard deviation, N = sample size, U = Mann-Whitney U.

| | **MBC genotype – CpG treatment** | | | **MBC genotype – PBS and no treatment pooled** | | | | |
|---|---|---|---|---|---|---|---|---|
| Parameter | Mean | SD | N | Mean | SD | N | P-value | U |
| **IL-6 (pg/ml)** | 3967 | 8515 | 5 | 802 | / | 1 | / | / |
| **Il-10 (pg/ml)** | 786 | 1102 | 5 | 16 | / | 1 | / | / |
| **IgM (ng/ml)** | 5.24E+06 | 3.41E+06 | 5 | 7.34E+06 | / | 1 | / | / |

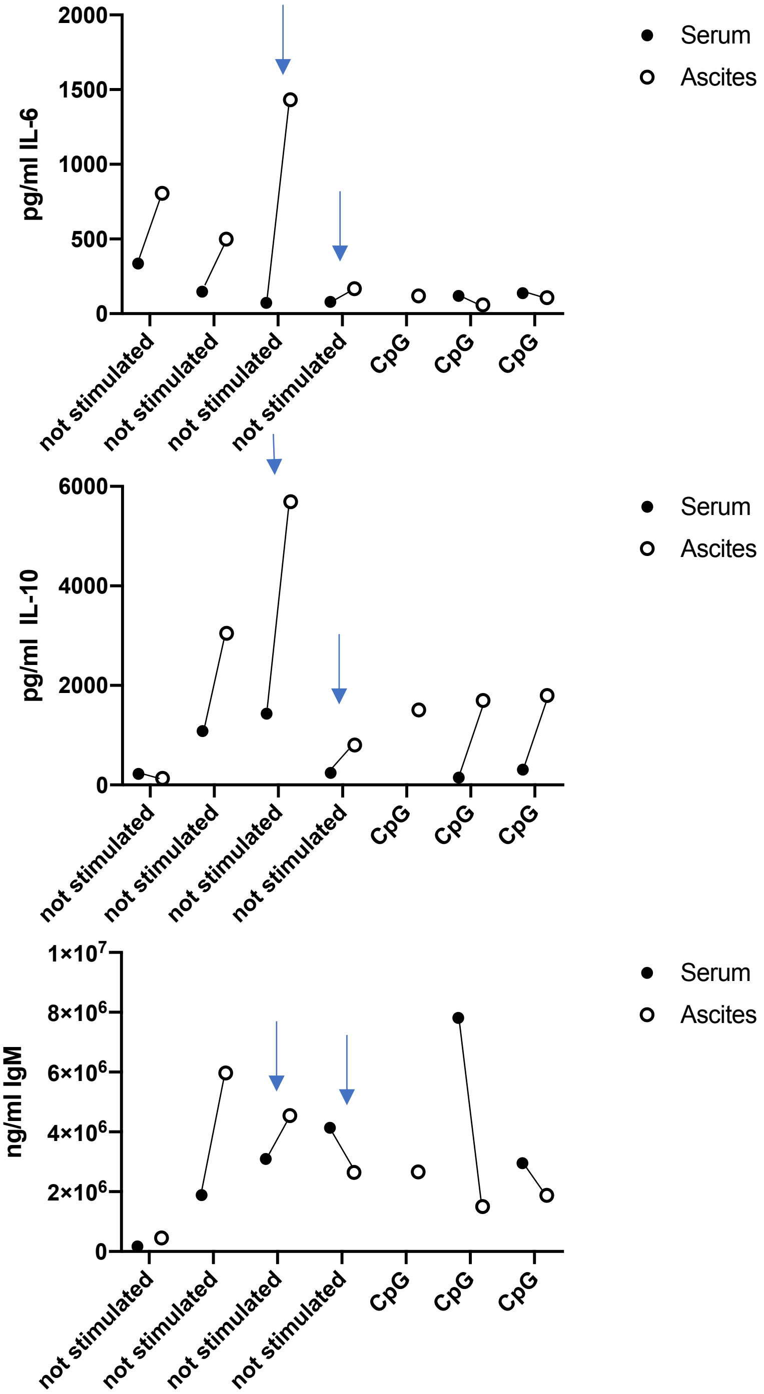

Figure 67 **Comparison of ascitic fluid and serum cytokine levels in individual mice suggests increased cytokine levels in ascitic fluid**. Although not statistically significant, IL-6 was higher in ascitic fluid than in serum in unstimulated mice but not in CpG-treated mice. Similarly, on an individual basis IL-10 was higher in ascitic fluid than in serum in both unstimulated mice and CpG-treated mice. IgM seems to be higher in ascitic fluid than in serum in unstimulated mice but lower in CpG-treated mice. Arrows indicate MBC mice in which an intestinal tumour was identified via autopsy at death. Each two dots connected represent one animal. For statistics see Table 38, Table 39 and Table 40.

Table 38 **Cytokine levels of CpG-treated MBC mice with ascites did not differ between serum and ascitic fluid**. Mean and SD values represent IL-6, IL-10 and IgM levels in CpG-treated MBC mice with ascites at the time of death, as measured using ELISA. Statistical analysis was performed using Wilcoxon matched-pairs signed rank tests, p-value refers to difference between serum and ascitic fluid. SD = standard deviation, N = sample size, W = sum of signed ranks.

| | **CpG-treated MBC mice with ascites - serum** | | | **CpG-treated MBC mice with ascites – ascitic fluid** | | | | |
|---|---|---|---|---|---|---|---|---|
| Parameter | Mean | SD | N | Mean | SD | N | P-value | W |
| **IL-6 (pg/ml)** | 129 | 14 | 2 | 95 | 31 | 3 | / | / |
| **Il-10 (pg/ml)** | 228 | 112 | 2 | 1667 | 148 | 3 | / | / |
| **IgM (ng/ml)** | 5.38E+06 | 3.44E+06 | 2 | 2.02E+06 | 5.91E+05 | 3 | / | / |

Table 39 **Cytokine levels of non-stimulated MBC mice with ascites did not differ between serum and ascitic fluid**. Mean and SD values represent IL-6, IL-10 and IgM levels in non-stimulated MBC mice with ascites at the time of death, as measured using ELISA. Non-stimulated refers to pooled data of PBS-treated MBC mice and untreated MBC mice. Statistical analysis was performed using Wilcoxon matched-pairs signed rank tests, p-value refers to difference between serum and ascitic fluid. SD = standard deviation, N = sample size, W = sum of signed ranks.

| | **Non-stimulated MBC mice with ascites - serum** | | | **Non-stimulated MBC mice with ascites – ascitic fluid** | | | | |
|---|---|---|---|---|---|---|---|---|
| Parameter | Mean | SD | N | Mean | SD | N | P-value | W |
| **IL-6 (pg/ml)** | 159 | 123 | 4 | 726 | 538 | 4 | 0.1250 | 10 |
| **Il-10 (pg/ml)** | 745 | 606 | 4 | 2419 | 2514 | 4 | 0.2500 | 8 |
| **IgM (ng/ml)** | 2.32E+06 | 1.70E+06 | 4 | 3.41E+06 | 2.39E+06 | 4 | 0.6250 | 4 |

Table 40 **Cytokine levels of MBC mice with ascites did not differ between serum and ascitic fluid**. Mean and SD values represent IL-6, IL-10 and IgM levels in MBC mice with ascites at the time of death, as measured using ELISA. Data from CpG-treated, PBS-treated and untreated MBC mice were pooled. Statistical analysis was performed using Wilcoxon matched-pairs signed rank tests, p-value refers to difference between serum and ascitic fluid. SD = standard deviation, N = sample size, W = sum of signed ranks.

| | **MBC mice with ascites, treatments pooled - serum** | | | **MBC mice with ascites, treatments pooled – ascitic fluid** | | | | |
|---|---|---|---|---|---|---|---|---|
| Parameter | Mean | SD | N | Mean | SD | N | P-value | W |
| **IL-6 (pg/ml)** | 149 | 97 | 6 | 456 | 509 | 7 | 0.1562 | 15 |
| **Il-10 (pg/ml)** | 573 | 543 | 6 | 2097 | 1824 | 7 | 0.0625 | 19 |
| **IgM (ng/ml)** | 3.34E+06 | 2.57E+06 | 6 | 2.81E+06 | 1.88E+06 | 7 | 0.8438 | - 3 |

## Declaration of own contributions

This thesis was conducted at the Interfaculty Institute for Cell Biology, Department of Immunology under the supervision of Prof. Dr. Alexander Weber.

The study was designed by Prof. Dr. Alexander Weber (habilitated supervisor), Dr. Olaf-Oliver Wolz (direct supervisor), Dr. Manfred Kneilling (group leader of first cooperating group), Dr. Barbara Schörg (direct supervisor in first cooperating group) and Dr. Dominik Sonanini (group leader of second cooperating group).

The experiments were executed by me in collaboration with Dr. Olaf-Oliver Wolz after initial training by the lab members Dr. Olaf-Oliver Wolz, Dr. Barbara Schörg and Sabine Dickhöfer. I was involved in one of four acquisition days of the PET-MRI data shown in section 2.7. The FACS analysis shown in section 2.2 was performed by Dr. Olaf-Oliver Wolz. Sabine Dickhöfer performed a part of the ELISAs shown in section 2.4 and 2.5. Data evaluation, analysis and statistical testing was performed independently by me. For a detailed list see the table attached below.

I ensure that I wrote the manuscript independently under the guidance of Dr. Alexander Weber and Dr. Olaf-Oliver Wolz and that I used no further sources as the ones indicated.

| **Figure/Table** | **Own contribution** |
|---|---|
| Figure 8, Figure 50, Figure 9<br>Table 5 | Autopsy and data acquisition performed by Dr. Olaf-Oliver Wolz: n = 7.<br>Autopsy and data acquisition performed by me and Dr. Olaf-Oliver Wolz: n = 9.<br>Data evaluation and analysis performed by me. |
| Figure 51, Figure 52, Figure 53, Figure 54, Figure 55, Figure 56<br>Table 6, Table 7, Table 29, | Isolation and stimulation of the cells performed by Dr. Olaf-Oliver Wolz.<br>ELISA performed by Sabine Dickhöfer: n = 12.<br>ELISA performed by me: n = 4.<br>Data evaluation and analysis performed by me. |

| | |
|---|---|
| Table 30, Table 31, Table 32, Table 33 | |
| Figure 10 | Data collection and analysis performed by Dr. Olaf-Oliver Wolz. |
| Figure 57<br>Table 8, Table 9, Table 10, Table 11 | Autopsies performed by Dr. Olaf-Oliver Wolz.<br>Data evaluation and analysis performed by me. |
| Figure 11, Figure 12, Figure 13, Figure 15, Figure 17, Figure 18, Figure 17, Figure 22, Figure 23, Figure 25, Figure 27, Figure 28, Figure 30, Figure 32, Figure 33, Figure 35, Figure 36, Figure 37, Figure 39, Figure 30, Figure 43, Figure 44, Figure 58, Figure 59, Figure 60, Figure 61, Figure 62<br>Table 12, Table 13, Table 14, Table 15, Table 16, Table 17, Table 18, Table 19, Table 20, Table 21, Table 22, Table 23, Table 24 | PET-MRI measurements in week 15, 21 and 27 performed by Dr. Olaf-Oliver Wolz and Dr. Barbara Schörg.<br>PET-MRI measurements in week 33 performed by Dr. Olaf-Oliver Wolz, Dr. Barbara Schörg and me.<br>Data evaluation and analysis performed by me. |
| Figure 45, Figure 63, Figure 64, Figure 65, Figure 66, Figure 67<br>Table 25, Table 34, Table 35, Table 36 and Table 37, Table 38, Table 39, Table 40 | Collection of serum performed by Dr. Olaf-Oliver Wolz.<br>ELISA performed by me.<br>Data evaluation and analysis performed by me. |

| | |
|---|---|
| Figure 46, Figure 47 | PET-MRI measurements performed by me and Dr. Dominik Sonanini.<br>Data evaluation and analysis performed by me and Dr. Dominik Sonanini. |
| Figure 48, Figure 49 | Cell preparation and flow cytometry measurements performed by me and Dr. Olaf-Oliver Wolz.<br>Data evaluation and analysis performed by me. |

Tübingen, the

C. Obermüller

[Signature doctoral candidate]

Tübingen, the 17th of May 2021

Alexander Weber

[Signature habilitated supervisor]

# Acknowledgement

I sincerely thank Dr. Olaf-Oliver Wolz and Dr. Alexander Weber for their continuous support, encouragement and mentorship throughout the entire project. My thanks also go to Dr. Barbara Schörg, Dr. Dominik Sonanini and Sabine Dickhöfer for their practical support and teaching throughout the project. Finally, I would like to thank the entire Weber lab for their ongoing feedback and support of my work.